UNIVERSIDAD DE LAS PALMAS
DE GRAN CANARIA

INSTITUTO UNIVERSITARIO
SIANI
INGENIERIA COMPUTACIONAL

TESIS DOCTORAL

NUMERICAL MODEL FOR THE DYNAMIC ANALYSIS OF PILE FOUNDATIONS

Luis Alberto Padrón Hernández

Las Palmas de Gran Canaria, Enero de 2009

Numerical model for the dynamic analysis of pile foundations

Programa de doctorado:
Sistemas Inteligentes y Aplicaciones Numéricas en Ingeniería
Instituto Universitario SIANI

Autor:	Director:	Director:
Luis A. Padrón Hernández	Orlando Maeso Fortuny	Juan J. Aznárez González

Las Palmas de Gran Canaria, Enero 2009

To my wife, Kathy

For her endless support
and all the time that I did not
spend with her to accomplish this task

Acknowledgements

I am deeply indebted to my supervisors, Prof. Orlando Maeso and Prof. Juan José Aznárez. It is not only that this thesis would not have been possible without their support, advice and encouragement, but, which is even more important to me, had it not been for them, I would not be pursuing a research career today. Thank you for your friendship and help, and for having put within my reach all the resources and opportunities I have had during these years.

I wish to thank the Professors of the Continuum Mechanics and Structures Division, Francisco Chirino and José María Emperador, who always helped me whenever I turned to them for assistance.

I also want to extent my appreciation to all the Professors and colleagues at the University Institute of Intelligent Systems and Numerical Applications in Engineering (SIANI), where I developed this work. Special thanks: to Professors Gabriel Winter, Blas Galván and Pedro Cuesta, who first introduced me to research and, since then, have always supported me; to Professors Rafael Montenegro and José María Escobar, who supervised my MS thesis; to Prof. Antonio Falcón for helping me several times during these last years; to Dr. Eduardo Barrera, who saved me one thousand times with the workstations, and from whom I learnt almost everything I know about Linux; and to Juan Ignacio González, for his valuable help with everything regarding everyday life in the institute. I also wish to thank all the people who have worked with me at the Continuum Mechanics and Structures Division and who cheered up and enriched my long hours. Special thanks to Juan José Pérez and Alejandro Mendoza, who left a big gap when leaving, and to Asunción González, Borja Guerra, Jaime Cambre and Ariel Santana.

I am highly greatful to Prof. Dimitri Beskos and Prof. George Mylonakis for hosting me at the University of Patras, and for their help, suggestions and supervision, leading to the results presented in chapter 5. I want to thank George Papagiannopoulous, Theodore Karavasilis, George Kamaris, Panos Papastylianou, Panos Kloukinas and many other Greek colleagues for their help and company during my stay.

I am beholden to Prof. Eduardo Kausel for receiving me warmly at the Massachusetts Institute of Technology, and for giving me the valuable opportunity to work with him and learn from him. Many thanks to my colleagues at the Department of Civil and Environmental Engineering, especially to Gonzalo Corral and Sherif Adel Akl for their help and kindness.

I would like to express special thanks to my beloved family: to my father and my mother, who taught and encouraged me to do my best always; to my brother, the best brother and friend that one can have; to my grandmothers, uncles, aunts and cousins, who were there during the good and the difficult times; and to my wife, Kathy, for without her love and wholehearted support at all times, these years of work would have been much harder to endure.

The author, who is recipient of the FPU research fellowship AP-2004-4858 from the Ministry of Education and Science of Spain, wishes to acknowledge this financial support.

This work was also supported by the Ministry of Education and Science of Spain through research projects BIA2004-03955-C02-02 (Dynamic behaviour of dams, piles and tunnels. Effects of the soil-structure interaction phenomena under seismic excitation and moving loads) and BIA2007-67612-C02-01 (Dynamic behaviour of dams and piles taking soil-structure interaction effects into account. Seismic loads and wave propagation) and co-financed by the European Fund of Regional Development.

Contents

List of Figures

List of Tables

Chapter 1

Introduction and Background

In many occasions, the characteristics of the location of a civil engineering structure, and the loads to which such construction is expected to be subjected, make it advisable to select pile foundations as the structural supporting system. This occurs, especially, when the underlying soil has a low bearing capacity or it is not stable enough, when there exists deeper rock or stiff soil with higher bearing capacity, when design loads are very large or relatively large horizontal or uplift loads are expected, or when the estimated settlement for other system foundations is unacceptable. Besides, the use of pile foundations can improve the seismic response of the structures by decreasing its seismic input and increasing the system damping. For all these reasons, pile foundations are often used to support tall buildings, tall bridge piers, nuclear reactor buildings, marine structures and offshore platforms.

In common engineering practice, simplified procedures are generally used for the design of pile foundations. They are based on experimental results, analytical and/or numerical parametric analyses, experience and simplified engineering approaches. These simplified methodologies are able to predict adequately the static or pseudo-static response of pile foundations, even when non-linearities are involved. On the contrary, they are not yet that accurate in modelling the dynamic behaviour of pile foundations, which is, in general, highly frequency-dependent. A related problem of special difficulty, due to the large number of phenomena involved, is that of the seismic response of pile foundations and pile supported structures, which is still not fully understood.

For this reason, and even though a great amount of research on the dynamic behaviour of pile foundations has been carried out during the last three decades, there exists yet the need of achieving a better understanding on the topic. Other related problems are those concerning the influence, on the dynamic response of structures, of the soil-foundation system compliance (Soil-Structure interaction effects) and of the presence of neighbouring constructions (Structure-Soil-Structure

interaction effects). Consequently, different research lines, based on both experimental and/or numerical/analytical techniques, are being carried out nowadays on these topics. One of them is focused on the formulation of numerical tools able to model the dynamic behaviour of the soil-foundation-structure system in a rigorous way, being this research line the frame of this work.

More specifically, a three-dimensional boundary element – finite element model for the dynamic analysis of pile foundations and pile supported structures has been formulated and implemented. It represents a direct approach to the problem in the frequency domain, and it is able to analyse the response of multiple multistorey pile supported structures founded on multilayered soils of generic stratigraphy and topography. In this coupling model, the Finite Element Method (FEM) is used to model piles and superstructures, while stratified soils are modelled by the Boundary Element Method (BEM), each stratum being considered as a continuum, semi-infinite, isotropic, viscoelastic medium.

As said above, the model presented in this dissertation is a linear formulation of the problem. Obviously, non-linear effects can be of primary importance on the dynamic response of pile foundations. For instance, liquefaction or slope movement can produce very large shear forces and moments on the piles. Gapping or sliding at the pile-soil interface, or partial losses of shear strength in the soil, due to strong shaking, can also affect the foundation response. However, soil-structure interaction effects, even in the linear range, are not yet fully understood and, therefore, the development of linear direct models such as the one presented herein is completely justified.

1.1 Literature review

Due to its ability to represent the dynamic behaviour of boundless regions, the boundary element method is particularly well suited to soil-structure interaction problems, since the radiation of waves towards infinity is inherent to the integral representation used for the model, and also because the domain does not need to be discretized. A broad range of engineering problems can be considered to belong to this subject of soil-structure interaction. Some good reviews on the application of boundary element techniques to this topic can be found, for instance, in the recent state of the art book by Hall and Oliveto [1], with contributions from leading experts on the subject, and a comprehensive review until 1997 was provided by Beskos in [2] and [3].

The dynamic analysis of foundations embedded in a uniform or layered elastic half-space has been the subject of much research. The time-harmonic boundary element method, in its direct and indirect forms, has been used extensively to compute the dynamic response of shallow and embedded foundations in the fre-

quency domain, both in two and three dimensions [4–24]. On the other hand, and focusing on the analysis of deep foundations, which is the main topic of this dissertation, the first works related to the dynamic response of piles appeared during the early sixties, and many of them are considered in the classic text on pile foundations by Poulos and Davis [25]. Two more recent reviews on the topic were contributed by Novak [26] and Pender [27], and more references can be found in the already mentioned papers by Beskos [2] and [3].

The steady-state dynamic response of pile foundations has been studied through rigorous analytical solutions [28–31], simplified semi-analytical procedures (including Winkler-type models) [32–43] and different numerical techniques: FEM models [44–50]; BEM-FEM schemes or boundary elements in conjunction with different half-space Green's functions formulations for the soil, and structural monodimensional elements for the piles [51–60]; and multidomain BEM formulations [61–64].

Although a great deal of this research has been focused on the forced vibration problem, much of it has also dealt with the kinematic response of pile foundations. For instance, parametric studies of the seismic response of single piles and pile groups to Rayleigh waves and to vertically and obliquely incident body waves have been reported in [65–73]. Some other works have dealt explicitly with the kinematic effects on pile forces and moments [74–77].

Each one of the groups of methods that has been proposed for the dynamic analysis of pile foundations has its own advantages and disadvantages. Rigorous analytical solutions allow gaining insight into the underlying physics of the problem, and offer solutions with very low computing effort. However, their inherent analytical complexity and their orientation on a specific problem make them inflexible and difficult to enhance. The main advantages of the simplified semi-analytical procedures are their low computing requirements and their relative simplicity, but most of them, as discrete models that do not include soil continua, are not able to model rigorously phenomena such as material and radiation damping, inertial effects of the soil media, and interaction effects between piles. As for the numerical schemes, finite element methods, with obvious limitation for modelling problems involving unbounded domains, need special care on the discretizations and the treatment of the radiated energy, though their flexibility has favoured the development of a number of techniques to address linear and non-linear response of piles. Boundary element - finite element formulations, including those based on particular Green's functions to model the pile-soil interaction, are probably the best option to address the problem because of their rigorousness and their low computing requirements. Finally, multidomain boundary element formulations are flexible and rigorous but require large computing times and important efforts in preparing meshes and data files.

Regarding the superstructure response, soil-structure interaction (SSI) in build-

ings has been a focus of attention for more than thirty years. Pioneering works, investigating the influence of soil compliance on the dynamic behaviour of one-storey shear-structures, were presented by Parmelee [78], Perelman et al [79], Parmelee et al [80] and Sarrazin et al [81]. Following these studies, Veletsos and Meek [82] and Bielak [83] proposed, separately, approximate one-degree-of-freedom substructure models for design purposes. In these cases, the available results for the soil impedance functions, *i.e.* rigid shallow circular plate solutions, were used. A decade later, Wolf presented a comprehensive study on SSI in his classic text [84]. Subsequent works enhanced these approaches and studied the influence of foundation embedment and kinematic interaction effects (*e.g.* [85–88]). As shown above, impedance functions and seismic response of piles and pile groups have been presented for several configurations and load conditions. Those and other results can be used to address soil-structure interaction problems of pile supported structures making use of substructuring approaches as, for instance, in [65,75,89–93], though direct formulations have also been proposed and implemented, for example, for the dynamic analysis of bridge-pier systems, long-span bridges and multi-storey structures supported on piles, taking SSI into account [59, 60, 94]. A comparison between field measurements, encompassing a wide range of structural configurations and geotechnical characteristics, and simplified procedures commonly used in practice to evaluate SSI effects, was provided by Stewart et al [95, 96].

The problem of the interaction of adjacent structures through the underlying and surrounding soil has received less attention. Lee and Wesley, in their pioneering work [97], investigated the influence of structure-soil-structure interaction (termed hereafter as "SSSI") on the seismic response of several adjacent nuclear reactors using a three-dimensional scheme and an approximate solution for the dynamic interaction between rigid surface circular plates. Soon after, Luco and Contesse [98], followed by Wong and Trifunac [99], addressed the two-dimensional antiplane problem of the interaction between infinite walls under incident SH waves making use of a solution for the interaction among semi-circular semi-infinite cross-sectional foundations. Later, two different finite elements - boundary elements coupling models were used by Wang and Schmid [100], and Lehmann and Antes [101] to investigate the dynamic interaction between three-dimensional structures founded on square embedded foundations, for point-loads applied on one of the structural nodes in the first work and for vertical loads on the soil between the two structures in the second. More recently, some work has been done on analysing the influence of large groups of buildings, together with site effects due to subsoil configuration, on the seismic response of the overall system by means of several experimental and numerical models [102–105].

Finally, it is worth noting again that this work is focused mainly on the numerical modelling in the frequency domain of the dynamic behaviour of pile foundations and pile supported structures embedded in viscoelastic soils and, conse-

quently, in the linear range, although, as stated above, the dynamic behaviour of pile foundations and pile supported structures is a complex engineering problem comprising a wide range of aspects. Therefore, experimental studies and computational works involving non-linear phenomena are beyond the scope of this literature review. The state of the art on these topics can be found, for instance, in [106–108].

1.2 Aims and objectives

This thesis represents another step in a research line that began with the pioneering works of Professors Enrique Alarcón and José Domínguez, who applied the direct boundary element method to elastodynamic problems [4,7,16,109,110]. The fruitful collaboration established later between the University of Seville and the University of Las Palmas de Gran Canaria, resulted in a three-dimensional multidomain boundary element code in the frequency domain [111–113], whose last stage was reached with the Ph.D thesis of Prof. Juan J. Aznárez [114], supervised by Prof. Orlando Maeso, when the possibility of modelling poroelastic subdomains, among other new features, was formulated and implemented. This last code was used to perform several works on the dynamic analysis of arch dams with porous sediments [115–118], and also to obtain impedance functions of piles and pile groups in viscoelastic and poroelastic soils [63, 64]. As said above, the major disadvantages of this kind of approach are the high computational cost and the efforts required for preparing meshes and data files. For these reasons, the analysis of large pile groups with this tool becomes prohibitive. Necessary, back then, was the development, and implementation in the previous BEM code, of a simplified but still rigorous formulation that allowed reducing the number of degrees of freedom in the problem.

Therefore, the main objective of this work is the formulation and implementation of a BEM-FEM model for the time harmonic dynamic analysis of pile foundations embedded in viscoelastic soils and of pile supported structures. The idea is assuming that the soil continuity is not altered by the presence of the piles and that tractions at the pile-soil interface can be considered, from the integral equation point of view, as body forces. This implies computing a domain integral involving the body forces, which are usually considered to be zero in most applications. However, these new integrals are extended only to the pile-soil interface, so there is no need of discretizing the whole domain. This idea is similar to that of a previous static model presented by Matos Filho et al [119]. The coupling scheme should allow the general and relatively simple modelling of multiple pile foundations made up by vertical piles and rigid caps. It should also be possible to model the topography and stratigraphy of the site, including deposits and inclusions,

layers and bedrocks. The effort needed for the mesh generation process should be significantly smaller than that needed for a similar analysis by the multidomain BEM code. In addition, the formulation should include the possibility of studying several multi-storey linear structures founded on one or more pile foundations.

The code should include a wide range of possible boundary conditions. For instance, it must be possible to impose harmonic displacements or tractions on the different boundaries, and harmonic motions or loads on pile heads, pile caps or each storey of a structure. This way, impedance functions of pile foundations, or interaction factors between piles or between groups of piles, can be computed. The dynamic response of the system to incident S, P and Rayleigh wave fields is also of interest, so any particular numerical aspect about its implementation in the coupling model must be formulated. Hence, not only kinematic interaction factors of pile foundations can be obtained, but also the seismic response of one or more pile supported structures can be evaluated.

Once the model is formulated and validated, it will be applied to three different kinds of problems: *(i)* the computation of impedance functions and kinematic interaction factors of pile foundations; *(ii)* the assessment of soil-structure interaction effects on pile supported structures, making use of previously computed dynamic stiffness and kinematic interaction factors in substructure methods; and *(iii)* the evaluation of the influence of the presence of nearby structures on the seismic response of pile supported buildings.

1.3 Structure of the dissertation

The basic concepts needed to address the problem in hand are briefly exposed in chapter 2. The governing equations of the elastodynamic problem are presented at the beginning of the chapter, followed by some ideas on wave propagation phenomena in elastic media, with special emphasis on plane harmonic waves. Then, making use of the reciprocal theorem in elastodynamics, the boundary integral representation of the problem is reached, which allows the subsequent formulation of the boundary element method. This numerical method is outlined at the end of the chapter, which finishes explaining how viscoelastic materials are studied using the same formulation.

The core of the dissertation is the boundary element – finite element formulation for the dynamic analysis of the pile foundation and pile supported structures, presented in chapter 3. The chapter begins deriving the boundary element equations and the finite element equations used to model soil and piles respectively. The coupling is then performed by imposing equilibrium and compatibility conditions at the pile-soil interface. Once the rigid pile caps are defined, the chapter presents the structure linear modelling, in which all degrees of freedom are con-

densed to the centre of gravity of slabs and pile caps. The chapter finishes with some remarks on the numerical evaluation of integrals concerning the piles.

The boundary element – finite element formulation presented in chapter 3 is used in chapter 4 to analyse the dynamic response of pile foundations. Before that, the model is validated through a number of comparisons with results obtained by other authors. Then, three different groups of original results are presented: first, the distribution of shear forces is studied along some of the piles of a 5×5 square pile group subjected to forced vibration; second, impedance functions of pile foundations in homogeneous strata are obtained, studying the influence of parameters such as pile-soil stiffness ratio, stratum depth and foundation configuration; and third, the last section of the chapter addresses the sensitivity of the seismic response of a 3×3 pile group to the soil stratigraphy, when the foundation is subjected to vertically-incident shear waves.

The dynamic and seismic behaviour of embedded footings supported by piles (called piled embedded footings), a problem that has received surprisingly little research attention, is studied in chapter 5. A simple engineering approach to obtain the impedance functions of such type of foundation, by superposition of the corresponding functions of embedded footing and pile group obtained separately, is presented in the first part of the chapter. Then, the best way of estimating the kinematic interaction factors of piled embedded footings is investigated. The chapter finishes analysing the influence of the existence of a separation between the footing underside and the soil – caused mainly by soil consolidation – on the dynamic stiffness functions of pile embedded foundations.

The main motivation in obtaining the impedance functions and kinematic interaction factors of foundations, as done in chapters 4 and 5, lies in the fact that they are a key part of the substructure models for SSI problems that are generally used in design. This way, chapter 6 proposes a substructure model for the analysis of dynamic SSI effects on one-storey linear shear structures founded on one pile group. Making use of it, the influence of SSI on the system fundamental period and equivalent damping is studied for different structural and soil-foundation configurations. Although this kind of analysis could be performed making use of the direct methodology presented in chapter 3, its special characteristics make advisable the use of a substructure approach, which provides accurate enough results with very little computational effort. The chapter begins by presenting the problem, the substructure model and the solution procedure. Afterwards, a parametric analysis of the dynamic response of structures, founded on 2×2 and 3×3 pile groups, is presented. The chapter finishes analysing the sensitivity of the results to variations of parameters such as the soil-structure mass density ratio, the foundation-structure mass ratio and the fixed-base structure damping.

The virtues and capabilities of the direct approach are exploited in chapter 7, where the dynamic through-soil interaction effects between neighbouring pile

supported structures are investigated making use of the formulation presented in chapter 3. After defining the problem, the influence of the interaction phenomena among the elements in groups of three, five and nine structures with similar or dissimilar dynamic characteristics, is evaluated. Parameters such as structural slenderness ratio, pile-soil stiffness ratio and distance between adjacent structures, are included in the study. The chapter finishes presenting several acceleration response spectra to measure the influence of SSSI on the seismic response of the structures subjected to an artificial earthquake motion.

Finally, a summary of the most outstanding achievements and conclusions that can be drawn from this work is given in chapter 8. The dissertation finishes discussing future research directions and developments that could shortly follow this work.

Chapter 2

The harmonic elastodynamic problem and its direct BEM formulation: an overview

2.1 Introduction

The dynamic behaviour of 3D pile foundations embedded in viscoelastic soils is numerically addressed in this work. It is framed, thus, within the three-dimensional elastodynamic problem, of which exact solutions are generally impracticable. For this reason, different approximate methodologies have been developed, among which the boundary element method has proven to be an accurate numerical approach, especially suitable for problems involving unbounded regions.

This introductory chapter begins by setting the basic governing equations of the elastodynamic problem and by briefly studying the wave propagation phenomena in elastic media, in sections 2.2 and 2.3 respectively. Then, section 2.4 presents the elastodynamic integral representation, allowing the formulation of the boundary element method (BEM) in section 2.5. Finally, the chapter ends in section 2.6 with a brief remark on how viscoelastic problems are modelled making use of the same formulation obtained for elastic media.

2.2 Governing equations of linear elastodynamics

The formulation presented in this work addresses the numerical solution of a steady-state dynamic problem posed on elastic, homogeneous, isotropic, linear regions. The first step is, therefore, the establishment of the corresponding gov-

erning equations, which can be obtained from the combination of kinematic relations, equilibrium equations and constitutive law, ruling the dynamic behaviour of elastic solids.

Let $\mathbf{x}$ be the position vector of a point in a body Ω with respect to a system of fixed rectangular Cartesian coordinates. The small strain tensor ε_{ij} at this point and at time t is defined in terms of the components of the displacement vector $u_i(\mathbf{x}, t)$ as

$$\varepsilon_{ij} = \frac{1}{2}(u_{i,j} + u_{j,i}) \qquad ; \qquad i, j = 1, 2, 3 \tag{2.1}$$

where commas indicate spatial differentiation.

On the other hand, the equilibrium conditions for the points of an elastic body can be expressed in terms of the following set of differential equations:

$$\sigma_{ij,j} + \rho b_i = \rho \ddot{u}_i \tag{2.2}$$

where σ_{ij} represents the stress tensor, b_i is the body force per unit mass acting in Ω, ρ is the mass density, dots indicate time derivatives and repeated subindex imply a summation.

Finally, the relationship between the stress and strain tensors for linear, elastic, isotropic, homogeneous solids is established by the Hooke's law, as

$$\sigma_{ij} = \lambda\, \delta_{ij} \varepsilon_{kk} + 2\mu \varepsilon_{ij} \tag{2.3}$$

where δ_{ij} is the Kronecker delta ($\delta_{ij} = 1$ if $i = j$; $\delta_{ij} = 0$ otherwise). λ and μ are the Lamé's constants, which are related to the Young's modulus E and the Poisson's ratio ν as

$$\mu = \frac{E}{2(1+\nu)} \qquad ; \qquad \lambda = \frac{\nu E}{(1+\nu)(1-2\nu)} \tag{2.4}$$

being μ the shear modulus.

The dynamic behaviour of an elastic, homogeneous, isotropic, linear body is governed by the expressions (2.1), (2.2) and (2.3), which form a complete system of equations (15 in the three-dimensional case). The substitution of (2.1) and (2.3) into (2.2) yields

$$\mu \boldsymbol{\nabla}^2 \mathbf{u} + (\lambda + \mu) \boldsymbol{\nabla} (\boldsymbol{\nabla} \cdot \mathbf{u}) + \rho \mathbf{b} = \rho \ddot{\mathbf{u}} \tag{2.5}$$

which are the Navier's equations, that represent the governing equations of motion in terms of the displacement vector $\mathbf{u}$. Here, $\mathbf{b}$ is the vector of body forces per unit mass. As a differential equation, the solution of eq. (2.5) requires the establishment of a set of boundary conditions, in this case, applied in terms of known tractions and/or displacements on the boundary Γ of the body Ω, as well as time initial conditions $\forall \mathbf{x} \in \Omega$.

2.3 Wave propagation in elastic media

The integration of eq. (2.5) for a general case is not a trivial task. Several procedures have been presented to express the Navier's equations in such a way that its solution can be reached more easily for certain problems. Among them, the formulation of the elastodynamic problems in terms of dilatation and rotation leads to a set of simpler differential wave equations which, in addition, depend on variables with a clear physical meaning. Let the dilatation e and the rotation vector $\boldsymbol{\omega}$ be

$$\mathsf{e} = \varepsilon_{kk} = \boldsymbol{\nabla} \cdot \mathbf{u} \tag{2.6a}$$

$$\boldsymbol{\omega} = \boldsymbol{\nabla} \times \mathbf{u} \tag{2.6b}$$

Taking the divergence and the curl of eq. (2.5) one obtains, respectively, the following two wave equations:

$$c_p^2 \boldsymbol{\nabla}^2 \mathsf{e} + \boldsymbol{\nabla} \cdot \mathbf{b} = \ddot{\mathsf{e}} \tag{2.7}$$

$$c_s^2 \boldsymbol{\nabla}^2 \boldsymbol{\omega} + \boldsymbol{\nabla} \times \mathbf{b} = \ddot{\boldsymbol{\omega}} \tag{2.8}$$

where

$$c_p^2 = \frac{\lambda + 2\mu}{\rho} \qquad \text{and} \qquad c_s^2 = \frac{\mu}{\rho} \tag{2.9}$$

Eqs. (2.7) and (2.8) represent the decoupled formulation of Navier's equations in terms of the dilatation and the three components of the rotation vector. Eq. (2.7) is a scalar wave equation with propagation velocity c_p, while eq. (2.8) is a vector wave equation with propagation velocity c_s. Therefore, waves within the elastic body can be classified as irrotational and equivolumial waves, also called compressional (or primary) and shear (or secondary) waves (P and S waves), respectively. The *primary* and *secondary* names come from the field of seismology, because $c_p > c_s$ and, consequently, the former kind reaches first the seismological station in case of an earthquake.

2.3.1 Plane harmonic waves

Let us focus now on the specific problem of plane elastic waves propagating in a certain direction defined by a unit vector $\mathbf{s}$. In this situation, all points on a common plane perpendicular to $\mathbf{s}$ are subject to the same motions, defined by unit vector $\mathbf{d}$. In the steady-state harmonic case, resulting displacements of a point $\mathbf{x}$ are of the form

$$\mathbf{u} = A\, e^{\mathrm{i}(\omega t - k\, \mathbf{s}\cdot\mathbf{x})} \mathbf{d} \tag{2.10}$$

where A is the amplitude of the motion, independent of t and $\mathbf{x}$, $\mathrm{i} = \sqrt{-1}$ and $k = \omega/c$ is the wave number, being c the wave velocity. On the other hand, defining the elastic characteristics of the solid by means of c_s and c_p, and assuming, for simplicity, zero body forces, Navier's equations can be written as

$$-c_s^2\,\boldsymbol{\nabla}\times\boldsymbol{\omega} + c_p^2\,\boldsymbol{\nabla}\mathsf{e} = \ddot{\mathbf{u}} \tag{2.11}$$

By substitution of eq. (2.10), each one of the terms of eq. (2.11) become

$$\boldsymbol{\nabla}\times\boldsymbol{\omega} = -k^2\mathbf{s}\times(\mathbf{s}\times\mathbf{d})\,e^{\mathrm{i}(\omega t - k\,\mathbf{s}\cdot\mathbf{x})} \tag{2.12a}$$

$$\boldsymbol{\nabla}\mathsf{e} = -k^2\,(\mathbf{s}\cdot\mathbf{d})\,\mathbf{s}\,e^{\mathrm{i}(\omega t - k\,\mathbf{s}\cdot\mathbf{x})} \tag{2.12b}$$

$$\ddot{\mathbf{u}} = -\omega^2\,e^{\mathrm{i}(\omega t - k\,\mathbf{s}\cdot\mathbf{x})}\mathbf{d} \tag{2.12c}$$

Therefore, and taking into account that $\mathbf{s}\times(\mathbf{s}\times\mathbf{d}) = (\mathbf{s}\cdot\mathbf{d})\,\mathbf{s} - \mathbf{d}$, eq. (2.11) becomes

$$(c_s^2 - c^2)\,\mathbf{d} + (c_p^2 - c_s^2)\,(\mathbf{s}\cdot\mathbf{d})\,\mathbf{s} = 0 \tag{2.13}$$

and consequently

$$\text{if}\begin{cases} c = c_s \;\Rightarrow\; \mathbf{s}\cdot\mathbf{d} = 0 & \Rightarrow \text{ motion perpendicular to propagation dir.} \\ c = c_p \;\Rightarrow\; \mathbf{s}\times\mathbf{d} = 0 & \Rightarrow \text{ motion parallel to propagation dir.} \end{cases}$$

as illustrated in fig. 2.1.

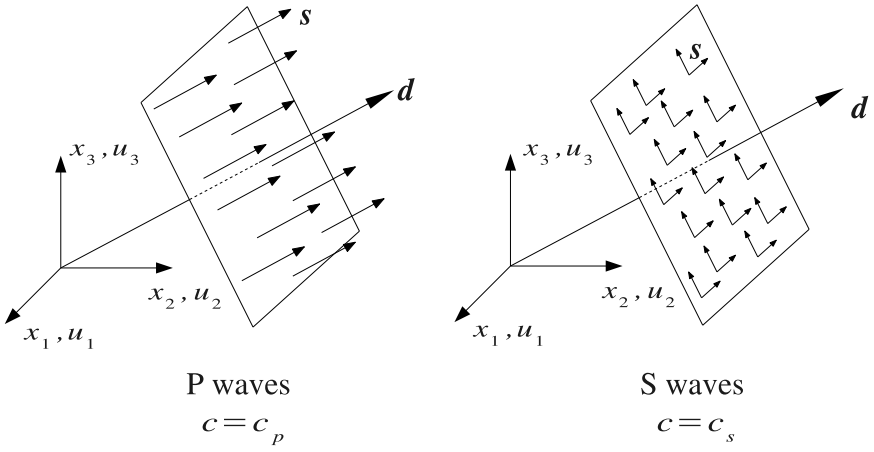

Figure 2.1: *Motions and propagation direction corresponding to P and S plane waves*

In this section, only some essential concepts of elastic wave propagation have been outlined in order to facilitate a better understanding of the subsequent

sections and chapters. A deeper exposition on wave propagation phenomena in elastodynamics, and its resolution with boundary elements, can be found in Domínguez [120]. A comprehensive analysis of the problem can be found in [121, 122].

2.4 The elastodynamic integral representation

In the previous sections, the dynamic behaviour of an elastic, homogeneous, isotropic, linear body has been described by means of its governing equations. The transformation of these differential equations into integral expressions will lead to the boundary element formulation of the problem.

2.4.1 Reciprocal theorem in elastodynamics

The starting point is the reciprocal work theorem between two elastodynamic states. It is an extension to the time domain of Betti's classical reciprocal theorem of elastostatics, being first stated by Graffi [123], and later extended by Wheeler and Sternberg [124] to infinite domains.

Let $\mathcal{S}(\mathbf{u}, \boldsymbol{\sigma}, \mathbf{b}; \Omega)$ and $\mathcal{S}^*(\mathbf{u}^*, \boldsymbol{\sigma}^*, \mathbf{b}^*; \Omega)$ be two distinct elastodynamic states that satisfy the Navier's equations (2.5) on a regular domain Ω. $\mathcal{S}^*$ will be a known reference solution used to solve the problem and obtain the unknown state $\mathcal{S}$. Assuming zero initial conditions, the dynamic reciprocal theorem can be written as

$$\begin{aligned} &\int_\Gamma (\mathbf{p} * \mathbf{u}^*)\, d\Gamma + \rho \int_\Omega (\mathbf{b} * \mathbf{u}^*)\, d\Omega = \\ &\int_\Gamma (\mathbf{p}^* * \mathbf{u})\, d\Gamma + \rho \int_\Omega (\mathbf{b}^* * \mathbf{u})\, d\Omega \end{aligned} \tag{2.14}$$

where $\mathbf{u}$ and $\mathbf{u}^*$ are the displacement vectors of any point of the domain; while $\mathbf{p}$ and $\mathbf{p}^*$ are the traction vectors on Γ, in equilibrium with the corresponding stress tensors $\boldsymbol{\sigma}$ and $\boldsymbol{\sigma}^*$, for states $\mathcal{S}$ and $\mathcal{S}^*$, respectively. Operator $*$ represents Riemann convolution.

The elastodynamic formulation developed in this work considers time-harmonic body forces and boundary conditions, with angular frequency ω, *i.e.*, of the type $\mathbf{f}(\mathbf{x}, t) = \mathbf{f}(\mathbf{x}; \omega) e^{\mathrm{i}\omega t}$. In this case, motions consist of a transient part $\mathbf{u}^t(\mathbf{x}, t)$ and a steady-state part $\mathbf{u}(\mathbf{x}; \omega)$ changing harmonically in time, so that

$$\mathbf{u}(\mathbf{x}, t) = \mathbf{u}^t(\mathbf{x}, t) + \mathbf{u}(\mathbf{x}; \omega) e^{\mathrm{i}\omega t} \tag{2.15}$$

However, all real physical systems contain some kind of energy dissipation mechanism so that, as $t \to \infty$, the transient part will disappear. This makes

always possible the formulation of the problem when only the steady state part (caused by the harmonically varying boundary conditions) prevails. In general, $\mathbf{u}(\mathbf{x};\omega)$ will be a complex function not in phase with the excitation. Then, assuming time-invariant properties of the elastic body, displacements and stress fields can be expressed as

$$\mathbf{u}(\mathbf{x},t) = \mathbf{u}(\mathbf{x};\omega)e^{\mathrm{i}\omega t} \tag{2.16a}$$

$$\boldsymbol{\sigma}(\boldsymbol{\sigma},t) = \mathbf{u}(\mathbf{x};\omega)e^{\mathrm{i}\omega t} \tag{2.16b}$$

The substitution of eqs. (2.16) into the governing equations allows removing the repeated term $e^{\mathrm{i}\omega t}$ and rewriting all the equations for the elastodynamic steady state. Therefore, it is possible to redefine the two distinct elastodynamic states in the frequency domain as $\mathcal{S}_\omega(\mathbf{u},\boldsymbol{\sigma},\mathbf{b};\omega,\Omega)$ and $\mathcal{S}^*_\omega(\mathbf{u}^*,\boldsymbol{\sigma}^*,\mathbf{b}^*;\omega,\Omega)$. Under these assumptions, convolution products disappear from eq. (2.14) and the expression is simplified as

$$\int_\Gamma \mathbf{p}\mathbf{u}^*\,d\Gamma + \rho\int_\Omega \mathbf{b}\mathbf{u}^*\,d\Omega = \int_\Gamma \mathbf{p}^*\mathbf{u}\,d\Gamma + \rho\int_\Omega \mathbf{b}^*\mathbf{u}\,d\Omega \tag{2.17}$$

2.4.2 Fundamental solution

The formulation of the elastodynamic integral equation from eq. (2.17) relies on choosing a suitable reference state $\mathcal{S}^*_\omega$, usually called *fundamental solution*. There exist different fundamental solutions (or Green's functions) for different reference problems. The one used in the present work is that representing the response, in terms of displacements and tractions, of an unbounded linear, elastic, homogeneous, isotropic domain to a harmonic concentrated unit load of the form

$$\rho b^*_k = \delta(\boldsymbol{\iota})\,\delta_{lk}\,e^{\mathrm{i}\omega t} \tag{2.18}$$

applied at the source point $\boldsymbol{\iota}$ in the direction l, being δ_{lk} the Kronecker delta and $\delta(\boldsymbol{\iota})$ the Dirac delta, defined as

$$\int_\Omega \delta(\boldsymbol{\iota})\,d\Omega = \begin{cases} 1, & \text{if } \boldsymbol{\iota}\in\Omega \\ 0, & \text{if } \boldsymbol{\iota}\notin\Omega \end{cases} \tag{2.19}$$

This is a classic problem solved by Stockes [125] in the time domain, by Cruse and Rizzo [126] in Laplace's domain, and some years before by Kupradze [127] for harmonic problems. As mentioned above, this fundamental solution corresponds to the complete space, which forces to discretize the free surface when studying a semi-infinite domain, as happens in the present work. In practice, however, only a small region around the analysis area has to be included in the model to reach accurate results.

Let $u^*_{lk}(\mathbf{x}, \boldsymbol{\iota}, \omega)$ be the displacements in the direction k at the field point $\mathbf{x}$ due to the source load. Let $p^*_{lk}(\mathbf{x}, \boldsymbol{\iota}, \omega)$ be the k component of tractions associated to a plane with exterior unit normal $\mathbf{n}$ at the field point $\mathbf{x}$. Their expressions, for $k, l = 1, 2$ or 3, are:

$$u^*_{lk}(\mathbf{x}, \boldsymbol{\iota}, \omega) = \frac{1}{4\pi\mu}\left[\psi\delta_{lk} - \chi r_{,k} r_{,l}\right] \tag{2.20}$$

$$\begin{aligned} p^*_{lk}(\mathbf{x}, \boldsymbol{\iota}, \omega) = \frac{1}{4\pi}\Bigg[&\left(\frac{\partial\psi}{\partial r} - \frac{\chi}{r}\right)\left(\delta_{kl}\,\frac{\partial r}{\partial \mathbf{n}} + r_{,k} n_l\right) - \frac{2}{r}\chi\left(n_k r_{,l} - 2\, r_{,k} r_{,l}\,\frac{\partial r}{\partial \mathbf{n}}\right) \\ &-2\frac{\partial\chi}{\partial r}\, r_{,k} r_{,l}\,\frac{\partial r}{\partial \mathbf{n}} + \left(\frac{c_p^2}{c_s^2} - 2\right)\left(\frac{\partial\psi}{\partial r} - \frac{\partial\chi}{\partial r} - \frac{2}{r}\chi\right) r_{,l}\, n_k\Bigg] \end{aligned} \tag{2.21}$$

where $r = |\mathbf{x} - \boldsymbol{\iota}|$ and

$$\begin{aligned} \psi &= -\left(\frac{c_s}{c_p}\right)^2\left(\frac{1}{z_p^2 r^2} - \frac{1}{z_p r}\right)\frac{e^{z_p r}}{r} + \left(\frac{1}{z_s^2 r^2} - \frac{1}{z_s r} + 1\right)\frac{e^{z_s r}}{r} \\ \chi &= -\left(\frac{c_s}{c_p}\right)^2\left(\frac{3}{z_p^2 r^2} - \frac{3}{z_p r} + 1\right)\frac{e^{z_p r}}{r} + \left(\frac{3}{z_s^2 r^2} - \frac{3}{z_s r} + 1\right)\frac{e^{z_s r}}{r} \end{aligned} \tag{2.22}$$

being

$$z_p = -\frac{\mathrm{i}\omega}{c_p} \qquad ; \qquad z_s = -\frac{\mathrm{i}\omega}{c_s} \tag{2.23}$$

It is worth noting that this fundamental solution exhibits a singularity when $\omega r \to 0$, which implies the need of a special treatment of the integrals of these functions around the source point (see, *e.g.*, [114, 120]).

2.4.3 Integral representation

The application of the equation of reciprocity (2.17) between the unknown state under study and the reference state $\mathcal{S}^*_\omega$ defined above yields the integral representation of the problem. Hereafter, equations will be written representing a set of three equations arising from the collocation of the unit load in the three directions of space, so that vectors $\mathbf{u}^*$, $\mathbf{p}^*$ and $\mathbf{b}^*$ will be arranged into 3×3 matrices $\mathbf{u}^*$, $\mathbf{p}^*$ and $\mathbf{b}^*$. This way, when the fundamental solution defined above is considered, and taking eq. (2.18) into account, the last term of eq. (2.17) becomes

$$\rho\int_\Omega \mathbf{b}^*\mathbf{u}\, d\Omega = \int_\Omega \delta(\boldsymbol{\iota})\mathbf{u}\, d\Omega = \mathbf{u}^\iota \tag{2.24}$$

which makes eq. (2.17) become

$$\mathbf{u}^{\iota} + \int_{\Gamma} \mathbf{p}^{*}\mathbf{u}\, d\Gamma = \int_{\Gamma} \mathbf{u}^{*}\mathbf{p}\, d\Gamma + \rho \int_{\Omega} \mathbf{u}^{*}\mathbf{b}\, d\Omega \tag{2.25}$$

which is the integral representation of the displacements field of the harmonic elastodynamic problem when the point load is applied at $\boldsymbol{\iota} \in \Omega$, where $\mathbf{u}$ and $\mathbf{p}$ are the displacement and traction vectors, while $\mathbf{u}^{*}$ and $\mathbf{p}^{*}$ are the fundamental solution tensors, which in matrix form can be written as

$$\mathbf{u} = \begin{bmatrix} u_1 \\ u_2 \\ u_3 \end{bmatrix}; \quad \mathbf{u}^{*} = \begin{bmatrix} u^{*}_{11} & u^{*}_{12} & u^{*}_{13} \\ u^{*}_{21} & u^{*}_{22} & u^{*}_{23} \\ u^{*}_{31} & u^{*}_{32} & u^{*}_{33} \end{bmatrix} \tag{2.26}$$

$$\mathbf{p} = \begin{bmatrix} p_1 \\ p_2 \\ p_3 \end{bmatrix}; \quad \mathbf{p}^{*} = \begin{bmatrix} p^{*}_{11} & p^{*}_{12} & p^{*}_{13} \\ p^{*}_{21} & p^{*}_{22} & p^{*}_{23} \\ p^{*}_{31} & p^{*}_{32} & p^{*}_{33} \end{bmatrix} \tag{2.27}$$

2.4.4 Boundary integral representation

Eq. (2.25) allows the computation of displacements at internal points of Ω when displacements and tractions are known on Γ. In order to formulate the problem so that, given the boundary conditions, the unknowns on the boundaries can be obtained, the integral equation must be written in terms only of variables on Γ, which implies applying the unit load on the boundary. However, this specific case of $\boldsymbol{\iota} \in \Gamma$, which will lead to the boundary integral representation of the problem, requires special attention due to the singularity of the fundamental solution when $r \to 0$.

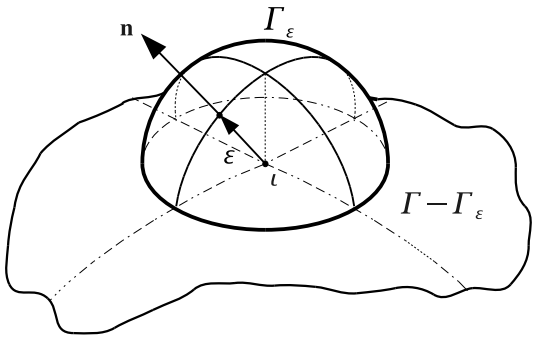

Figure 2.2: *Procedure for the singularity subtraction. Semisphere around the collocation point for integration*

The singularity subtraction is usually carried out by slightly modifying Γ in order to avoid the $r = 0$ situation. To this end, an approximate boundary is considered, made up by the boundary Γ of the domain Ω itself but augmented by a semisphere Γ_ε of radius $\varepsilon \to 0$. As shown in fig. 2.2, the collocation point $\boldsymbol{\iota}$ is considered to be the centre of this semisphere. Therefore, each of the boundary integrals can be decomposed into another two extended over $\Gamma - \Gamma_\varepsilon$ and Γ_ε, respectively. Consequently, eq. (2.25) can be written as

$$\mathbf{u}^\iota + \int_{\Gamma-\Gamma_\varepsilon} \mathbf{p}^* \mathbf{u}\, d\Gamma + \int_{\Gamma_\varepsilon} \mathbf{p}^* \mathbf{u}\, d\Gamma = \int_{\Gamma-\Gamma_\varepsilon} \mathbf{u}^* \mathbf{p}\, d\Gamma + \int_{\Gamma_\varepsilon} \mathbf{u}^* \mathbf{p}\, d\Gamma + \rho \int_\Omega \mathbf{u}^* \mathbf{b}\, d\Omega \quad (2.28)$$

Integrals extended over $\Gamma - \Gamma_\varepsilon$ do not contain the singularity, and for $\varepsilon \to 0$ they represent the Cauchy principal value of the original integral.

$$\lim_{\varepsilon\to 0} \int_{\Gamma-\Gamma_\varepsilon} \mathbf{p}^* \mathbf{u}\, d\Gamma = \text{pr. v.} \int_\Gamma \mathbf{p}^* \mathbf{u}\, d\Gamma \quad (2.29)$$

$$\lim_{\varepsilon\to 0} \int_{\Gamma-\Gamma_\varepsilon} \mathbf{u}^* \mathbf{p}\, d\Gamma = \text{pr. v.} \int_\Gamma \mathbf{u}^* \mathbf{p}\, d\Gamma \quad (2.30)$$

On the other hand, integrals extended over Γ_ε are defined in the limit. Taking into account that $\mathbf{u}^* \sim O(1/\varepsilon)$, $\mathbf{p}^* \sim O(1/\varepsilon^2)$ and $d\Gamma \sim O(\varepsilon^2)$ one can write

$$\lim_{\varepsilon\to 0} \int_{\Gamma_\varepsilon} \mathbf{u}^* \mathbf{p}\, d\Gamma = 0 \quad (2.31)$$

$$\mathbf{u}^\iota + \lim_{\varepsilon\to 0} \int_{\Gamma_\varepsilon} \mathbf{p}^* \mathbf{u}\, d\Gamma = \mathbf{c}^\iota \mathbf{u}^\iota \quad (2.32)$$

where $\mathbf{c}^\iota$ is the *free term* that, in the three-dimensional case, is a 3×3 tensor depending on the boundary geometry at point $\boldsymbol{\iota}$ and on Poisson's ratio ν of the domain (see, *e.g.*, [128]). If the boundary is smooth at $\boldsymbol{\iota}$, then $\mathbf{c}^\iota = 1/2\,\mathbf{I}$, while $\mathbf{c}^\iota = \mathbf{I}$ at internal points, $\mathbf{I}$ being the unit 3×3 diagonal matrix. Taking eqs. (2.29) to (2.32) into account, eq. (2.28) becomes

$$\mathbf{c}^\iota \mathbf{u}^\iota + \int_\Gamma \mathbf{p}^* \mathbf{u}\, d\Gamma = \int_\Gamma \mathbf{u}^* \mathbf{p}\, d\Gamma + \rho \int_\Omega \mathbf{u}^* \mathbf{b}\, d\Omega \quad (2.33)$$

where all integrals are Cauchy principal value integrals, even though *pr. v.* has been omitted for the sake of simplicity.

2.5 The boundary element method

For points $\boldsymbol{\iota} \in \Gamma$, eq. (2.33), together with the boundary conditions, constitutes a closed formulation that would allow obtaining the solution for the displacement and traction fields on the boundary. Then, displacements at any point $\boldsymbol{\iota} \in \Omega$ could be computed from eq. (2.25). However, the analytical solution of the problem is not possible, in general, except for some simple cases. For this reason, a discretization process is carried out in order to obtain a linear system of algebraic equations from which the numerical solution of the problem in a set of points can be found.

In this section, body forces will be assumed to be zero, as usual. Therefore, eq. (2.33) becomes

$$\mathbf{c}^{\iota}\mathbf{u}^{\iota} + \int_{\Gamma} \mathbf{p}^{*}\mathbf{u}\, d\Gamma = \int_{\Gamma} \mathbf{u}^{*}\mathbf{p}\, d\Gamma \tag{2.34}$$

2.5.1 Discretization process

The numerical solution of eq. (2.34) requires, first, the discretization of the boundary surface into $\mathcal{N}_e$ elements Γ_j and $\mathcal{N}_n$ nodes so that

$$\Gamma \simeq \bigcup_{j=1}^{\mathcal{N}_e} \Gamma_j \tag{2.35}$$

where each element is defined by $\mathcal{N}_n^j$ nodes. Over each element j, displacement $\mathbf{u}$ and traction $\mathbf{p}$ fields are approximated in terms of their values at nodal points making use of a set of polynomial interpolation functions $\boldsymbol{\Phi}(\boldsymbol{\xi})$. Here, $\boldsymbol{\xi}$ represents the set of natural coordinates used to define a point in the reference element, which will be presented below. This way, the fields $\mathbf{u}(\boldsymbol{\xi})$ and $\mathbf{p}(\boldsymbol{\xi})$ within an element are approximated as

$$\mathbf{u}(\boldsymbol{\xi}) = \boldsymbol{\Phi}(\boldsymbol{\xi})\,\mathbf{u}^{j} \qquad ; \qquad \mathbf{p}(\boldsymbol{\xi}) = \boldsymbol{\Phi}(\boldsymbol{\xi})\,\mathbf{p}^{j} \tag{2.36}$$

where $\mathbf{u}^j$ and $\mathbf{p}^j$ are vectors of dimension $3\mathcal{N}_n^j \times 1$ containing the element nodal displacements and tractions, and $\boldsymbol{\Phi}(\boldsymbol{\xi})$ is a matrix of dimensions $3 \times 3\mathcal{N}_n^j$ of the form

$$\boldsymbol{\Phi}(\boldsymbol{\xi}) = \begin{bmatrix} \phi_1 & 0 & 0 & \phi_2 & 0 & 0 & \cdots & \phi_{\mathcal{N}_n^j} & 0 & 0 \\ 0 & \phi_1 & 0 & 0 & \phi_2 & 0 & \cdots & 0 & \phi_{\mathcal{N}_n^j} & 0 \\ 0 & 0 & \phi_1 & 0 & 0 & \phi_2 & \cdots & 0 & 0 & \phi_{\mathcal{N}_n^j} \end{bmatrix} \tag{2.37}$$

containing the specific polynomial interpolation functions for the element, which will be defined later. On the other hand, the element geometry can be defined

using the same interpolation functions as

$$\mathbf{x}(\boldsymbol{\xi}) = \boldsymbol{\Phi}(\boldsymbol{\xi})\,\mathbf{x}^j \tag{2.38}$$

where $\mathbf{x}^j$ is a vector of dimension $3\mathcal{N}_n^j \times 1$ containing the coordinates of nodes defining element j. This kind of element, on which the same functions are used to approximate both geometry and unknowns, receives the name of *isoparametric element*.

It is worth noting here that the geometry approximated by eq. (2.38) will not be, in general, completely coincident with the original boundary, as expressed by eq. (2.35). The error of the approximation depends on the complexity of the original geometry, the performed discretization and the interpolation functions ϕ_i. However, this kind of errors, also existent in the estimated fields, is inherent to the concept of approximation on which the boundary element method, and many other methods, rely, and consequently, does not invalidate at all this type of approach.

Once all boundaries have been discretized, and taking into account that $\mathbf{u}^j$ and $\mathbf{p}^j$ are constant vectors in Γ_j, the substitution of eqs. (2.36) into eq. (2.34) yields

$$\mathbf{c}^\iota\mathbf{u}^\iota + \sum_{j=1}^{\mathcal{N}_e}\left\{\int_{\Gamma_j}\mathbf{p}^*\boldsymbol{\Phi}\,d\Gamma\right\}\mathbf{u}^j = \sum_{j=1}^{\mathcal{N}_e}\left\{\int_{\Gamma_j}\mathbf{u}^*\boldsymbol{\Phi}\,d\Gamma\right\}\mathbf{p}^j \tag{2.39}$$

which constitutes a set of three algebraic equations depending on displacements on the collocation point and on displacements and tractions of all nodes in the corresponding boundary. Eq. (2.39) can be written, in matrix form, as

$$\mathbf{c}^\iota\mathbf{u}^\iota + \sum_{m=1}^{\mathcal{N}_n}\hat{\mathbf{H}}^{\iota m}\mathbf{u}^m = \sum_{m=1}^{\mathcal{N}_n}\mathbf{G}^{\iota m}\mathbf{p}^m \tag{2.40}$$

where now summations extend over all nodes in the discretization.

Note that only one value of the displacement is possible at a certain point. However, different values of tractions may exist at the same point when this belongs to more than one element with non-parallel exterior normals. This situation is solved by considering more than one node at the same point. When at least one of the tractions is known, the displacements of both nodes will result equal from the solution of the resulting system of equations. On the contrary, when both tractions are unknown, the system matrix becomes singular because the equations associated to the duplicated nodes are equal one to another. In this case, known as the *corner problem*, a non-nodal collocation strategy is carried out. This procedure, which was first employed by Medina [129], was studied in depth by Aznárez [114].

Now, vectors $\mathbf{u}^m$ and $\mathbf{p}^m$, of dimensions 3×1, represent the three nodal components of displacements and tractions at node m. Matrices $\hat{\mathbf{H}}^{\iota m}$ and $\mathbf{G}^{\iota m}$, of dimensions 3×3, represent the response at node m due to the harmonic unit load at collocation point $\boldsymbol{\iota}$, and are defined as

$$\hat{\mathbf{H}}^{\iota m} = \sum_{e_m} \int_{\Gamma_{e_m}} \mathbf{p}^* \phi_k \, d\Gamma \tag{2.41}$$

$$\mathbf{G}^{\iota m} = \sum_{e_m} \int_{\Gamma_{e_m}} \mathbf{u}^* \phi_k \, d\Gamma \tag{2.42}$$

where summations extend over all elements e_m to which node m belongs, and ϕ_k is the shape function corresponding to node m within the element Γ_{e_m}. Usually, collocation point $\boldsymbol{\iota}$ will correspond to a certain node m of the discretization. In this case, calling

$$\mathbf{H}^{\iota m} = \begin{cases} \hat{\mathbf{H}}^{\iota m} & \text{, if } \boldsymbol{\iota} \neq m \\ \mathbf{c}^{\iota} + \hat{\mathbf{H}}^{\iota m} & \text{, if } \boldsymbol{\iota} = m \end{cases} \tag{2.43}$$

eq (2.40) can be written as

$$\sum_{m=1}^{\mathcal{N}_n} \mathbf{H}^{\iota m} \mathbf{u}^m = \sum_{m=1}^{\mathcal{N}_n} \mathbf{G}^{\iota m} \mathbf{p}^m \tag{2.44}$$

which represents the discretized representation of the boundary integral equation.

2.5.2 System of equations arising from the boundary element method

Finally, writing eq. (2.44) for every single node, a system of equations of the type

$$\mathbf{H}\bar{\mathbf{u}} = \mathbf{G}\bar{\mathbf{p}} \tag{2.45}$$

is obtained, where $\bar{\mathbf{u}}$ and $\bar{\mathbf{p}}$ are vectors of dimensions $3\mathcal{N}_n \times 1$ containing the problem nodal values, and where matrices $\mathbf{H}$ and $\mathbf{G}$ are composed by submatrices $\mathbf{H}^{\iota m}$ and $\mathbf{G}^{\iota m}$. Applying boundary conditions and rearranging the columns so that all unknowns (displacements or tractions) are grouped in a vector $\bar{\mathbf{x}}$, a square system of linear independent algebraic equations of the form

$$\mathbf{A}\bar{\mathbf{x}} = \bar{\mathbf{f}} \tag{2.46}$$

can be written, where $\bar{\mathbf{f}}$ is the known vector arising from the application of the boundary conditions and the subsequent rearrangement of equations.

2.5.3 Boundary element typology

Although the formulation presented above is generic for any type of elements, quadratic elements of quadrilateral and triangular shape, with nine and six nodes, respectively, have been used in this work. These elements, together with their approximation functions (also called shape functions), which are written in terms of natural coordinates ξ_1 and ξ_2, are defined in table 2.1. Note that approximation function ϕ_i has a unit value at node i and a zero at all other nodes of the element.

2.5.4 Coupling between subregions

If the domain under study is defined, not only by one region, but by several regions with different elastic properties, the integral formulation and its discretization are still valid for each subdomain. Therefore, for the example depicted in fig. 2.3, two independent sets of equations, corresponding to regions 1 and 2, must first be obtained. Then, equilibrium and compatibility conditions are imposed in order to write a single system of equations representing the whole problem.

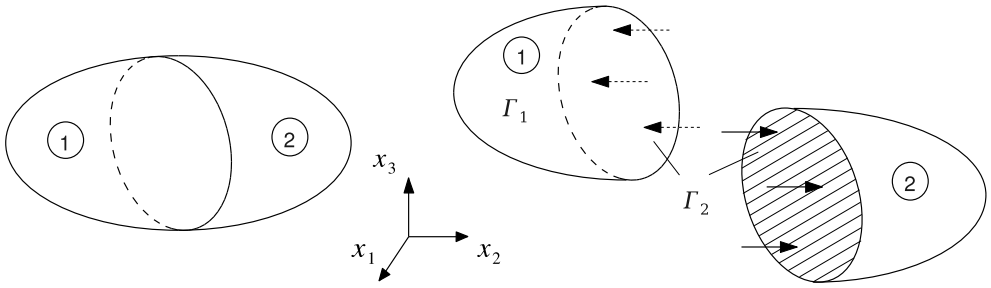

Figure 2.3: *Coupling between two solid regions*

Then, for two regions, one can write

$$\begin{aligned} \mathbf{H}_1^1\,\bar{\mathbf{u}}_1^1 + \mathbf{H}_2^1\,\bar{\mathbf{u}}_2^1 &= \mathbf{G}_1^1\,\bar{\mathbf{p}}_1^1 + \mathbf{G}_2^1\,\bar{\mathbf{p}}_2^1 \\ \mathbf{H}_2^2\,\bar{\mathbf{u}}_2^2 + \mathbf{H}_3^2\,\bar{\mathbf{u}}_3^2 &= \mathbf{G}_2^2\,\bar{\mathbf{p}}_2^2 + \mathbf{G}_3^2\,\bar{\mathbf{p}}_3^2 \end{aligned} \tag{2.47}$$

that, together with

$$\bar{\mathbf{u}}_2^1 = \bar{\mathbf{u}}_2^2 = \bar{\mathbf{u}}_2 \qquad ; \qquad \bar{\mathbf{p}}_2^1 = -\bar{\mathbf{p}}_2^2 = \bar{\mathbf{p}}_2 \tag{2.48}$$

yields a single system of equation of the form

$$\begin{bmatrix} \mathbf{H}_1^1 & \mathbf{H}_2^1 & \mathbf{0} \\ \mathbf{0} & \mathbf{H}_2^2 & \mathbf{H}_3^2 \end{bmatrix} \begin{bmatrix} \bar{\mathbf{u}}_1^1 \\ \bar{\mathbf{u}}_2 \\ \bar{\mathbf{u}}_3^2 \end{bmatrix} = \begin{bmatrix} \mathbf{G}_1^1 & \mathbf{G}_2^1 & \mathbf{0} \\ \mathbf{0} & -\mathbf{G}_2^2 & \mathbf{G}_3^2 \end{bmatrix} \begin{bmatrix} \bar{\mathbf{p}}_1^1 \\ \bar{\mathbf{p}}_2 \\ \bar{\mathbf{p}}_3^2 \end{bmatrix} \tag{2.49}$$

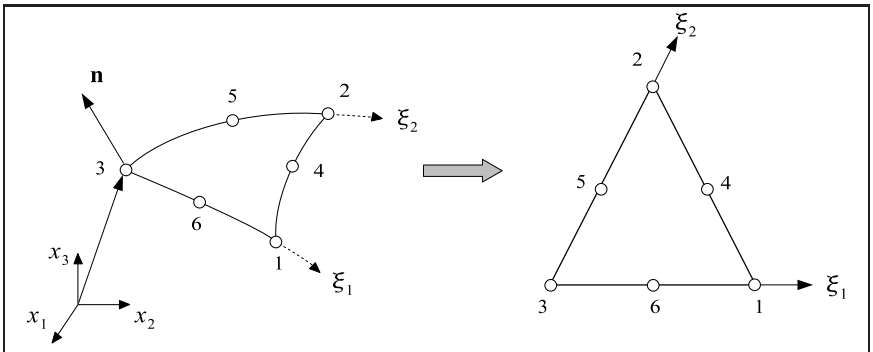

$$\phi_1 = \xi_1(2\xi_1 - 1) \quad ; \quad \phi_4 = 4\xi_1\xi_2$$
$$\phi_2 = \xi_2(2\xi_2 - 1) \quad ; \quad \phi_5 = 4\xi_2\xi_3$$
$$\phi_3 = \xi_3(2\xi_3 - 1) \quad ; \quad \phi_6 = 4\xi_1\xi_3$$
$$\xi_3 = 1 - \xi_2 - \xi_3 \quad ; \quad 0 \le \xi_1 \le 1 \quad ; \quad 0 \le \xi_2 \le 1$$

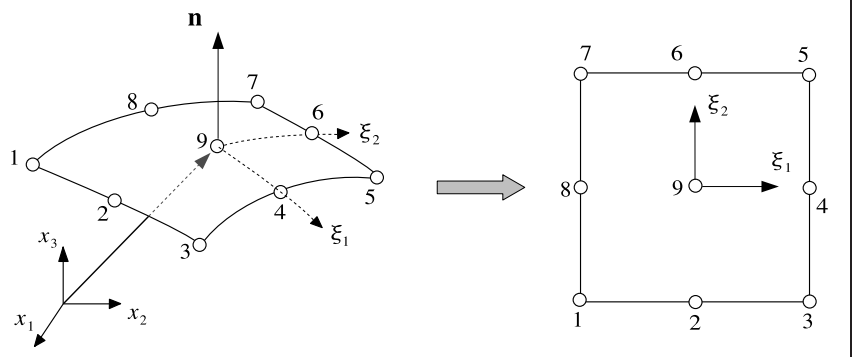

$$\phi_1 = \tfrac{1}{4}\xi_1(\xi_1 - 1)\xi_2(\xi_2 - 1) \quad ; \quad \phi_2 = \tfrac{1}{2}(1 - \xi_1^2)\xi_2(\xi_2 - 1)$$
$$\phi_3 = \tfrac{1}{4}\xi_1(\xi_1 + 1)\xi_2(\xi_2 - 1) \quad ; \quad \phi_4 = \tfrac{1}{2}(1 + \xi_1)\xi_2(1 - \xi_2^2)$$
$$\phi_5 = \tfrac{1}{4}\xi_1(\xi_1 + 1)\xi_2(\xi_2 + 1) \quad ; \quad \phi_6 = \tfrac{1}{2}(1 - \xi_1^2)\xi_2(\xi_2 + 1)$$
$$\phi_7 = \tfrac{1}{4}\xi_1(\xi_1 - 1)\xi_2(\xi_2 + 1) \quad ; \quad \phi_8 = \tfrac{1}{2}(\xi_1 - 1)\xi_2(1 - \xi_2^2)$$
$$\phi_9 = (1 - \xi_1^2)(1 - \xi_2^2)$$
$$-1 \le \xi_1 \le 1 \quad ; \quad -1 \le \xi_2 \le 1$$

Table 2.1: *Quadratic triangular and quadrilateral element types*

2.5.5 Numerical aspects of the BEM

As seen above, the resolution of the boundary value problem by the boundary element method rests on the problem discretization; the numerical evaluation of submatrices $\mathbf{H}^{\imath m}$ and $\mathbf{G}^{\imath m}$; the assembly of the system matrix of equations $\mathbf{A}$ and the computation of the known vector, by applying boundary conditions; and finally the resolution of the resulting linear system of algebraic equations. This way, a numerical approximation of the solution fields, in a set of points of the boundaries, is obtained, and then, displacements at any internal point $\mathbf{x} \in \Omega$ can be computed from eq. (2.25). Thus, one of the key points of the method is the correct and efficient numerical evaluation of integrals.

When the collocation point does not belong to the integrated element j, the integrands in eqs. (2.41) and (2.42) are regular in Γ_j and, consequently, the integrals can be evaluated making use of standard Guassian quadratures (see. *e.g.* [130, 131]). However, when the distance r from the source point to the integrated element is relatively small, those integrals are nearly singular because the integrands are inversely proportional to r. In this case, a regularization scheme, as the one presented by Telles [132], must be used. On the contrary, when the collocation point belongs to the integrated element j, the fundamental solution tensors $\mathbf{u}^*$ and $\mathbf{p}^*$ present singularities of order $O(1/r)$ and $O(1/r^2)$, respectively. The first kind of singularity, also known as *weak singularity*, is addressed through an element subdivision technique (similar to that presented by Li et al. [133] in polar co-ordinates) in conjunction with a co-ordinate transformation procedure (similar to those presented by Telles [132] or by Cerrolaza and Alarcón [134]) to make the integrand regular. The second type of terms, called *strongly-singular terms*, are evaluated making use of a direct technique proposed by Chirino et al. [135] in the line of previous works by Cruse et al. [136], and Li et al. [133]. These strongly-singular integrals are evaluated by identifying the $O(1/r^2)$ terms and splitting them up into a regular surface integral and a linear integral over the element perimeter. Then, singularities get cancelled with the contribution of adjacent elements.

The meticulous exposition of these numerical details is out of the scope of this work. A more detailed explanation of the numerical evaluation of integrals and other numerical aspects of the boundary element method can be found in [114,120].

2.6 Modelling of material damping

The integral formulation of the elastodynamic problem, together with a numerical method (the BEM) for the resolution of the boundary value problem, have been presented along this chapter, being the elastic domain behaviour defined through

a series of governing equations depending on a set of constitutive material parameters.

Up to now, there has been no mention of the possible existence of energy dissipation mechanisms. However, it can be shown that the formulation so far is valid for both damped and undamped materials.

2.6.1 Linear viscoelastic materials

In this work, material damping has been included in the model by considering BEM regions to be linear viscoelastic materials. In viscoelastic regions, as in elastic solids, stress and strain are assumed to be linearly related at a given time t, and the linear superposition principle is assumed to be applicable. However, contrary to what happens with elastic solids, stress and strain values in viscoelastic materials depend not only on the situation at time t, but also on the previous configurations.

This way, creep and relaxation phenomena occur in viscoelastic solids, being creep the gradual deformation of a material due to prolonged stress, and relaxation the slow reduction of the stress level of a solid when subject to constant strain. A comprehensive description of viscoelasticity can be found in the reference text by Christensen [137].

2.6.2 Harmonic viscoelastic constitutive relation

It can be shown that the time-harmonic behaviour of linear, homogeneous, isotropic, viscoelastic media can be described by the constitutive relation

$$\sigma_{ij} = \lambda(\omega)\,\delta_{ij}\varepsilon_{kk} + 2\mu(\omega)\varepsilon_{ij} \tag{2.50}$$

which is identical to eq. (2.3) for linear elastic problems, but now depending on complex-valued frequency-dependent constitutive material parameters (see e.g. Domínguez [120]). Therefore, being the formulation identical in both cases, undamped (elastic) or damped (viscoelastic) materials can be considered by simply assuming the Lamé's parameters to be real-valued or complex-valued quantities, the latter of the form

$$\mu(\omega) = \mathrm{Re}[\mu](1 + \mathrm{i}2\beta_\mu(\omega)) \tag{2.51a}$$
$$\lambda(\omega) = \mathrm{Re}[\lambda](1 + \mathrm{i}2\beta_\lambda(\omega)) \tag{2.51b}$$

where β_μ and β_λ are usually set to the same value β. As λ and μ are complex values in case of viscoelastic materials, c_s, c_p and wave numbers k will also have an imaginary part. Consequently, according to eq. (2.10), the wave motion will be multiplied by an exponentially decreasing function, arising from the imaginary

part of k, in such a way that, as distance in the propagation direction grows, the amplitude of the motion decays, being this phenomenon produced by material damping.

2.6.3 Linear hysteretic viscoelastic model

This way of modelling damped materials corresponds to the three-dimensional Kelvin-Voigt model, whose one-dimensional picture is that of a linear spring $\mathcal{R}$ and a linear dashpot $\mathcal{C}$ connected in parallel, so that

$$\sigma = \mathcal{R}\varepsilon + \mathcal{C}\dot{\varepsilon} = (\mathcal{R} + \ \mathrm{i}\omega\mathcal{C})\varepsilon = \mathcal{R}(1 + \mathrm{i}2\beta(\omega))\varepsilon \tag{2.52}$$

Then, if $\beta(\omega)$ is assumed to be directly proportional to ω, material damping, increasing linearly with frequency, would be of *viscous* type. On the contrary, linear *hysteretic* damping can be modelled by considering a frequency-independent damping coefficient β.

This last model, the linear hysteretic viscoelastic damping model, where the Lamé's constants are of the form

$$\mu = \mathrm{Re}[\mu](1 + \mathrm{i}2\beta) \tag{2.53a}$$

$$\lambda = \mathrm{Re}[\lambda](1 + \mathrm{i}2\beta) \tag{2.53b}$$

is considered to represent best the dynamic behaviour of materials included in the subsequent analyses and, consequently, has been implemented in the codes used in the work.

Chapter 3

BEM-FEM coupling model for the dynamic analysis of pile foundations and pile supported structures

3.1 Introduction

In the previous chapter, the direct boundary element method was formulated to address the elastodynamic problem in the frequency domain. The boundary integral equation was inferred from the reciprocal theorem in elastodynamics, taking into account the body forces per unit mass. However, before the discretization process leading to the BEM system of equations, these body forces were assumed to be zero, as usually done in most applications, which cancels the last term of eq. (2.33).

On the contrary, the approach presented in this work, similar to that of a previous static model by Matos Filho et al [119], does include this term by considering the tractions at pile-soil interfaces as body forces acting within the domain. For this reason, while body forces were defined per unit mass in the previous chapter, hereafter they will be assumed to be of the kind $\mathbf{X} = \rho\mathbf{b}$. The stiffness of piles is introduced by longitudinal finite elements linking the internal nodes of the soil. This way, there is no need to discretize the pile-soil interfaces by boundary elements, with the consequent saving in degrees of freedom. Therefore, there is no pile bore, and the medium remains continuous.

Section 3.2 presents the boundary integral equations for the layered media, where pile-soil interaction forces and pressures are introduced as load-lines and internal forces within the domain. Then, the finite element formulation used to

model the piles is explained in section 3.3, being now possible to pose the BEM-FEM coupling, as done in section 3.4. Later, piles are arranged in pile groups in section 3.5, and the way in which structures founded on those pile foundations are included in the model is presented in section 3.6. The exposition of the numerical BEM-FEM model ends with section 3.7, where the assembly process of the final system of equations is outlined. Some numerical aspects about the evaluation of integrals along load-lines are explained in section 3.8. Part of this material has already been published in some works by the author and the supervisors of this thesis [138, 139].

3.2 Soil BE equations

As seen in chapter 2, each stratum of the soil is modelled by the BEM as a linear, homogeneous, isotropic, viscoelastic, unbounded region with complex valued shear modulus μ of the type $\mu = Re[\mu](1 + 2\mathrm{i}\beta)$, where β is the damping coefficient. The boundary integral equation for a time-harmonic elastodynamic state defined in a domain Ω_m with boundary Γ^m can be written in a condensed and general form as

$$\mathbf{c}^{\iota}\mathbf{u}^{\iota} + \int_{\Gamma^m} \mathbf{p}^*\mathbf{u}\, d\Gamma = \int_{\Gamma^m} \mathbf{u}^*\mathbf{p}\, d\Gamma + \int_{\Omega_m} \mathbf{u}^*\mathbf{X}\, d\Omega \tag{3.1}$$

where $\mathbf{c}^{\iota}$ is the local free term matrix at collocation point $\mathbf{x}^{\iota}$, $\mathbf{X}$ are the body forces in the domain Ω_m, $\mathbf{u}$ and $\mathbf{p}$ are the displacement and traction vectors, and $\mathbf{u}^*$ and $\mathbf{p}^*$ are the elastodynamic fundamental solution tensors representing the response of an unbounded region to a harmonic concentrated unit load with a time variation $e^{\mathrm{i}\omega t}$ applied at a point $\mathbf{x}^{\iota}$.

Generally, body forces $\mathbf{X}$ are considered to be zero in most of the elastodynamic problems. Nevertheless, in this approach, from the integral equation point of view, the pile-soil interaction takes place through internal punctual forces placed at the geometric piles tip and through load-lines placed along the piles axis, as it is assumed that the soil continuity is not altered by the presence of the piles. The load-lines within the soil, the tractions along the pile-soil interface acting over the pile and within the soil ($\mathbf{q}^{p_j} = -\mathbf{q}^{s_j}$), and the internal punctual forces F_{p_j} at the tip of the piles, are represented in fig. 3.1, where a sketch of the model is shown.

Under these assumptions, eq. (3.1) can be written as

$$\mathbf{c}^{\iota}\mathbf{u}^{\iota} + \int_{\Gamma^m} \mathbf{p}^*\mathbf{u}\, d\Gamma = \int_{\Gamma^m} \mathbf{u}^*\mathbf{p}\, d\Gamma + \sum_{j=1}^{n_{ll}^m} \left[\int_{\Gamma_{p_j}^m} \mathbf{u}^*\mathbf{q}^{s_j}\, d\Gamma_{p_j} - \delta_j \boldsymbol{\Upsilon}_k^j F_{p_j} \right] \tag{3.2}$$

where $\Gamma_{p_j}^m$ is the pile-soil interface along the load-line j within the domain Ω_m; n_{ll}^m is the total number of load-lines in the domain Ω_m; δ_j is equal to one if the

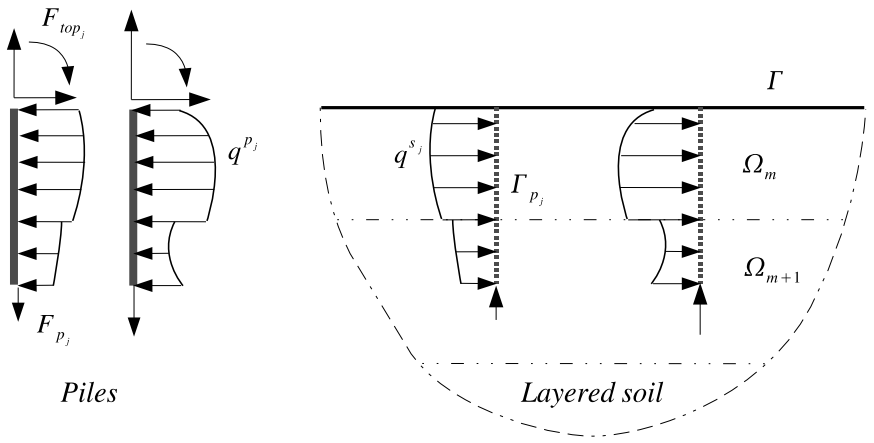

Figure 3.1: *Load-lines representation.*

load-line j contains the tip of a floating pile and zero otherwise; and $\boldsymbol{\Upsilon}_k^j$ is a three-component vector that represents the contribution of the axial force F_{p_j} at the tip of the j^{th} load-line.

The boundaries Γ^m are discretized into quadratic elements of triangular and quadrilateral shapes with six and nine nodes, respectively. Once all boundaries have been discretized, eq. (3.2) can be written, for each region Ω_m, in all nodes on Γ^m in order to obtain a matrix equation of the type

$$\mathbf{H}^{ss}\mathbf{u}^s - \mathbf{G}^{ss}\mathbf{p}^s - \sum_{j=1}^{n_{ll}^m} \mathbf{G}^{sp_j}\mathbf{q}^{s_j} + \sum_{j=1}^{n_{ll}^m} \delta_j \boldsymbol{\Upsilon}^{sj} F_{p_j} = 0 \tag{3.3}$$

where $\mathbf{u}^s$ and $\mathbf{p}^s$ are the vectors of nodal displacements and tractions of boundary elements; $\mathbf{H}^{ss}$ and $\mathbf{G}^{ss}$ are coefficient matrices obtained by numerical integration over the boundary elements of the fundamental solution times the corresponding shape functions; and $\mathbf{G}^{sp_j}$ is the coefficient matrix obtained by numerical integration over load-line j of the fundamental solution times the interpolation functions (3.13), when the unit load is applied on Γ^m.

Furthermore, eq. (3.2) will be also applied on internal nodes belonging to load-line $\Gamma_{p_i}^m$, so that one can write

$$\mathbf{c}\,\mathbf{u}^{p_i} + \mathbf{H}^{p_i s}\mathbf{u}^s - \mathbf{G}^{p_i s}\mathbf{p}^s - \sum_{j=1}^{n_{ll}^m} \mathbf{G}^{p_i p_j}\mathbf{q}^{s_j} + \sum_{j=1}^{n_{ll}^m} \delta_j \boldsymbol{\Upsilon}^{p_i j} F_{p_j} = 0 \tag{3.4}$$

where $\mathbf{H}^{p_i s}$ and $\mathbf{G}^{p_i s}$ are coefficient matrices obtained by numerical integration over the boundary elements of the fundamental solution times the corresponding shape functions; and $\mathbf{G}^{p_i p_j}$ is the coefficient matrix obtained by numerical

integration over load-line j of the fundamental solution times the interpolation functions (3.13), when the unit load is applied on load-line $\Gamma^m_{p_i}$. Here, $\mathbf{u}^{p_i}$ is the vector of nodal displacements of the load-line i, which is multiplied by vector $\mathbf{c}$, valued 1/2 in positions corresponding to pile nodes placed on a smooth surface (as e.g. pile heads) and the unity in the rest of positions. Note that a pile head node and a boundary node can coincide on the same point. When this happens, there exist two nodes with identical coordinates. Then, two equations, one written for the surface node and another written for the load-line node, will be equivalent, but free-terms will occupy different positions on the coefficients matrix, not yielding a singular system of equations.

On the other hand, since an axial force at the pile tip is considered for floating piles, an extra equation needs to be written. To do so, the unit load must be applied in the x_3 direction at any non-nodal point. The point with elemental dimensionless coordinate $\xi = -1/2$ in the bottom element of the pile has been chosen because of its nearness to the tip (see section 3.3.2). This way, the extra equation is

$$\begin{aligned} \frac{1}{8}\left(3u_3^{b_k} + 6u_3^{b_l} - u_3^{b_m}\right) + \int_{\Gamma^m} \hat{\mathbf{p}}^* \mathbf{u}\, d\Gamma = \\ = \int_{\Gamma^m} \hat{\mathbf{u}}^* \mathbf{p}\, d\Gamma + \sum_{j=1}^{n^m_{ll}} \left[\int_{\Gamma^m_{p_j}} \hat{\mathbf{u}}^* \mathbf{q}^{s_j}\, d\Gamma_{p_j} - \delta_j \left(\Upsilon^j_b\right)_3 F_{p_j} \right] \end{aligned} \tag{3.5}$$

where $u_3^{b_k}$,$u_3^{b_l}$ and $u_3^{b_m}$ are the vertical displacements of nodes k,l and m of the bottom element, $\hat{\mathbf{p}}^* = \{p^*_{31}, p^*_{32}, p^*_{33}\}$ and $\hat{\mathbf{u}}^* = \{u^*_{31}, u^*_{32}, u^*_{33}\}$. In matrix form, eq. (3.5) can be written as

$$\mathbf{D}^T \mathbf{u}_b^{p_i} + \mathbf{H}_e^{p_i s} \mathbf{u}^s - \mathbf{G}_e^{p_i s} \mathbf{p}^s - \sum_{j=1}^{n^m_{ll}} \mathbf{G}_e^{p_i p_j} \mathbf{q}^{s_j} + \sum_{j=1}^{n^m_{ll}} \delta_j \Upsilon_{b_3}^{p_i j} F_{p_j} = 0 \tag{3.6}$$

where $\mathbf{u}_b^{p_i}$ is the vector of nodal displacements at the bottom element nodes of the load-line i (which must correspond to the bottom end of a floating pile) where the unit load is applied, $\mathbf{H}_e^{p_i s}$ and $\mathbf{G}_e^{p_i s}$ are vectors obtained by numerical integration over Γ^m of the 3D elastodynamic fundamental solution times the shape functions of the boundary elements, and $\mathbf{G}_e^{p_i p_j}$ is a vector obtained by integration over $\Gamma^m_{p_j}$ of the 3D elastodynamic fundamental solution times the interpolation functions defined in (3.13), when the unit load is applied on the extra point of the load-line i. Finally, $\mathbf{D}^T$ is $1/8\{0,0,3,0,0,6,0,0,-1\}$.

About piles crossing an interface between regions

The situation of a pile crossing interfaces between adjacent regions, as shown in fig. 3.2, is worthy of attention. In this case, as depicted in fig. 3.1, the distribution

of tractions q^s along the pile-soil interface is not continuous between layers, and different load-lines are considered in the upper and lower layers. This fact causes a kind of corner problem which can be overcome by applying a non-nodal collocation strategy. For nodes placed on the interface, eq. (3.4) is applied on an inner point of the pertinent element k, so that the integral equation becomes

$$\mathbf{\Phi u}_k^{p_i} + \mathbf{H}^{p_i s}\mathbf{u}^s - \mathbf{G}^{p_i s}\mathbf{p}^s - \sum_{j=1}^{n_{ll}^m} \mathbf{G}^{p_i p_j}\mathbf{q}^{s_j} + \sum_{j=1}^{n_{ll}^m} \delta_j \mathbf{\Upsilon}^{p_i j} F_{p_j} = 0 \tag{3.7}$$

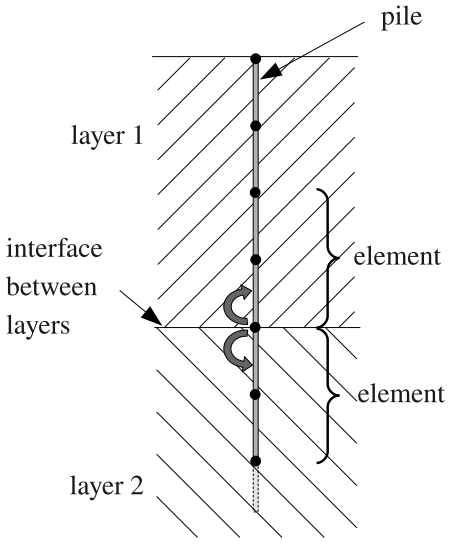

Figure 3.2: *Pile crossing an interface*

where $\mathbf{u}_k^{p_i}$ is the vector of nodal displacements of element Γ_k and $\mathbf{\Phi}$ is the matrix of shape functions specified at the collocation point.

3.3 Pile foundation FE equations

3.3.1 Equation of motion

The behaviour of a pile submitted to dynamic loads can be described by the following differential equation

$$\mathbf{M}\,\ddot{\mathbf{u}}(t) + \mathbf{C}\,\dot{\mathbf{u}}(t) + \mathbf{K}\,\mathbf{u}(t) = \mathbf{f}(t) \tag{3.8}$$

where $\mathbf{M}$, $\mathbf{C}$ and $\mathbf{K}$ are the mass, damping and stiffness matrices of the pile, $\mathbf{u}(t)$ is the vector of nodal displacements and $\mathbf{f}(t)$ the vector of nodal forces over the pile.

It will be assumed now that the pile is subjected to a harmonically varying load. In this case, the vectors of nodal displacements and forces can be expressed as

$$\mathbf{u}(t) = \mathbf{u}^p \, e^{\mathrm{i}\omega t} \quad \text{and} \quad \mathbf{f}(t) = \mathbf{F} \, e^{\mathrm{i}\omega t} \tag{3.9}$$

where $\mathbf{u}^p$ is the vector of nodal translations and rotations amplitudes, $\mathbf{F}$ is the vector of nodal forces and moments amplitudes, ω the circular frequency of the excitation and $\mathrm{i} = \sqrt{-1}$. Then, and considering a pile with zero internal damping, eq. (3.8) becomes

$$(\mathbf{K} - \omega^2 \mathbf{M}) \, \mathbf{u}^p = \mathbf{F} \tag{3.10}$$

3.3.2 Beam element definition

Piles are modelled by FEM as vertical beams according to the Euler-Bernoulli hypothesis, and are discretized using a three-node element, shown in fig. 3.3, that has been defined in order to be able to adjust the deformed shape accurately with a scarce number of elements. There are 13 degrees of freedom defined on it: one vertical and two lateral displacements on each node, and two rotations θ on each one of the extreme nodes, one about x_1 axis and another one about x_2.

The lateral displacements u_1 and u_2 along the element are approximated by a set of fourth degree shape functions, while vertical displacements u_3 are approximated by one of second degree. Thus

$$u_i = \varphi_1 u_{k_i} + \varphi_2 \theta_{k_i} + \varphi_3 u_{l_i} + \varphi_4 u_{m_i} + \varphi_5 \theta_{m_i} \quad ; \quad i = 1, 2 \tag{3.11a}$$

$$u_3 = \phi_1 u_{k_3} + \phi_2 u_{l_3} + \phi_3 u_{m_3} \tag{3.11b}$$

where

$$\begin{aligned}
\varphi_1 &= \xi(-\frac{3}{4} + \xi + \frac{1}{4}\xi^2 - \frac{1}{2}\xi^3) \\
\varphi_2 &= \frac{1}{4}\xi(-1 + \xi + \xi^2 - \xi^3) \\
\varphi_3 &= 1 - 2\xi^2 + \xi^4 \\
\varphi_4 &= \xi(\frac{3}{4} + \xi - \frac{1}{4}\xi^2 - \frac{1}{2}\xi^3) \\
\varphi_5 &= \frac{1}{4}\xi(-1 - \xi + \xi^2 + \xi^3)
\end{aligned} \tag{3.12}$$

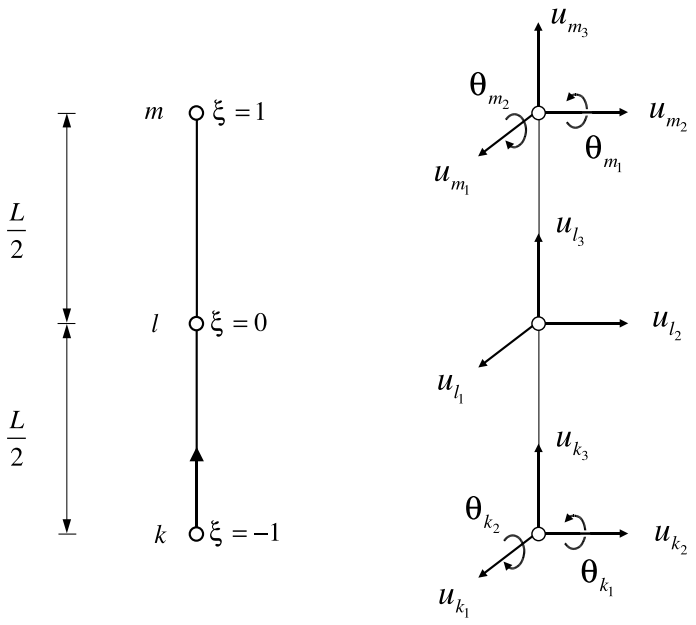

Figure 3.3: *Finite element definition*

and

$$\begin{aligned}\phi_1 &= \frac{1}{2}\xi(\xi-1)\\ \phi_2 &= 1-\xi^2\\ \phi_3 &= \frac{1}{2}\xi(\xi+1)\end{aligned} \tag{3.13}$$

being ξ the elemental dimensionless coordinate varying from $\xi = -1$ to $\xi = +1$.

The stiffness sub-matrices for the lateral and axial behaviour of this element (denoted by l and a respectively), can be obtained using the shape functions defined above and the principle of virtual displacements (see *e.g.* reference [140]) as

$$k^l_{ij} = \int_L \varphi''_i EI \varphi''_j \, dx_3 \quad ; \quad i,j = 1,...,5 \tag{3.14}$$

and

$$k^a_{ij} = \int_L \phi'_i EA \phi'_j \, dx_3 \quad ; \quad i,j = 1,2,3 \tag{3.15}$$

where primes denote derivative referring to x_3 coordinate. This way, stiffness sub-matrices are

$$\mathbf{K}^l = \frac{EI}{5L}\begin{bmatrix} \frac{316}{L^2} & \frac{94}{L} & \frac{-512}{L^2} & \frac{196}{L^2} & \frac{-34}{L} \\ \frac{94}{L} & 36 & \frac{-128}{L} & \frac{34}{L} & -6 \\ \frac{512}{L^2} & \frac{-128}{L} & \frac{1024}{L^2} & \frac{-512}{L^2} & \frac{128}{L} \\ \frac{196}{L^2} & \frac{34}{L} & \frac{-512}{L^2} & \frac{316}{L^2} & \frac{-94}{L} \\ \frac{-34}{L} & -6 & \frac{-128}{L} & \frac{-94}{L} & 36 \end{bmatrix} \quad , \quad \mathbf{K}^a = \frac{EA}{3L}\begin{bmatrix} 7 & -8 & 1 \\ -8 & 16 & -8 \\ 1 & -8 & 7 \end{bmatrix} \tag{3.16}$$

where E is the Young's Modulus for the pile, A and I are the area and the mass moment of inertia of the pile section, and L is the element length. Here, the mass moments of inertia with respect to both principal axes of inertia of the pile section have been assumed to be identical.

Similarly, the mass influence coefficients for an element, that represent the inertia force opposing the acceleration experimented by a certain degree of freedom, can be evaluated by a similar procedure as

$$m^l_{ij} = \int_L \varphi_i \bar{m} \varphi_j \, dx_3 \quad ; \quad m^a_{ij} = \int_L \phi_i \bar{m} \phi_j \, dx_3 \tag{3.17}$$

Thus, considering a beam with uniformly distributed mass $\bar{m}$, the consistent mass matrices obtained for the lateral and axial behaviours are, respectively

$$\mathbf{M}^l = L\,\bar{m}\begin{bmatrix} \frac{13}{63} & \frac{L}{63} & \frac{4}{63} & \frac{-23}{630} & \frac{L}{180} \\ \frac{L}{63} & \frac{L^2}{630} & \frac{2L}{315} & \frac{-L}{180} & \frac{L^2}{1260} \\ \frac{4}{63} & \frac{2L}{315} & \frac{128}{315} & \frac{4}{63} & \frac{-2L}{315} \\ \frac{-23}{630} & \frac{-L}{180} & \frac{4}{63} & \frac{13}{63} & \frac{-L}{63} \\ \frac{L}{180} & \frac{L^2}{1260} & \frac{-2L}{315} & \frac{-L}{63} & \frac{L^2}{630} \end{bmatrix} \quad ; \quad \mathbf{M}^a = \frac{L\,\bar{m}}{15}\begin{bmatrix} 2 & 1 & \frac{-1}{2} \\ 1 & 8 & 1 \\ \frac{-1}{2} & 1 & 2 \end{bmatrix} \tag{3.18}$$

3.3.3 Forces over the pile

The considered forces acting over the pile are punctual forces and moments applied at the top of the pile and distributed forces arising from pile-soil interaction. An axial force at the tip of the pile has been taken into account also. So, the vector of nodal forces $\mathbf{F}$ can be decomposed as

$$\mathbf{F} = \mathbf{F}^{ext} + \mathbf{F}^{eq} = \mathbf{F}_{top} + \mathbf{F}_p + \mathbf{F}^{eq} \tag{3.19}$$

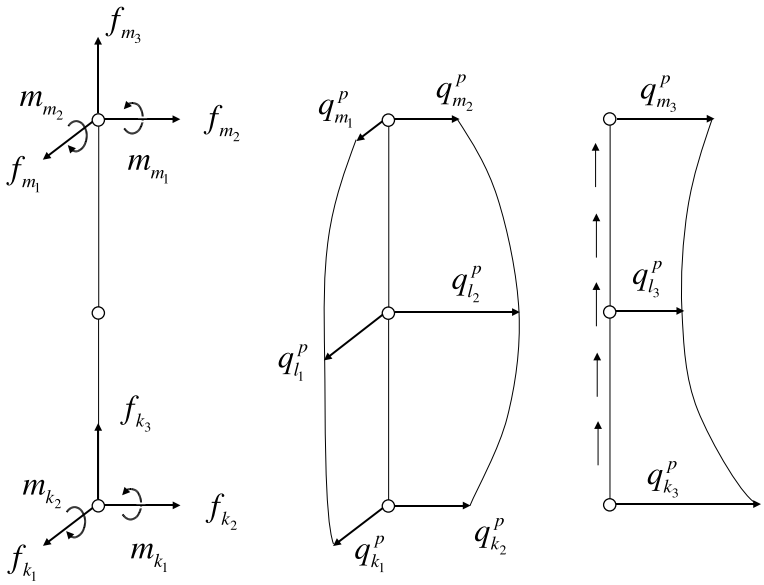

Figure 3.4: *External punctual forces (left) and tractions along the pile-soil interface defined on the generic element*

where $\mathbf{F}^{ext}$ includes the forces at the top $\mathbf{F}_{top}$ and the axial force at the tip of the pile $\mathbf{F}_p$; and $\mathbf{F}^{eq}$ is the vector of the equivalent nodal forces from the pile-soil interaction, that can be calculated as $\mathbf{F}^{eq} = \mathbf{Q} \cdot \mathbf{q}^p$, where $\mathbf{Q}$ is the matrix that transforms nodal force components to equivalent nodal forces.

The external forces defined over the generic element are schematized in fig. 3.4. The tractions $\mathbf{q}^p$ along the pile-soil interface are approximated by

$$q_i = \phi_1 q_{k_i} + \phi_2 q_{l_i} + \phi_3 q_{m_i} \quad ; \quad i = 1, 2, 3 \tag{3.20}$$

using the set of shape functions defined by eq. (3.13). The distribution of tractions along the pile-soil interface is continuous between elements, except for a pile going through an interface between soil layers, case on which q_i will be different above and below that point.

Again, using the principle of virtual displacements, the coefficients of matrix $\mathbf{Q}$ for lateral forces can be obtained as

$$q^l_{ij} = \int_L \varphi_i \phi_j \, dx \quad ; \quad i = 1, ..., 5 \; ; \; j = 1, 2, 3 \tag{3.21}$$

and the ones for axial forces as

$$q^a_{ij} = \int_L \phi_i \phi_j \, dx \quad ; \quad i, j = 1, 2, 3 \tag{3.22}$$

from which the following matrices for lateral and axial equivalent nodal forces, respectively, can be derived

$$\mathbf{Q}^l = \begin{bmatrix} \frac{23L}{140} & \frac{11L}{105} & \frac{-L}{28} \\ \frac{L^2}{84} & \frac{L^2}{105} & \frac{-L^2}{210} \\ \frac{4L}{105} & \frac{16L}{35} & \frac{4L}{105} \\ \frac{-L}{28} & \frac{11L}{105} & \frac{23L}{140} \\ \frac{L^2}{210} & \frac{-L^2}{105} & \frac{-L^2}{84} \end{bmatrix} \quad , \quad \mathbf{Q}^a = \frac{L}{30} \begin{bmatrix} 4 & 2 & -1 \\ 2 & 16 & 2 \\ -1 & 2 & 4 \end{bmatrix} \tag{3.23}$$

3.3.4 Single pile FE system of equations

Once all elemental matrices have been obtained for the whole pile, one can write, for each one, the following expression

$$\bar{\mathbf{K}}\,\mathbf{u}^p = \mathbf{F}^{ext} + \mathbf{Q}\,\mathbf{q}^p \tag{3.24}$$

where $\bar{\mathbf{K}} = \mathbf{K} - \omega^2\mathbf{M}$. As each pile will be discretized using as many elements as necessary to follow its deformed shape accurately, matrices $\bar{\mathbf{K}}$ and $\mathbf{Q}$ are global matrices, obtained as usual from the elemental ones.

It is worth noting that, as it is assumed that the soil continuity is not altered by the presence of the pile, the value of distributed mass assigned to the pile should be modified as $\bar{m} = A(\rho_p - \rho_s)$ so as not to overestimate the total mass introduced in the model, being ρ_p and ρ_s the pile and soil densities. A similar consideration was assumed in [28, 51, 53].

3.4 BEM-FEM coupling

Now, a global system of equations must be built using the expressions defined above. The links between piles and soil that will allow to do the coupling are the tractions $\mathbf{q}^{sj} = -\mathbf{q}^{pj}$ along the pile-soil interface and the displacements $\mathbf{u}^{pj}$ along the pile j.

Eq. (3.24), for the pile j, becomes

$$\bar{\mathbf{K}}^{pj}\,\mathbf{u}^{pj} - \mathbf{F}_{pj} + \mathbf{Q}\,\mathbf{q}^{sj} = \mathbf{F}^j_{top} \tag{3.25}$$

Then, imposing equilibrium and compatibility conditions along the pile-soil interfaces, and assuming the tractions $\mathbf{q}^s$ as positive, eqs. (3.3), (3.4), (3.6) and (3.25)

can be rearranged in a system of equations representing the layered soil – pile foundation problem. For a uniform half-space, the system is of the form

$$\begin{bmatrix} \mathbf{H}^{ss} & -\mathbf{G}^{sp} & \boldsymbol{\Upsilon}^{s} & \emptyset \\ \mathbf{H}^{ps} & -\mathbf{G}^{pp} & \boldsymbol{\Upsilon}^{p} & \mathbf{C}' \\ \mathbf{H}_e^{ps} & -\mathbf{G}_e^{pp} & \boldsymbol{\Upsilon}_{b_3}^{p} & \mathbf{D}' \\ \emptyset & \mathbf{Q} & -\mathbf{I}' & \bar{\mathbf{K}} \end{bmatrix} \begin{bmatrix} \mathbf{u}^{s} \\ \mathbf{q}^{s} \\ \mathbf{F}_{p} \\ \mathbf{u}^{p} \end{bmatrix} = \mathcal{B} \tag{3.26}$$

where $\mathbf{H}^{ss}$ is the $3N \times 3N$ matrix obtained by integration of the 3D time harmonic traction fundamental solution times the shape functions, over the boundary elements, when applying on the boundaries; N is the number of nodes on the boundary; $\mathbf{D}'$ is a matrix made up by $\mathbf{D}$ vectors; $\mathbf{C}'$ contains the free terms corresponding to the collocation over the pile nodes; $\mathbf{I}'$ is a zero matrix with the unity in terms corresponding to the unknown F_{p_j}; the rest of submatrices are

$$\mathbf{G}^{pp} = \begin{bmatrix} \mathbf{G}^{p_1p_1} & \mathbf{G}^{p_1p_2} & \cdots & \mathbf{G}^{p_1p_n} \\ \mathbf{G}^{p_2p_1} & \mathbf{G}^{p_2p_2} & \cdots & \mathbf{G}^{p_2p_n} \\ \vdots & \vdots & \ddots & \vdots \\ \mathbf{G}^{p_np_1} & \mathbf{G}^{p_np_2} & \cdots & \mathbf{G}^{p_np_n} \end{bmatrix}$$

$$\mathbf{G}_e^{pp} = \begin{bmatrix} \mathbf{G}_e^{p_1p_1} & \mathbf{G}_e^{p_1p_2} & \cdots & \mathbf{G}_e^{p_1p_n} \\ \mathbf{G}_e^{p_2p_1} & \mathbf{G}_e^{p_2p_2} & \cdots & \mathbf{G}_e^{p_2p_n} \\ \vdots & \vdots & \ddots & \vdots \\ \mathbf{G}_e^{p_np_1} & \mathbf{G}_e^{p_np_2} & \cdots & \mathbf{G}_e^{p_np_n} \end{bmatrix}$$

$$\boldsymbol{\Upsilon}^{p} = \begin{bmatrix} \boldsymbol{\Upsilon}^{p_1 1} & \boldsymbol{\Upsilon}^{p_1 2} & \cdots & \boldsymbol{\Upsilon}^{p_1 n} \\ \boldsymbol{\Upsilon}^{p_2 1} & \boldsymbol{\Upsilon}^{p_2 2} & \cdots & \boldsymbol{\Upsilon}^{p_2 n} \\ \vdots & \vdots & \ddots & \vdots \\ \boldsymbol{\Upsilon}^{p_n 1} & \boldsymbol{\Upsilon}^{p_n 2} & \cdots & \boldsymbol{\Upsilon}^{p_n n} \end{bmatrix}$$

$$\boldsymbol{\Upsilon}_{b_3}^{p} = \begin{bmatrix} \Upsilon_{b_3}^{p_1 1} & \Upsilon_{b_3}^{p_1 2} & \cdots & \Upsilon_{b_3}^{p_1 n} \\ \Upsilon_{b_3}^{p_2 1} & \Upsilon_{b_3}^{p_2 2} & \cdots & \Upsilon_{b_3}^{p_2 n} \\ \vdots & \vdots & \ddots & \vdots \\ \Upsilon_{b_3}^{p_n 1} & \Upsilon_{b_3}^{p_n 2} & \cdots & \Upsilon_{b_3}^{p_n n} \end{bmatrix}$$

$$\mathbf{G}^{sp} = \left[\begin{array}{cccc} \mathbf{G}^{sp_1} & \mathbf{G}^{sp_2} & \cdots & \mathbf{G}^{sp_n} \end{array} \right]$$

$$\mathbf{\Upsilon}^{s} = \left[\begin{array}{cccc} \mathbf{\Upsilon}^{s1} & \mathbf{\Upsilon}^{s2} & \cdots & \mathbf{\Upsilon}^{sn} \end{array} \right]$$

$$\mathbf{H}^{ps} = \left[\begin{array}{cccc} \mathbf{H}^{p_1 s} & \mathbf{H}^{p_2 s} & \cdots & \mathbf{H}^{p_n s} \end{array} \right]^T$$

$$\mathbf{H}_e^{ps} = \left[\begin{array}{cccc} \mathbf{H}_e^{p_1 s} & \mathbf{H}_e^{p_2 s} & \cdots & \mathbf{H}_e^{p_n s} \end{array} \right]^T$$

$$\mathbf{Q} = \left[\begin{array}{cccc} \mathbf{Q}^{p_1} & \emptyset & \cdots & \emptyset \\ \emptyset & \mathbf{Q}^{p_2} & \cdots & \emptyset \\ \vdots & \vdots & \ddots & \vdots \\ \emptyset & \emptyset & \cdots & \mathbf{Q}^{p_n} \end{array} \right]$$

$$\bar{\mathbf{K}} = \left[\begin{array}{cccc} \bar{\mathbf{K}}^{p_1} & \emptyset & \cdots & \emptyset \\ \emptyset & \bar{\mathbf{K}}^{p_2} & \cdots & \emptyset \\ \vdots & \vdots & \ddots & \vdots \\ \emptyset & \emptyset & \cdots & \bar{\mathbf{K}}^{p_n} \end{array} \right]$$

and $\mathcal{B}$ is the known right-hand vector when all external conditions have been imposed, and the vector of unknowns is

$$\mathbf{x} = \{\mathbf{u}^s, \mathbf{q}^{s_1}, \mathbf{q}^{s_2}, \ldots, \mathbf{q}^{s_n}, F_{p_1}, F_{p_2}, \ldots, F_{p_n}, \mathbf{u}^{p_1}, \mathbf{u}^{p_2}, \ldots, \mathbf{u}^{p_n}\}^T \tag{3.27}$$

In case of multilayered domains, the structure of the system is the same, though equilibrium and compatibility fully bonded contact conditions have to be imposed over the different interfaces of the problem, and the assembly of BE matrices is done according to section 2.5.4.

3.5 Rigid cap formulation

Several piles can be set to work together in a pile group by linking their heads through a pile cap. In this work, piles in a group have been assumed to be fixedly connected to a rigid pile cap. The kinematic constraints between pile heads, as well as the cap equilibrium equations for the system, are presented in the following sections.

3.5.1 Kinematic constraints at pile heads

The constraint of the displacements is carried out by defining the rigid body motion equations and then by condensation. In order to make the computational implementation easier, the already existent degrees of freedom (DoF) of certain pile heads will be used as master degrees of freedom. As only five DoF are defined on pile heads, while six DoF (three displacements and three rotations) are needed to represent the behaviour of the pile cap, at least two piles in the group will be used. These will be labelled as *reference* and *peripheral* piles, this last one used only to define the cap rotation around a vertical axis.

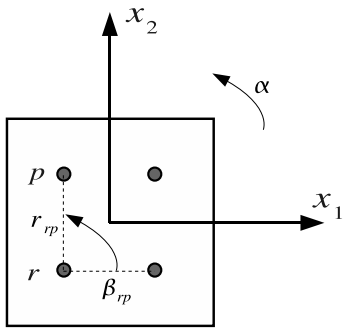

Figure 3.5: *Reference (r) and peripheral (p) piles*

Let β_{rp} and r_{rp} be the angle and the distance between *reference* and *peripheral* pile heads (see fig. 3.5). Assuming small deformations, one can write

$$u_{p_1} = u_{r_1} - r_{rp}\alpha \sin(\beta_{rp}) \tag{3.28a}$$

$$u_{p_2} = u_{r_2} + r_{rp}\alpha \cos(\beta_{rp}) \tag{3.28b}$$

where subindexes 1 and 2 denote motions along axes x_1 and x_2, respectively. Hence, the cap rotation angle α can be defined between these two piles as

$$if \begin{cases} 45^o \leq \beta_{rp} \leq 135^o \\ 225^o \leq \beta_{rp} \leq 315^o \end{cases} \quad \text{then} \quad \alpha = \frac{u_{r_1} - u_{p_1}}{r_{rp}\, \sin(\beta_{rp})} \quad \text{(case a)}$$

$$if \begin{cases} 315^o \leq \beta_{rp} \leq 45^o \\ 135^o \leq \beta_{rp} \leq 225^o \end{cases} \quad \text{then} \quad \alpha = \frac{u_{p_2} - u_{r_2}}{r_{rp}\, \cos(\beta_{rp})} \quad \text{(case b)} \tag{3.29}$$

so that in case a, the auxiliary DoF used from the *peripheral* pile is u_{p_1} while in case b, the used DoF is u_{p_2}. Now, according to the set of six DoF chosen to define

cap displacements and rotations, the next coupling matrices between *peripheral* and *reference* pile heads can be written for cases a and b respectively:

$$\begin{bmatrix} u_{p_2} \\ u_{p_3} \\ \theta_{p_1} \\ \theta_{p_2} \end{bmatrix} = \begin{bmatrix} \tan(\beta_{rp})^{-1} & 1 & 0 & 0 & 0 & -\tan(\beta_{rp})^{-1} \\ 0 & 0 & 1 & -d_{rp_1} & -d_{rp_2} & 0 \\ 0 & 0 & 0 & 1 & 0 & 0 \\ 0 & 0 & 0 & 0 & 1 & 0 \end{bmatrix} \begin{bmatrix} u_{r_1} \\ u_{r_2} \\ u_{r_3} \\ \theta_{r_1} \\ \theta_{r_2} \\ u_{p_1} \end{bmatrix} \tag{3.30}$$

and

$$\begin{bmatrix} u_{p_1} \\ u_{p_3} \\ \theta_{p_1} \\ \theta_{p_2} \end{bmatrix} = \begin{bmatrix} 1 & \tan(\beta_{rp}) & 0 & 0 & 0 & -\tan(\beta_{rp}) \\ 0 & 0 & 1 & -d_{rp_1} & -d_{rp_2} & 0 \\ 0 & 0 & 0 & 1 & 0 & 0 \\ 0 & 0 & 0 & 0 & 1 & 0 \end{bmatrix} \begin{bmatrix} u_{r_1} \\ u_{r_2} \\ u_{r_3} \\ \theta_{r_1} \\ \theta_{r_2} \\ u_{p_2} \end{bmatrix} \tag{3.31}$$

where $d_{rp_i} = x_{p_i} - x_{r_i}$, being $\mathbf{x}$ the position vector of a certain point. Let β_{rj} and r_{rj} be the angle and the distance between the head of the reference pile and that of any other pile j. Coupling matrices between them are, for cases a and b, respectively:

$$\begin{bmatrix} u_{j_1} \\ u_{j_2} \\ u_{j_3} \\ \theta_{j_1} \\ \theta_{j_2} \end{bmatrix} = \begin{bmatrix} 1-\frac{r_{rj}}{r_{rp}}\frac{\sin(\beta_{rj})}{\sin(\beta_{rp})} & 0 & 0 & 0 & 0 & \frac{r_{rj}}{r_{rp}}\frac{\sin(\beta_{rj})}{\sin(\beta_{rp})} \\ \frac{r_{rj}}{r_{rp}}\frac{\cos(\beta_{rj})}{\sin(\beta_{rp})} & 1 & 0 & 0 & 0 & -\frac{r_{rj}}{r_{rp}}\frac{\cos(\beta_{rj})}{\sin(\beta_{rp})} \\ 0 & 0 & 1 & -d_{rj_1} & -d_{rj_2} & 0 \\ 0 & 0 & 0 & 1 & 0 & 0 \\ 0 & 0 & 0 & 0 & 1 & 0 \end{bmatrix} \begin{bmatrix} u_{r_1} \\ u_{r_2} \\ u_{r_3} \\ \theta_{r_1} \\ \theta_{r_2} \\ u_{p_1} \end{bmatrix} \tag{3.32}$$

and

$$\begin{bmatrix} u_{j_1} \\ u_{j_2} \\ u_{j_3} \\ \theta_{j_1} \\ \theta_{j_2} \end{bmatrix} = \begin{bmatrix} 1 & \frac{r_{rj}}{r_{rp}}\frac{\sin(\beta_{rj})}{\cos(\beta_{rp})} & 0 & 0 & 0 & -\frac{r_{rj}}{r_{rp}}\frac{\sin(\beta_{rj})}{\cos(\beta_{rp})} \\ 0 & 1-\frac{r_{rj}}{r_{rp}}\frac{\cos(\beta_{rj})}{\cos(\beta_{rp})} & 0 & 0 & 0 & \frac{r_{rj}}{r_{rp}}\frac{\cos(\beta_{rj})}{\cos(\beta_{rp})} \\ 0 & 0 & 1 & -d_{rj_1} & -d_{rj_2} & 0 \\ 0 & 0 & 0 & 1 & 0 & 0 \\ 0 & 0 & 0 & 0 & 1 & 0 \end{bmatrix} \begin{bmatrix} u_{r_1} \\ u_{r_2} \\ u_{r_3} \\ \theta_{r_1} \\ \theta_{r_2} \\ u_{p_2} \end{bmatrix} \tag{3.33}$$

where $d_{rj_i} = x_{j_i} - x_{r_i}$. These matrices are used to condense DoF of all pile heads in a group to six reference ones.

3.5.2 Equilibrium equations

Dynamic equilibrium is imposed at the pile cap between external forces, inertial forces and reactions at pile heads. Let F_i^e be the applied external forces on the cap centre of gravity $\mathbf{x}_{cg}^c$ on direction i, and M_1^e, M_2^e and M_3^e the applied external moments on the pile cap around axes x_2, x_1 and x_3, respectively. The inertial properties of the pile cap are the pile cap mass m^c, and the moments of inertia I_1, I_2 and I_3 around axes x_2, x_1 and x_3, respectively. Finally, the reactions at j^{th} pile head are the reaction forces F_{j_i} and the reaction torques M_{j_1} and M_{j_2} around axes x_2 and x_1, respectively. With this nomenclature, dynamic equilibrium equations of cap c can be written as

$$\begin{aligned} F_i^e + \sum_{j=1}^{n_p^c} F_{j_i} &= -\omega^2 m^c u_{cg_i} && \text{i} = 1,2,3 \\ M_i^e + \sum_{j=1}^{n_p^c} \left(M_{j_i} - (x_{j_i} - x_{cg_i})F_{j_3} + (x_{j_3} - x_{cg_3})F_{j_i}\right) &= -\omega^2 I_i \theta_i && \text{i} = 1,2 \\ M_3^e + \sum_{j=1}^{n_p^c} \left((x_{j_1} - x_{cg_1})F_{j_2} - (x_{j_2} - x_{cg_2})F_{j_1}\right) &= -\omega^2 I_3 \alpha \end{aligned} \tag{3.34}$$

where n_p^c is the number of piles grouped by cap c.

3.6 Pile supported structures model

3.6.1 Introduction

This section describes the adopted formulation for the analysis of the dynamic behaviour of pile supported multistorey structures, which are assumed to be composed by any number of vertical extensible piers and horizontal rigid slabs (see fig. 3.6). Piers are modelled as massless Euler-Bernoulli beams, with axial and lateral deformation, and with hysteretic damping through a complex valued stiffness of the type $k = Re[k](1 + 2\mathrm{i}\zeta)$. Torsional stiffness is not considered in the piers. The principal axes of inertia of rigid slabs are assumed to be parallel to the global coordinate axes, though the position of their centre of gravity on the horizontal plane can change between storeys.

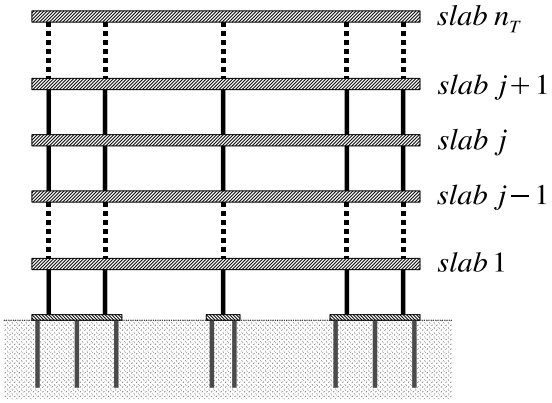

Figure 3.6: *Two-dimensional sketch of considered pile supported structures*

In order to write the equations directly in terms of slabs displacements and rotations (most interesting parameters in this kind of study), all DoF at piers ends are condensated to the centre of gravity of slabs and pile caps. As piers stiffness matrices will be expressed, initially, with respect to piers ends, kinematic relations between piers ends and centres of gravity of slabs or pile caps are established firstly. Then, a general elemental inter-storey stiffness matrix is defined between upper and lower storeys.

3.6.2 Kinematic relations

Let $\mathbf{X}^j = \left\{u_{cg_1{}^j}, u_{cg_2{}^j}, u_{cg_3{}^j}, \alpha_{cg^j}, \Theta_{cg_1{}^j}, \Theta_{cg_2{}^j}\right\}^T$ be the vector defining displacements and rotations at slab or pile cap j centre of gravity, where α_{cg^j}, $\Theta_{cg_1{}^j}$ and $\Theta_{cg_2{}^j}$ are the anticlockwise rotations about axes x_3, x_2 and x_1, respectively. Let

$\mathbf{Y}_i^j = \{u_{i_1}, u_{i_2}, u_{i_3}, \theta_{i_1}, \theta_{i_2}\}_j^T$ be the vector defining displacements and rotations at one end of pier i connected to slab of pile cap j. The compatibility between $\mathbf{X}^j$ and $\mathbf{Y}_i^j$ can be expressed, in matrix form, as

$$\begin{bmatrix} u_{i_1} \\ u_{i_2} \\ u_{i_3} \\ \theta_{i_1} \\ \theta_{i_2} \end{bmatrix}_j = \begin{bmatrix} 1 & 0 & 0 & (x_{cg_2^j} - x_{i_2}) & 0 & 0 \\ 0 & 1 & 0 & (x_{i_1} - x_{cg_1^j}) & 0 & 0 \\ 0 & 0 & 1 & 0 & (x_{i_1} - x_{cg_1^j}) & (x_{i_2} - x_{cg_2^j}) \\ 0 & 0 & 0 & 0 & 1 & 0 \\ 0 & 0 & 0 & 0 & 0 & 1 \end{bmatrix} \begin{bmatrix} u_{cg_1^j} \\ u_{cg_2^j} \\ u_{cg_3^j} \\ \alpha_{cg^j} \\ \Theta_{cg_1^j} \\ \Theta_{cg_2^j} \end{bmatrix} \quad (3.35)$$

About cap-piers coupling

However, as seen in section 3.5, the degrees of freedom corresponding to the centre of gravity of the cap, are not explicitly present in the final system of equations. Instead, the displacements and rotations of the rigid cap are defined by two piles in the group, labelled *reference* and *peripheral* piles. For this reason, the elemental inter-storey stiffness submatrix of columns at ground floor must be written in terms of these auxiliary DoF.

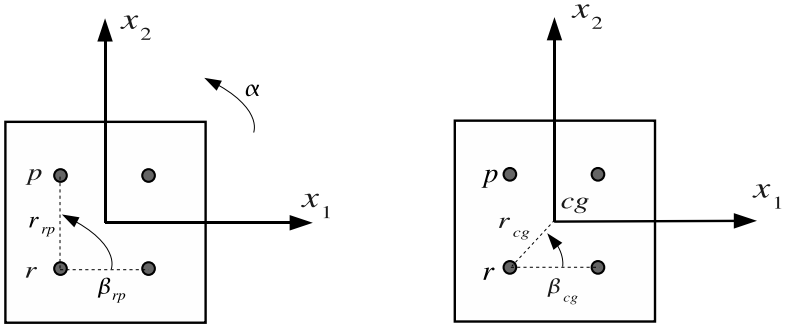

Figure 3.7: *DoF in cap-piers coupling*

To do this, let β_{rp} and r_{rp} be the angle and the distance between *reference* and *peripheral* pile heads, and β_{cg} and r_{cg} the angle and the distance between *reference* pile and cap centre of gravity (see fig. 3.7). According to the set of six DoF chosen to define cap displacements and rotations, the following coupling matrices between *reference* pile head and cap centre of gravity can be written, for

cases a and b (see section 3.5):

$$\begin{bmatrix} u_{cg_1} \\ u_{cg_2} \\ u_{cg_3} \\ \alpha_{cg} \\ \Theta_{cg_1} \\ \Theta_{cg_2} \end{bmatrix} = \begin{bmatrix} 1-\frac{r_{cg}}{r_{rp}}\frac{\sin\beta_{cg}}{\sin\beta_{rp}} & 0 & 0 & 0 & 0 & \frac{r_{cg}}{r_{rp}}\frac{\sin\beta_{cg}}{\sin\beta_{rp}} \\ \frac{r_{cg}}{r_{rp}}\frac{\cos\beta_{cg}}{\sin\beta_{rp}} & 1 & 0 & 0 & 0 & -\frac{r_{cg}}{r_{rp}}\frac{\cos\beta_{cg}}{\sin\beta_{rp}} \\ 0 & 0 & 1 & -d_{rp_1} & -d_{rp_2} & 0 \\ \frac{1}{r_{rp}\sin\beta_{rp}} & 0 & 0 & 0 & 0 & -\frac{1}{r_{rp}\sin\beta_{rp}} \\ 0 & 0 & 0 & -1 & 0 & 0 \\ 0 & 0 & 0 & 0 & -1 & 0 \end{bmatrix} \begin{bmatrix} u_{r_1} \\ u_{r_2} \\ u_{r_3} \\ \theta_{r_1} \\ \theta_{r_2} \\ u_{p_1} \end{bmatrix} \tag{3.36}$$

and

$$\begin{bmatrix} u_{cg_1} \\ u_{cg_2} \\ u_{cg_3} \\ \alpha_{cg} \\ \Theta_{cg_1} \\ \Theta_{cg_2} \end{bmatrix} = \begin{bmatrix} 1 & \frac{r_{cg}}{r_{rp}}\frac{\sin\beta_{cg}}{\cos\beta_{rp}} & 0 & 0 & 0 & -\frac{r_{cg}}{r_{rp}}\frac{\sin\beta_{cg}}{\cos\beta_{rp}} \\ 0 & 1-\frac{r_{cg}}{r_{rp}}\frac{\cos\beta_{cg}}{\cos\beta_{rp}} & 0 & 0 & 0 & \frac{r_{cg}}{r_{rp}}\frac{\cos\beta_{cg}}{\cos\beta_{rp}} \\ 0 & 0 & 1 & -d_{rp_1} & -d_{rp_2} & 0 \\ 0 & -\frac{1}{r_{rp}\cos\beta_{rp}} & 0 & 0 & 0 & \frac{1}{r_{rp}\cos\beta_{rp}} \\ 0 & 0 & 0 & -1 & 0 & 0 \\ 0 & 0 & 0 & 0 & -1 & 0 \end{bmatrix} \begin{bmatrix} u_{r_1} \\ u_{r_2} \\ u_{r_3} \\ \theta_{r_1} \\ \theta_{r_2} \\ u_{p_2} \end{bmatrix} \tag{3.37}$$

respectively, where $d_{rp_i} = x_{p_i} - x_{r_i}$.

3.6.3 Inter-storey stiffness matrix

The elemental 10×10 stiffness submatrix of a pier i, modelled as an Euler-Bernoulli beam, can be defined as

$$\begin{bmatrix} \mathbf{f}_i^{j-1} \\ \mathbf{f}_i^{j} \end{bmatrix} = \begin{bmatrix} a_{x_1} & 0 & 0 & -b_{x_1} & 0 & -a_{x_1} & 0 & 0 & -b_{x_1} & 0 \\ & a_{x_2} & 0 & 0 & -b_{x_2} & 0 & -a_{x_2} & 0 & 0 & -b_{x_2} \\ & & c & 0 & 0 & 0 & 0 & -c & 0 & 0 \\ & & & d_{x_1} & 0 & b_{x_1} & 0 & 0 & \frac{d_{x_1}}{2} & 0 \\ & & & & d_{x_2} & 0 & b_{x_2} & 0 & 0 & \frac{d_{x_1}}{2} \\ & & & & & a_{x_1} & 0 & 0 & b_{x_1} & 0 \\ & & & & & & a_{x_2} & 0 & 0 & b_{x_2} \\ & & sym & & & & & c & 0 & 0 \\ & & & & & & & & d_{x_1} & 0 \\ & & & & & & & & & d_{x_2} \end{bmatrix} \begin{bmatrix} \mathbf{Y}_i^{j-1} \\ \mathbf{Y}_i^{j} \end{bmatrix} \tag{3.38}$$

where

$$a_{x_i} = 12\frac{E\,I_{x_i}}{L^3} \quad ; \quad b_{x_i} = 6\frac{E\,I_{x_i}}{L^2} \quad ; \quad c = \frac{E\,A}{L} \quad ; \quad d_{x_i} = 4\frac{E\,I}{L}$$

and $\mathbf{f}_i{}^j = \{f_{x_1{}^i}, f_{x_2{}^i}, f_{x_3{}^i}, m_{x_1{}^i}, m_{x_2{}^i}\}^{jT}$ are the reaction forces at the slab-column connection.

In order to build an equivalent inter-storey elemental stiffness matrix $\mathcal{K}^i$ relating directly DoF of upper and lower slabs, the stiffness submatrix at the end of pier i is post-multiplied by eq. (3.35), yielding stiffness submatrices expressed in terms of DoF at centres of gravity of slabs or pile caps. Then, rows are operated in order to define resulting forces with respect to slabs centre of gravity. This process yields the following inter-storey elemental stiffness matrix for pier i between lower and upper storeys $j-1$ and j, respectively:

$$\begin{bmatrix} \mathcal{F}^i_{j-1} \\ \mathcal{F}^i_j \end{bmatrix} = \begin{bmatrix} \mathcal{K}^i_{11_{(6x6)}} & \mathcal{K}^i_{12_{(6x6)}} \\ \mathcal{K}^i_{21_{(6x6)}} & \mathcal{K}^i_{22_{(6x6)}} \end{bmatrix} \begin{bmatrix} \mathbf{X}^{j-1} \\ \mathbf{X}^j \end{bmatrix} \tag{3.39}$$

where

$$\mathcal{K}_{11} = \begin{bmatrix} 12\frac{EI_{x_1}}{L^3} & 0 & 0 & -12\frac{EI_{x_1}}{L^3}x_2^b & -6\frac{EI_{x_1}}{L^2} & 0 \\ 0 & 12\frac{EI_{x_2}}{L^3} & 0 & 12\frac{EI_{x_2}}{L^3}x_1^b & 0 & -6\frac{EI_{x_2}}{L^2} \\ 0 & 0 & \frac{EA}{L} & 0 & \frac{EA}{L}x_1^b & \frac{EA}{L}x_2^b \\ -12\frac{EI_{x_1}}{L^3}x_2^b & 12\frac{EI_{x_2}}{L^3}x_1^b & 0 & 12\frac{E}{L^3}IX^b & 6\frac{EI_{x_1}}{L^2}x_2^b & -6\frac{EI_{x_2}}{L^2}x_1^b \\ -6\frac{EI_{x_1}}{L^2} & 0 & \frac{EA}{L}x_1^b & 6\frac{EI_{x_1}}{L^2}x_2^b & 4\frac{EI_{x_1}}{L}+\frac{EA}{L}{x_1^b}^2 & \frac{EA}{L}x_2^bx_1^b \\ 0 & -6\frac{EI_{x_2}}{L^2} & \frac{EA}{L}x_2^b & -6\frac{EI_{x_2}}{L^2}x_1^b & \frac{EA}{L}x_2^bx_1^b & 4\frac{EI_{x_2}}{L}+\frac{EA}{L}{x_2^b}^2 \end{bmatrix}$$

$$\mathcal{K}_{12} = \begin{bmatrix} -12\frac{EI_{x_1}}{L^3} & 0 & 0 & 12\frac{EI_{x_1}}{L^3}x_2^a & -6\frac{EI_{x_1}}{L^2} & 0 \\ 0 & -12\frac{EI_{x_2}}{L^3} & 0 & -12\frac{EI_{x_2}}{L^3}x_1^a & 0 & -6\frac{EI_{x_2}}{L^2} \\ 0 & 0 & -\frac{EA}{L} & 0 & -\frac{EA}{L}x_1^a & -\frac{EA}{L}x_2^a \\ 12\frac{EI_{x_1}}{L^3}x_2^b & -12\frac{EI_{x_2}}{L^3}x_1^b & 0 & -12\frac{E}{L^3}IX^{ab} & 6\frac{EI_{x_1}}{L^2}x_2^b & -6\frac{EI_{x_2}}{L^2}x_1^b \\ 6\frac{EI_{x_1}}{L^2} & 0 & -\frac{EA}{L}x_1^b & -6\frac{EI_{x_1}}{L^2}x_2^a & 2\frac{EI_{x_1}}{L}+\frac{EA}{L}x_1^ax_1^b & -\frac{EA}{L}x_2^ax_1^b \\ 0 & 6\frac{EI_{x_2}}{L^2} & -\frac{EA}{L}x_2^b & 6\frac{EI_{x_2}}{L^2}x_1^a & -\frac{EA}{L}x_1^ax_2^b & 2\frac{EI_{x_2}}{L}-\frac{EA}{L}x_2^ax_2^b \end{bmatrix}$$

$$\mathcal{K}_{21} = \begin{bmatrix} -12\frac{EI_{x_1}}{L^3} & 0 & 0 & 12\frac{EI_{x_1}}{L^3}x_2^b & 6\frac{EI_{x_1}}{L^2} & 0 \\ 0 & -12\frac{EI_{x_2}}{L^3} & 0 & -12\frac{EI_{x_2}}{L^3}x_1^b & 0 & 6\frac{EI_{x_2}}{L^2} \\ 0 & 0 & -\frac{EA}{L} & 0 & -\frac{EA}{L}x_1^b & -\frac{EA}{L}x_2^b \\ 12\frac{EI_{x_1}}{L^3}x_2^a & -12\frac{EI_{x_2}}{L^3}x_1^a & 0 & -12\frac{E}{L^3}IX^{ab} & -6\frac{EI_{x_1}}{L^2}x_2^a & 6\frac{EI_{x_2}}{L^2}x_1^a \\ -6\frac{EI_{x_1}}{L^2} & 0 & -\frac{EA}{L}x_1^a & 6\frac{EI_{x_1}}{L^2}x_2^b & 2\frac{EI_{x_1}}{L} - \frac{EA}{L}x_1^a x_1^b & -\frac{EA}{L}x_2^b x_1^a \\ 0 & -6\frac{EI_{x_2}}{L^2} & -\frac{EA}{L}x_2^a & -6\frac{EI_{x_2}}{L^2}x_1^b & -\frac{EA}{L}x_1^b x_2^a & 2\frac{EI_{x_2}}{L} - \frac{EA}{L}x_2^b x_2^a \end{bmatrix}$$

$$\mathcal{K}_{22} = \begin{bmatrix} 12\frac{EI_{x_1}}{L^3} & 0 & 0 & -12\frac{EI_{x_1}}{L^3}x_2^a & 6\frac{EI_{x_1}}{L^2} & 0 \\ 0 & 12\frac{EI_{x_2}}{L^3} & 0 & 12\frac{EI_{x_2}}{L^3}x_1^a & 0 & 6\frac{EI_{x_2}}{L^2} \\ 0 & 0 & \frac{EA}{L} & 0 & \frac{EA}{L}x_1^a & \frac{EA}{L}x_2^a \\ -12\frac{EI_{x_1}}{L^3}x_2^a & 12\frac{EI_{x_2}}{L^3}x_1^a & 0 & 12\frac{E}{L^3}IX^a & -6\frac{EI_{x_1}}{L^2}x_2^a & 6\frac{EI_{x_2}}{L^2}x_1^a \\ 6\frac{EI_{x_1}}{L^2} & 0 & \frac{EA}{L}x_1^a & -6\frac{EI_{x_1}}{L^2}x_2^a & 4\frac{EI_{x_1}}{L} + \frac{EA}{L}x_1^{a\,2} & \frac{EA}{L}x_2^a x_1^a \\ 0 & 6\frac{EI_{x_2}}{L^2} & \frac{EA}{L}x_2^b & 6\frac{EI_{x_2}}{L^2}x_1^a & \frac{EA}{L}x_2^a x_1^a & 4\frac{EI_{x_2}}{L} + \frac{EA}{L}x_2^{a\,2} \end{bmatrix}$$

being

$$IX^a = I_{x_1}(x_2^a)^2 + I_{x_2}(x_1^a)^2$$
$$IX^{ab} = I_{x_1}x_2^a x_2^b + I_{x_2}x_1^a x_1^b$$
$$IX^b = I_{x_1}(x_2^b)^2 + I_{x_2}(x_1^b)^2$$

In the above expressions, $x_k^a = x_{i_k} - x_{cg_k^a}$ and $x_k^b = x_{i_k} - x_{cg_k^b}$ are the relative horizontal coordinates of the pier axis with respect to the centre of gravity of the storey above and below, respectively, and $\mathcal{F}_j{}^T = \{F_{x_1}, F_{x_2}, F_{x_3}, M_\alpha, M_{x_1}, M_{x_2}\}^j$ stands for the slab-column connection reactions expressed with respect to the centre of gravity of the corresponding slab.

Having defined a general element inter-storey stiffness matrix, the general assembly process of the Finite Element Method can be followed to build a discretized equation of motion for the structure of the form

$$\left(\mathcal{K} - \omega^2 \mathcal{M}\right) \mathcal{X} = \mathcal{F} \tag{3.40}$$

where $\mathcal{K}$ is the global stiffness matrix of the structure, $\mathcal{X}$ is the vector of displacements and rotations at slabs, $\mathcal{F}$ is the vector of external forces over the structure and $\mathcal{M}$ is the matrix of inertial properties of the structure, defined at each slab.

3.7 Assembly of the global system matrix of equations

The way in which eqs. (3.24), (3.3), (3.4), (3.6) and (3.40) are arranged into a global system of equations depends on the specific configuration and the boundary conditions, but equilibrium and compatibility fully-bonded contact conditions over the different interfaces of the problem are always imposed. The most general situation is that of a problem in which there exist multiple superstructures founded on different pile caps on a layered soil, being the system subject to external forces and/or incident seismic waves. In such a general case, the system of equations is of the form

$$\mathcal{A}\left\{\mathbf{u}^s, \mathbf{p}^s, \mathbf{q}^s, \mathbf{F}_p, \mathbf{u}^p, \mathbf{X}^j, \mathbf{F}_{top}, \mathbf{f}_o\right\}^T = \mathcal{B} \tag{3.41}$$

where $\mathcal{A}$, whose structure is sketched in fig. 3.8, is the square matrix of coefficients, and $\mathcal{B}$ is the known vector, both computed by rearranging the equations and prescribing the known boundary conditions. The vector of unknowns includes the displacements $\mathbf{u}^s$ and/or tractions $\mathbf{p}^s$ at boundary element nodes, the tractions at pile-soil interface $\mathbf{q}^s$, the forces at pile tips $\mathbf{F}_p$, the nodal translations and rotations on pile nodes $\mathbf{u}^p$, the degrees of freedom defined at the structures $\mathbf{X}^j$, the reactions at pile-cap joints $\mathbf{F}_{top}$ and the forces at structure base $\mathbf{f}_o$.

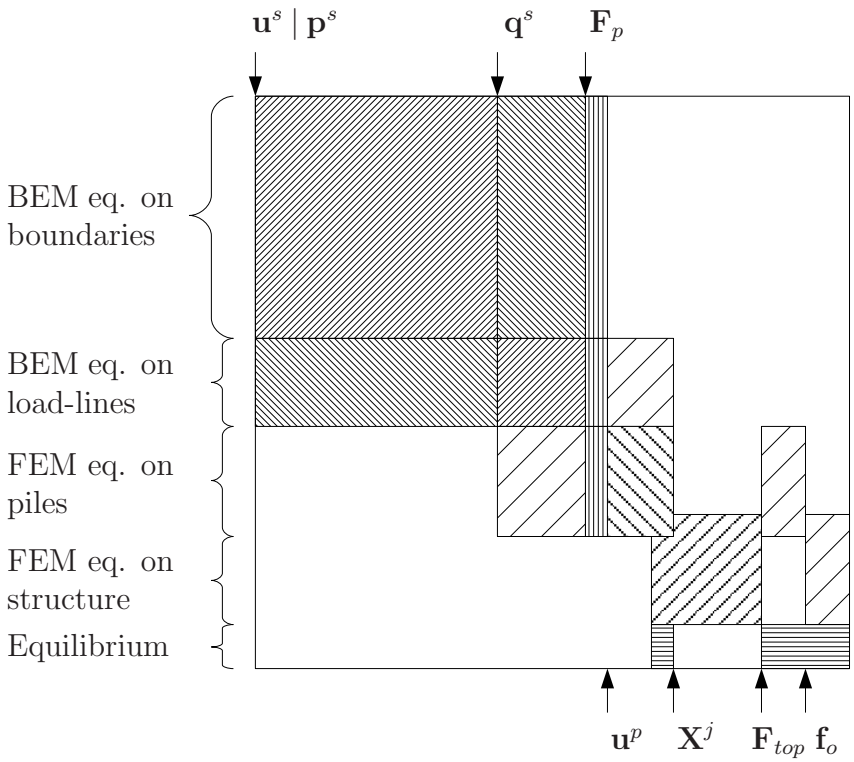

Figure 3.8: *Structure of the system matrix of coefficients* $\mathcal{A}$

3.8 Numerical evaluation of integrals over load lines

The integrals over the load-line Γ_{p_j} of $\mathbf{u}^*\mathbf{q}^{s_j}$ and $\hat{\mathbf{u}}^*\mathbf{q}^{s_j}$ in eqs. (3.2) and (3.5), respectively, are computed as monodimensional integrals extended to a line defined by the pile axis when the collocation point is outside load-line j. On the other hand, these integrals have a singularity at the collocation point when applied on the integrated line. In this case, in order to avoid this singularity, the integrals are evaluated over a cylinder whose radius R_p is $\sqrt{A/\pi}$. This way, let us consider the pile-soil interface Γ_p (whatever the kind of section) as a cylinder of radius R_p where tractions $\boldsymbol{\sigma}_{ps}$ are applied. The last term of eq. (3.1) includes integrals of the type

$$\int_{\Gamma_p} \mathbf{u}^* \boldsymbol{\sigma}_{ps}\, d\Gamma_p = \int_{\Gamma_p} \mathbf{u}^* \frac{\mathbf{q}^s}{2\pi R_p}\, d\Gamma_p = \frac{1}{2\pi R_p} \sum_{e=1}^{N_e} \sum_{i=k,l,m} \left[\int_{\Gamma_{p_e}} \mathbf{u}^* \phi_i\, d\Gamma_p \right] \mathbf{q}_i^s \tag{3.42}$$

where N_e is the number of elements in which the load-line has been discretized, and where eq. (3.20) has been used to express $\mathbf{q}^s$ along each element. As seen in chapter 2, the elastodynamic fundamental solution used herein, that gives the displacement at point $\mathbf{x}$ in the direction k when the source load is applied at point $\mathbf{x}^\iota$ in the l direction, can be written as

$$\begin{aligned} u_{lk}^* &= \frac{1}{4\pi\mu} \left[\psi \delta_{lk} - \chi r_{,k} r_{,l} \right] \\ \psi &= -\left(\frac{c_s}{c_p}\right)^2 \left(\frac{1}{z_p^2 r^2} - \frac{1}{z_p r} \right) \frac{e^{z_p r}}{r} + \left(\frac{1}{z_s^2 r^2} - \frac{1}{z_s r} + 1 \right) \frac{e^{z_s r}}{r} \\ \chi &= -\left(\frac{c_s}{c_p}\right)^2 \left(\frac{3}{z_p^2 r^2} - \frac{3}{z_p r} + 1 \right) \frac{e^{z_p r}}{r} + \left(\frac{3}{z_s^2 r^2} - \frac{3}{z_s r} + 1 \right) \frac{e^{z_s r}}{r} \end{aligned} \tag{3.43}$$

where μ is the shear modulus, δ_{lk} is the Kronecker delta function, and $r = |\mathbf{x} - \mathbf{x}^\iota|$. For this specific case (see fig. 3.9), the derivatives of the position vector $\mathbf{r} = \mathbf{x} - \mathbf{x}^\iota$ are

$$r_{,1} = \frac{x_1^r}{r} = \frac{R_p \cos(\gamma)}{r} \tag{3.44a}$$

$$r_{,2} = \frac{x_2^r}{r} = \frac{R_p \sin(\gamma)}{r} \tag{3.44b}$$

$$r_{,3} = \frac{x_3^r}{r} \tag{3.44c}$$

Then, the integrals in the last term of eq. (3.42) can be evaluated, in cylindrical

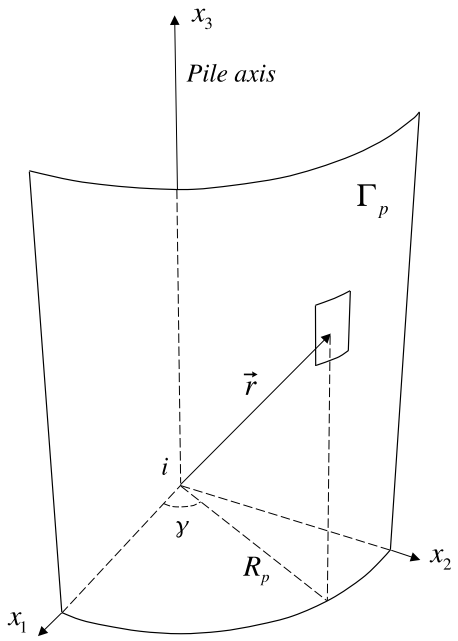

Figure 3.9: *Cylindrical surface for integration over pile-soil interface when the collocation point belongs to the pile*

coordinates (see fig. 3.9), as

$$\begin{aligned}\int_{\Gamma_{pe}} \mathbf{u}^* \phi_i \, d\Gamma_p &= \int_{x_3^r} \int_\theta \frac{1}{4\pi\mu} \left[\psi \delta_{lk} - \chi r_{,k} r_{,l}\right] \phi_i R_p \, d\theta \, dx_3 \\ &= \frac{R_p}{4\pi\mu} \int_{x_3^r} \left[2\pi\psi\delta_{lk} - \chi \int_0^{2\pi} r_{,k} r_{,l} \, d\theta\right] \phi_i \, dx_3 \\ &= \frac{R_p}{4\mu} \int_{x_3^r} \left[2\psi\delta_{lk} - \frac{1}{r^2}\chi \mathbf{R}_{lk}\right] \phi_i \, dx_3\end{aligned} \tag{3.45}$$

where $x_3^r = x_3 - x_3^k$ and

$$\mathbf{R}_{lk} = \begin{pmatrix} R_p^2 & 0 & 0 \\ 0 & R_p^2 & 0 \\ 0 & 0 & 2(x_3^r)^2 \end{pmatrix} \tag{3.46}$$

Now, the integral of eq. (3.42) can be written as

$$\int_{\Gamma_p} \mathbf{u}^* \boldsymbol{\sigma}_{ps} \, d\Gamma_p = \sum_{e=1}^{N_e} \frac{L_e}{16\pi\mu} \sum_{i=k,l,m} \left[\int_{-1}^{1} \left(2\psi\delta_{lk} - \frac{\chi}{r^2}\mathbf{R}_{lk}\right) \phi_i \, d\xi\right] \mathbf{q}_i^s \tag{3.47}$$

Nevertheless, to compute integrals over Γ_{p_j} from the same pile, a non-nodal collocation strategy could also be carried out. This will lead to a procedure that allows the reinterpretation of the previous equation. This way, in order to avoid breaking the problem symmetries, at least four collocation points, symmetrically placed around the pile, should be chosen (see fig. 3.10). A single equation is obtained by adding these four equations divided by four, so that the arising coefficients are of the same order. In this case, integrating over the load-line, the last term of eq. (3.1) becomes

$$\begin{aligned}\int_{\Gamma_p} \mathbf{u}^* \mathbf{q}^s \, d\Gamma_p =& \frac{1}{4} \sum_{\substack{n=1 \\ c.p.}}^{4} \sum_{e=1}^{N_e} \sum_{i=k,l,m} \frac{1}{4\pi\mu} \left[\int_{x_3^r} (\psi \delta_{lk} - \chi r_{,k} r_{,l}) \, \phi_i \, dx_3 \right] \mathbf{q}_i^s \\ =& \frac{1}{4} \sum_{\substack{n=1 \\ c.p.}}^{4} \sum_{e=1}^{N_e} \sum_{i=k,l,m} \frac{1}{4\pi\mu} \left[\int_{x_3^r} \phi_i \left(\psi \delta_{lk} - \frac{\chi}{r^2} \mathbf{R}_{lk}^n \right) \, dx_3 \right] \mathbf{q}_i^s \end{aligned} \tag{3.48}$$

where

$$\begin{aligned} \underset{n=1,2}{\mathbf{R}_{lk}^n} &= \begin{pmatrix} 0 & 0 & 0 \\ 0 & R_p^2 & (-1)^n R_p x_3^r \\ 0 & (-1)^n R_p x_3^r & (x_3^r)^2 \end{pmatrix} \\ \underset{n=3,4}{\mathbf{R}_{lk}^n} &= \begin{pmatrix} R_p^2 & 0 & (-1)^n R_p x_3^r \\ 0 & 0 & 0 \\ (-1)^n R_p x_3^r & 0 & (x_3^r)^2 \end{pmatrix} \end{aligned} \tag{3.49}$$

As it can be seen, this procedure leads to an equation in each direction completely equivalent to eq. (3.47), which means that both methods are analogous.

On the other hand, when the collocation point 'k' is placed outside the load-line j, one can write

$$\boldsymbol{\Upsilon}_k^j = \{ u_{13}^* \; u_{23}^* \; u_{33}^* \}_k \tag{3.50}$$

However, when the collocation point is placed at the bottom node of load-line j (provided it corresponds to the bottom end of a pile), $\boldsymbol{\Upsilon}_k^j F_{p_j}$ becomes singular. In this case, to avoid this singularity, the axial force at the tip can be considered as a uniform pressure σ_b over a circular surface with radius $R_p = \sqrt{A/\pi}$. In this work, this strategy has been used whenever the collocation point is placed on the axis of load-line j. According to this, one can write

$$\boldsymbol{\Upsilon}_k^j F_{p_j} = \int_{\Gamma_b} u_{i3}^* \, \sigma_b \, d\Gamma_b \tag{3.51}$$

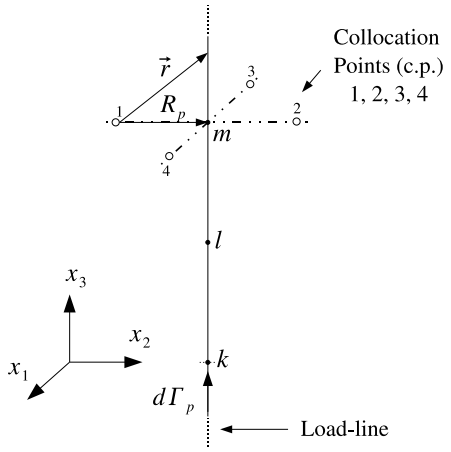

Figure 3.10: *Non-nodal collocation strategy*

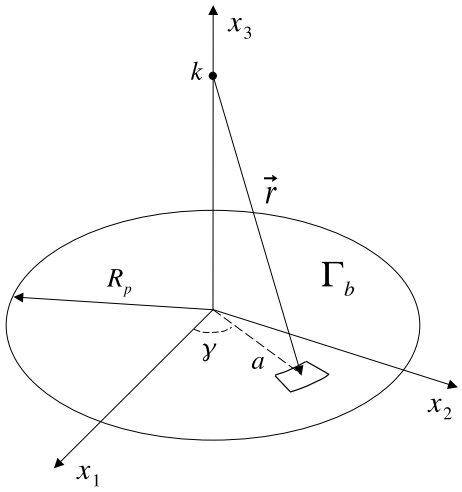

Figure 3.11: *Integration over pile tip surface*

where Γ_b is the tip surface and $\sigma_b = F_p/A$. Then, in cylindrical coordinates (see fig. 3.11), eq. (3.51) becomes

$$\Upsilon_k^j = \frac{1}{4\pi\mu A}\int_0^{2\pi}\int_0^{R_p}\left[\psi\delta_{i3} - \chi r_{,i}r_{,3}\right]\, a\, da\, d\theta = \\ = \frac{1}{2\mu A}\int_0^{R_p}\delta_{i3}\left[\psi - (x_3^r)^2\,\frac{\chi}{r^2}\right]\, a\, da \quad (3.52)$$

which integral is regular and can be evaluated numerically.

Chapter 4

Dynamic analysis of pile foundations

4.1 Introduction

The BEM-FEM coupling model for the dynamic analysis of piles and pile groups, presented in chapter 3, is used herein to compute time-harmonic stiffness functions, together with the seismic response, of pile foundations embedded in viscoelastic zoned-homogeneous layered soils.

The forced vibration and the seismic excitation models are first explained in sections 4.2 and 4.3, respectively. Then, in order to validate the numerical model proposed in this work, several results are presented in section 4.4 in comparison to others obtained by different authors.

Afterwards, three sets of results corresponding to different kinds of problems are presented and discussed. First, section 4.5 analyses the distribution of shear forces along and between piles in a group. A specific case of a 5×5 pile group, for which dynamic stiffnesses are also presented in section 4.4, is selected. Secondly, several results of vertical, horizontal and rocking time-harmonic stiffness functions of single piles and 2×2 pile groups embedded in a stratum resting on a rigid bedrock, are presented in section 4.6. Different depths of the stratum and three foundation configurations are studied, and the effects associated to these parameters are discussed. Finally, the influence of the stratigraphy on the seismic response of a 3×3 pile group is analysed in section 4.7. To this end, displacement transfer functions for vertically-incident plane time-harmonic shear waves and response spectra for a particular configuration, under two different strong ground motions, are presented for several soil profiles. Pile-to-pile kinematic interaction and wave-scattering phenomena, are also investigated. Some of the results presented in this chapter have been previously presented in some works by the author and the supervisors of this thesis [138, 139, 141, 142].

4.2 Forced vibration model

In order to compute impedance functions of pile foundations, pile heads are subjected to forced vibration in each of the oscillation modes (vertical, horizontal and rocking). This way, the ratio between each component of the vector of forces (and moments) applied at the pile top and the corresponding term of the resulting vector of displacements (and rotations) at the same point, yields the dynamic stiffness matrix K_{ij} of the foundation. For a group of piles, it is assumed that the pile heads are constrained by a rigid pile-cap, and the foundation stiffness can be computed as the addition of the contributions of each pile. Fig. 4.1 illustrates the approached problem for a usual configuration, where L and d are used to denote the length and diameter of the piles, and s refers to the distance between adjacent piles.

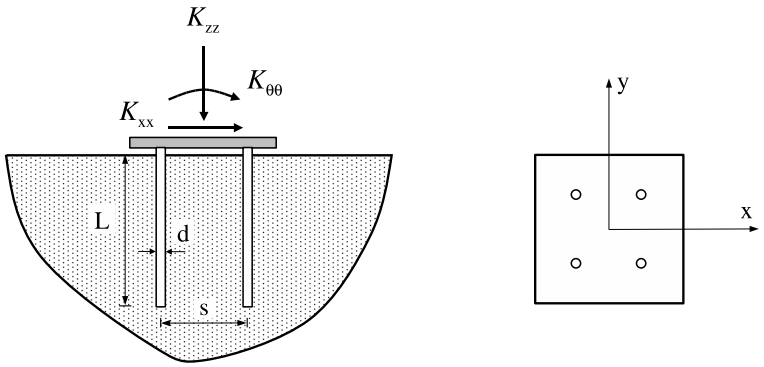

Figure 4.1: 2×2 *pile group embedded in a half-space. Problem geometry definition.*

The dynamic stiffness terms for a time harmonic excitation are functions of frequency ω and they are usually written as

$$K_{ij} = k_{ij} + \mathrm{i} a_o c_{ij} \tag{4.1}$$

where k_{ij} and c_{ij} are the frequency dependent dynamic stiffness and damping coefficients, respectively, a_o is the dimensionless frequency

$$a_o = \frac{\omega d}{c_s} \tag{4.2}$$

and c_s is the soil shear-wave velocity.

Once the problem has been solved for a unitary displacement applied at the cap, and the vectors $\mathbf{u}^s$ and $\mathbf{q}^s$ have been computed, the dynamic stiffness at a

certain frequency can be easily obtained by applying eq. (3.24) at the top element of each pile.

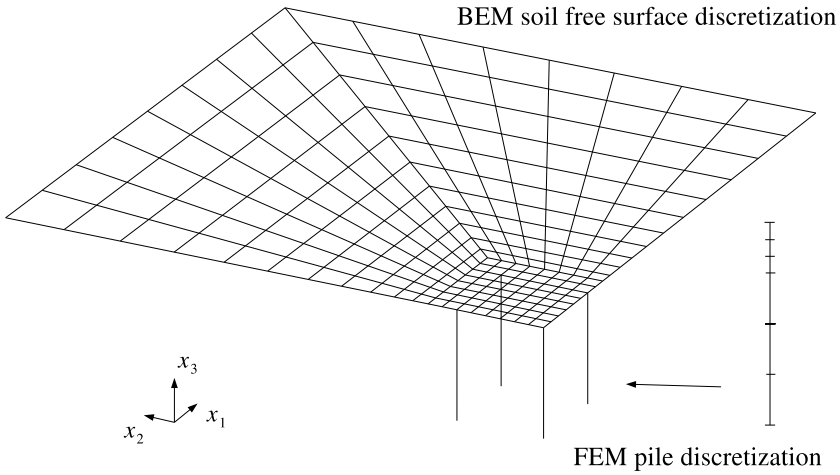

Figure 4.2: 3×3 *pile group BEM-FEM discretization for horizontal problems*

Fig. 4.2 shows a sketch of a discretization used to obtain the impedances of different pile groups embedded in a viscoelastic half-space, where boundary elements for the soil and mono-dimensional finite elements for the piles were used. As the developed software incorporates symmetry properties, only a quarter of the total geometry of the problem has to be discretized. The length of free surface needed is, approximately, three times the pile length, and the element size is chosen in such a way that its main dimension is always shorter than the half of the wave length. On the other hand, the three-node element defined in section 3.3 is used on the pile. Three equal elements for vertical problems and six elements, of which three concentrated on the top, for horizontal and rocking problems, were used. It should be noted that the model allows to change the number and position of piles without modifying the free surface discretization.

4.3 Seismic excitation model

When seismic waves impinge on the site under study, reflection and refraction phenomena take place, and the arising wave field modifies the incident wave train. The original wave field, which is assumed to come from a far source, is the *incident field* $\mathbf{u}_I$, while the one produced by the reflection and refraction phenomena receives the name of *scattered field* $\mathbf{u}_S$. The resulting displacement and traction fields (*total fields*) can be obtained by superposition as $\mathbf{u} = \mathbf{u}_I + \mathbf{u}_S$ and $\mathbf{p} = \mathbf{p}_I + \mathbf{p}_S$.

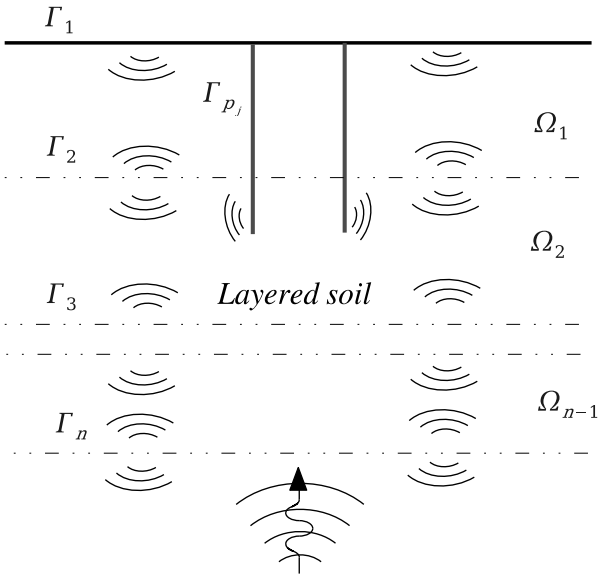

Figure 4.3: *Incident and scattered fields for piles embedded in a layered soil*

Let us consider that a pile foundation embedded in a layered soil is subjected to time-harmonic incident waves, as depicted in fig. 4.3. Assume that the semi-infinite domain Ω_1 is defined by the boundary $\Gamma_{s_1} \equiv \Gamma_1 \cup \Gamma_2$, and consequently, Ω_i is defined by the boundary $\Gamma_{s_i} \equiv \Gamma_i \cup \Gamma_{i+1}$. If the deepest domain is a half-space, then $\Gamma_{s_n} \equiv \Gamma_n$. Note that the magnitude of the scattered field decreases with distance due to the existing material and radiation damping in the soil, and consequently, boundaries far from the pile foundation do not need to be discretized.

Eq. (3.3) can be written for Ω_i, in terms of the total field, as

$$\mathbf{H}^{s_i s_i}\mathbf{u}^{s_i} - \mathbf{G}^{s_i s_i}\mathbf{p}^{s_i} - \sum_{j=1}^{n_{ll}^m} \mathbf{G}^{s_i p_j}\mathbf{q}^{s_j} + \sum_{j=1}^{n_{ll}^m} \delta_j \boldsymbol{\Upsilon}^{s_i j} F_{p_j} = 0 \tag{4.3}$$

On the other hand, as incident, scattered and total fields satisfy the governing equations, eq. (3.3) can also be written in terms of the incident field as

$$\mathbf{H}^{s_i s_i}\mathbf{u}_I^{s_i} - \mathbf{G}^{s_i s_i}\mathbf{p}_I^{s_i} = 0 \tag{4.4}$$

where tractions along the pile-soil interface q^{s_j} and forces at piles tip F_{p_j} are not present because they only exist in the scattered fields. The subtraction of eq. (4.4) from eq. (4.3) yields

$$\mathbf{H}^{s_i s_i}\mathbf{u}^{s_i} - \mathbf{G}^{s_i s_i}\mathbf{p}^{s_i} - \sum_{j=1}^{n_{ll}^m} \mathbf{G}^{s_i p_j}\mathbf{q}^{s_j} + \sum_{j=1}^{n_{ll}^m} \delta_j \boldsymbol{\Upsilon}^{s_i j} F_{p_j} = \mathbf{H}^{s_i s_i}\mathbf{u}_I^{s_i} - \mathbf{G}^{s_i s_i}\mathbf{p}_I^{s_i} \quad (4.5)$$

where the right hand vector is known because the analytic expressions of $\mathbf{u}_I^{s_i}$ and $\mathbf{p}_I^{s_i}$ can be easily obtained. The same procedure can be repeated to obtain the BE equations (3.4) and (3.6) for load-lines. On the contrary, the pile FE eq. (3.24) contains variables existing only in the scattered field, and consequently does not need to be rewritten.

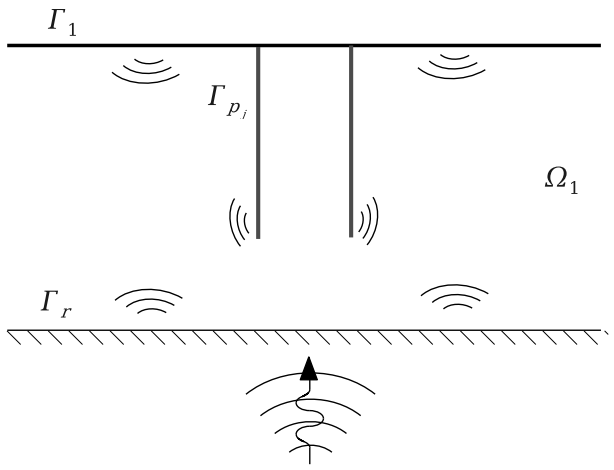

Figure 4.4: *Incident and scattered fields for piles embedded in a layered soil on a rigid bedrock.*

About the presence of a rigid bedrock

A slightly special case arises when the seismic excitation comes through an existent bedrock. In order to clarify this situation, let us consider now the presence of a rigid bedrock, as depicted in fig. 4.4, and let superindex ^{r} denote fields along such bedrock. Then, eq. (4.5) becomes

$$\begin{aligned}\mathbf{H}^{s_i s_i}\mathbf{u}^{s_i} - \mathbf{G}^{s_i s_i}\mathbf{p}^{s_i} - \ \mathbf{G}^{s_i r}\mathbf{p}^{r} - \sum_{j=1}^{n_{ll}^m} \mathbf{G}^{s_i p_j}\mathbf{q}^{s_j} + \sum_{j=1}^{n_{ll}^m} \delta_j \boldsymbol{\Upsilon}^{s_i j} F_{p_j} = \\ = \mathbf{H}^{s_i s_i}\mathbf{u}_I^{s_i} + \mathbf{H}^{s_i r}\mathbf{u}_I^{r} - \mathbf{H}^{\ s_i r}\mathbf{u}^{r} - \mathbf{G}^{s_i s_i}\mathbf{p}_I^{s_i} - \mathbf{G}^{s_i r}\mathbf{p}_I^{r} \quad (4.6)\end{aligned}$$

where $\mathbf{u}^r = \mathbf{u}_I^r$ so that the corresponding addends in the right-hand side, having opposite signs, could cancel one another. However, for simplicity reasons from the point of view of the computer code, it could be advisable to compute and add both addends. In any case, boundary conditions must be carefully applied in this situation.

4.4 Comparison results

4.4.1 Dynamic stiffnesses of pile foundations in a homogeneous half-space

Comparison with Kaynia [51]

In this first set, several results are computed and compared with those of Kaynia [51], obtained from a formulation where piles are modelled as linear elastic prismatic members and soil as semi-infinite viscoelastic media. To this end, the requisite Green functions are constructed using a discrete layer matrix approach.

In the following, results obtained by the proposed technique are noted by BEM-FEM in the figures. In all cases, piles are embedded in a homogeneous isotropic viscoelastic half-space. The system properties, taken from Kaynia [51], are: soil internal damping coefficient $\beta = 0.05$; soil-pile densities ratio $\rho_s/\rho_p = 0.7$; piles aspect ratio $L/d = 15$; and Poisson's ratios $\nu_s = 0.4$ (for the soil) and $\nu_p = 0.25$ (for the pile, though not taken into account in the proposed technique). Two different pile-soil modulus ratios are considered: $E_p/E_s = 10^3$ (soft soil) and $E_p/E_s = 10^2$ (stiff soil).

The vertical and horizontal impedance functions are normalized with respect to the respective single pile static stiffness (k^s) times the number (N) of piles in the group. The rocking impedances are normalized with respect to the sum of the products of the corresponding single pile static stiffness (k^s_{zz}) times the square of the distance to the rotation axis (x_i). All results are plotted versus the dimensionless frequency parameter defined by eq. (4.2). This notation will be used from now on wherever impedances are presented.

Horizontal and vertical impedances (stiffness and damping coefficients) of single piles embedded in a soft soil half-space are presented in fig. 4.5. Horizontal, vertical and rocking impedances of 2×2, 3×3 and 4×4 pile groups are shown from fig. 4.6 to 4.14, all for $s/d = 2, 5, 10$, and soft soil. Lateral, vertical and rocking impedances of 2×2, 3×3 and 4×4 pile groups embedded in stiff soils are shown from fig. 4.15 to 4.17.

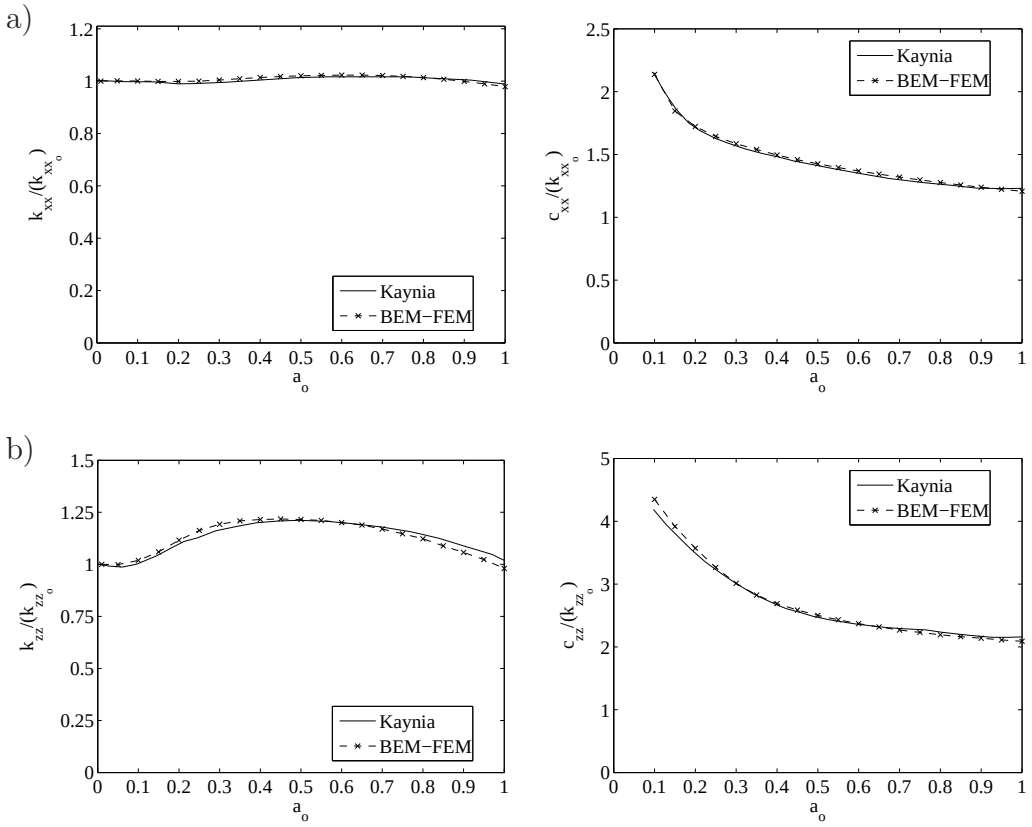

Figure 4.5: *Horizontal (a) and vertical (b) impedances of a single pile in soft soil. Comparison with Kaynia's solution.*

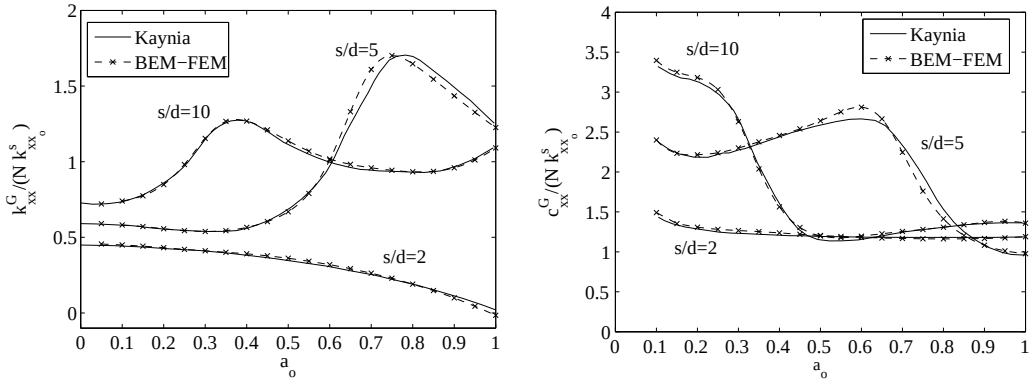

Figure 4.6: *Horizontal impedances of* 2×2 *pile groups in soft soil. Comparison with Kaynia's solution.*

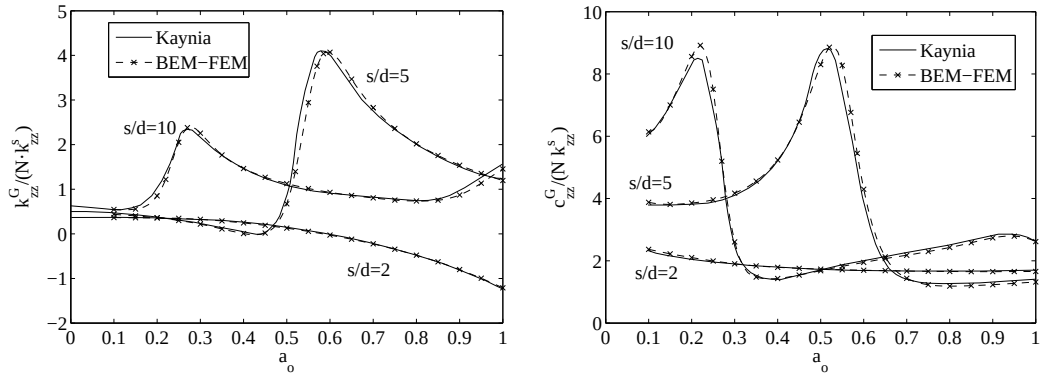

Figure 4.7: *Vertical impedances of* 2×2 *pile groups in soft soil. Comparison with Kaynia's solution.*

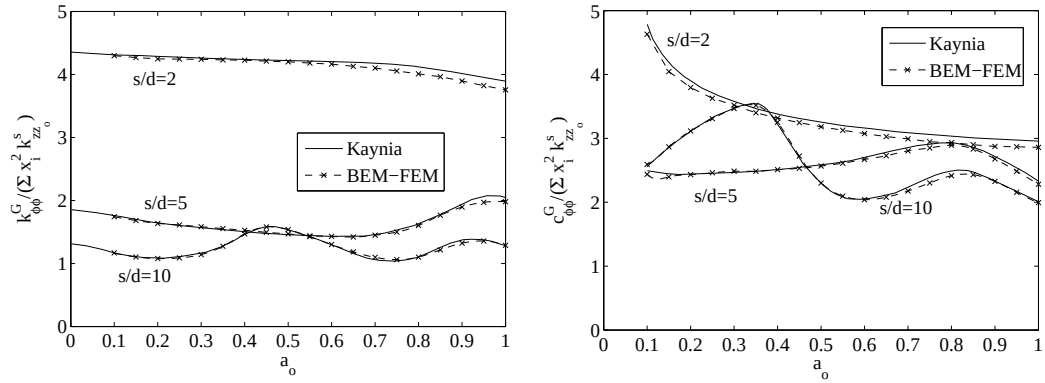

Figure 4.8: *Rocking impedances of* 2×2 *pile groups in soft soil. Comparison with Kaynia's solution.*

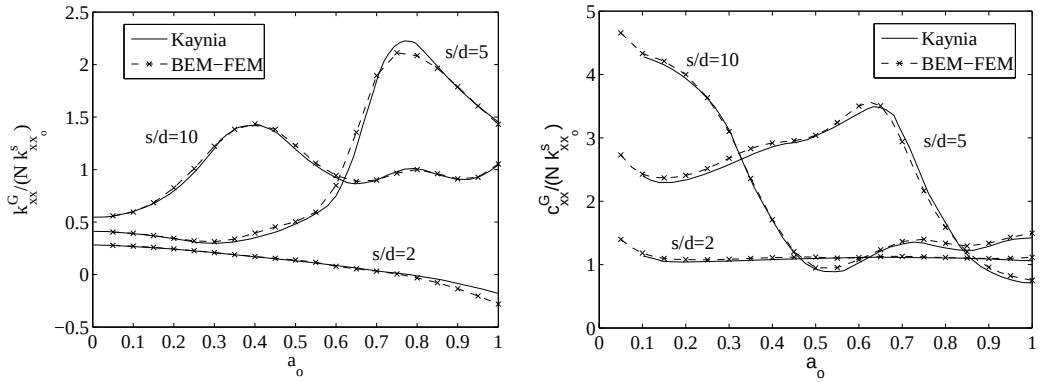

Figure 4.9: *Horizontal impedances of* 3×3 *pile groups in soft soil. Comparison with Kaynia's solution.*

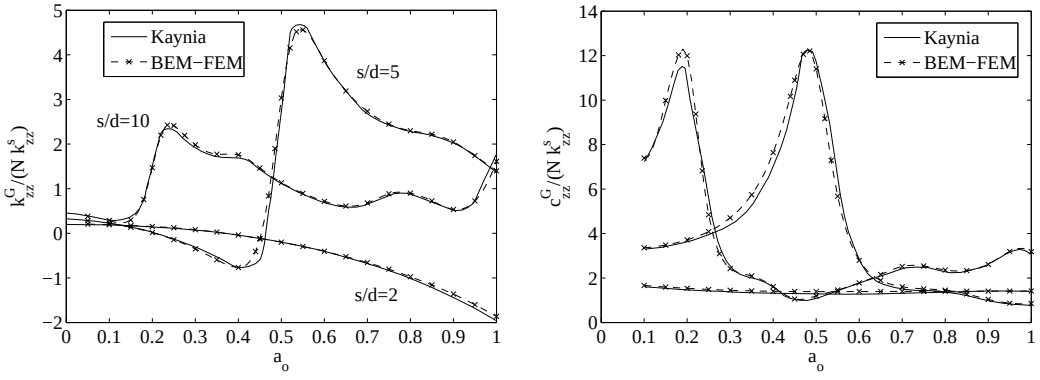

Figure 4.10: *Vertical impedances of* 3×3 *pile groups in soft soil. Comparison with Kaynia's solution.*

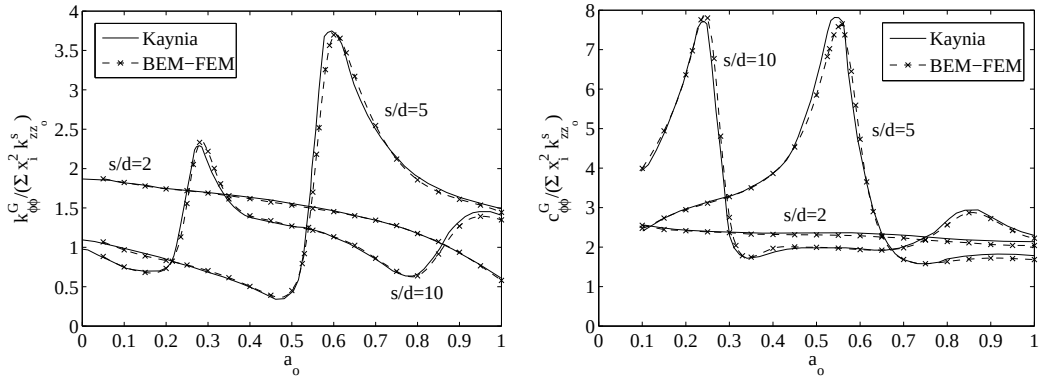

Figure 4.11: *Rocking impedances of* 3×3 *pile groups in soft soil. Comparison with Kaynia's solution.*

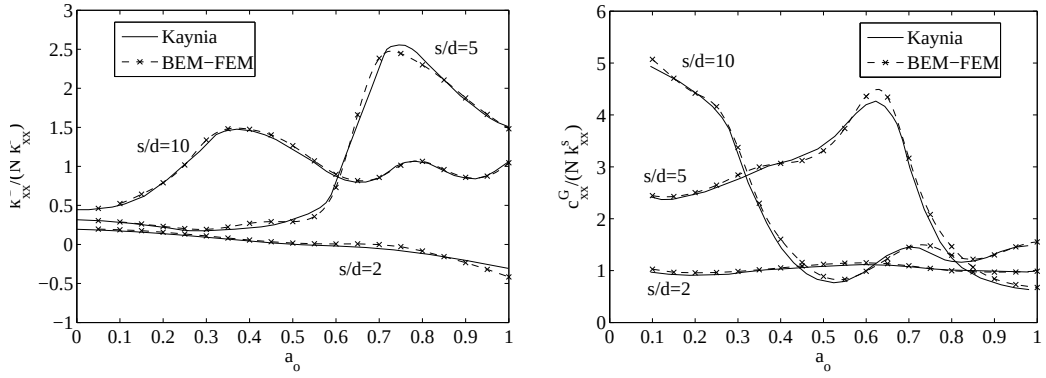

Figure 4.12: *Horizontal impedances of* 4×4 *pile groups in soft soil. Comparison with Kaynia's solution.*

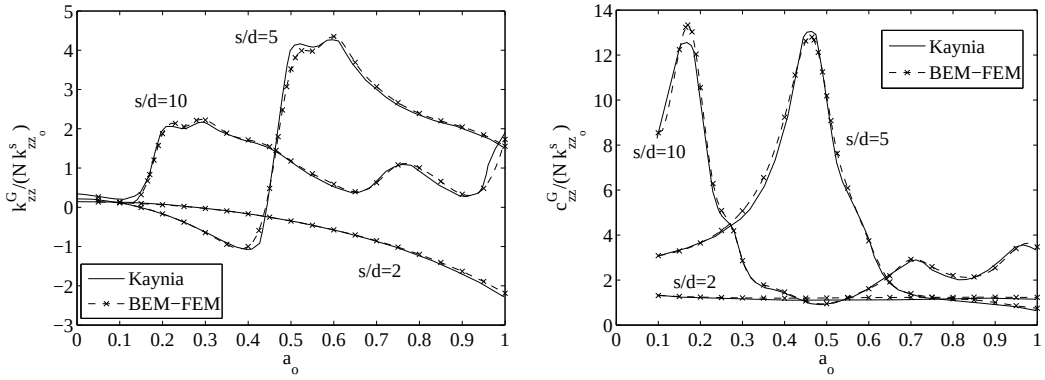

Figure 4.13: *Vertical impedances of* 4×4 *pile groups in soft soil. Comparison with Kaynia's solution.*

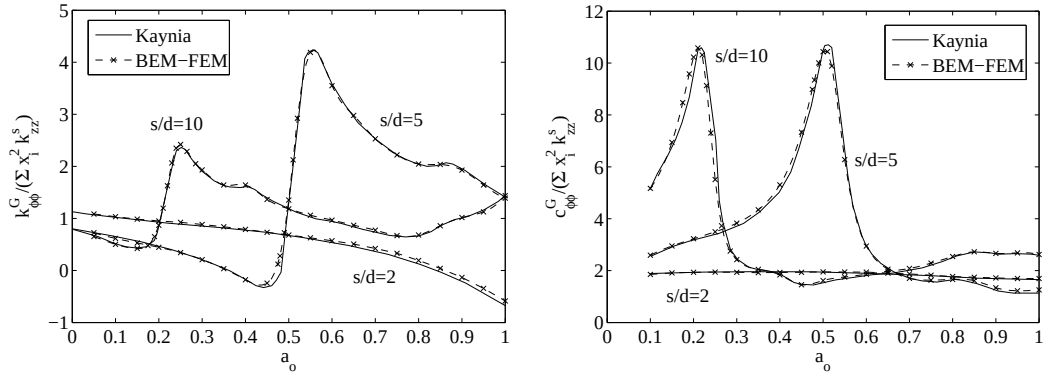

Figure 4.14: *Rocking impedances of* 4×4 *pile groups in soft soil. Comparison with Kaynia's solution.*

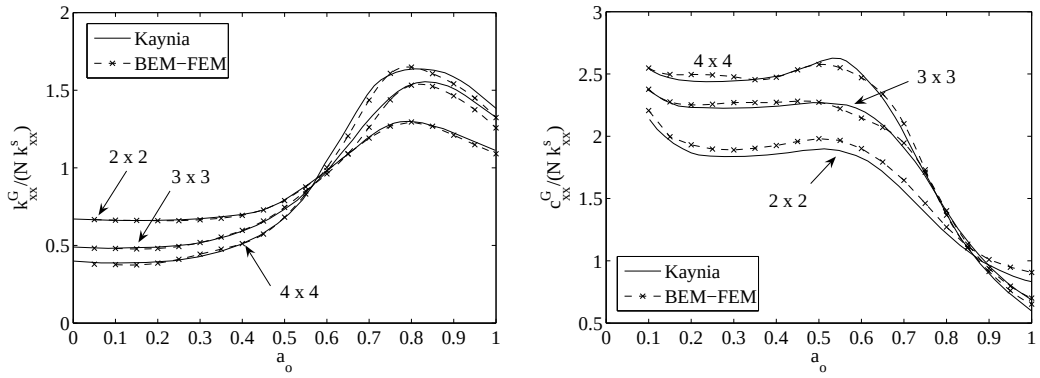

Figure 4.15: *Horizontal impedances of different pile groups embedded in a stiff soil with s/d=5. Comparison with Kaynia's solution.*

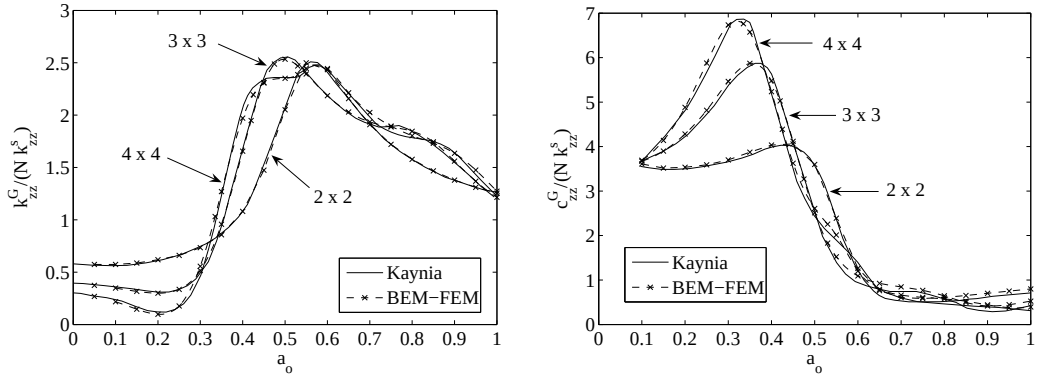

Figure 4.16: *Vertical impedances of different pile groups embedded in a stiff soil with s/d=5. Comparison with Kaynia's solution.*

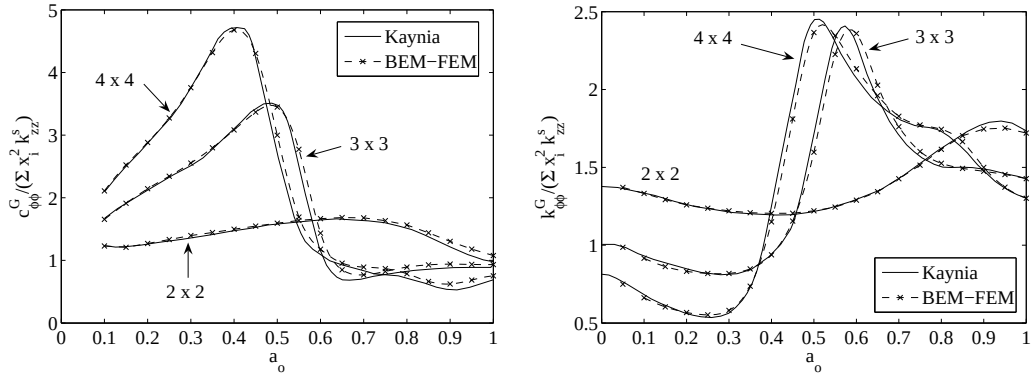

Figure 4.17: *Rocking impedances of different pile groups embedded in a stiff soil with s/d=5. Comparison with Kaynia's solution.*

Comparison with BEM-BEM model

In this set, some comparisons are made against results obtained by the multi-region boundary element code of Maeso, Aznárez and García [64], into which the present coupling formulation was implemented. Fig. 4.18 shows the meshes, for both BEM-BEM and BEM-FEM models, used to compute the results presented in this section. In this case, the BEM-BEM mesh is composed by 766 nodes and 162 elements, while the mesh used to solve the vertical mode with the BEM-FEM formulation has only 215 nodes and 46 elements.

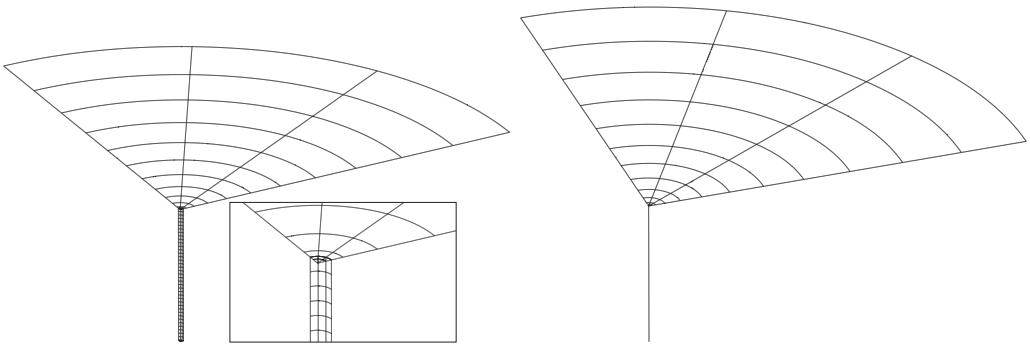

Figure 4.18: *Meshes. BEM-BEM model (left) and BEM-FEM model (right).*

In this subsection, the properties used are: soil internal damping coefficient $\beta = 0.05$; ratio between the material modulae $E_p/E_s = 10^2$; ratio between densities $\rho_s/\rho_p = 0.7$; piles aspect ratio $L/d = 20$; and Poisson's ratios $\nu_s = 0.4$ (for the soil) and $\nu_p = 0.25$ (for the piles).

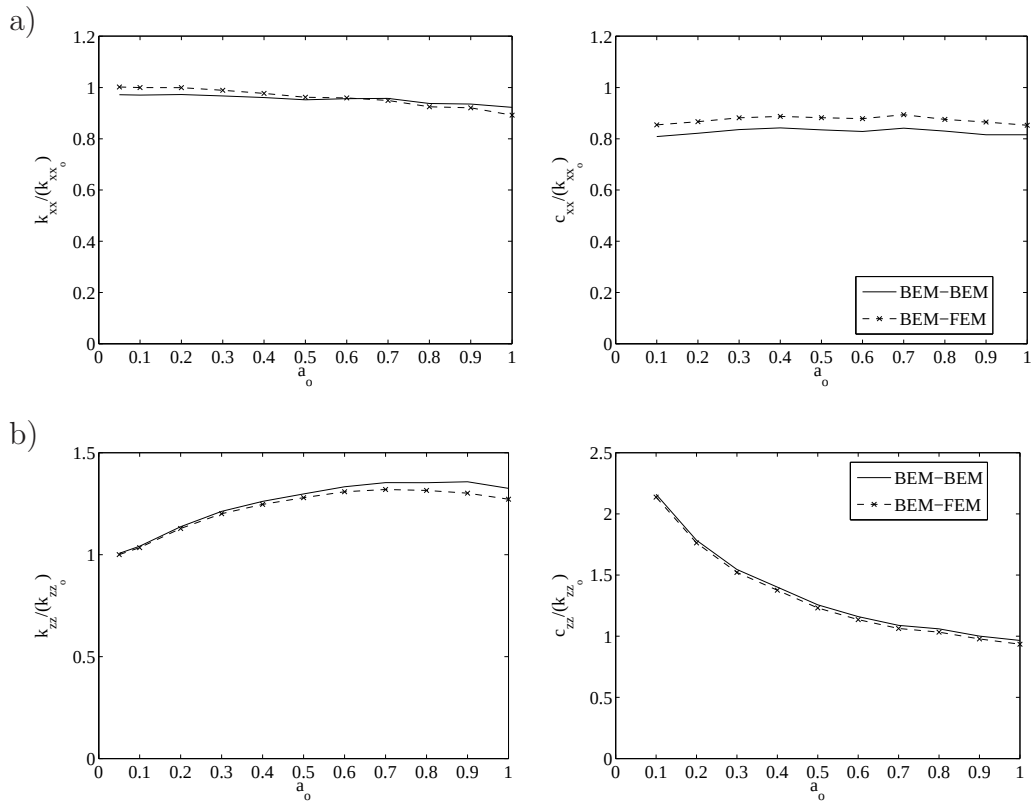

Figure 4.19: *Horizontal (a) and vertical (b) impedances of a single pile. Comparison with results obtained with the code of Maeso et al.*

Fig. 4.19 presents the comparison between horizontal and vertical impedances of a single pile. Both BEM-BEM and BEM-FEM results are normalized by the same value. It can be observed that both methods are in very good agreement, though a maximum difference exists in the horizontal damping coefficient, 7 per cent higher for the proposed coupling model.

Displacements and tractions along a single pile

So far, comparisons have been exclusively presented in terms of the foundation stiffness. For this reason, tractions and displacements will be studied now. The same set of results will be used to study the variation of the solution with the number of elements used to discretize the pile.

Deformed shapes and distributions of tractions along a single pile, for a certain frequency ($a_o = 0.05$ in this case), obtained by both methods, are compared in fig. 4.20. Cases of horizontal (a) and vertical (b) unitary displacements imposed

at the pile head are studied. Horizontal and vertical displacements are plotted on the left figures, normalized by the respective value of displacement imposed at the pile head. The distributions of the corresponding tractions are presented on the right in terms of the nodal value of tractions at the pile-soil interface (q_x or q_z) multiplied by the pile radius r and divided by the static stiffness of a single pile (k_{xx_o} or k_{zz_o}, respectively). The values of q_x and q_z for the BEM-BEM model were obtained by integration of the tractions around the section at depth z.

Deformed shapes are in very good agreement, though the tractions computed by the BEM-FEM coupling model show a more unstable behaviour. It would be worth investigating if this instability is related to the way in which the equilibrium has been posed. It is possible that a weaker formulation leads to a more accurate estimation of tractions. Despite this somewhat unstable behaviour of tractions, all related variables, such as internal forces, can be computed with high accuracy.

It can be seen that the proposed method is able to reach an accurate solution with a relatively low number of elements. The analysis of the foundation behaviour subjected to horizontal displacements demands a higher number of elements in comparison to the vertical excitation, due to the faster variation of both displacements and tractions for the horizontal mode. More specifically, in this case and at low or intermediate frequencies, vertical analysis of piles can be performed using 2-4 elements per pile. The accurate analysis of the pile behaviour subjected to horizontal loads, however, demands 20 elements if equally distributed, though similar results can be achieved with a smaller number of elements if the bottom half of the pile is discretized with larger elements.

Comparison with Miura et al. [58]

In this third set, several results for slender piles ($L/d = 20$) are compared with those of Miura et al. [58], where a 3D formulation based on Green's functions of cylindrical loads in layered semi-infinite media is employed. The properties used are: soil internal damping coefficient $\beta = 0.05$; ratio between the material modulae $E_p/E_s = 10^2$; ratio between densities $\rho_s/\rho_p = 0.7$; and Poisson's ratios $\nu_s = 0.4$ (for the soil) and $\nu_p = 0.25$ (for the piles). The ratio between pile separation and diameter is $s/d = 5$.

Horizontal and vertical stiffness and damping coefficients of 2×2 and 4×4 pile groups, embedded in a homogeneous isotropic viscoelastic half-space, are shown in figs. 4.21 and 4.22.

Miura et al. also analyse the load distribution among the piles in a 4×4 pile group. In fig. 4.23, the distribution of shear and axial forces due to horizontal and vertical excitations, respectively, are shown and compared with those given in [58]. Note that these results are presented in terms of the absolute value of the contribution of each pile to the corresponding dynamic stiffness of the foundation,

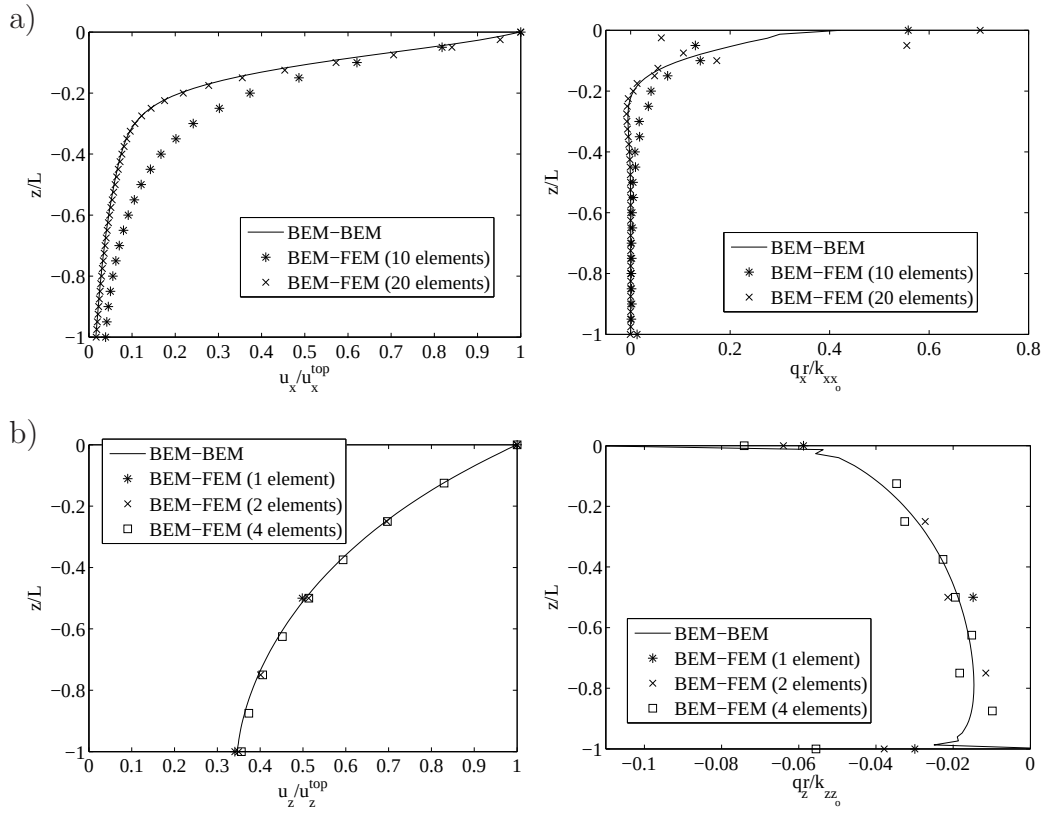

Figure 4.20: *Deformed shapes (left) and distributions of tractions (right) along a single pile for* $a_o = 0.05$ *and horizontal (a) and vertical (b) unitary displacement imposed at the pile head. Comparison with results obtained with the code of Maeso et al.*

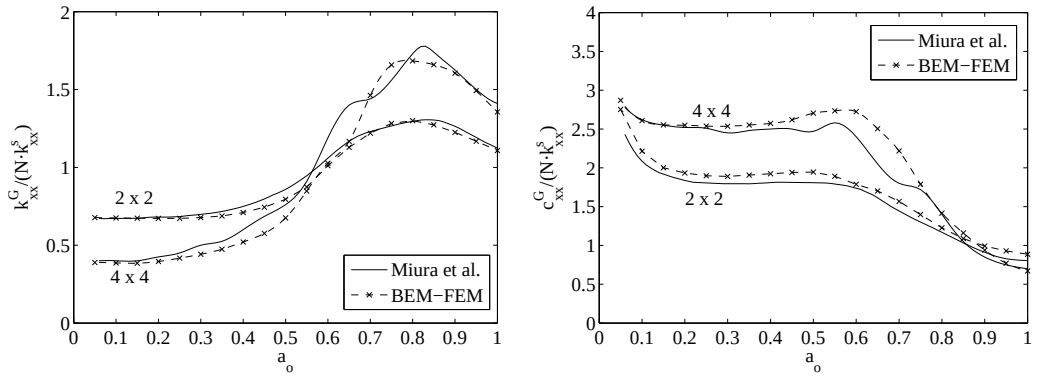

Figure 4.21: *Horizontal impedances of* 2×2 *and* 4×4 *pile groups. Comparison with solution from Miura et al.*

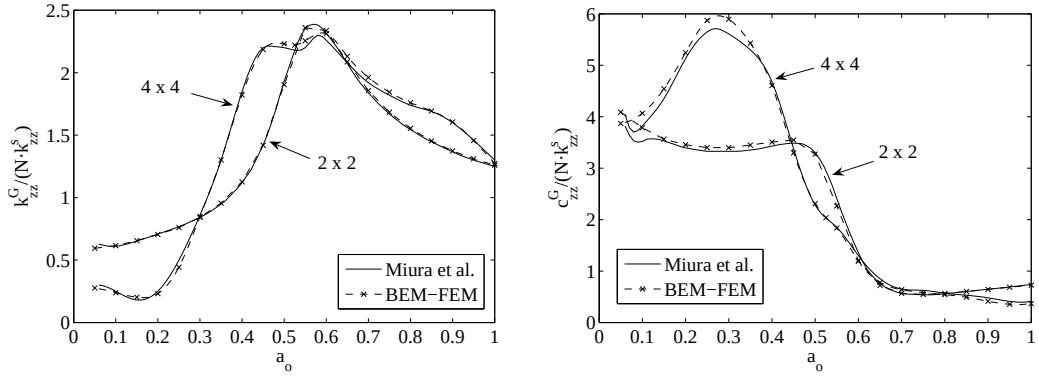

Figure 4.22: *Vertical impedances of* 2×2 *and* 4×4 *pile groups. Comparison with solution from Miura et al.*

for every value of frequency. Consequently, as only results for piles of the first quadrant are shown (for symmetry reasons), all values add up to 0.25 for each abscissa. It can be seen that there exists a very good agreement between the results.

(a) Shear forces due to horizontal excitation (b) Axial forces due to vertical excitation

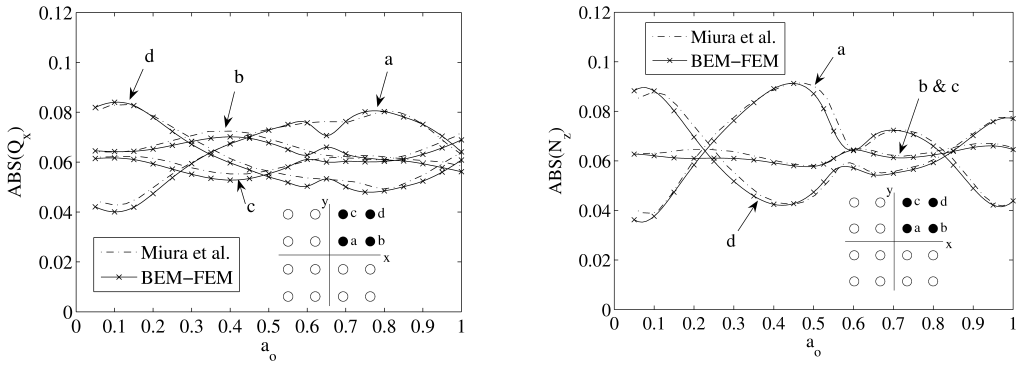

Figure 4.23: *Forces on pile caps of a* 4×4 *pile group*

Comparison with Kaynia and Mahzooni [75]

In order to study the case of a larger pile foundation, fig. 4.24 compares horizontal and rocking impedances computed for 5×5 pile groups with those presented by Kaynia and Mahzooni [75], obtained using the formulation proposed before by Kaynia and Kausel [57]. The mesh used to obtain the results with the proposed BEM-FEM formulation is sketched in fig. 4.25. The configuration is very similar to those of previous cases: isotropic, viscoelastic half-space with $\nu_s = 0.4$ and $\beta = 0.05$, being the contrast between pile and soil densities $\rho_p/\rho_s = 1.4$; slenderness ratio $L/d = 20$; pile spacing $s/d = 3$ and 6; and pile-soil modulus ratios $E_p/E_s = 10^3$ and 10^2. Kaynia and Mahzooni presented results only until $a_o = 0.5$. Up to this frequency, the agreement is very good. Fig. 4.24 presents, however, the impedance functions obtained by the proposed method until $a_o = 1$.

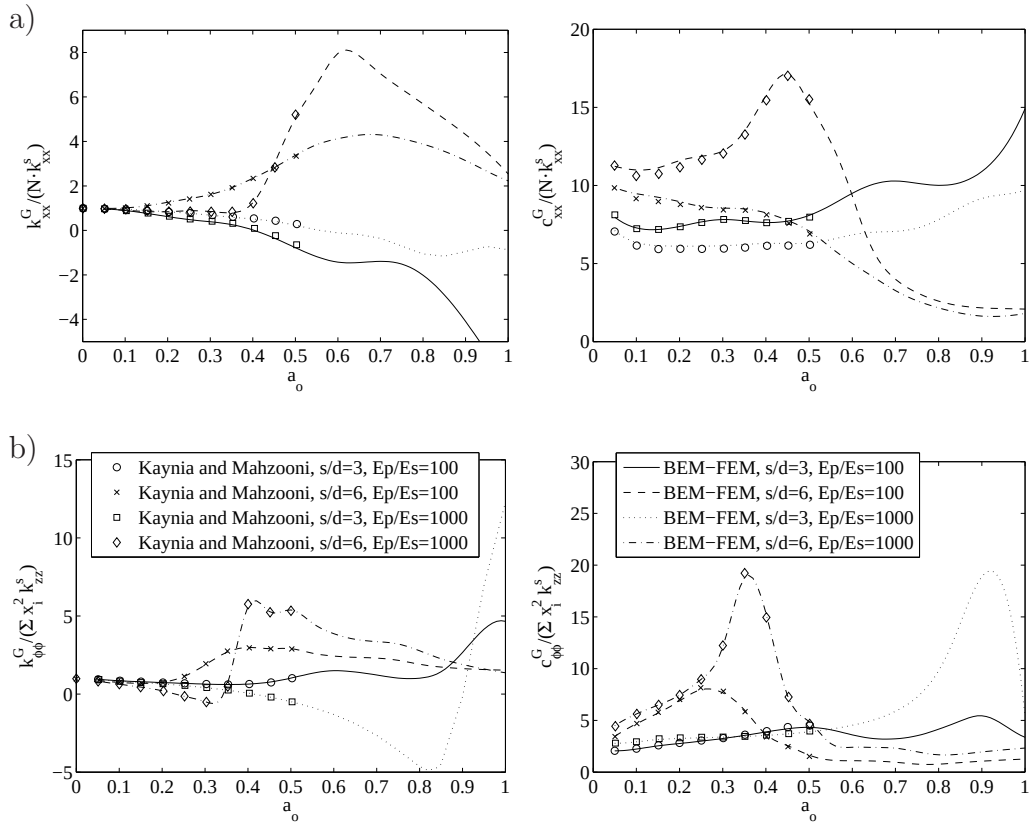

Figure 4.24: *Horizontal (a) and rocking (b) impedances of* 5×5 *pile groups in soft soil. Comparison with Kaynia and Mahzooni*

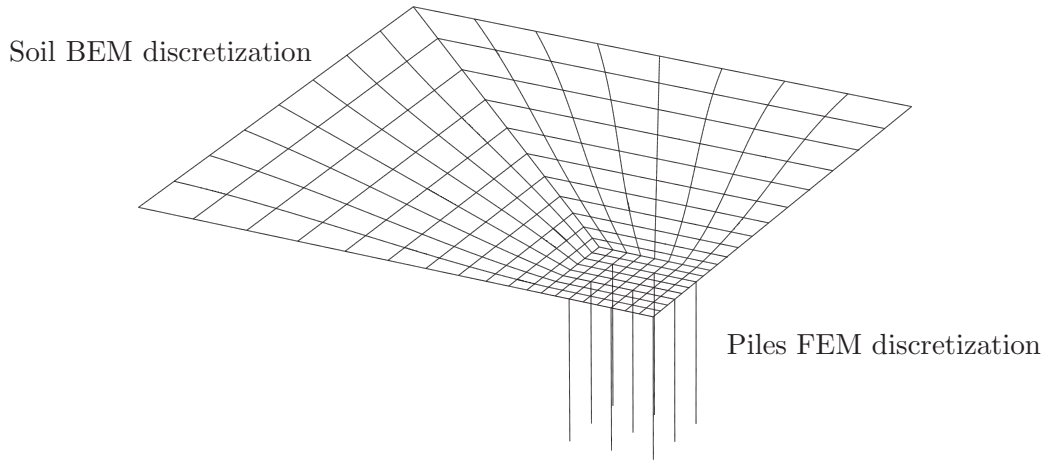

Figure 4.25: *Sketch of mesh used to analyse a 5×5 pile group*

4.4.2 Dynamic stiffnesses of pile foundations in a homogeneous stratum

In this set of comparison results, the capacity of the model to account for the presence of a rigid bedrock is tested. The problem geometry is depicted in fig. 4.26, where H is the depth of the stratum. Two cases are considered: floating piles in a soil deposit ($H > L$) and hinged piles ($H = L$).

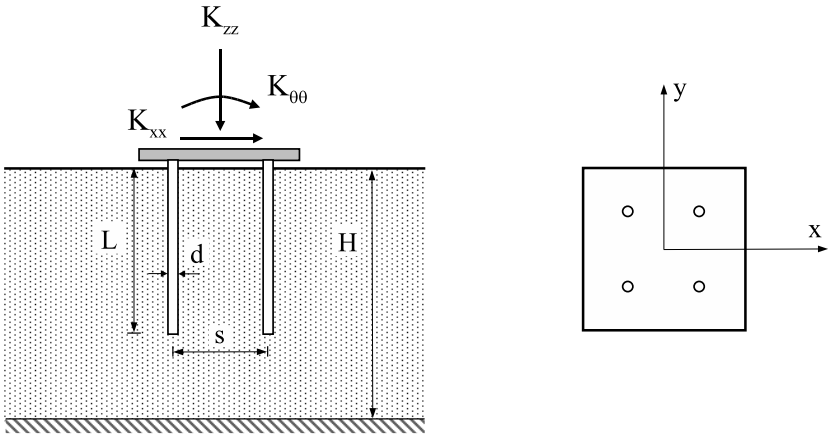

Figure 4.26: 2×2 *pile group embedded in a stratum resting on a rigid bedrock. Problem geometry definition.*

Floating piles in a stratum on a rigid bedrock

A comparison between results obtained through the present model and those reported by Nogami [143] and Kaynia [51], for the vertical stiffness and damping functions of a 2×2 pile group embedded in a homogeneous stratum resting on a rigid bedrock, are shown in fig. 4.27. The stratum thickness is $H = 75d$, the piles aspect ratio is $L/d = 37.5$, the ratio between separation and diameter of piles is $s/d = 5$, and the dimensionless properties of stratum and piles (denoted by subindexes s and p respectively) are characterized by: ratio between densities $\rho_s/\rho_p = 0.7$; Poisson's ratio and internal damping coefficient for the soil $\nu_s = 0.4$ and $\beta = 0.05$, respectively; and $\pi\mu L^2/E_p A = 1$, being E_p the Young's modulus of the pile, A the pile cross section area and μ the soil shear modulus. The impedance vertical functions (k^G_{zz} and c^G_{zz}) of the group are normalized with respect to the single pile static stiffness ($k^s_{zz_o}$) times the number (N) of piles in the group, and are plotted versus the dimensionless frequency a_o defined by eq. (4.2).

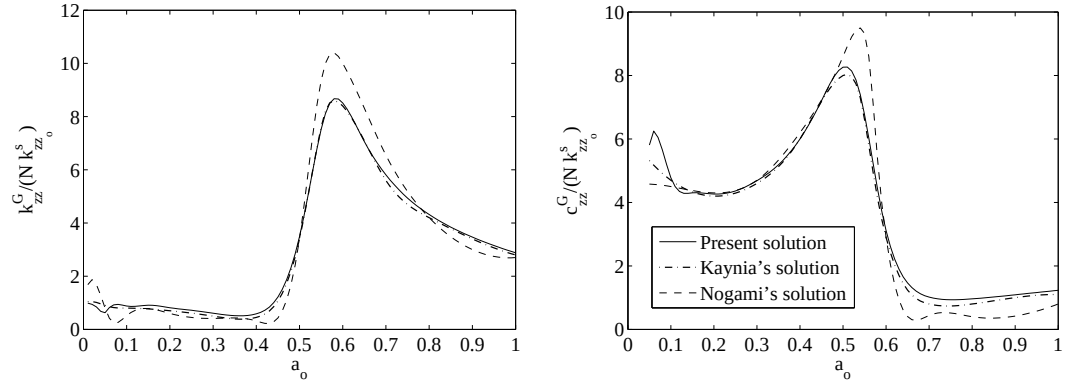

Figure 4.27: *Vertical impedances of a floating* 2×2 *pile group embedded in a homogeneous stratum resting on a rigid bedrock. Comparison with Nogami's and Kaynia's solutions.*

As can be seen from the figures, the agreement with both results is good, particularly with Kaynia's. Note that the fundamental natural frequency of the stratum in the dilatational mode, at about $a_o = 0.05$, is highlighted by Nogami's and present solutions.

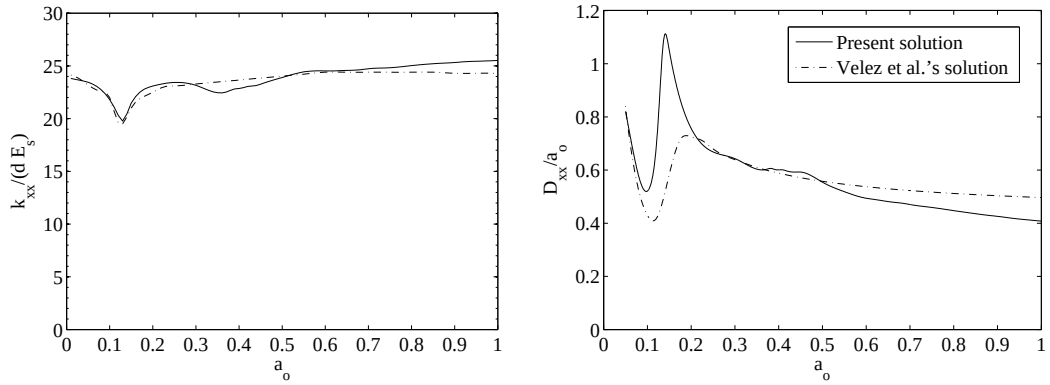

Figure 4.28: *Horizontal impedances of a hinged pile. Comparison with results of Velez et al.*

Hinged piles embedded in a soil deposit

A comparison between results obtained using the present model and those reported by Velez et al. [48], for the horizontal stiffness and damping functions of a hinged pile embedded in a homogeneous stratum resting on a rigid bedrock, are shown in fig. 4.28. In this problem, the pile aspect ratio is $L/d = 25$, the ratio between

Young's moduli is $E_p/E_s = 8233.3$, the ratio between densities is $\rho_p/\rho_s = 1.6$, the Poisson ratio for the soil is $\nu_s = 0.4$ and the internal damping coefficient for the soil is $\beta = 0.05$. Here, the damping coefficient is presented in terms of the ratio D_{xx}/a_o, being $D_{xx} = \omega c_{xx}/2k_{xx}$, and the stiffness coefficient is normalized with respect to the diameter of the pile and the pile Young's modulus. The results are in very good agreement, though there are small differences in the damping coefficients. Note that in the model used by Velez et al., the hysteretic damping ratio of the soil is not constant. On the contrary, it is taken as a decreasing function of depth which varies from a maximum value of 8% at the ground surface to a minimum of 2% at the bedrock. This is the reason why the Velez et al. model is more damped at high frequencies. Note also that the present model highlights the second natural frequency of the stratum related to the shear mode.

4.4.3 Dynamic response of pile foundations under seismic excitation

Comparison with BEM-BEM model

In this set, kinematic responses of a floating single pile embedded in a half-space, obtained with the proposed BEM-FEM methodology, are presented and compared to results obtained by the multi-region boundary element code of Maeso, Aznárez and García [64]. In these numerical examples, the soil internal damping coefficient is $\beta = 0.05$, the ratio between the material modulae is $E_p/E_s = 10^3$, the ratio between densities is $\rho_s/\rho_p = 0.7$, the piles aspect ratio is $L/d = 20$, and the Poisson's ratios are $\nu_s = 0.4$ (for the soil) and $\nu_p = 0.25$ (for the piles).

Fig. 4.29 presents the comparison for the real and the imaginary parts of the kinematic responses of a single pile subjected to vertically incident SH and P waves. Results are presented in terms of horizontal or vertical displacements at the pile head u_{cap} with respect to the corresponding free field motion u_{ff}. A very good agreement can be observed.

Comparison with Gazetas et al. [71]

A Beam-on-Dynamic-Winkler-Foundation (BDWF) model was used by Gazetas and co-workers [71] to determine the seismic response of piles. One interesting result appearing in this article is presented herein in comparison to the proposed BEM-FEM model.

In this case, a fixed-head single pile is considered to be embedded in a soil deposit with a thin soft top layer of depth $h_l = 5d$, being the ratio between shear soil velocities $c_s/c_s^l = 3$. The profile is depicted in fig. 4.30, where it is shown that the tip of the pile is hinged to a rigid bedrock. In this problem, the pile aspect

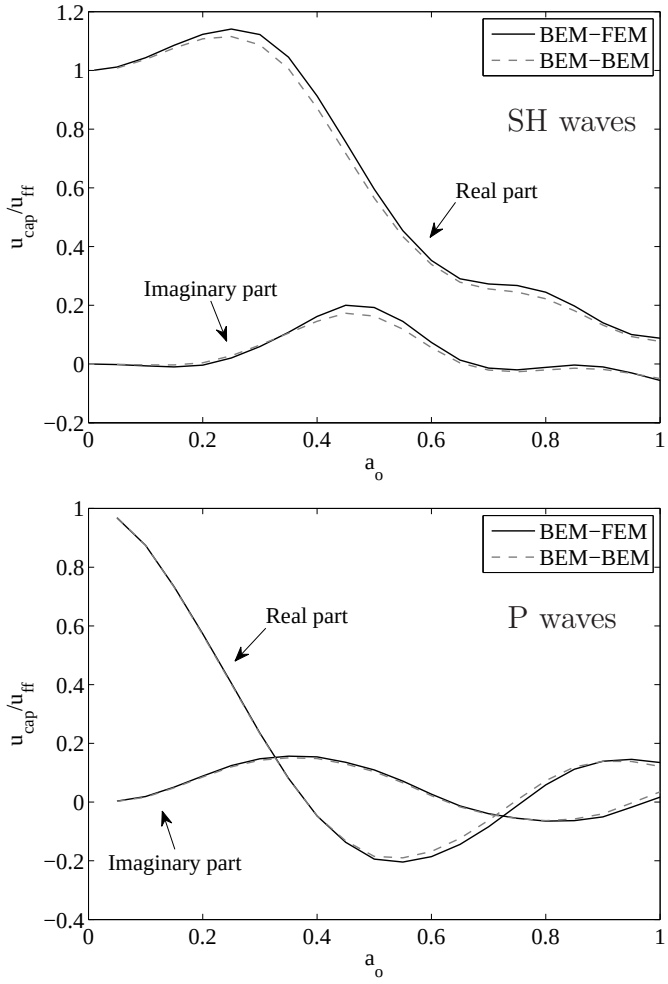

Figure 4.29: *Transfer functions for a single pile subjected to vertically incident SH and P waves. Comparison with Maeso et al.*

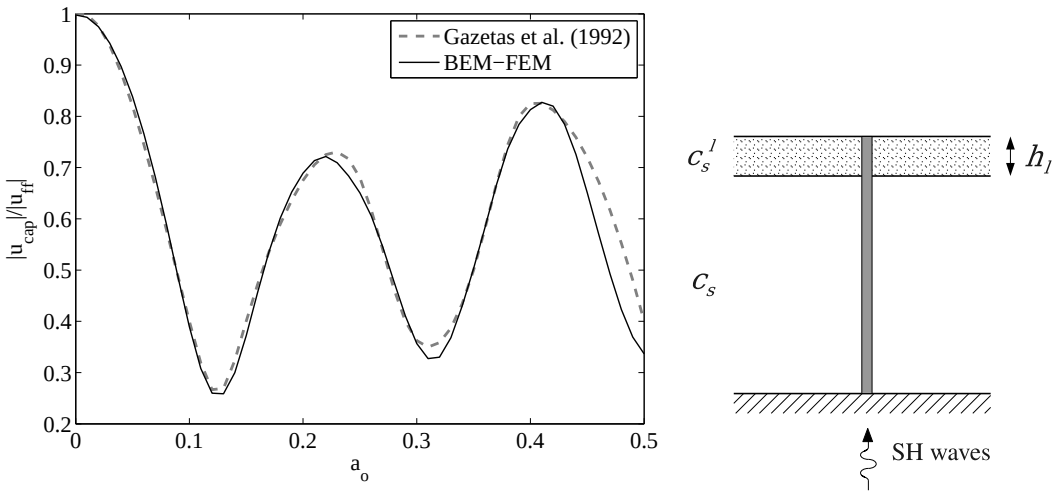

Figure 4.30: *Transfer functions for a single pile in a soil deposit containing a thin soft top layer, subjected to vertically incident SH waves. Comparison with Gazetas et al.*

ratio is $L/d = 20$, the ratio between Young's modulus is $E_p/E_s = 10^3$, the ratio between densities is $\rho_p/\rho_s = 1.4$, the Poisson ratio for the soil is $\nu_s = 0.4$ and the internal damping coefficient for the soil is $\beta = 0.05$.

Fig. 4.30 shows the kinematic displacement functions obtained by both methods, being the agreement very good. As the dimensionless frequency is referred to deposit shear wave velocity c_s, while the response is measured at the surface, on the soft top layer, the response fluctuates highly, as both methods reflect.

Comparison with Kaynia and Novak [70]

In this last set of results, some examples of floating single piles and 3×3 pile groups under Raleigh waves and vertically incident SH waves are presented. Results obtained by Kaynia and Novak [70], making use of the three-dimensional model presented by Kaynia and Kausel [57], will be used for comparison. The system properties are: Young's modulus ratios $E_p/E_s = 10^2$ and 10^3, pile-soil densities ratio $\rho_p/\rho_s = 1.5$, soil Poisson's ratio $\nu_s = 1/3$, soil damping ratio $\beta = 0.05$ and pile slenderness ratio $L/d = 20$. Pile foundations are assumed to be embedded in a homogeneous half-space, and, in the case of 3×3 pile groups, the separation between adjacent piles is defined as $s/d = 5$. In this case, Rayleigh waves are assumed to impinge perpendicularly to one side of the square foundation.

Fig. 4.31 presents the transfer functions, in terms of horizontal displacements at the pile cap, for a 3×3 pile group subjected to SH waves, for Young's modulus

ratios $E_p/E_s = 10^2$ and 10^3. On the other hand, fig. 4.32 shows the transfer functions, in terms of horizontal displacements and rocking measured at the pile cap, of a single pile and a 3×3 pile group under Rayleigh waves, for $E_p/E_s = 10^2$. In both cases, it can be seen that the agreement is very good.

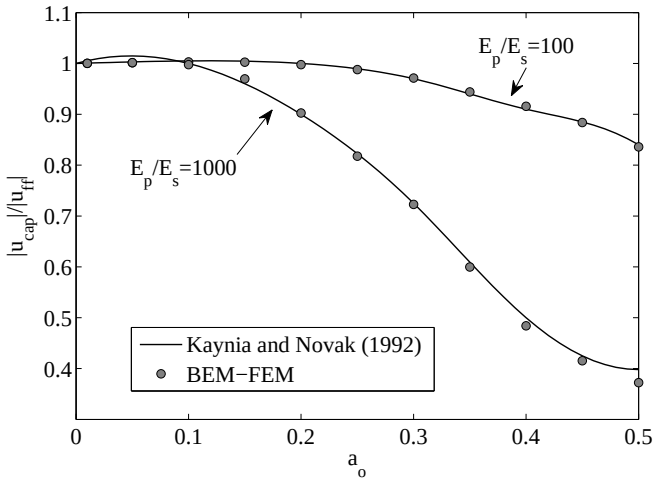

Figure 4.31: *Transfer functions for a 3×3 pile group in a half-space, subjected to vertically incident SH waves. Comparison with results of Kaynia and Novak.*

4.4.4 Conclusions

It has been shown that the results obtained by the proposed technique are in very good agreement with results obtained by several authors, making use of different tools. (Note that most results by other authors have been taken directly from the corresponding publications, and may consequently contain small errors). Comparisons have been shown for several kinds of problems and for different configurations. Therefore, the validity of the proposed technique, under the assumptions explained in previous chapters, has been proved.

Note the numerous advantages of the proposed technique in contrast to the other models that have been used for comparison. With respect to BEM-BEM techniques, the following advantages can be listed:

- As the pile boundaries do not need to be discretized by boundary elements, a small number of degrees of freedom is needed for each pile. Consequently, lower computing times and memory requirements are needed to analyse a problem.

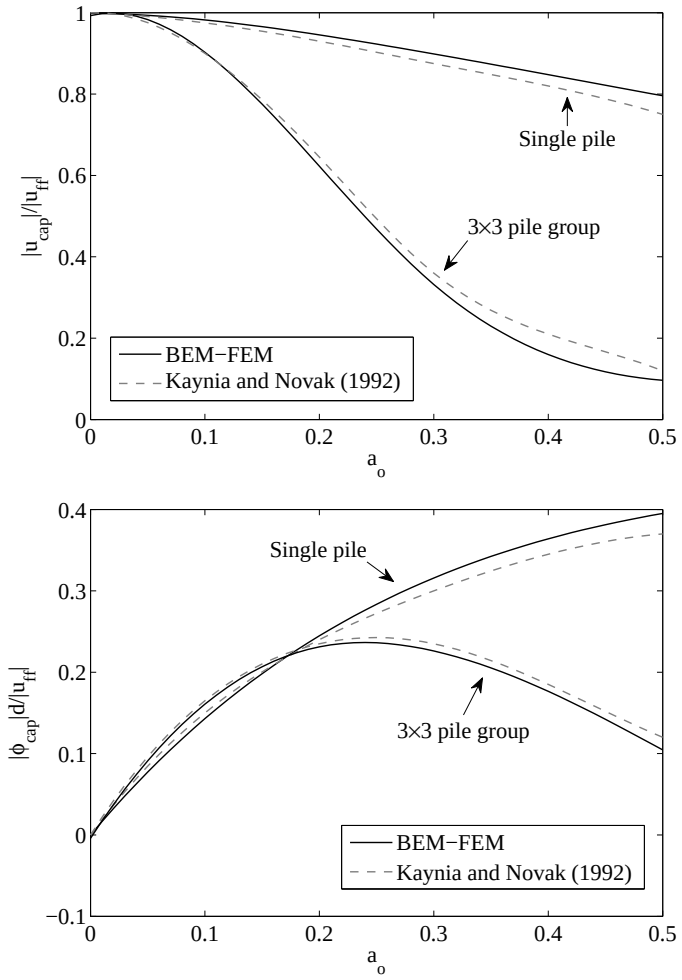

Figure 4.32: *Transfer functions for a single pile and a* 3×3 *pile group in a half-space, subjected to Raleigh waves. Comparison with results of Kaynia and Novak.*

- For the same reason, mesh preparation times are drastically reduced. In fact, as BEM and FEM meshes are independent, once the soil mesh is defined, the pile foundation configuration can be changed very easily without modifying the boundary element mesh.

- Different boundary conditions on pile foundations are more easily defined and imposed. In addition, it is easier to establish, for example, rigid cap boundary conditions so that different piles are made to work together in a group.

- Enhancing the code, in order to be able to link the piles to other structures, is easier.

With respect to other techniques:

- It takes implicitly into account the dynamic interaction between piles, or between piles and any other body or characteristic of the model.

- It can be relatively easy implemented in previously existent boundary element codes.

- It allows the analysis of problems including soil strata, rigid rocky beds and any topography for the soil surface.

4.5 Analysis of the distribution of shear forces along piles in a group

An analysis of the distribution of shear forces along some of the piles in the 5×5 pile group, studied in section 4.4.1, is going to be performed herein. The results are presented for a unitary horizontal displacement imposed at the pile cap. Only results corresponding to the more representative piles are plotted, as specified in the corresponding sketches. Figs. 4.33 and 4.34 show results for $s/d = 3$, while figs. 4.35 and 4.36 present results for $s/d = 6$. In both sets, the first figure corresponds to $E_p/E_s = 10^3$ and the second one to $E_p/E_s = 10^2$. Curves are plotted in terms of dimensionless depth z/L (being $z/L = 0$ the free surface) against the shear force (real part on the left and absolute value on the right) normalized with respect to the static horizontal stiffness of the corresponding single pile (k_{xx_o}). Results for frequencies $a_o = 0.1, 0.4$ and 0.8 are presented on the first, second and third rows, respectively.

The conclusions that can be drawn from these results, some of them already widely known, are:

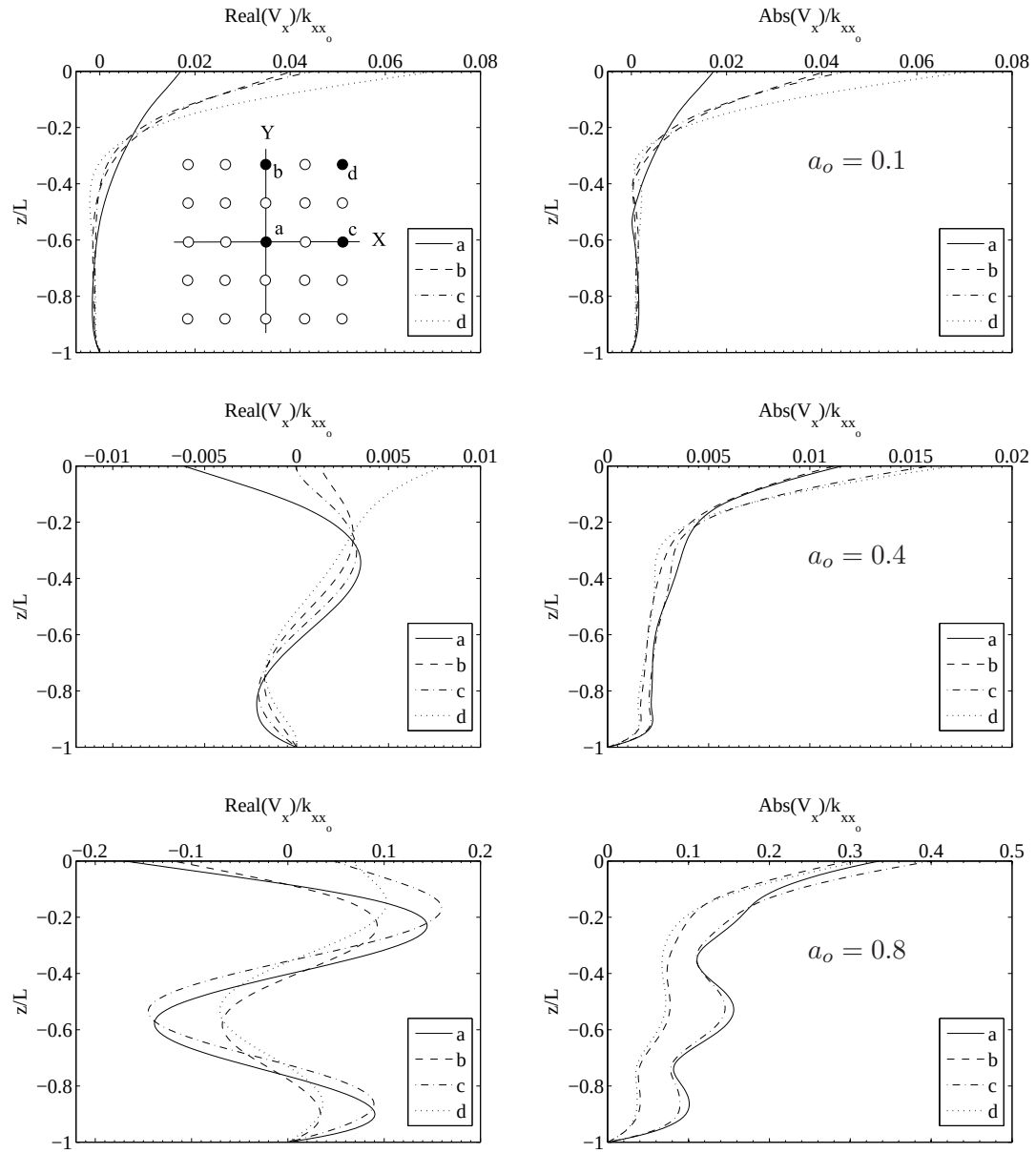

Figure 4.33: *Distribution of shear forces in piles of a 5×5 pile group.* $s/d = 3$. $E_p/E_s = 10^3$.

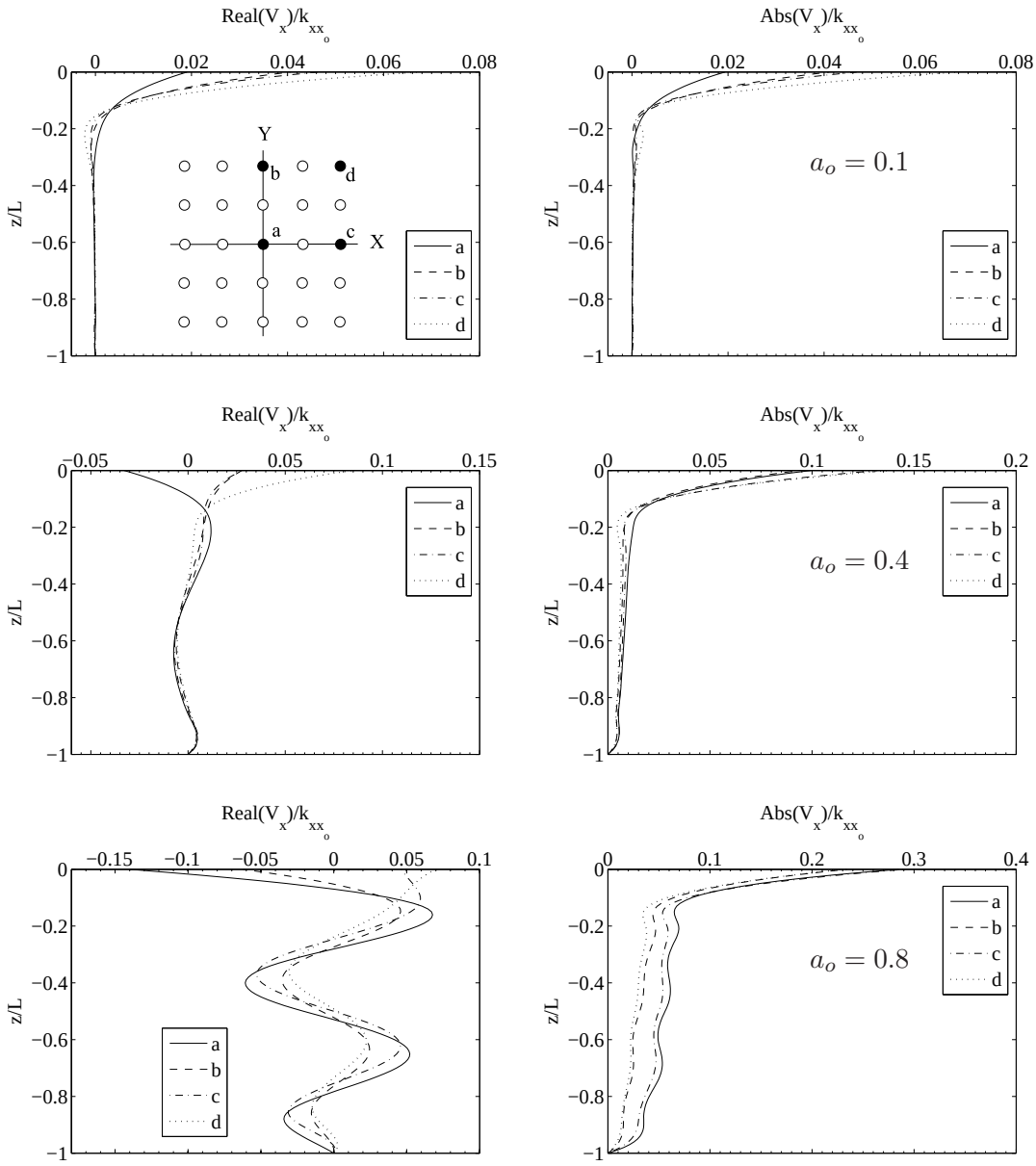

Figure 4.34: *Distribution of shear forces in piles of a 5×5 pile group.* $s/d = 3$. $E_p/E_s = 10^2$.

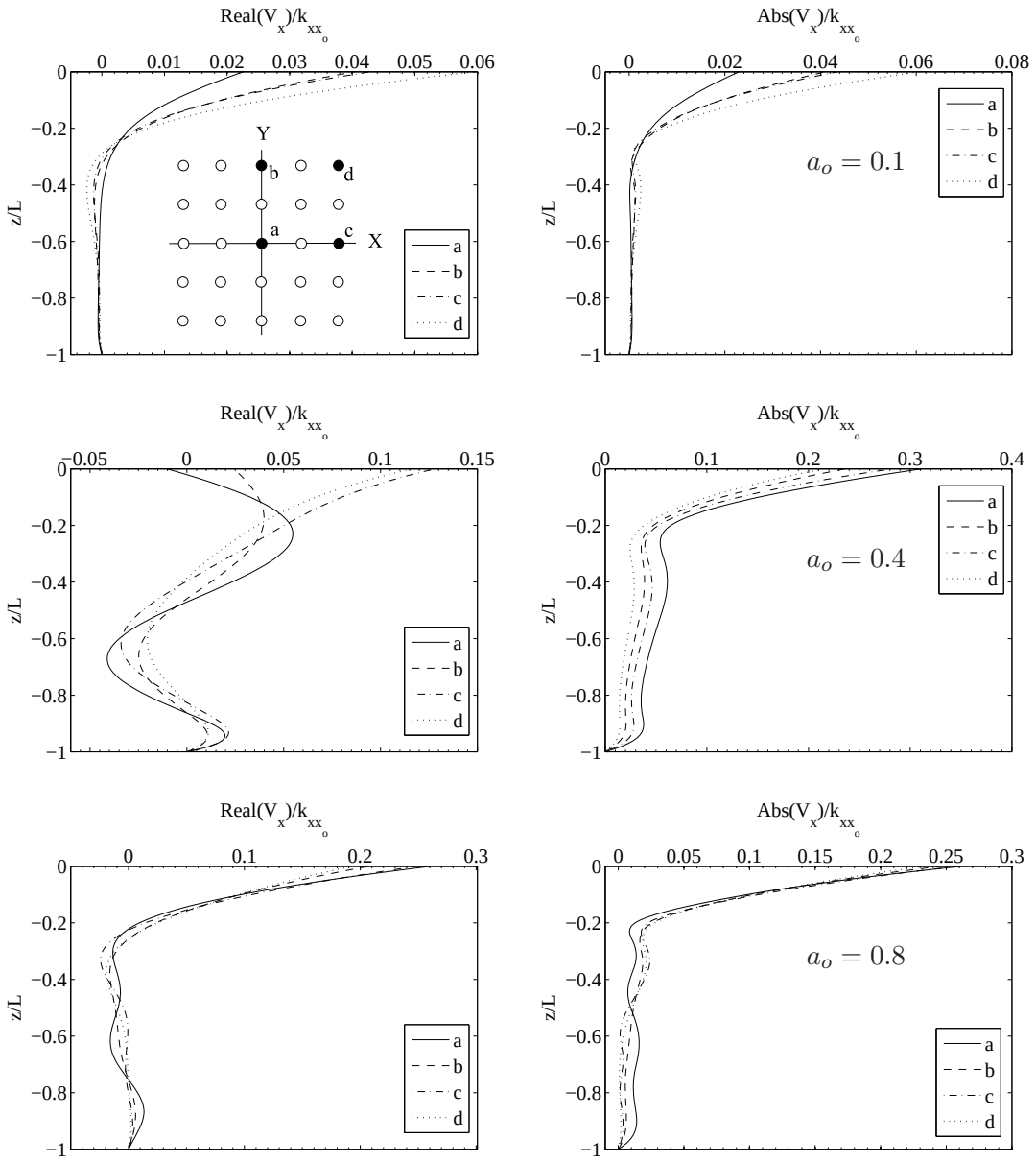

Figure 4.35: *Distribution of shear forces in piles of a 5×5 pile group.* $s/d = 6$. $E_p/E_s = 10^3$.

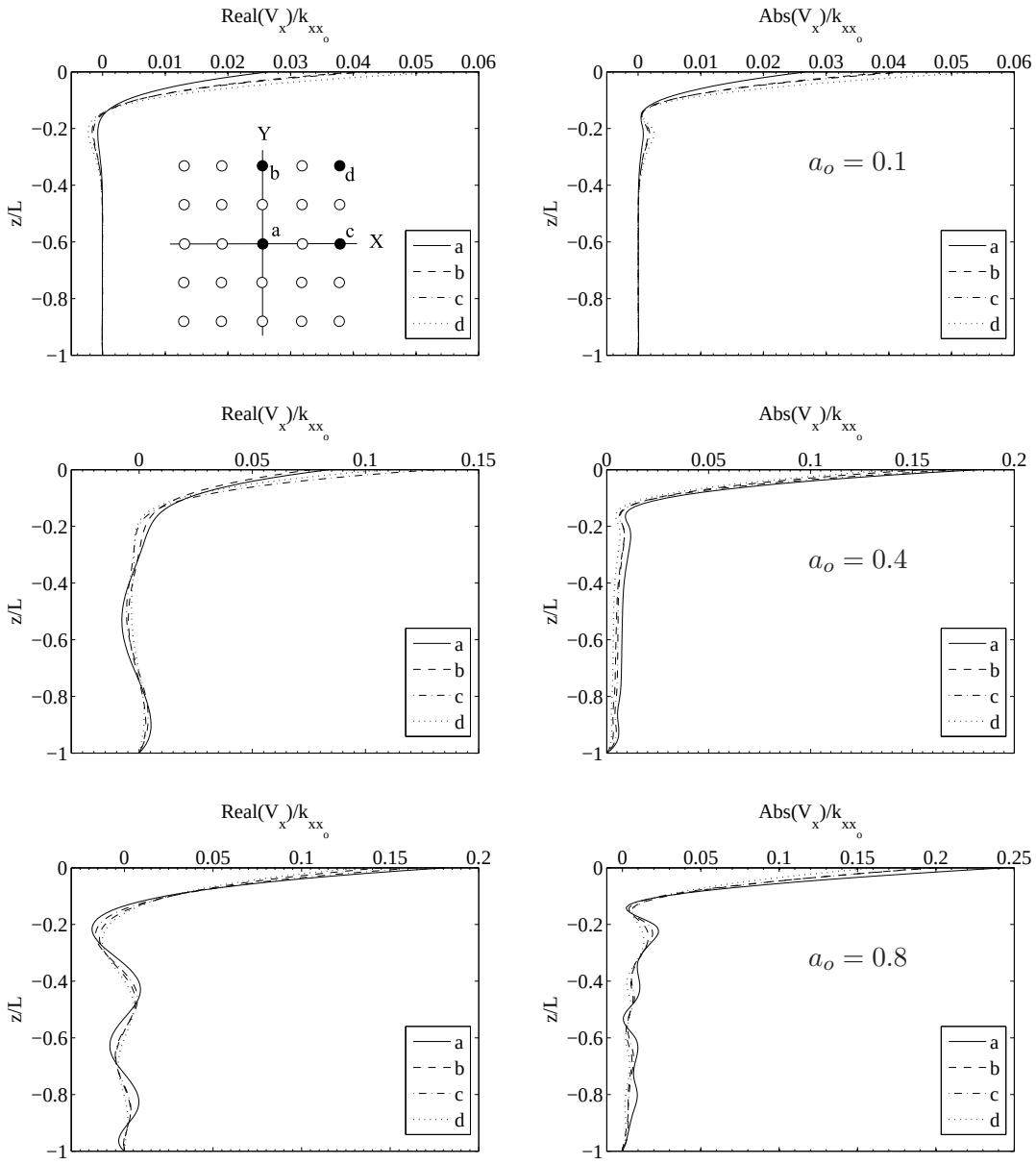

Figure 4.36: *Distribution of shear forces in piles of a 5×5 pile group.* $s/d = 6$. $E_p/E_s = 10^2$.

- In the quasi-static state,
  - the distribution of shear forces is approximately exponential with depth, being the lateral loads withstood mainly by the upper part of the piles.
  - the *active length* of the piles is shorter for $E_p/E_s = 10^2$ (stiffest soil)
  - the central pile a and corner pile d are the ones withstanding, respectively, the lowest and the highest fraction of load.
- For intermediate and high frequencies,
  - the distribution of shear forces at a certain time t fluctuates around zero and, the higher the frequency, the shorter the wave length.
  - the magnitude of the shear forces is maximum at pile heads, but it can also reach relatively high values in the bottom half of the pile.
  - significant shear forces may appear along the whole length of the pile, and not only along its *active length*.
  - the fraction of load withstood by each pile in the group, as well as the position of the pile resisting the highest fraction, depends on the frequency.

4.6 Dynamic stiffness of pile foundations in homogeneous strata

Due to the fact that piles are commonly used when avoiding shallow soil of low bearing capacity and transferring load to deeper soil or rock of higher bearing capacity is needed, a particular case of interest in the dynamic analysis of pile foundations is that of piles and pile groups in a soil deposit on a bedrock, for both floating and hinged piles. For this reason, the aim of this section is to investigate the influence of the presence of a rigid bedrock on the impedance functions of pile foundations. Fig. 4.37 illustrates the approached problem for a usual configuration, where L and d are used to denote the length and diameter of the piles, s refers to the distance between adjacent piles and H denotes the depth of the stratum.

Below, vertical, horizontal and rocking impedances of different pile foundation configurations are presented. In the case of single piles, the stiffness and damping functions are normalized by the respective static stiffness. As for the pile groups, the vertical and horizontal impedance functions are normalized by the corresponding single pile static stiffness (k_{zz_o} and k_{xx_o}) times the number (N) of piles in the group. The rocking impedances are normalized with respect to the sum of the

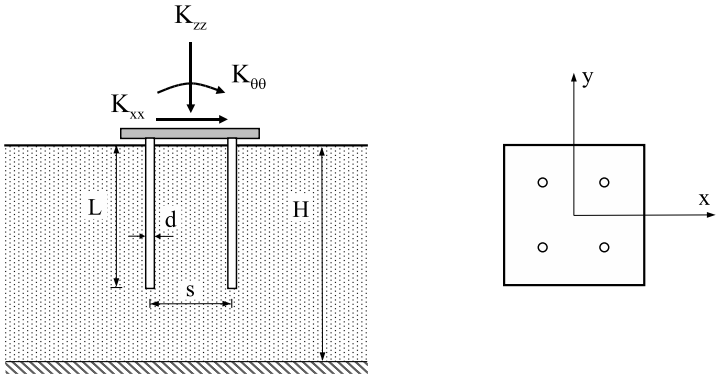

Figure 4.37: 2×2 *pile group embedded in a stratum resting on a rigid bedrock. Problem geometry definition.*

products of the vertical static stiffness of the respective single pile (k_{zz_o}) times the square of the distance to the rotation axis (x_i). All results are plotted versus the dimensionless frequency defined by eq. (4.2). Several ratios H/L and two ratios E_p/E_s have been considered.

In the first place, vertical impedances of a single pile embedded in a homogeneous stratum of depth H resting on a rigid bedrock are shown in fig. 4.38 for two different ratios between the Young's modulus: $E_p/E_s = 10^3$ (soft soil) and $E_p/E_s = 10^2$ (stiff soil). It is assumed that the stratum characteristics are: internal damping coefficient $\beta = 0.05$ and Poisson ratio $\nu_s = 0.4$. The ratio between densities is $\rho_s/\rho_p = 0.7$ and the aspect ratio of the pile is $L/d = 15$. Results for ratios between stratum depth and pile length of $H/L = 1$ (hinged pile), 1.5, 2, 3, 5 and 10, as well as the response for the half-space, are shown.

As can be seen from the figures, the presence of a rigid bedrock below a floating pile has a strong influence on the impedances in the frequency band from the static value to approximately 1.5 times the dimensionless fundamental natural frequency of the stratum in the dilatational mode. Above this frequency, stiffness and damping coefficient are coincident with those of a floating pile in a half-space, which reveals that the main damping mechanism at intermediate and high frequencies is the energy dissipation through surface waves for both the half-space and the stratum. Below the first natural frequency, the damping coefficients are far lower than the ones corresponding to the floating pile in a half-space, because there cannot be surface waves in a stratum at low frequencies and, thus, the energy is confined in it. As it is expected, the static value of the vertical stiffness of a hinged pile is, in the case of a soft soil, much higher than that corresponding to a floating pile. More precisely, it is 5.1 times higher than that corresponding

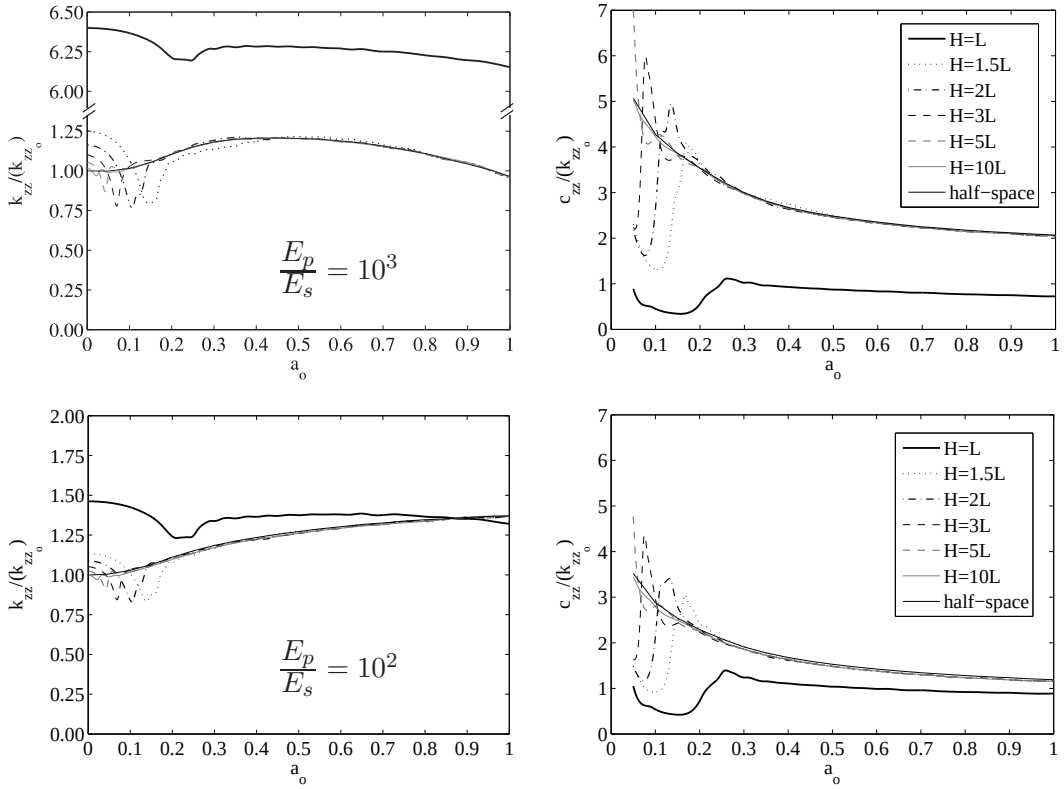

Figure 4.38: *Vertical impedances of a single pile in soft soil ($E_p/E_s = 10^3$) and stiff soil ($E_p/E_s = 10^2$).*

to a floating pile embedded in a stratum of depth $H = 1.5L$, and this relation is rather constant for all frequencies. On the contrary, in the case of a stiff soil, it is only 1.3 times higher, and the difference decreases with the frequency. On the other hand, the fundamental natural frequency of the system related to the dilatational mode is clearly highlighted in each case. Note that the influence of the presence of the rigid bedrock is still noticeable for a stratum depth five times the pile length, while it is hardly significant when the stratum depth is ten times the pile length. Table 4.1 compares the dimensionless fundamental frequencies in the dilatational mode numerically computed for a pile embedded in a soft soil with the fundamental frequencies analytically obtained for an undamped stratum. As can be seen, the proposed method predicts adequately the actual fundamental frequencies.

Horizontal and rocking impedances of a single pile embedded in a homogeneous stratum of depth H resting on a rigid bedrock are shown in figs. 4.39 and 4.40 respectively. The characteristics of piles and soils for these and further cases are the ones defined above. For the sake of clarity, only results for ratios between

H/L	**1**	**1.5**	**2**	**3**	**5**	**10**
Undamped stratum	0.257	0.171	0.127	0.086	0.051	0.026
Pile-soil system	0.245	0.150	0.105	0.070	0.042	0.022

Table 4.1: *Comparison between fundamental frequencies computed for an undamped stratum and for a pile embedded in a soft stratum.*

stratum depth and pile length of $H/L = 1$ (hinged pile), 1.5 and 2, together with the response for the half-space, are presented. The range of interest in all four stiffness figures has been enlarged and the natural frequencies to which every peak is associated have been labelled for the horizontal cases.

In this case, the resonance effects are associated to both the shear and the dilatational modes. The influence of the presence of the rigid bedrock is significant approximately until the second natural frequency related to the shear mode for the soft soil, and until the third for the stiff soil. In this range, the impedances fluctuate about the half-space solution for both the stiffness and the damping coefficients. As for the latter, it is small at low frequencies as discussed above. For higher frequencies, the impedance behaviour is similar to the one corresponding to a pile embedded in a half-space.

	Stratum natural frequencies in			
	shear mode		**dilatational mode**	
	$\mathbf{a^s_{o(1)}}$	$\mathbf{a^s_{o(2)}}$	$\mathbf{a^p_{o(1)}}$	**H/L**
Undamped stratum	0.105	0.314	0.257	1
Pile group-soil system	0.120	0.330	0.250	
Undamped stratum	0.070	0.209	0.171	1.5
Pile group-soil system	0.085	0.230	0.175	
Undamped stratum	0.052	0.157	0.127	2
Pile group-soil system	0.065	0.160	0.118	

Table 4.2: *Comparison between natural frequencies for an undamped stratum and for a 2×2 pile group embedded in a soft stratum.*

Vertical and horizontal impedances of a 2×2 pile group embedded in a homogeneous stratum of depth H resting on a rigid bedrock are shown in figs. 4.41

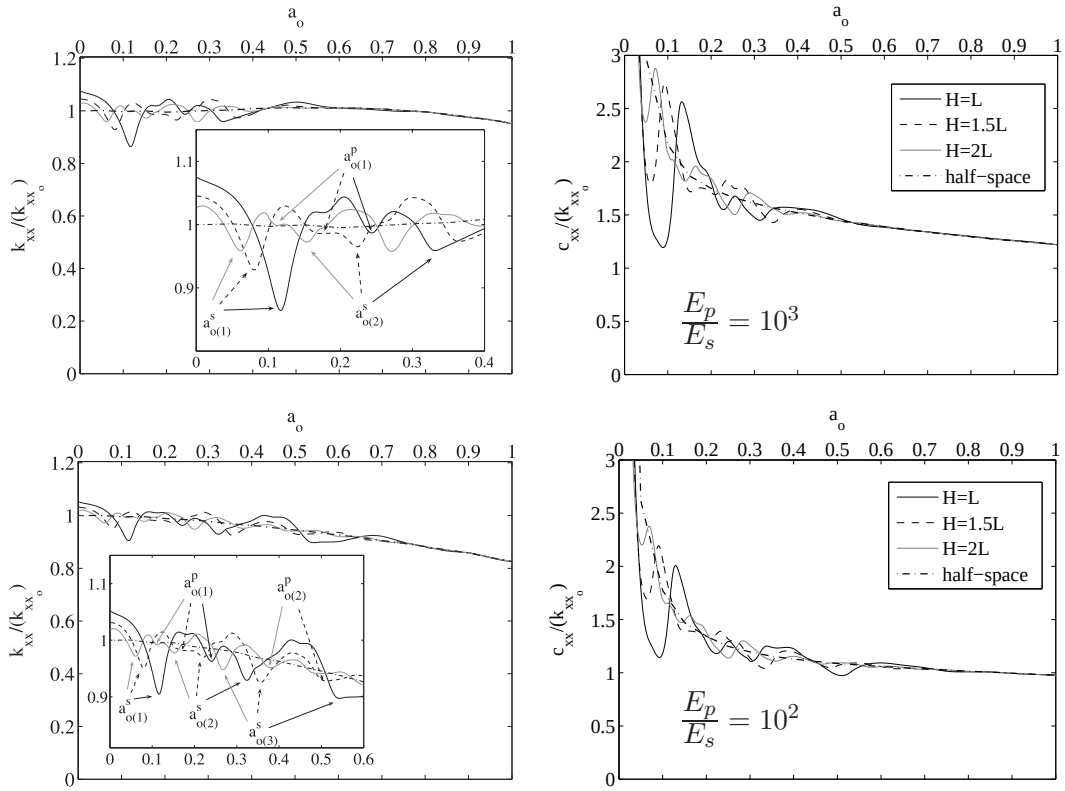

Figure 4.39: *Horizontal impedances of a single pile in soft soil ($E_p/E_s = 10^3$) and stiff soil ($E_p/E_s = 10^2$).*

and 4.42, and figs. 4.43 and 4.44, respectively. Ratios between pile separation and diameter of $s/d = 2$, 5 and 10, and ratios between stratum depth and pile length of $H/L = 1$ (hinged pile), 1.5 and 2, as well as the response for the half-space, are presented. Fig. 4.45 shows a sketch of one of the discretizations used to obtain the impedances. Note that, as the developed software incorporates symmetry properties, only a quarter of the total geometry of the problem has to be discretized.

For scale reasons, the peaks associated to the stratum natural frequencies do not appear very clearly in the figures, but their magnitudes are proportional to the values of the single pile case and even increase with the ratio s/d. Besides, the vertical impedances at intermediate and high frequencies are equivalent to those of a floating pile group embedded in a half-space. However, the group effect is predominant over the influence of the presence of the rigid bedrock.

On the other hand, for the horizontal case, the influence of the rigid bedrock is relatively much more important, even though the group effect is still predominant. The impedances fluctuate about the half-space solution, and the amplitude of this

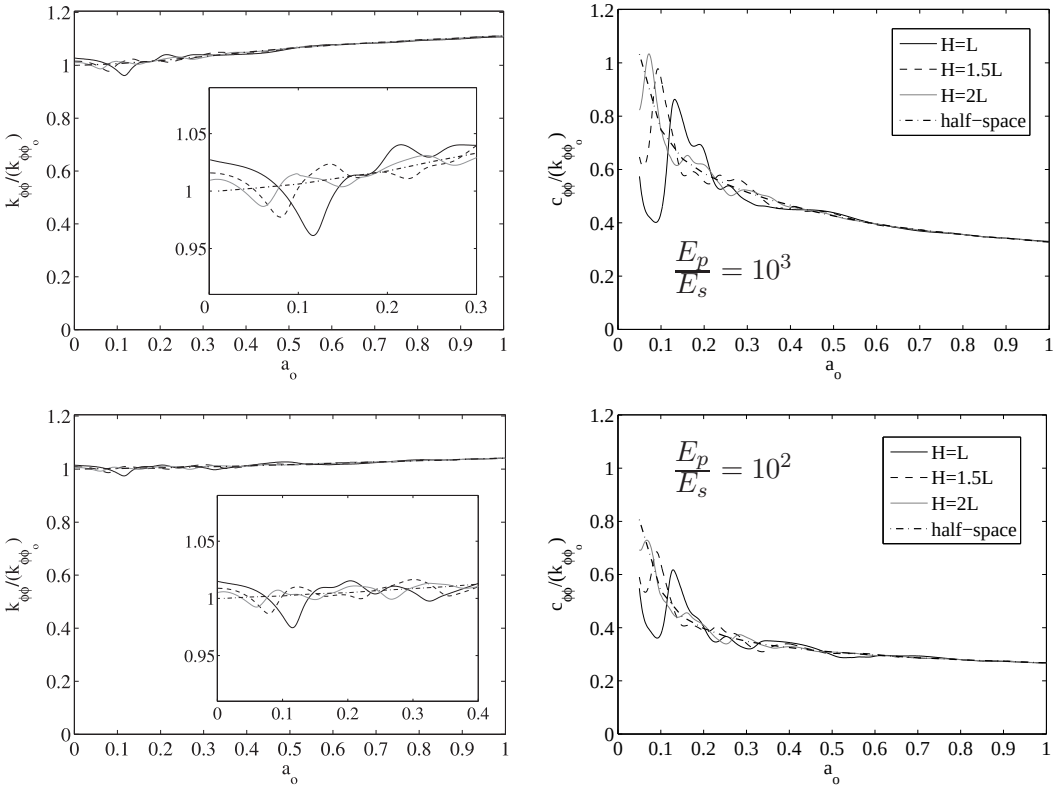

Figure 4.40: *Rocking impedances of a single pile in soft soil ($E_p/E_s = 10^3$) and stiff soil ($E_p/E_s = 10^2$).*

fluctuation increases with the ratio s/d.

Table 4.2 presents the comparison between the values of dimensionless natural frequencies obtained with the presented coupling model and those analytically computed for an undamped stratum. Only the values obtained for the horizontal impedance of a pile group with a ratio $s/d = 10$ in a soft soil are presented.

Finally, rocking impedances of a 2×2 pile group embedded in a homogeneous stratum on a rigid bedrock are shown in fig. 4.46. Ratios between stratum depth and pile length of $H/L = 1$ (hinged pile), 1.5 and 2, together with the response for the half-space, are presented. Only the ratio s/d =10, for which the influence of the rigid bedrock is stronger, has been displayed in order to illustrate the fact that the rocking impedances of pile groups are little influenced by the presence of the bedrock.

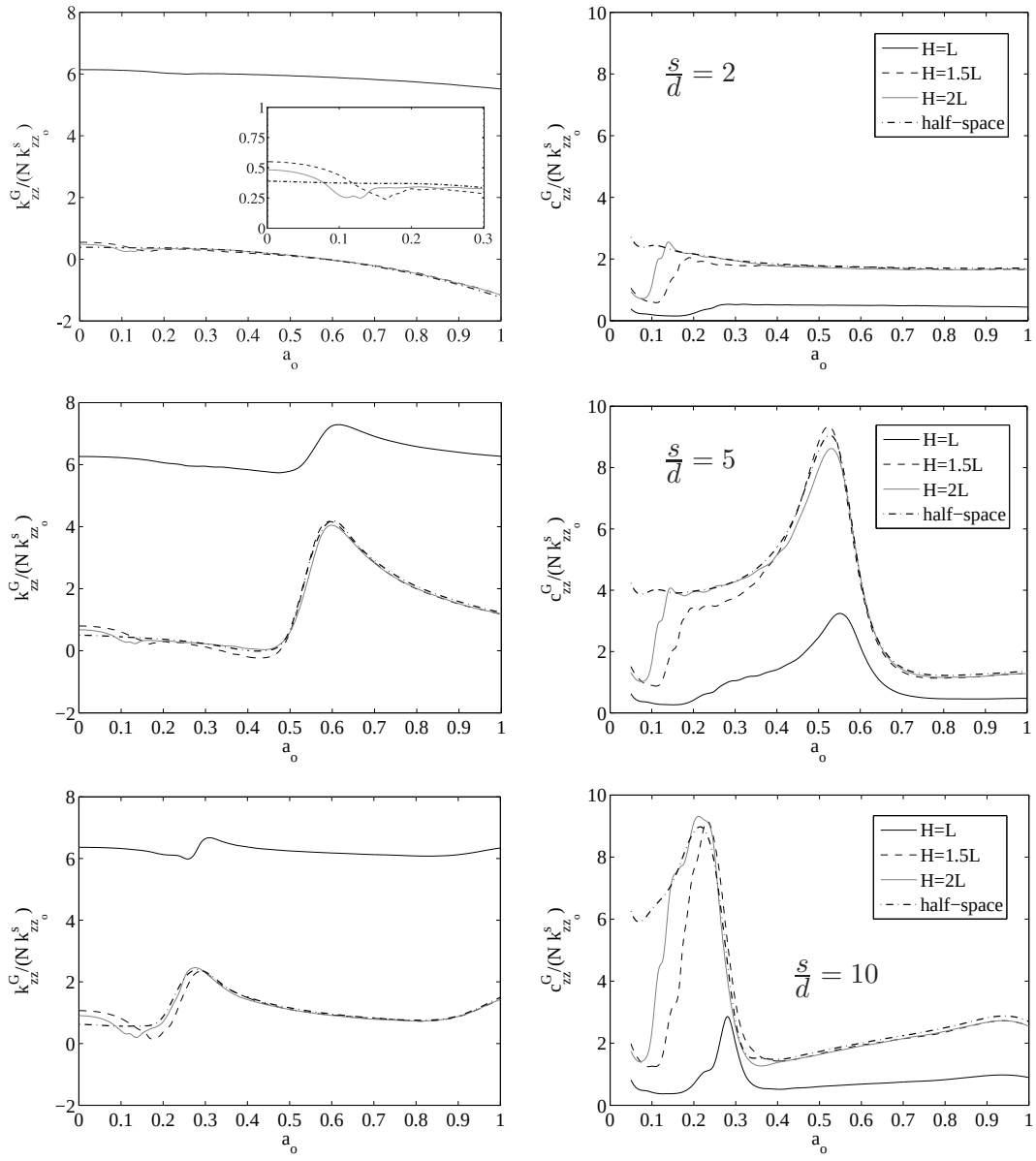

Figure 4.41: *Vertical impedances of a* 2×2 *pile group in soft soil* ($E_p/E_s = 10^3$). $s/d = 2, 5$ *and* 10.

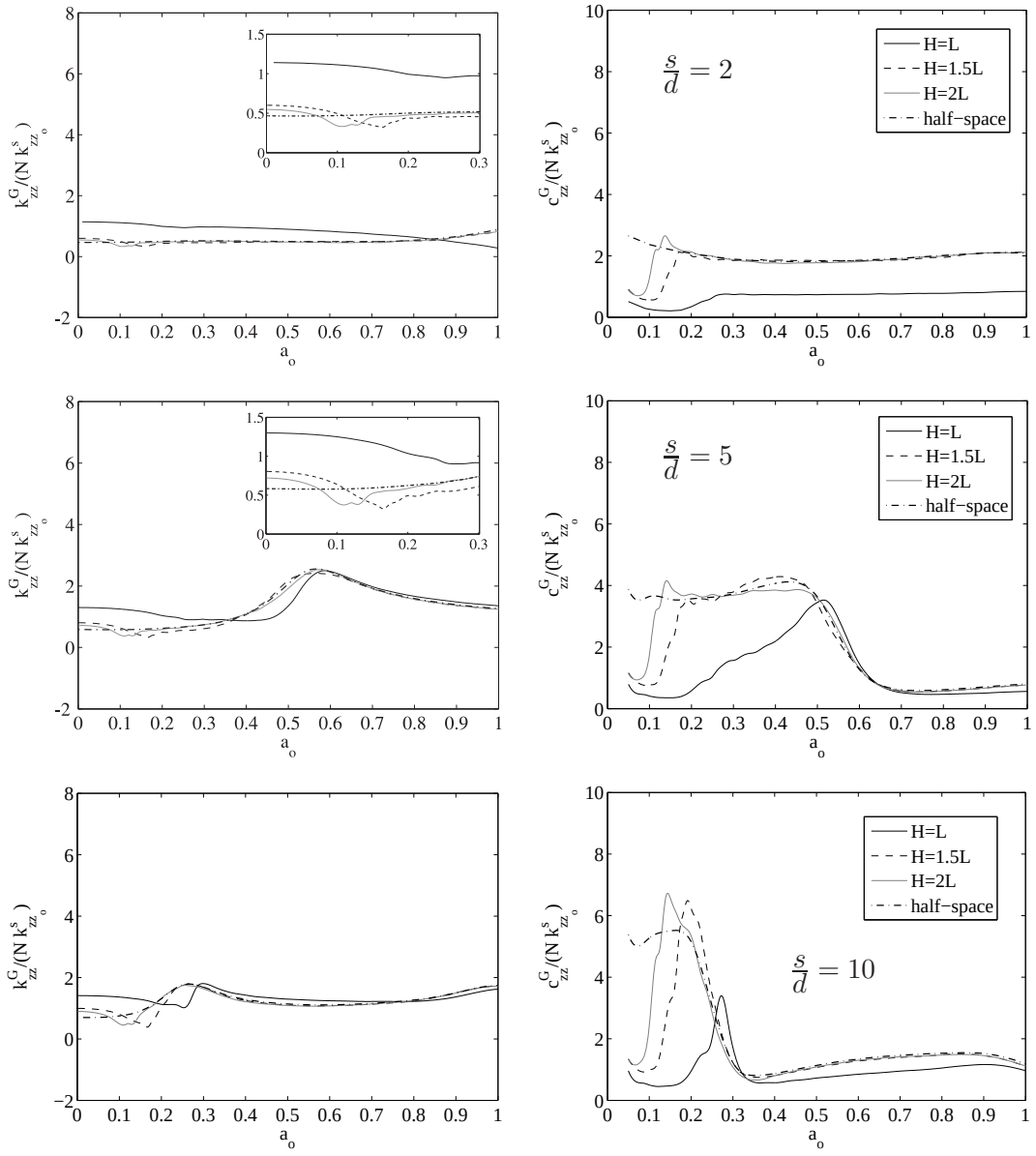

Figure 4.42: *Vertical impedances of a* 2×2 *pile group in stiff soil* ($E_p/E_s = 10^2$). $s/d = 2, 5$ *and* 10.

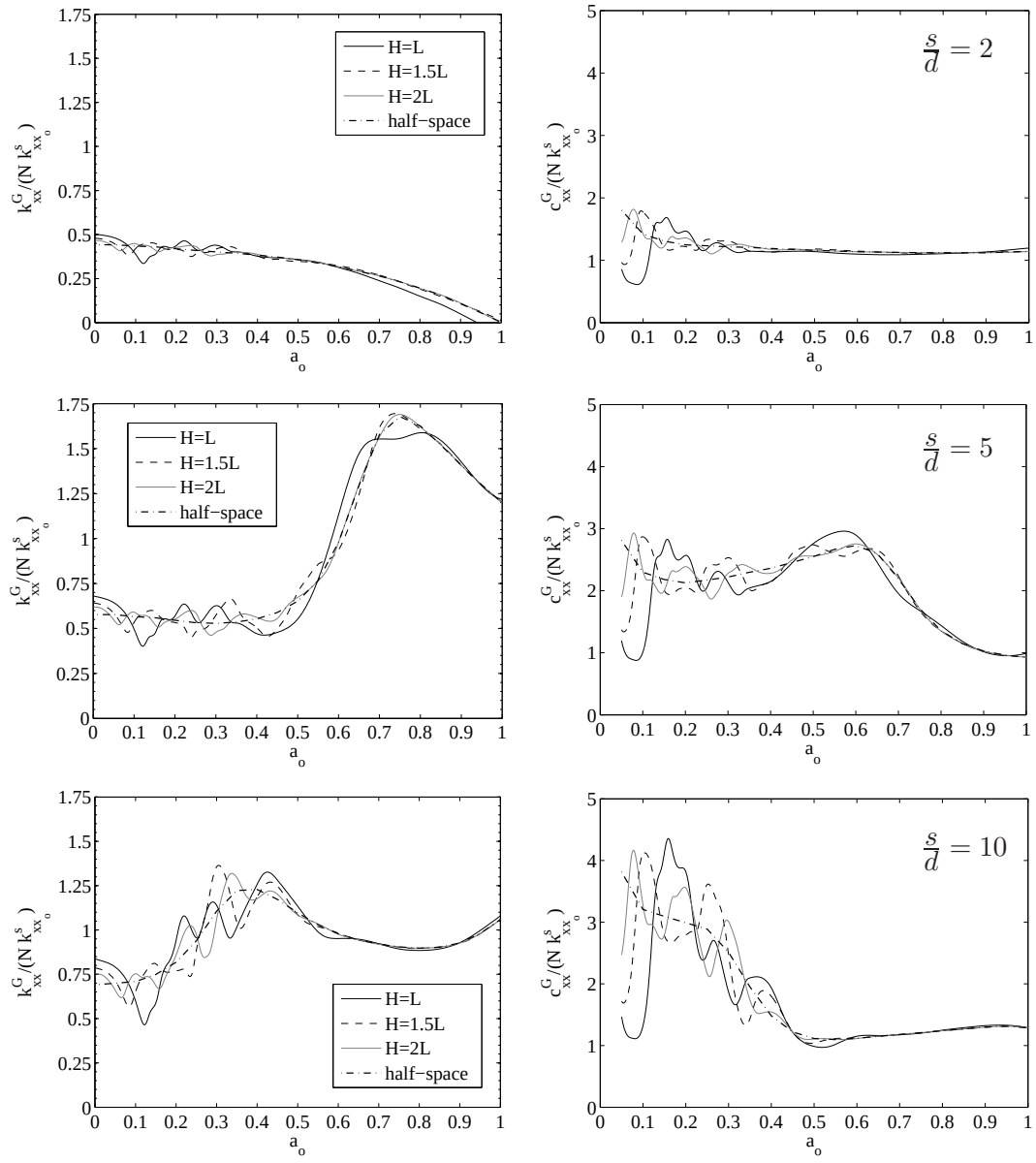

Figure 4.43: *Horizontal impedances of a* 2×2 *pile group in soft soil* ($E_p/E_s = 10^3$). $s/d = 2, 5$ *and* 10.

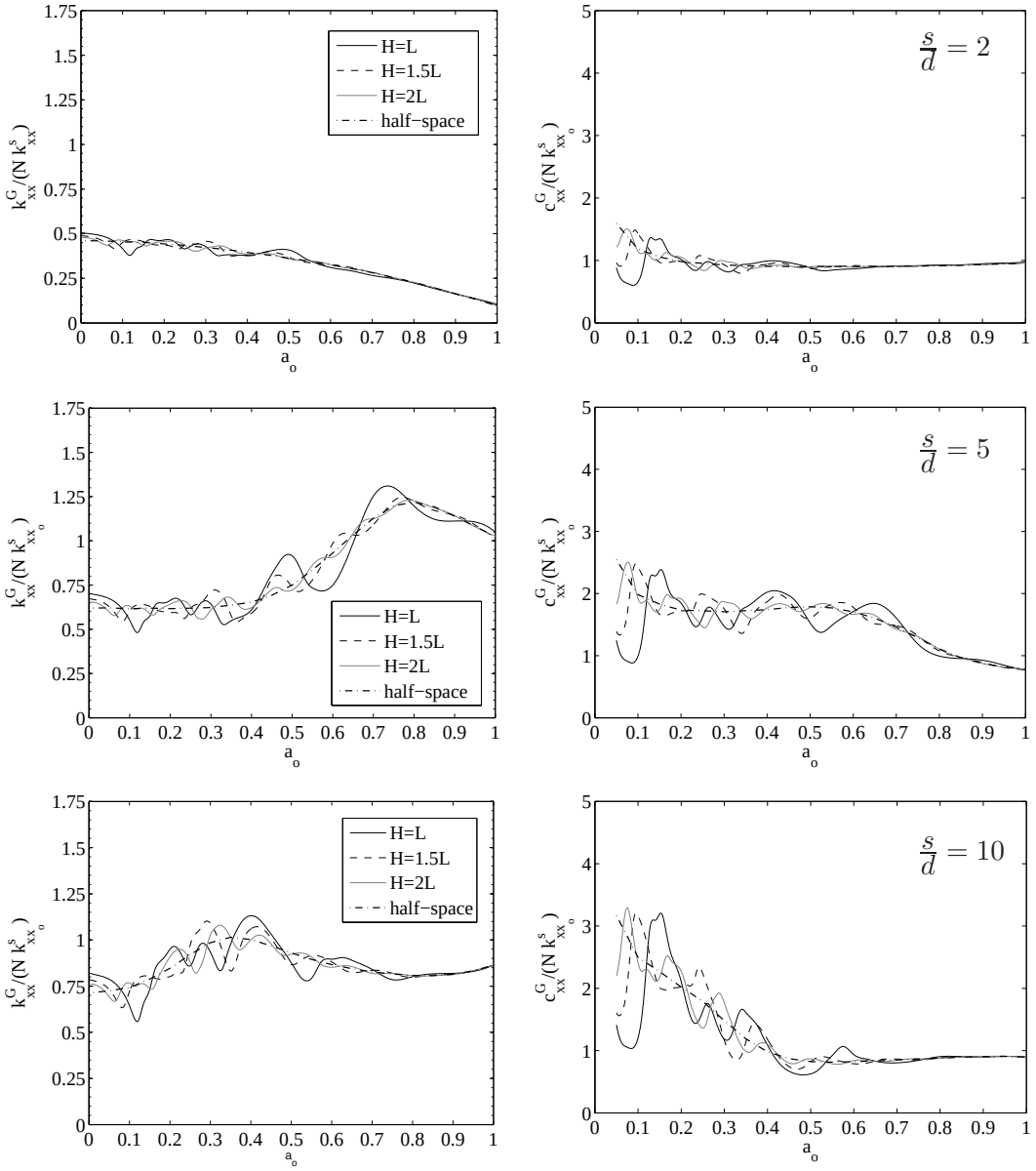

Figure 4.44: *Horizontal impedances of a* 2×2 *pile group in stiff soil* ($E_p/E_s = 10^2$). $s/d = 2, 5$ *and* 10.

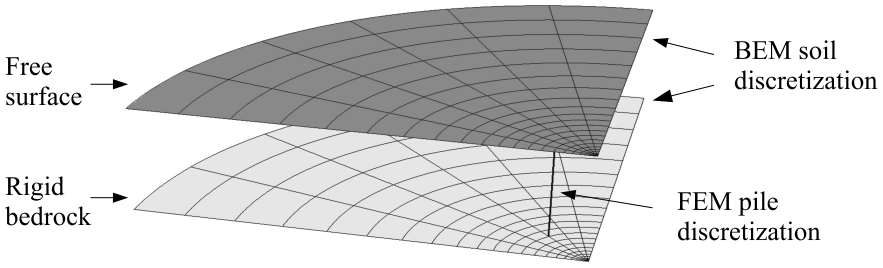

Figure 4.45: 2×2 *hinged pile group and stratum BEM-FEM discretization (only a quarter of the geometry is shown).*

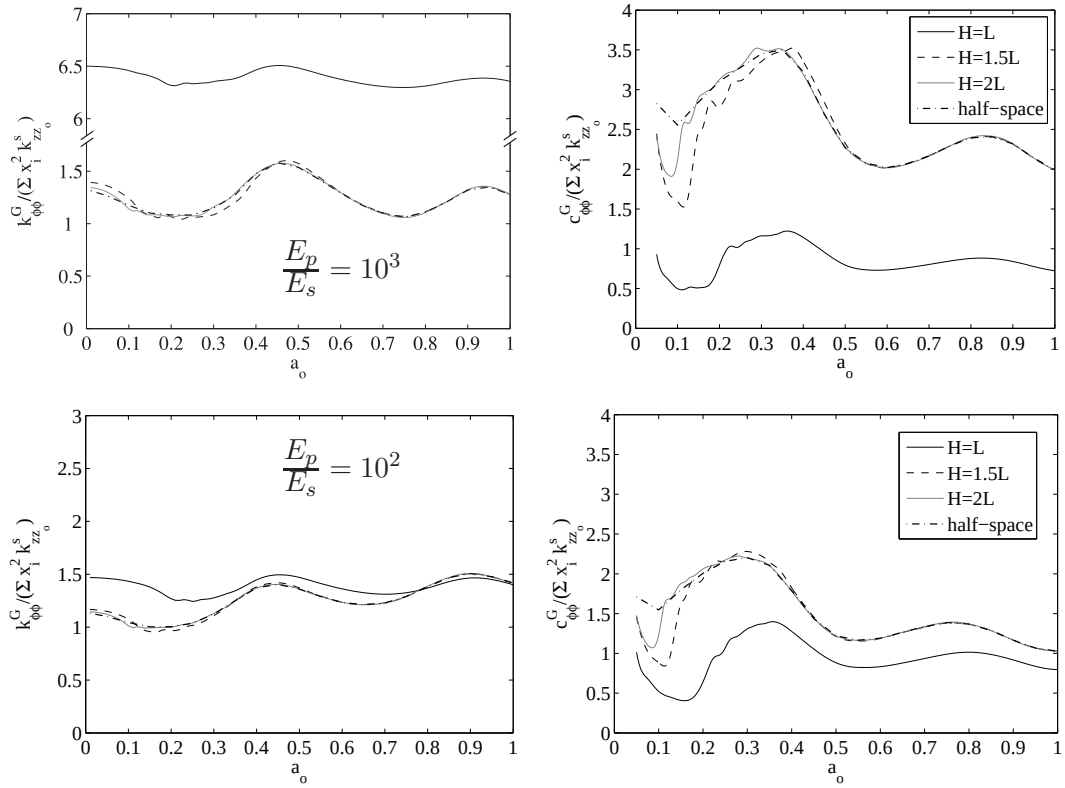

Figure 4.46: *Rocking impedances of a* 2×2 *pile group in soft soil* ($E_p/E_s = 10^3$) *and stiff soil* ($E_p/E_s = 10^2$). *s/d=10.*

4.6.1 Conclusions

From the analysis of these results, the following conclusions can be drawn:

- The pile-soil system presents small peaks associated to the stratum natural frequencies that the numerical model is able to predict adequately.
- The vertical impedance functions of a pile foundation embedded in strata of the analysed depths are equivalent to those embedded in a half-space at frequencies above 1.5 times the fundamental natural frequency of the stratum in the dilatational mode. Besides, the foundation vertical behaviour is only influenced by this natural frequency.
- The influence of the stratum depth over the horizontal impedance functions of a pile foundation is significant over a broader band of frequencies. Thus, several peaks associated to both the shear and the dilatational modes appear in the foundation response.
- This influence is even more evident in the damping functions, which at low frequencies are much smaller than those corresponding to the half-space. On the contrary, their values are similar at higher frequencies, which reveals that the main damping mechanism at intermediate and high frequencies is the energy dissipation through surface waves for both the half-space and the strata.
- The influence of the presence of the rigid bedrock is still noticeable for a stratum depth five times the pile length.
- The group effect is predominant over the influence of the presence of the rigid bedrock, especially in vertical and rocking impedances, in which the peaks associated to the natural frequencies of the stratum are of small magnitude. However, the effects of the presence of the bedrock on the horizontal behaviour are stronger and become evident along a broader frequency band. In all cases, the influence of the rigid bedrock increases with the ratio s/d.
- The frequency band in which the foundation response is influenced by the rigid bedrock broadens with the increase of the soil stiffness and, at the same time, a larger number of natural frequencies of the stratum in both the shear and the dilatational modes becomes evident for the horizontal and rocking cases.
- The group effect becomes more evident as the ratio E_p/E_s increases.
- The rocking behaviour is the less influenced by the presence of a rigid bedrock.

- The difference between the vertical response of floating and hinged pile foundations increases with the ratio E_p/E_s, and is always noticeable.
- The group effect becomes apparent in the case of hinged pile groups. In fact, for hinged pile groups embedded in a stiff stratum, the vertical stiffness functions tend to be equivalent to those of floating pile groups above a certain frequency which decreases when the ratio s/d increases. Thus, in these cases, the active pile length is far shorter than the stratum depth.

As can be seen from the foregoing discussion, the effect of the presence of the rigid bedrock is vital for the horizontal behaviour of single piles and pile groups, and also for the rocking behaviour of single piles, while it is almost negligible for the rocking behaviour of pile groups. Regarding the vertical behaviour of floating pile foundations, the effect of the bedrock is not important except for frequencies below 1.5 times the fundamental natural frequency of the stratum. At the same time, the influence of the surrounding soil is of great importance even for hinged pile foundations, due to the fact that the influence of the boundary condition at the piles tips becomes less significant as the ratio E_p/E_s decreases.

4.7 Seismic response of pile groups to vertically-incident shear waves

The influence of the stratigraphy on the seismic behaviour of a pile foundation is studied in this section. To this end, the seismic response of a hinged pile group under vertically-incident plane S waves is analysed. The cases included in this experiment are sketched in fig. 4.47. Three different layered soils resting on a rigid bedrock, formed by up to four different layers with shear wave velocity increasing with depth, are considered. Besides, two limiting cases corresponding to homogeneous profiles with the properties of the softest and stiffest layers, respectively, as well as the half-space case, are also taken into account. The properties of the stiffest layer are taken as those of a reference soil. As it is well known that the number of piles is not a significant parameter in the horizontal seismic response of pile foundations (see e.g. [69]), only the case of a square 3×3 hinged pile group is presented.

The non-dimensional properties of the reference soil (with shear wave velocity c_s) and pile group are: internal damping coefficient of the soil $\beta = 0.05$, Poisson ratio of the soil $\nu_s = 0.4$, ratio between densities $\rho_s/\rho_p = 0.7$, pile/soil modulus ratio $E_p/E_s = 10^2$, aspect ratio of the piles $L/d = 15$, ratio between stratum depth and pile length $H/L = 1$ (hinged piles), and ratio between pile separation and diameter $s/d = 10$. Damping coefficient, Poisson ratio and density are kept constant for all layers.

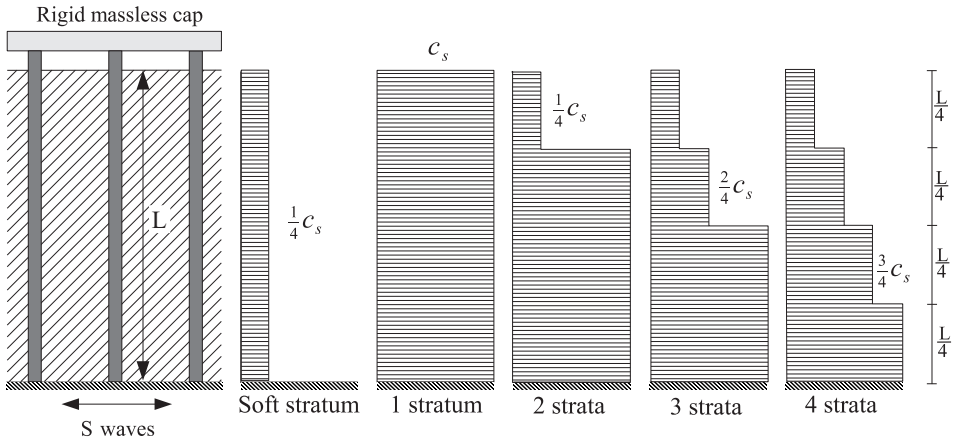

Figure 4.47: *Sketch of studied soil profiles.*

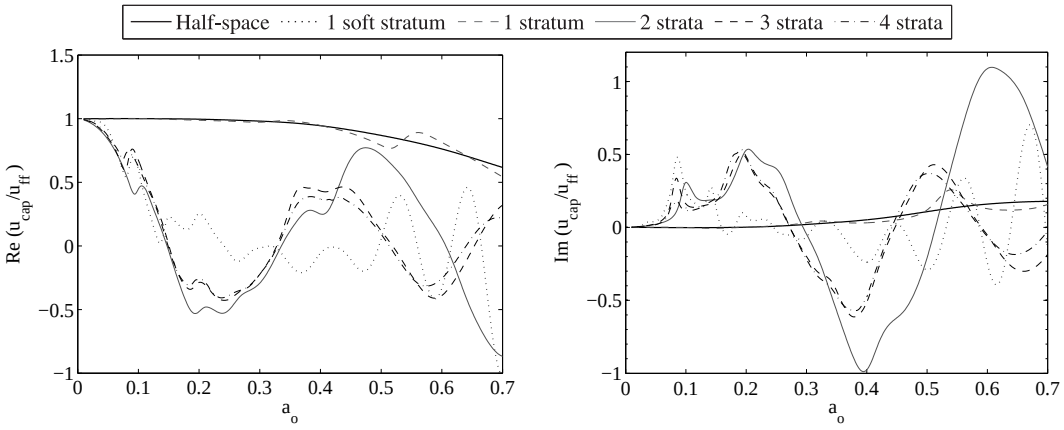

Figure 4.48: *Time-harmonic displacement transfer functions at the pile cap.*

The first step is obtaining the time-harmonic transfer functions relating horizontal displacement amplitudes at the pile cap (u_{cap}) to the free field surface horizontal displacement (u_{ff}), for vertically-incident plane time-harmonic S waves. Real and imaginary parts of these transfer functions are presented in fig. 4.48 for the six profiles defined above, being a_o referred to the stiffest soil for all cases. Comparing the one-stratum reference soil case with the two-strata case, it can be seen that taking into account a soft layer atop yields to much more rapidly decreasing transfer functions (as highlighted before, for instance, in [69,71]), while the addition of intermediate shear wave velocity layers in between does not alter significantly the response up to $a_o = 0.4$ with respect to the two-strata profile. Also, the difference between the transfer functions for the half-space and the stratum are rather small, only noticeable at the stratum natural frequencies.

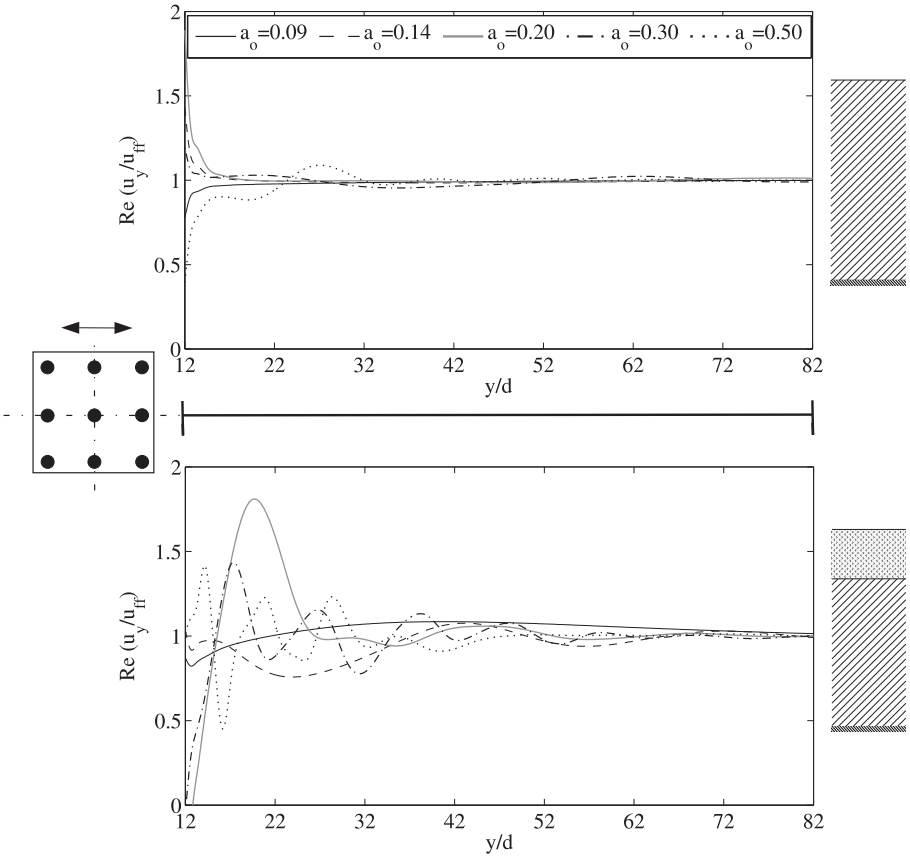

Figure 4.49: *Horizontal deformation of free surface, due to vertically incident S waves, along direction of shaking (axis* y*).*

A phenomenon that can be studied here, in reference to the difference between

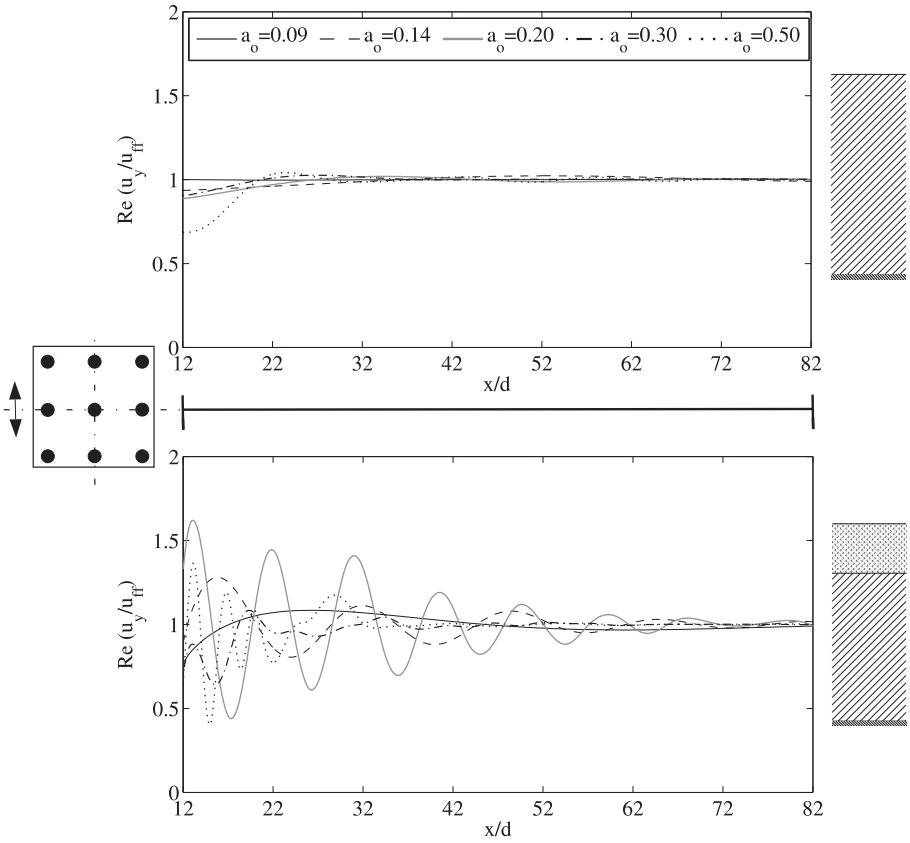

Figure 4.50: *Horizontal deformation of free surface, due to vertically incident S waves, perpendicularly to the direction of shaking (axis* x*).*

homogeneous and stratified strata transfer functions, is the horizontal deformation of the free surface. Assuming S waves acting along direction y, figs. 4.49 and 4.50 show, for the one-layer and two-layer profiles, and several frequencies, the real part of the horizontal displacements of points on the free surface placed along axis y and x, for horizontal coordinates from 12 to 82 times the diameter of the piles. It can be seen that the perturbation generated by the presence of the piles on the incident field is much more stronger, both in amplitude and extension, when a soft soil stratum exists atop, which is related to the more rapidly varying transfer function of this case. Obviously, the magnitude and shape of this perturbation is a function of the wave length in the soil. In all cases, the perturbation is not significant at distances from the foundation axis higher than $70d$.

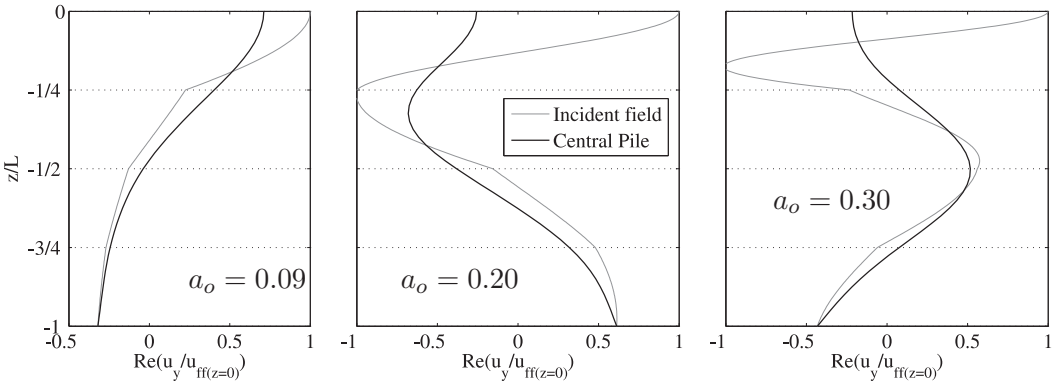

Figure 4.51: *Distributions of incident field and central pile displacements along depth for the four-layer soil profile.*

On the other hand, fig. 4.51 presents the distributions of incident field and central pile displacements along depth for the four-layer soil profile. Non-dimensional frequencies $a_o = 0.09$, 0.20 and 0.30 are shown. It can be seen that the pile is able to submit approximately to the incident field within the deep layers, where the wave length is long enough. In the upper layers, on the contrary, where wave lengths are shorter, the pile is not flexible enough to follow the free field ground motion, which causes the difference between pile cap and free field surface motions. Additionally, fig. 4.52 compares the deformed shapes of all piles in the 3×3 pile group, and also of a fixed head single pile (no rotations allowed), for the four-layer soil profile. It can be seen that, for a certain non-dimensional frequency, all deformed shapes are very close to one another. Thus, there seem to be no significant pile-to-pile interaction effects under seismic excitation in the problem at hand. However, as this is only shown for this particular case, general conclusions would need of further studies.

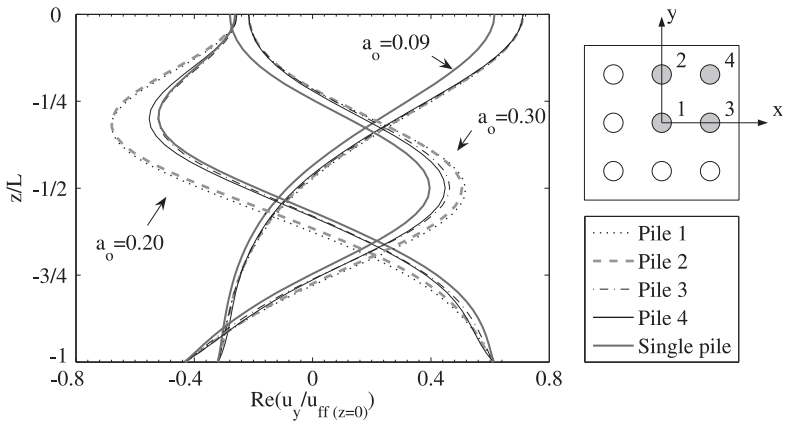

Figure 4.52: *Comparison of deformed shapes of all piles in the group, and of a single pile, for the four-layer soil profile.*

Acceleration time-histories and response spectra can now be obtained for particular cases. The chosen problem, whose parameters are summarized in Table 4.3, is that of a group of concrete piles of diameter $d = 1.0$ m., being worth noting that the resulting properties for the softest layer correspond to the case of a considerably soft soil. The system is subjected to the two following simulated earthquakes, specified at the free surface:

- The N-S component recorded at the Imperial Valley Irrigation District substation in El Centro, California, during the Imperial Valley, California, earthquake of May 18^{th}, 1940.
- The S50W component recorded at Bonds Corner substation in El Centro, California, during the Imperial Valley, California, earthquake of October 15^{th}, 1979.

Soil	**Piles**	**Pile group**
$c_s = 239\ m/s$	$E_p = 2.76 \cdot 10^{10}\ N/m^2$	$s/d = 10$
$\rho_s = 1750\ kg/m^3$	$\rho_p = 2500\ kg/m^3$	$L/d = 15$
$\nu_s = 0.4$	$d = 1\ m$	$H/L = 1$

Table 4.3: *Reference soil, pile and pile group properties.*

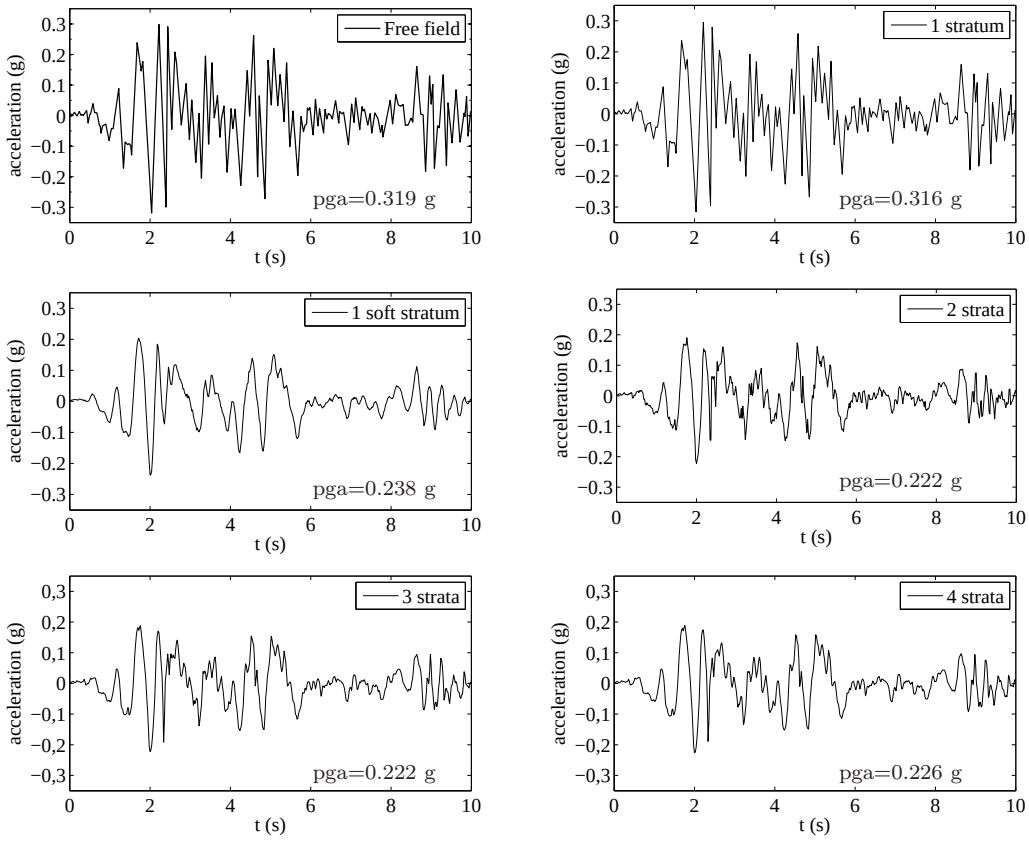

Figure 4.53: *Response acceleration histories for El Centro (1940) earthquake specified at the free surface.*

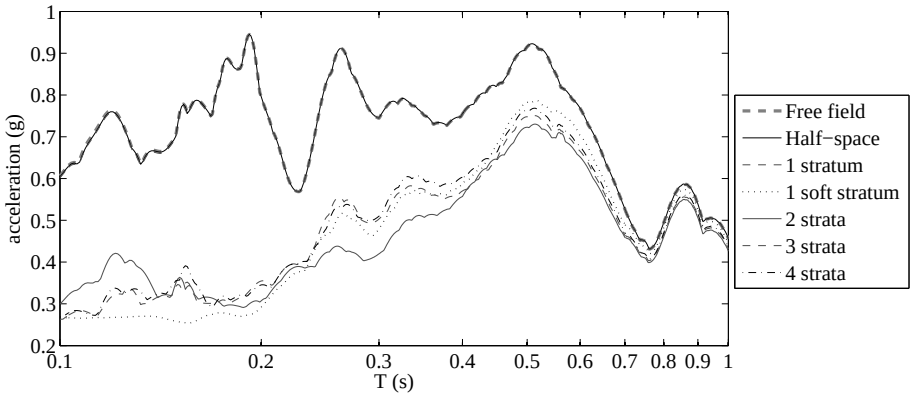

Figure 4.54: *Five per cent-damped acceleration response spectra for El Centro (1940) earthquake specified at the free surface.*

Figs. 4.53 to 4.56 show the acceleration time-histories and response spectra ($\xi = 5\%$), for both earthquake ground motions, all of them measured at the pile-cap. As expected in view of the transfer functions presented above, it can be seen that the responses of the pile foundation embedded in a half-space and in a stratum, both with the reference soil properties, are almost coincident with the excitation. As for the rest of the cases, the acceleration response spectra values are significantly smaller in the range of periods shown in figs. 4.54 and 4.56. However, there is not a clear tendency between the response spectra for the different profiles as for to say that the more layers considered, the more conservative estimate, neither the contrary. For instance, for periods below 0.2 seconds, the response for the soft stratum is the lowest one, while between 0.25 and 0.4 seconds, it is the two-strata profile whose values are the smallest.

Up to now, the same seismic excitation has been specified at the free surface for all soil profiles, but it is also worth investigating the system behaviour when the seismic input is specified at the bedrock. In this case, different amplification phenomena due to the soil stratigraphy take place in each profile, as can be seen in fig. 4.57, which presents the free field and pile cap acceleration response spectra ($\xi = 5\%$) obtained when El Centro (1940) earthquake is specified at the bedrock. Indeed, the strong ground motion, measured at the free surface, is significantly amplified, especially at frequencies near the strata natural frequencies. However, the attenuating effect of the pile foundation seen before, is also evident in this case. As expected, one-stratum reference soil free field response spectra and pile cap response spectra are once again almost coincident, but as for the rest of cases, the presence of the piles always leads to smaller responses.

Since further parametric studies should be carried out with a greater variety of

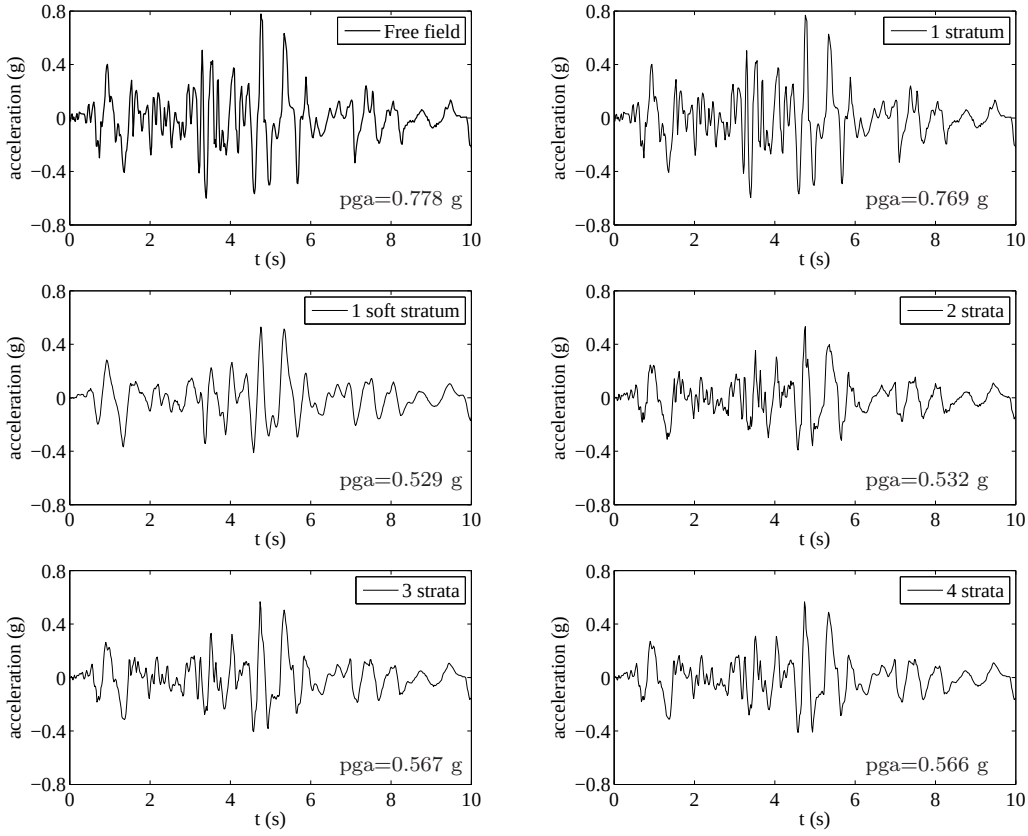

Figure 4.55: *Response acceleration histories for El Centro (1979) earthquake specified at the free surface.*

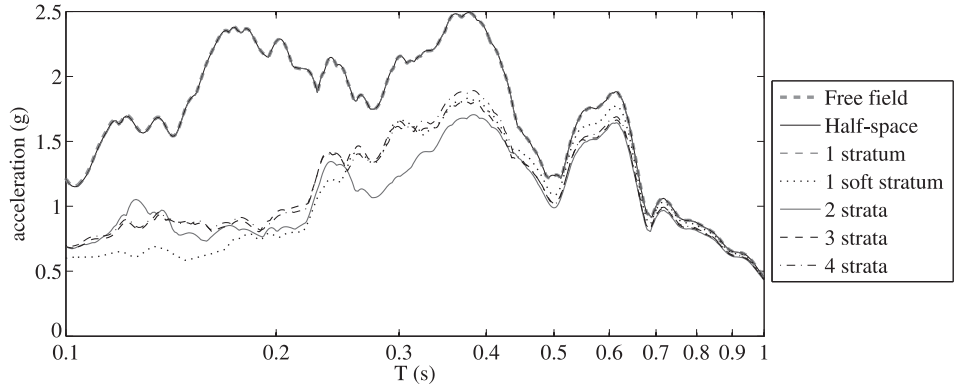

Figure 4.56: *Five per cent-damped acceleration response spectra for El Centro (1979) earthquake specified at the free surface.*

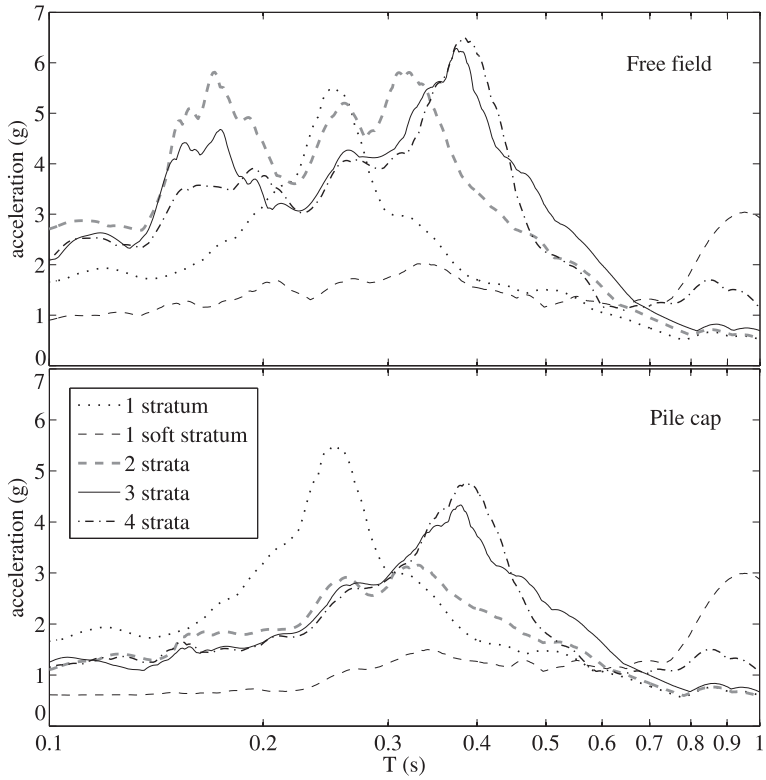

Figure 4.57: *Five per cent-damped acceleration response spectra for El Centro (1940) earthquake, specified at the bedrock.*

profiles, including parameters such as densities, damping coefficients and Poisson ratios, conclusions from this study may not be generalized. On the other hand, only the horizontal response has been treated here but, depending on the problem, the rocking behaviour could also be an important parameter.

4.7.1 Conclusions

The seismic response of a square 3×3 hinged pile group embedded in different soil profiles and under vertically-incident plane time-harmonic shear waves and two different strong ground motions, has been studied. General conclusions cannot be drawn without more and deeper analysis on the subject but, as for the presented case, it has been shown that:

- the presence of a soft layer atop the soil yields to much more rapidly decreasing displacement transfer functions than those corresponding to foundations in the reference homogeneous soil. In fact, two different trends are clearly defined, depending on whether the soft layer is considered or not.
- the addition of further intermediate shear wave velocity layers in between is of minor importance.
- the incident field at the free surface is perturbed by the presence of the pile foundation, being the magnitude of this perturbation larger when a soft layer exists atop. The maximum value of this perturbation is of similar order in both the direction of motions induced by the S waves and its perpendicular.
- pile-to-pile interaction under seismic excitation is almost non-existent.
- pile foundations embedded in the non-homogeneous soil profiles studied here filter out a great part of the harmonic components of the seismic input, in such a way that the resulting acceleration response spectra are significantly lower than those corresponding to the free field.
- the simplification of the soil profile to just one stratum or to a half-space would lead to over- or underestimating, depending on the chosen properties, the excitation at the base of a superstructure in a substructuring analysis.
- these conclusions are valid for earthquake motions specified at either the free surface or at the bedrock.

Chapter 5

Dynamic analysis of piled embedded footings

5.1 Introduction

A great amount of research has been reported on the dynamic performance of pile foundations in elastic or viscoelastic soil, as shown in the introductory chapter, but also on the dynamic response of embedded footings (see e.g. reviews by Gazetas and Mylonakis [144] and Mylonakis et al. [145]). A more complex foundation type is that of rigid embedded footings supported by piles under the base slab. Even though such foundations (to be referred to hereafter as piled embedded footings) are widely used for supporting high-rise structures (see e.g. [146]), they have received little research attention. To the extent of the author's knowledge, only a few pieces of research have dealt with piled embedded footings (see e.g. [147, 148]). This is in contrast to piled rafts [149–152] and soil-pile cap interaction problems [153–155] for which a wider set of research results has been reported.

On the other hand, when soil under a footing consolidates, significant settlement may be generated depending on the compressibility and thickness of the soil material. When this phenomenon is expected to take place, the magnitude of settlement can be limited by the addition of piles under the footing. In this case, foundation stiffness is increased, but the contact between soil and pile cap underside may be lost and a series of gaps form under the footing. The importance of the presence of this separation on the dynamic behaviour of a piled embedded footing has not been assessed to date.

The lack of knowledge about these topics provided the initial motivation for the work presented in this chapter, which has three main objectives: *a*) to provide insight into the dynamic and seismic behaviour of piled embedded footings; *b*) to offer a practical way to estimate, with engineering accuracy and using information widely available in the literature, the dynamic stiffness and the basic

kinematic response functions (for vertical S waves) of this class of foundations; and *c*) to evaluate the influence on the impedance functions of the possible existence of gaps between the soil and the footing underside. In order to fulfil these objectives, several numerical parametric analyses in the frequency domain have been performed for different pile-soil stiffness ratios, embedment ratios, pile-to-pile separations and pile group configurations, making use of the rigorous linear boundary element – finite element coupling formulation described in chapter 3.

After establishing the set of parameters used to define the problem and the subsequent parametric analyses, the two main sections of this chapter present the two performed studies:

- Section 5.3 studies the accuracy of simple procedures to estimate the dynamic behaviour of piled embedded footings when the independent responses of its parts (i.e. footing walls and pile group) are known. Vertical, horizontal, rocking and cross-coupled horizontal-rocking impedance functions, together with translational and rotational kinematic response functions, are discussed. A set of dimensionless graphs and simple expressions is provided for estimating the dynamic response of such foundations based on available results for embedded footings and pile groups. Differences up to 100%, 50% and 20% for the vertical, horizontal and rocking cases, respectively, are observed, though average differences in each response mode are limited to 10-30%, suggesting that the superposition concept can be employed in geotechnical design. For kinematic effects, the response functions of the embedded footing are found to provide reasonable estimates of the system's behaviour.

- Section 5.4 assesses the influence of a possible loss of contact between soil and footing underside on the impedance functions of piled embedded footings. Vertical, horizontal and rocking oscillation modes are analysed. A series of plots, relating the impedances of piled embedded footings with and without soil–footing underside separation, are presented. It is shown that the influence is negligible for frequencies below those for which dynamic pile group effects start to become apparent. Redistribution of stiffness between piles and footing is also discussed.

Finally, some conclusions are drawn from the presented results.

5.2 Problem parameters

The geometry of the model is depicted in fig. 5.1, where B and D are the foundation halfwidth and depth of embedment, L and d are the length and sectional

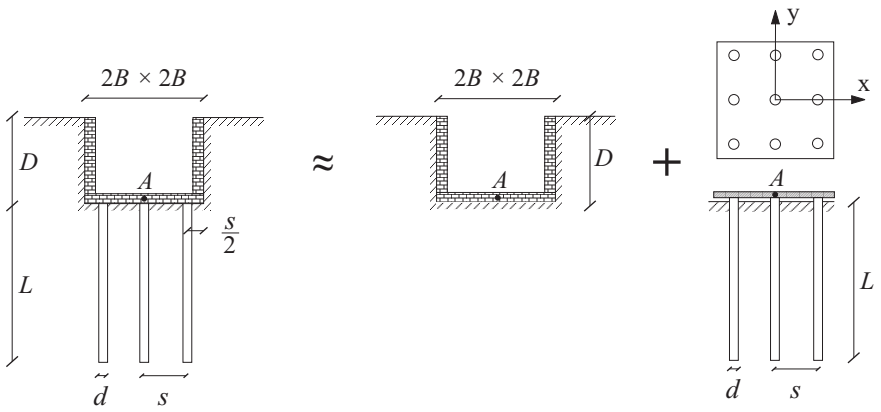

Figure 5.1: *Problem statement and simple superposition approach.*

diameter of piles, respectively, and s is the centre-to-centre spacing between adjacent piles. In the above, $B/s = n/2$, with n being the number of piles per side in square configuration. The dimensionless parameter sets considered as a part of this investigation are $s/d = 2$ and 5, $D/B = 1$ and 2, pile-soil stiffness contrasts $E_p/E_s = 1000$ and 100, $n = 2$ and 3 (leading to $B/s = 1$ and 1.5), and dimensionless frequency $a_o = \omega d/c_s$ from 0 to 1 in steps of 0.05, with c_s being the shear wave propagation velocity in the soil. The rest of properties, having generally second-order influence on dynamic response, are: mass density contrast between soil and pile $\rho_s/\rho_p = 0.7$, pile slenderness ratio $L/d = 15$, soil material damping coefficient $\xi_s = 0.05$ and soil Poissons ratio $\nu_s = 0.4$. The total number of dimensionless parameters describing the response is ten (L/d, s/d, B/s, D/B, E_p/E_s, ρ_s/ρ_p, a_o, n, β_s, ν_s), being equal to the difference between the thirteen independent (dimensional and dimensionless) variables (L, s, d, B, D, E_p, E_s, ρ_s, ρ_p, ω, n, β, ν_s) and three fundamental units (Mass, Length, Time) [156]. Note that the pile length to diameter ratio L/d is of secondary importance, as it exceeds the critical slenderness ratio beyond which the pile behaves essentially as an infinitely long beam [46, 157]. Also, note that shear wave velocity c_s is not an independent parameter, being merely a function of soil stiffness and density.

A sensitivity analysis was performed to establish the characteristics of the optimal meshes. Eventually, in the present work, meshes of the kind shown in fig. 5.2 were adopted, in which the free surface discretization extends to eight times the embedment depth D from the footing edge. Due to the symmetry of the problem, only a quarter of the geometry needs to be discretized. The total number of nodes and elements resulting from such discretization is 3203 and 816, respectively. In the numerical analyses, a minimum of 1145 nodes and 255 elements and a maximum of 3600 nodes and 830 elements were used depending

on the configuration. A study about the optimal meshing of embedded footings can be found in Vinciprova et al. [63].

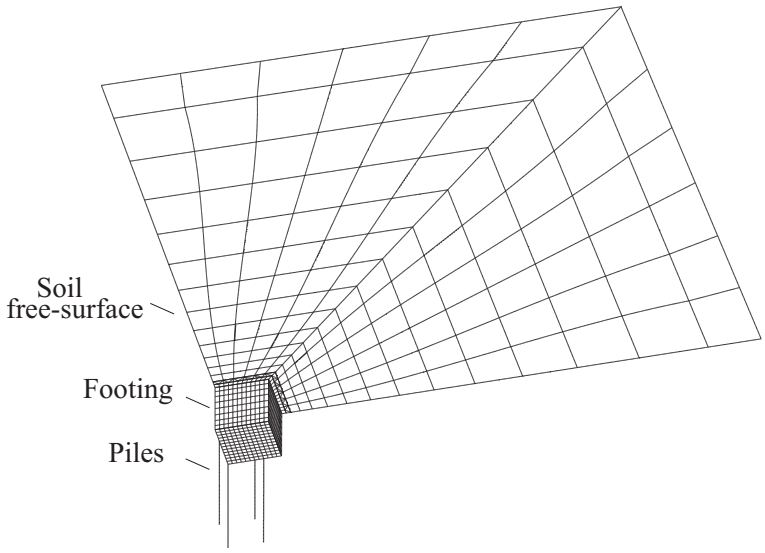

Figure 5.2: *Discretization of one-quarter of an embedded footing on a* 3×3 *pile group.*

5.3 Estimation of the dynamic response of piled embedded footings through a simple superposition approach

Given the two-component structure of piled embedded footings (i.e., footing walls and pile group), it is of interest to investigate whether or not their dynamic behaviour can be approximated by that of their parts analysed separately and then superimposed. The idea is illustrated in fig. 5.1, in which the system is conceptually decomposed into a pile group with a ground-raised pile cap (i.e., having no contact with the soil) at depth D, and an embedded footing. Fully bonded contact conditions are considered in the vertical and horizontal interfaces between soil and footing, and soil and pile.

The concept is only approximate, yet appealing, as it is intuitive and can incorporate a wealth of available data for both pile groups and embedded footings. Note that the embedment effect for the pile group is not considered in order not to be counted twice, and that this approximation is acceptable since the response is linear. This is in contrast to the bearing capacity problem for which embedment

effects should be taken into account when determining the ultimate resistance of all foundation components.

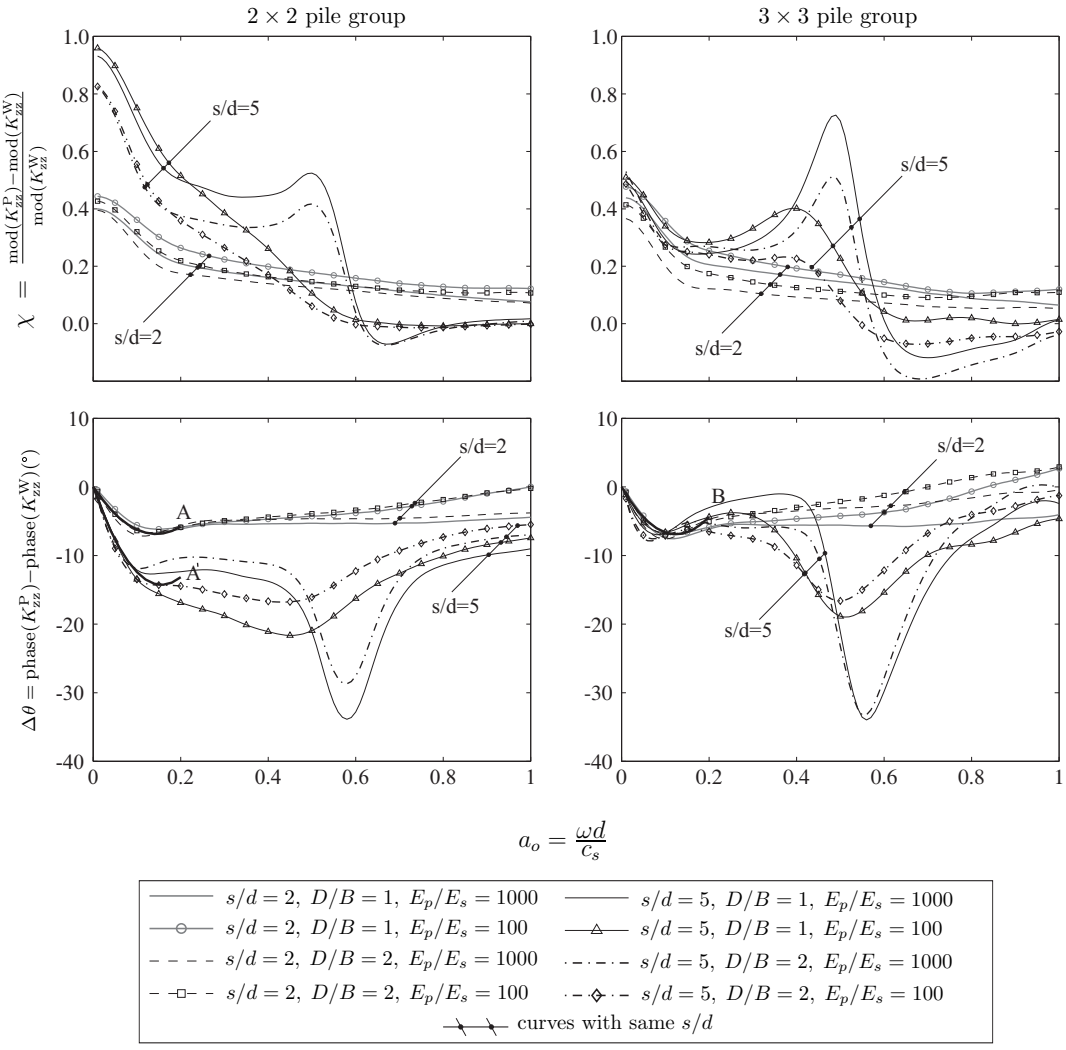

Figure 5.3: *Comparison between modulus and phase of vertical impedances of embedded footings on piles, obtained rigorously, K^P_{zz} and by superposition K^W_{zz}.*

5.3.1 Impedance functions

The impedance functions of 2×2 and 3×3 piled embedded footings are computed as a whole (K^W) and as a superposition of the dynamic stiffness functions of pile group and embedded footing treated separately (K^P). Comparisons between the

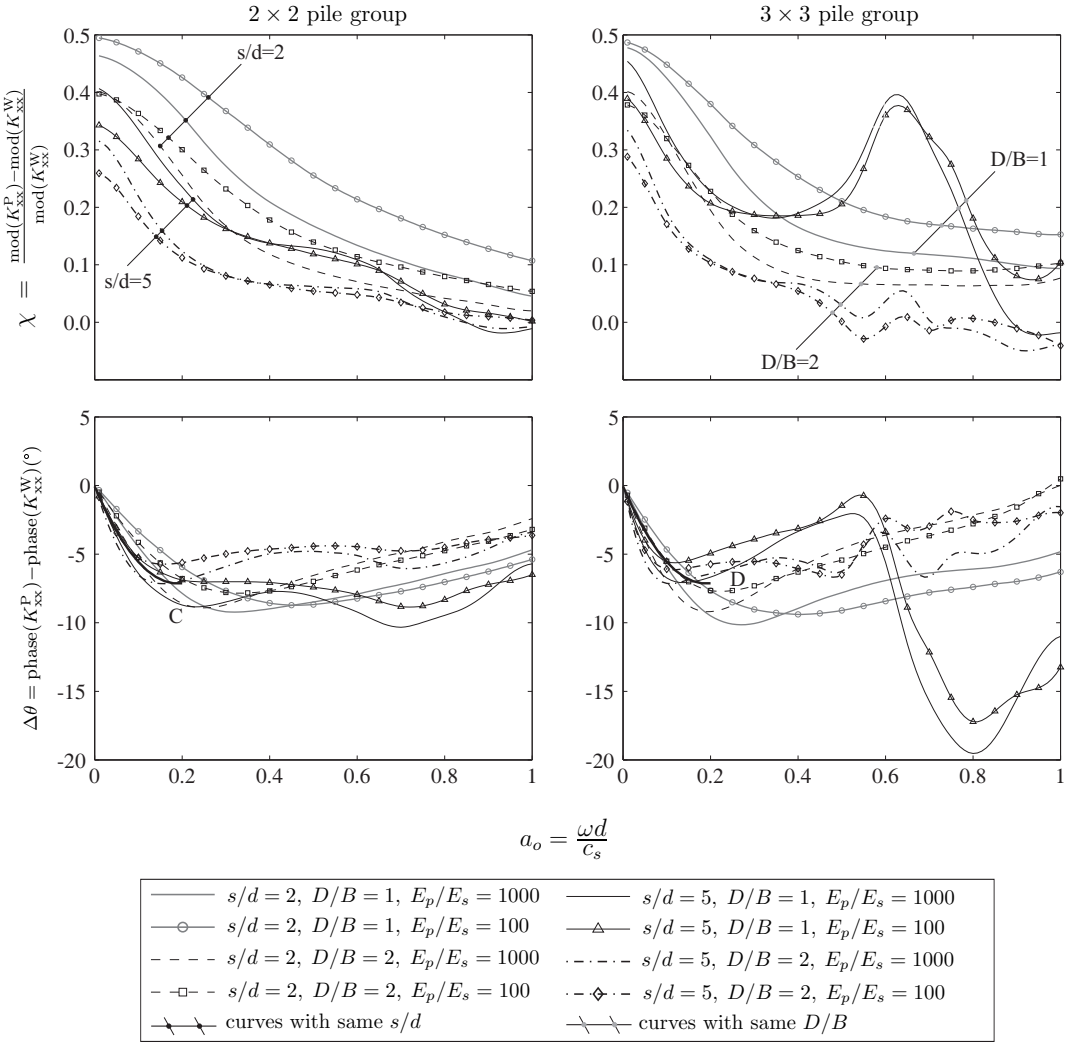

Figure 5.4: *Comparison between modulus and phase of horizontal impedances of embedded footings on piles, obtained rigorously, K_{xx}^P and by superposition K_{xx}^W.*

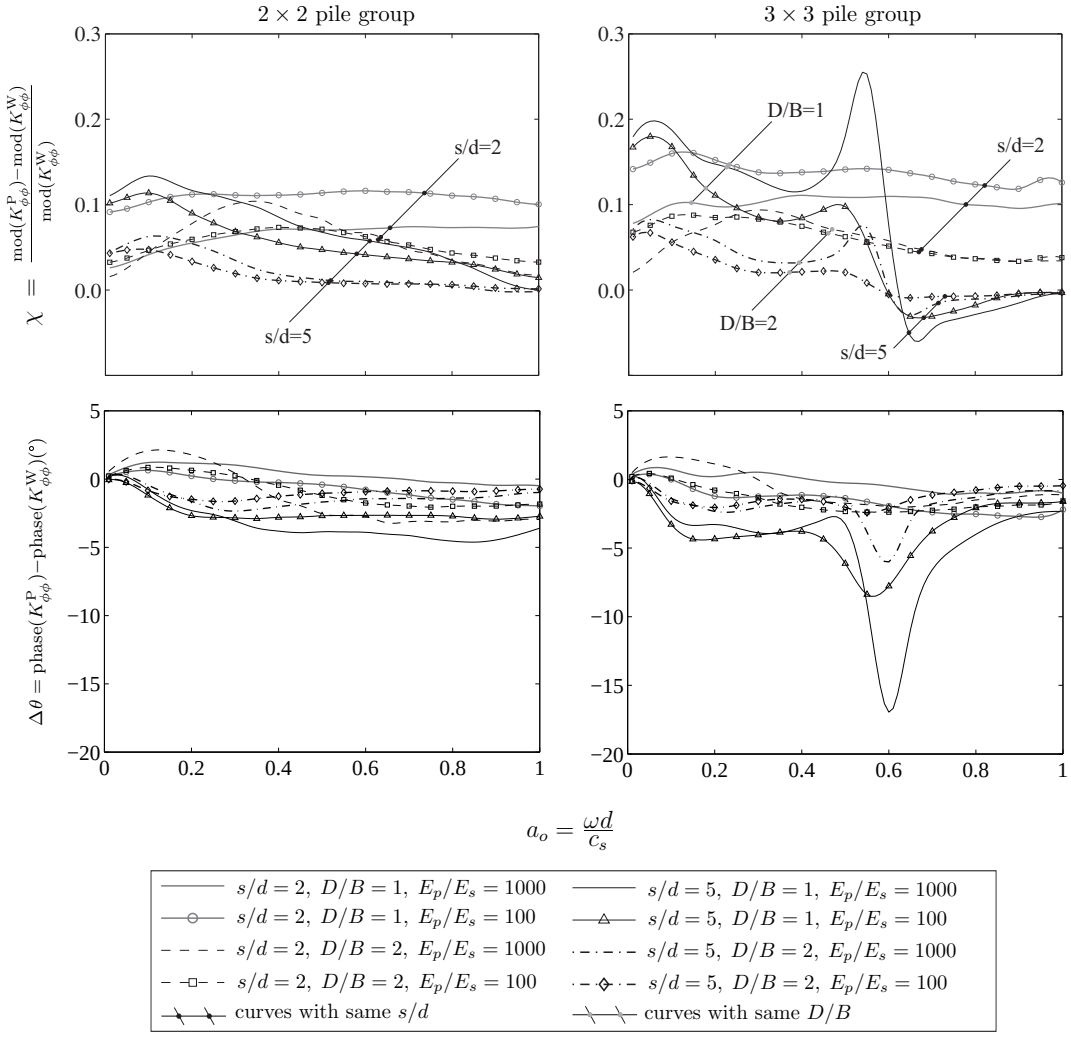

Figure 5.5: *Comparison between modulus and phase of rocking impedances of embedded footings on piles, obtained rigorously, $K^P_{\phi\phi}$ and by superposition $K^W_{\phi\phi}$.*

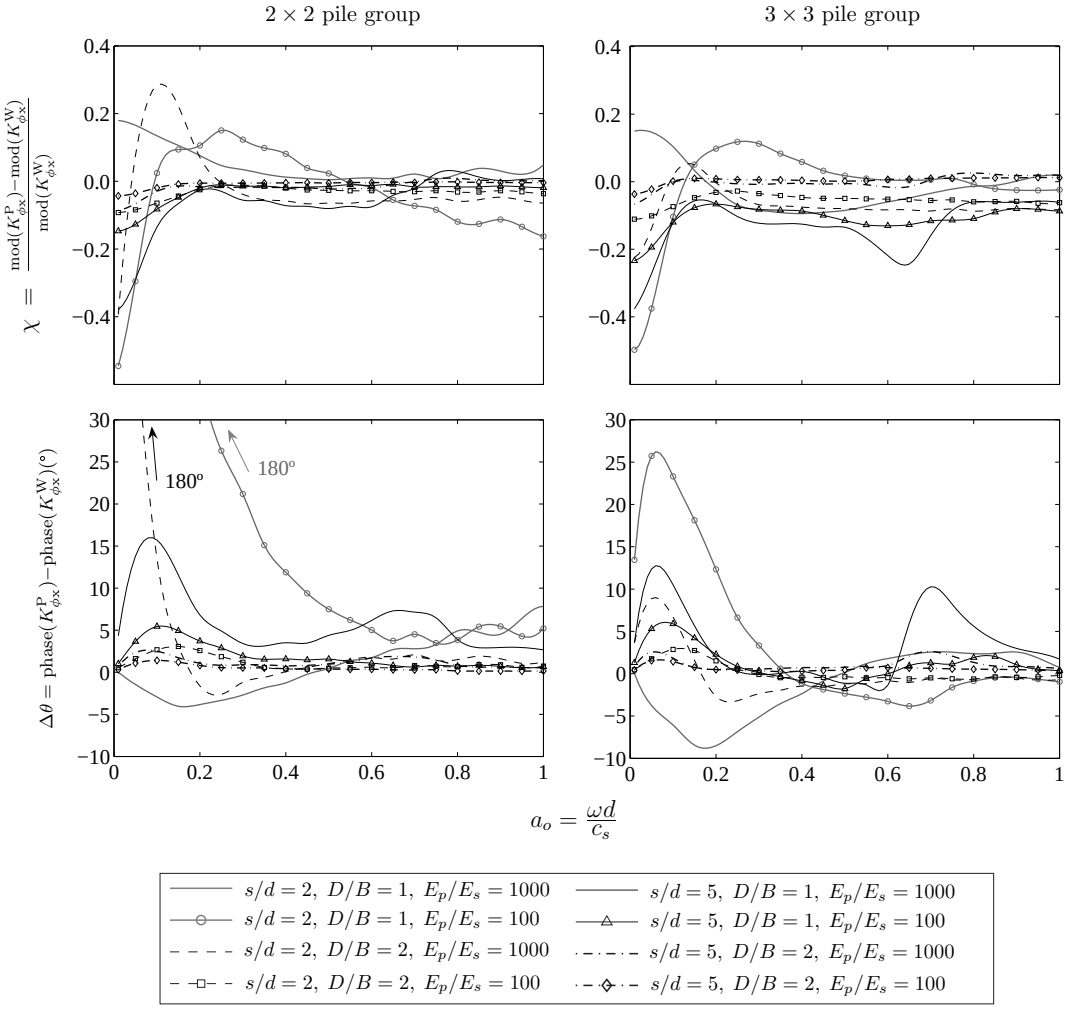

Figure 5.6: *Comparison between modulus and phase of cross-coupled horizontal-rocking impedances of embedded footings on piles, obtained rigorously, $K^P_{\phi\mathrm{x}}$ and by superposition $K^W_{\phi\mathrm{x}}$.*

two methods are shown in figs. 5.3 to 5.6, where the vertical, horizontal, rocking and cross-coupled horizontal-rocking modes, respectively, are depicted. As impedances are complex-valued functions of frequency, the comparisons are presented in terms of dimensionless real valued relative difference of moduli (χ) and phase in degrees ($\Delta\Theta$) versus dimensionless frequency a_o. Thus, the modulus and phase of the complex valued dynamic stiffness functions of a complete pile group – embedded foundation system can be estimated with the help of the aforementioned plots in terms of eqs. 5.1 and 5.2.

$$\mathrm{mod}(K^W) = \frac{\mathrm{mod}(K^P)}{1+\chi} \tag{5.1}$$

$$\mathrm{phase}(K^W) = \mathrm{phase}(K^P) - \Delta\Theta \tag{5.2}$$

where

$$\mathrm{mod}(K) = \sqrt{k^2 + (a_o c)^2} \tag{5.3}$$

$$\mathrm{phase}(K) = \arctan\left(\frac{-k}{a_o c}\right) + \frac{\pi}{2} \tag{5.4}$$

Evidently, the limits $\chi \to 0$ and $\Theta \to 0$ indicate insignificant interaction between embedded footing and pile group, whereas $\chi \to -1$ or $\chi \to \infty$ and $\Theta \to \pm\pi$ suggest dominant interaction effects.

Different trends can be observed for each oscillation mode. The parameters s/d and n appear to govern the difference of vertical impedances though relative pile-soil stiffness and embedment ratio are also relevant. The difference decreases for narrowly spaced large pile groups, high relative pile-soil stiffness and high embedment ratios. As for the horizontal mode, χ and $\Delta\Theta$ are practically independent of n and decrease for narrowly spaced piles and high embedment ratios. On the other hand, the embedment ratio governs the difference of rocking impedances, which decreases with increasing D/B, though it can also be seen that the difference is smaller for small size pile groups. In this case, $\Delta\Theta$ is, except for a few cases in high frequency conditions, smaller than 5^o, which, from a practical viewpoint, can be neglected. It is also observed that the difference in the coupled term is independent of n and is not significant for highly spaced pile groups and high embedment ratios, and that a greater variability in the results exists compared to the other impedance functions. Note that $\Delta\Theta$ tends to 180^o as a_o goes to zero in some cases, because $K^W_{\phi x}$ and $K^P_{\phi x}$ have opposite signs for static conditions. The decrease in χ with an increase in embedment ratio is a common trend to all oscillation modes. Another interesting observation is the increase of χ and $\Delta\Theta$ at frequencies for which the group effect makes the pile foundation stiffer. This is

due to the fact that the interaction between both types of foundation reduces the contribution of the pile group at such frequencies when analysing the system as a whole. On the other hand, $\Delta\Theta$ is always negative in the vertical and horizontal cases at low frequencies, which suggests a higher damping capacity of the pile-reinforced footing than that estimated by superposition. Approximate estimates of $\Delta\Theta$ for the vertical, horizontal and rocking modes can be obtained from the regression formulas of table 5.1.

Rocking		0
Horizontal		$197a_o^2 - 75a_o - 0.06$
Vertical	2×2	$(s/d)^{0.62}215a_o^2 - (s/d)^{0.17}58a_o$
	3×3	$446a_o^2 - 111a_o - 0.3$

Table 5.1: *Approximate expressions for* $\Delta\Theta$ $(^o)$

5.3.2 Kinematic interaction factors

Moduli of translational and rotational kinematic response functions I_U and I_ϕ, respectively, of 2×2 and 3×3 piled embedded footings, pile groups and embedded footings under vertically-incident plane shear waves are shown in figs. 5.7 and 5.8 for $s/d = 2$ and 5, respectively. Both factors are measured at pile cap level (point A in fig. 5.1) and are normalized with the free-field motion at the surface, u_{ff} both being functions of the dimensionless frequency $a_o = \omega d/c_s$, as expressed in eqs. 5.5 and 5.6:

$$I_U = I_U(a_o) = \frac{u_A}{u_{ff}} \tag{5.5}$$

$$I_\phi = I_\phi(a_o) = \frac{\Theta_A B}{u_{ff}} \tag{5.6}$$

Note that all functions are plotted against the dimensionless frequency a_o referred to pile diameter, even though kinematic response functions for footings are usually plotted with a dimensionless frequency proportional to the width of the footing (i.e. $a_o' = \omega B/c_s$). In this case, the change in scale is linear as $B/d = (n/2)(s/d)$, which can be used to interpret the results in the alternative way.

For $a_o < 0.2$, a frequency range of importance in earthquake engineering, the pile group considered alone tends to follow the movement of the soil, having a translational kinematic response coefficient of approximately one. On the

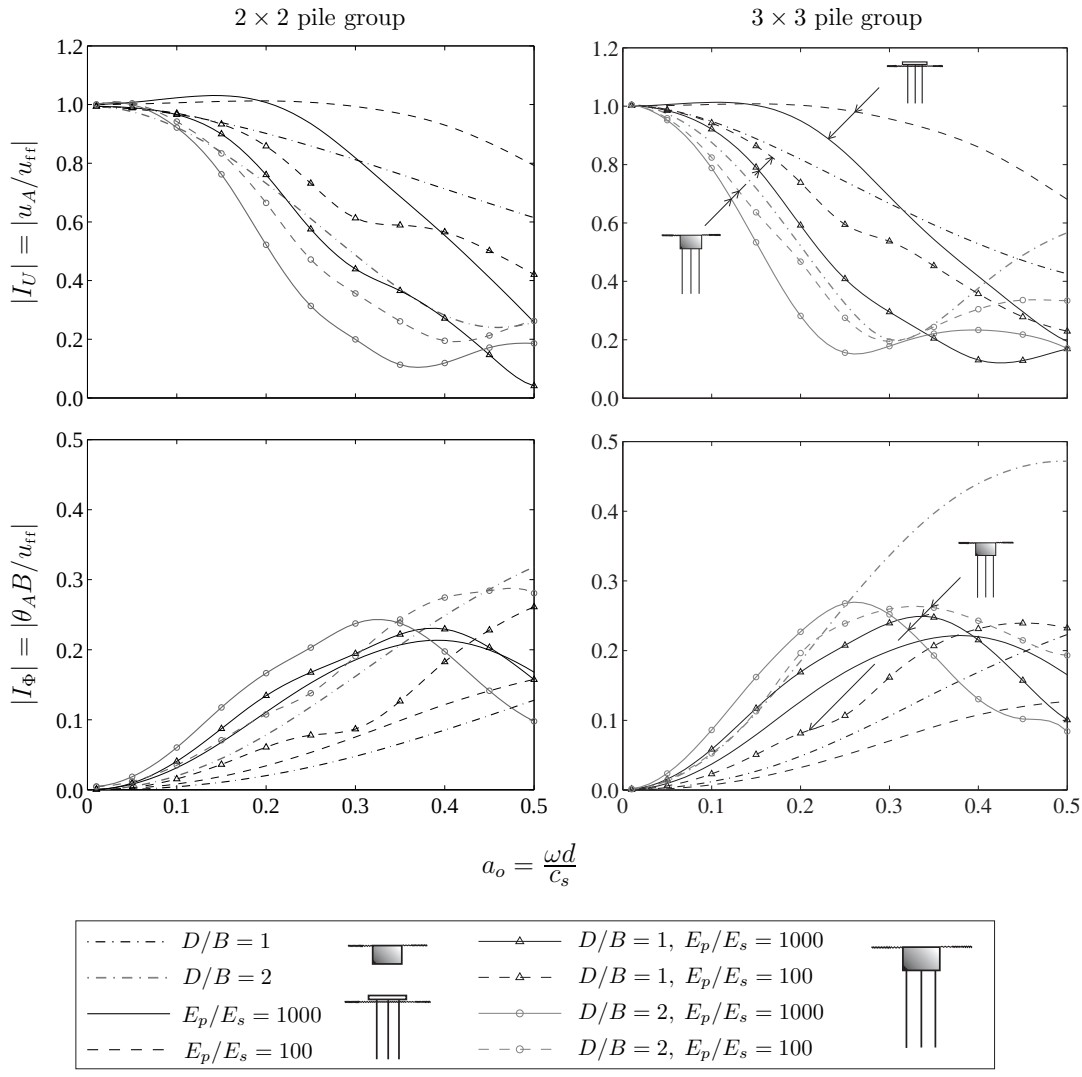

Figure 5.7: *Moduli of translational and rotational kinematic interaction factors for embedded footings, pile groups and embedded footings on pile groups under vertically incident SH waves.* $s/d = 2$.

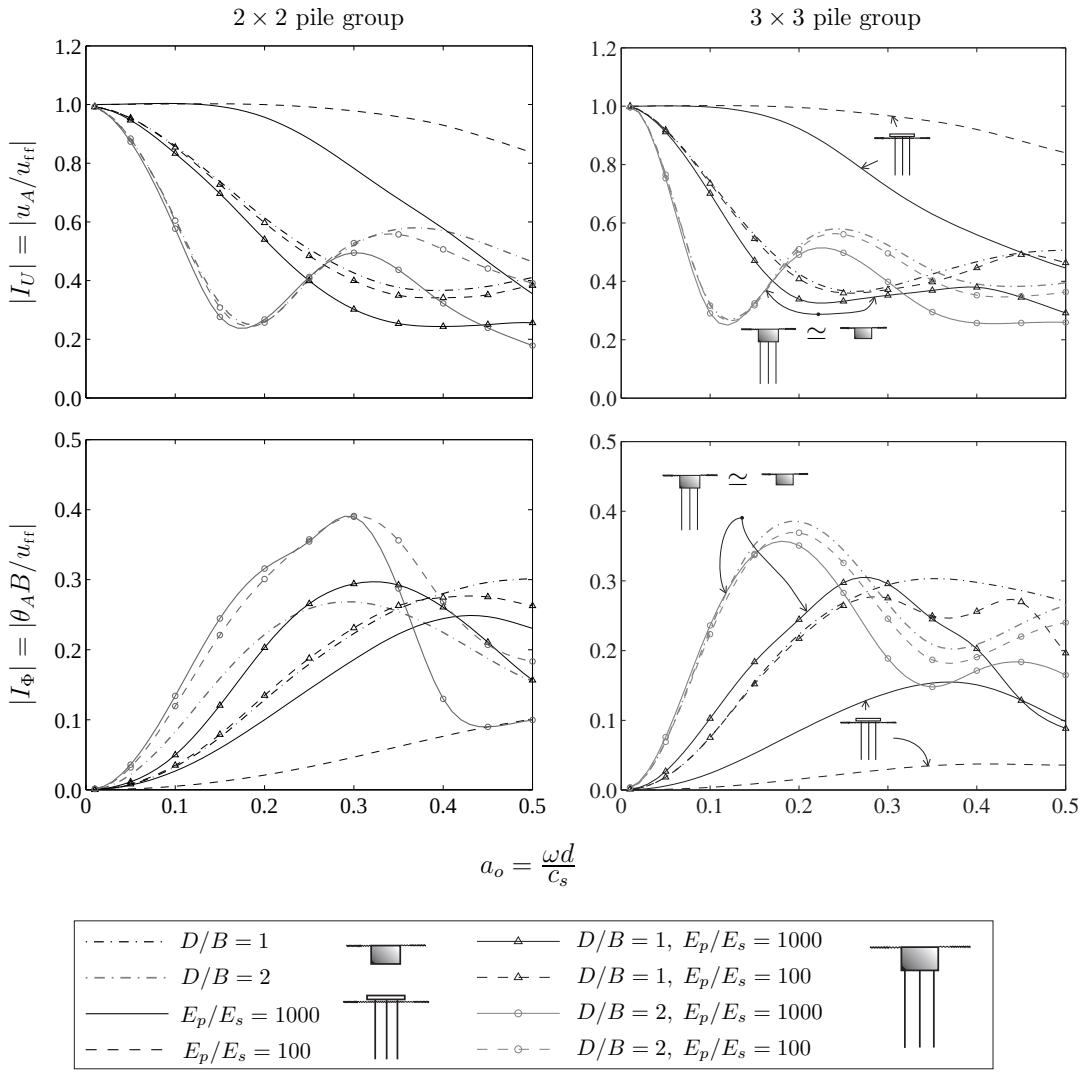

Figure 5.8: *Moduli of translational and rotational kinematic interaction factors for embedded footings, pile groups and embedded footings on pile groups under vertically incident SH waves.* $s/d = 5$.

contrary, the piled embedded footing exhibits strong kinematic effects, as its displacements are smaller than those of the pile group and its rotations larger. For amply spaced groups ($s/d = 5$, fig. 5.8), the embedded footing response is an excellent approximation of the piled footing response. On the other hand, for closely spaced groups ($s/d = 2$, fig. 5.7), the approximation is not as accurate, being slightly conservative for the translational case, but non-conservative for the rotational one. These features should be recognized when analysing tall structures for which the rotational behaviour of the foundation is important.

5.4 Importance of footing-soil separation on dynamic stiffness functions of piled embedded footings

In this section, the influence of footing-soil separation at the base of a rigid piled embedded footing on dynamic stiffness and damping is assessed. The problem is illustrated in fig. 5.9, where the geometry of an embedded footing on piles with footing-soil separation at the base is depicted. Note that the opening of the gap between soil and pile cap is not defined, as re-establishment of contact during dynamic response is not considered. In this study, fully bonded contact conditions are considered in the vertical interfaces between soil and footing, and soil and pile. The gap between soil and the underside of the footing is modelled by pertinent zero-traction boundary conditions on the horizontal interface.

The relation between complex impedance functions of piled embedded footings considering either a gap (K^G) or bonded contact conditions (K^B) between soil and footing underside is determined for different oscillation modes. Differences in modulus and phase of the impedance functions are presented in terms of the following real-valued parameters:

$$\chi_G = \frac{\mathrm{mod}(K^B) - \mathrm{mod}(K^G)}{\mathrm{mod}(K^B)} \tag{5.7}$$

$$\Theta_G = \mathrm{phase}(K^B) - \mathrm{phase}(K^G) \tag{5.8}$$

Evidently, the limits $\chi_G \to 0$ and $\Theta_G \to 0$ indicate an insignificant effect of separation on the impedances, whereas $\chi_G \to \pm 1$ and $\Theta_G \to \pm\pi$ suggest a dominant influence of gapping.

Results are shown in figs. 5.10, 5.11 and 5.12 for vertical, horizontal and rocking oscillations, respectively. It can be observed that the differences between impedance functions for separated and bonded conditions are negligible for frequencies below those for which dynamic group effects start making the system

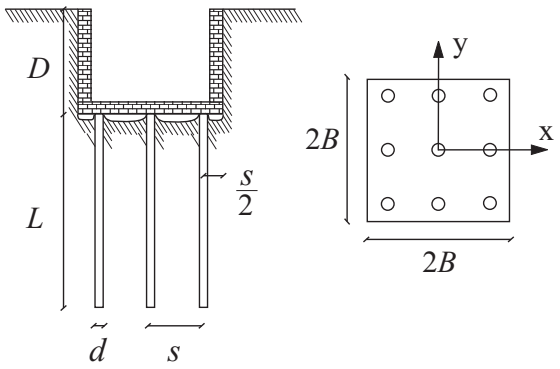

Figure 5.9: *Geometry of an embedded footing on piles with footing-soil separation at the base.*

stiffer. Hence, for closely spaced groups ($s/d = 2$), differences are almost zero for $a_o < 1$. For larger pile spacings ($s/d = 5$), they become significant for $a_o > 0.25$ in the vertical mode and for $a_o > 0.4$ in the horizontal and rocking modes. These threshold frequencies are in accord with those reported for dynamic group effects [51, 90]. Interestingly, these differences can be either positive or negative, that is, gap may decrease or increase the stiffness of the system, due to wave interference, depending on excitation frequency. The effect of separation is, naturally, more noticeable in the vertical mode and may decrease the stiffness of the system by 50% beyond $a_o = 0.5$. On the other hand, the change in stiffness in the lateral mode is smaller and does not exceed a mere 20%.

An important issue relates to the redistribution of the relative contributions of piles and footing to overall stiffness, so that the difference between K^G and K^B is negligible at low frequencies. To investigate this, fig. 5.13 shows a comparison between the impedance functions of simple embedded footings whose piles have been removed (termed unpiled footing), and the contribution of the footing to the stiffness of a ground-contacting piled footing for different embedment ratios, $E_p/E_s = 1000$ and $s/d = 5$. As expected, the stiffness of the un-piled footing is higher than its contribution to the overall stiffness in a pile foundation. On the other hand, fig. 5.14 compares the impedance functions of a 2×2 pile group with a cap at ground surface level and the contribution of the pile group to the stiffness of a ground-contacting piled footing for the same embedment ratios ($E_p/E_s = 1000$ and $s/d = 5$). In this case, the static stiffness of the ground-raised cap pile group is twice the contribution of the pile group to the overall stiffness of a piled ground-contacting foundation. Then, when a gap develops at the underside of a piled footing, the loss of stiffness of the footing is counterbalanced by the increase in stiffness of the pile group.

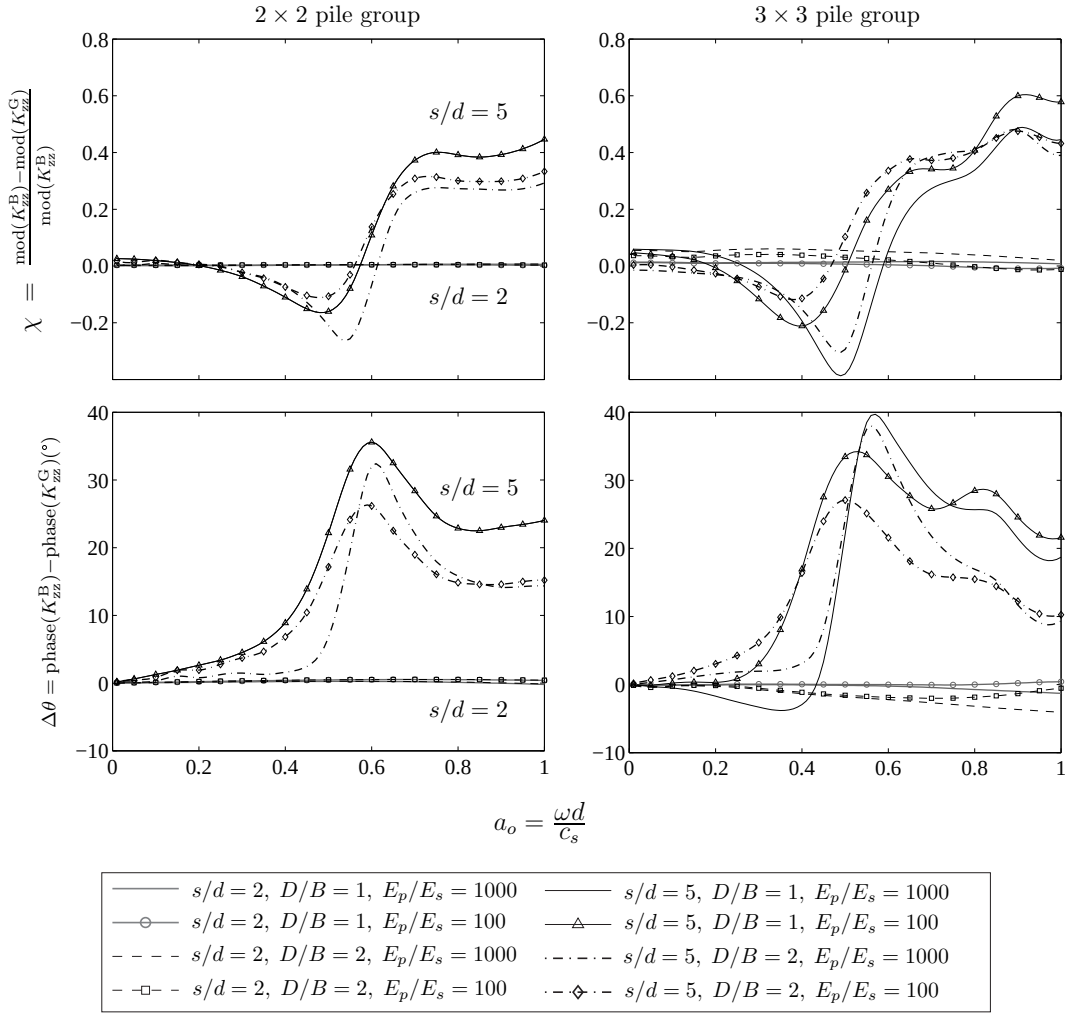

Figure 5.10: *Comparison between modulus and phase of vertical dynamic stiffnesses of embedded footings on piles considering a gap (K_{zz}^G) or bonded contact conditions (K_{zz}^B) between soil and footing underside.*

Moreover, fig. 5.14 shows that the contribution of the pile group to the overall stiffness of the piled footing is independent of embedment ratio. This suggests that the impedance functions of a pile group are governed by the boundary conditions at the surface immediately above the cap, which should be taken into account when estimating impedances of piled footings by superposition.

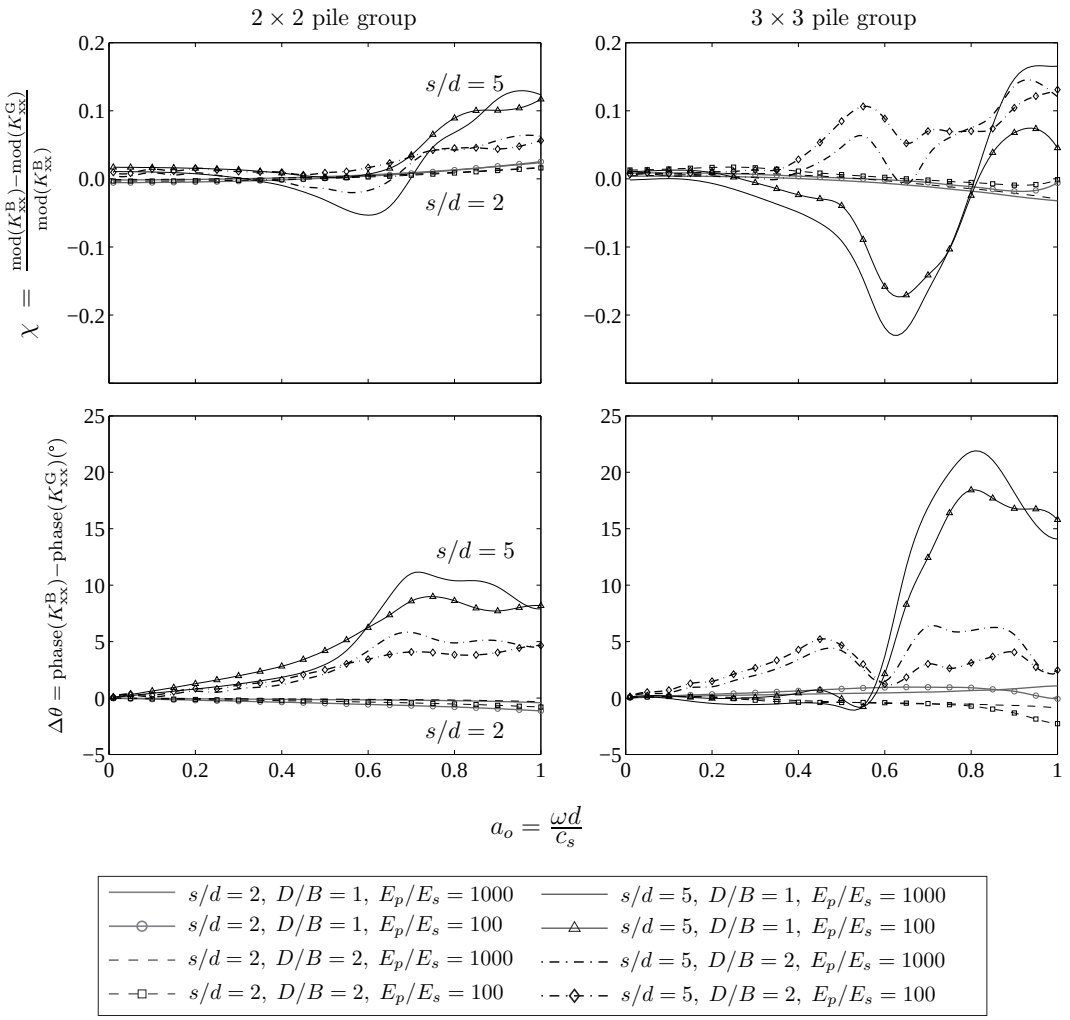

Figure 5.11: *Comparison between modulus and phase of horizontal dynamic stiffnesses of embedded footings on piles considering a gap (K^G_{xx}) or bonded contact conditions (K^B_{xx}) between soil and footing underside.*

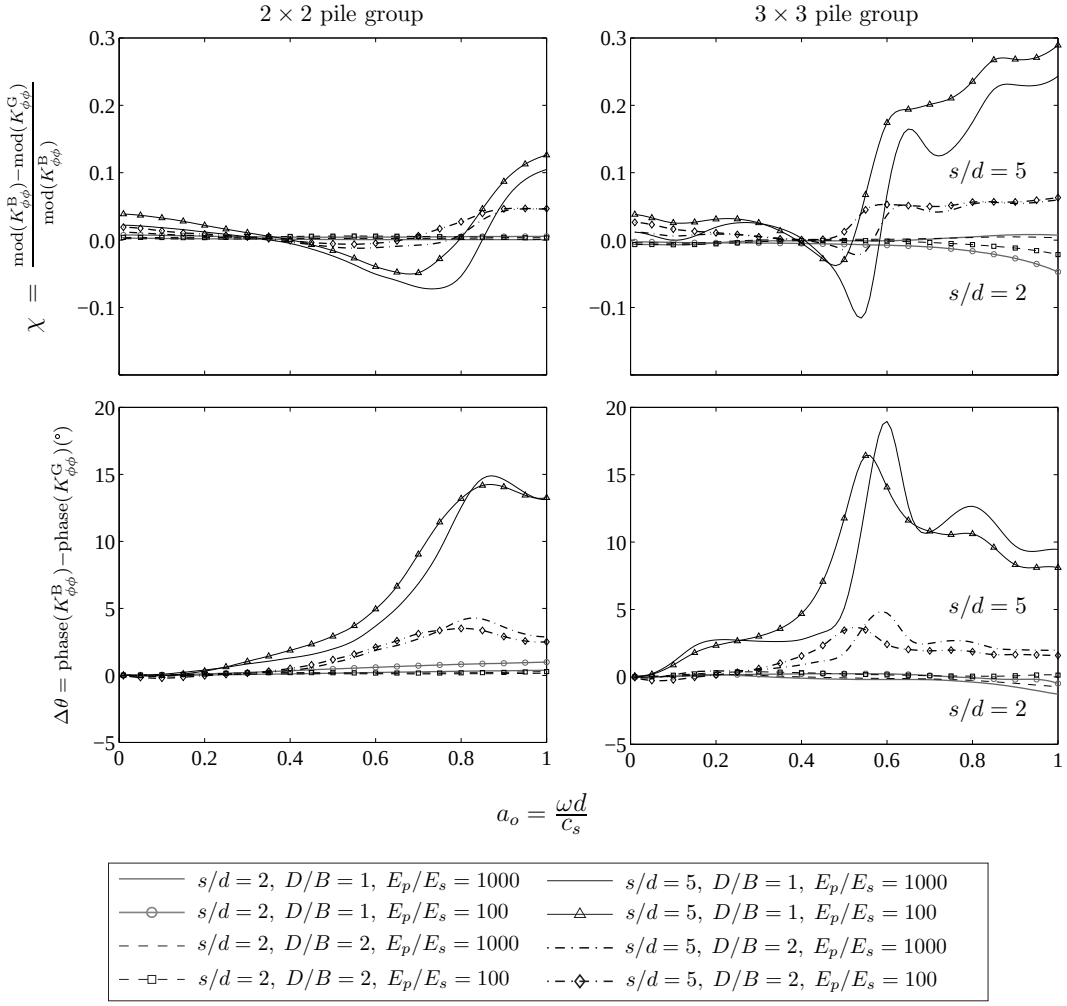

Figure 5.12: *Comparison between modulus and phase of rocking dynamic stiffnesses of embedded footings on piles considering a gap ($K^G_{\phi\phi}$) or bonded contact conditions ($K^B_{\phi\phi}$) between soil and footing underside.*

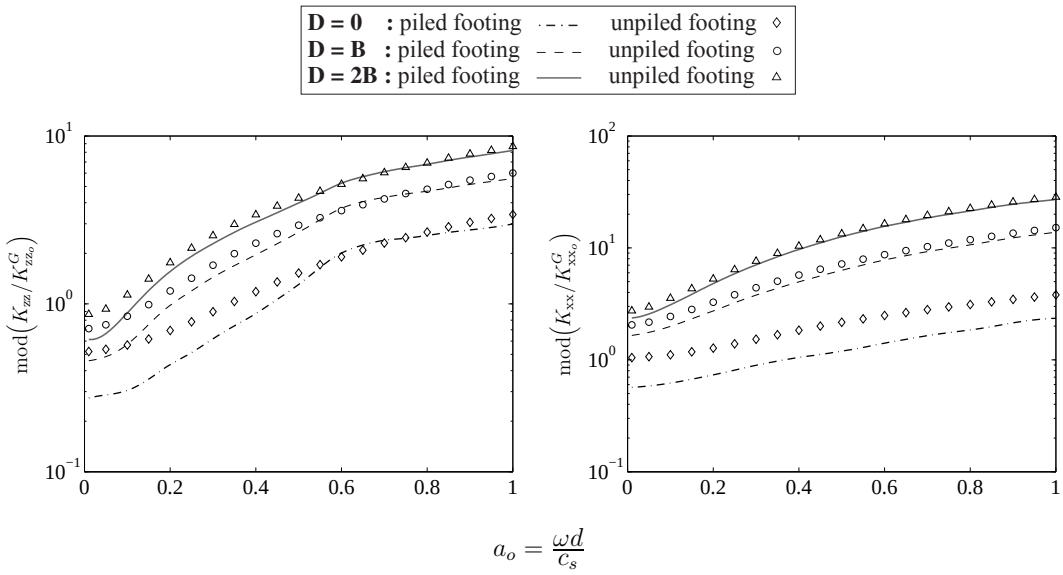

Figure 5.13: *Comparison between the dynamic stiffnesses of unpiled footings and the contribution of the footing to the impedance function of a ground-contacting piled footing for different embedments.* $E_p/E_s = 1000$, $s/d = 5$.

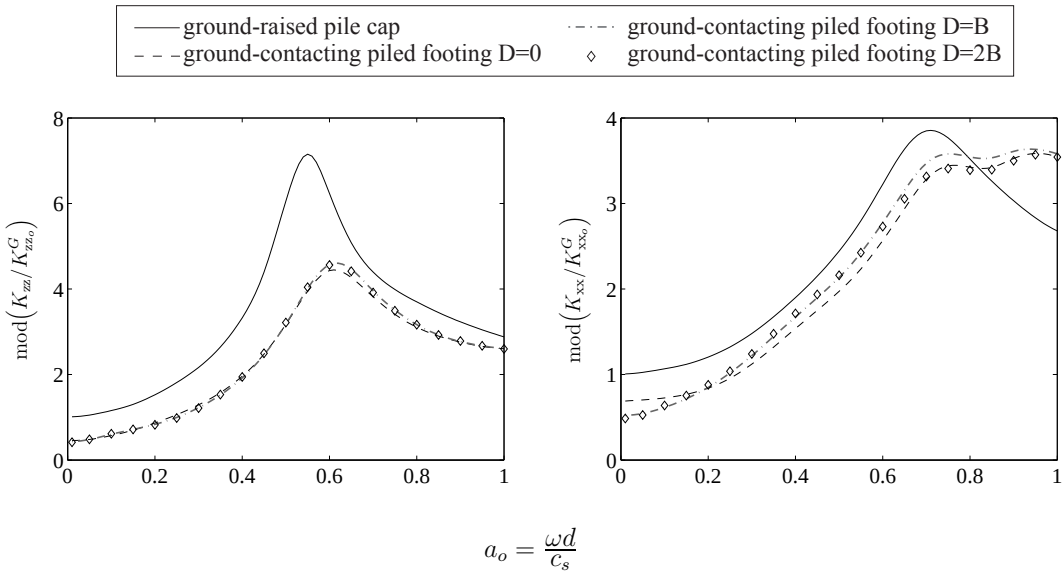

Figure 5.14: *Comparison between the dynamic stiffnesses of a ground-raised-cap* 2×2 *pile group and the contribution of the pile group to the impedance function of a ground-contacting piled footing for different embedments.* $E_p/E_s = 1000$, $s/d = 5$.

5.5 Conclusions

It has been shown that the impedances obtained by superposition of pile group and footing stiffness functions are generally higher than that arising from the analysis of the system as a single problem. This difference can be attributed to interaction phenomena between the pile group and the embedded footing, which are neglected in the superposition approach. More precisely, vertical, horizontal, rocking and cross-coupled terms can be up to 100%, 50%, 20% and 20% higher, respectively, though differences decrease rapidly with frequency. On the other hand, phase differences are normally below 20^o and denote that the damping capacity of the system acting as a whole is greater than that estimated from the superposition. This effect is particularly apparent in the vertical and horizontal mode and at low frequencies. Besides, the dependence of the response to parameters such as separation between adjacent piles and pile-soil stiffness ratio was elucidated. The effect of embedment was shown to be particularly important, for it was observed that the more embedment, the smaller the difference between rigorous and superposition-based estimates. This trend can be understood given the omission of embedment effects in the assessment of pile group impedance. Overall, the superposition approach was found to be sound as an engineering tool, with average discrepancies not exceeding 20%.

Regarding kinematic effects, piled embedded footings were found to be less compliant to the soil movement than their parts analysed separately. Translational kinematic response factors decrease faster with frequency than those corresponding to pile groups or footings alone, while rotational kinematic interaction factors were found to increase more rapidly. Overall, kinematic response of embedded footings has been found to provide suitable estimates of the piled embedded footings behaviour.

As for the importance of footing-soil separation on dynamic stiffness functions of piled embedded footings, it was demonstrated that

- The influence of separation is negligible for frequencies below those for which dynamic group effects start becoming apparent.

- The effect of separation is more noticeable in the vertical mode and may decrease the stiffness of the system by 50% beyond $a_o = 0.5$. On the other hand, the change in stiffness is minimized in the lateral mode and does not exceed 20%.

- The overall stiffness of the foundation when no separation exists is not necessarily higher than that corresponding to the system after soil consolidation. The relationship between the dynamic stiffness in both cases depends on the

constructive and destructive interference of the waves generated at the pile-soil and the footing-soil interfaces, and, therefore, is frequency-dependent.

- A counterbalance between footing and pile group stiffness contributions was found to exist under loss of soil-pile cap contact.
- The contribution of the pile group to the overall stiffness of the system is independent of embedment, although it depends on the ground-cap contact condition, i.e., changes between ground-raised and ground-contacting caps. This property can be used to simplify the models when estimating the impedance functions of piled footings by superposition approaches.

Chapter 6

SSI analysis of pile supported structures by substructuring

6.1 Introduction

Dynamic stiffness functions and kinematic interaction factors of foundations, as those obtained in previous chapters, are commonly used to predict the seismic behaviour of structures taking Soil-Structure Interaction (SSI) effects into account. This is achieved through the use of more or less elaborated *substructure models* in which the soil is replaced by springs and dashpots representing the soil stiffness and damping. Besides, the seismic input motion to be used in the substructure model can be significantly modified by the presence of the foundation into the soil. Therefore, in many occasions, the foundation input motion should be computed taking into account these kinematic interaction effects.

Direct approaches, modelling the main aspects of the problem and their mutual interactions more rigorously, constitute a more precise way of analysing the system response when SSI effects can be of importance. However, these models are both more complex and more demanding from the computational point of view, and are consequently not frequently used for the analysis of this kind of problems. The direct model for the dynamic analysis of pile supported structures that was presented in chapter 3 will be used in the next chapter to analyse the interaction phenomena between nearby structures, problem for which the use of direct approaches is almost mandatory.

This chapter, on the contrary, exploits the advantages of the substructure methodology. This methodology is simple and easy to implement, provides accurate results for the kind of problems addressed in this chapter, and at the same time allows performing parametric analyses with very little computational effort (provided that impedance functions and kinematic interaction factors are previously known). Firstly, the problem under investigation is defined in section 6.2.

Then, the substructure model to be employed throughout the rest of the chapter is presented in section 6.3, where its equations of motion are also derived. The set of dimensionless parameters chosen to define the investigated systems are listed in section 6.4. Finally, section 6.5 presents the algorithm used to perform the parametric analyses of which the results are shown in section 6.6.

6.2 Problem definition

This chapter focuses on the dynamic response of linear shear structures that behave mainly as single-degree-of-freedom systems in their fixed-base condition. This model may correspond either to one-storey buildings or to the fixed-base fundamental mode of vibration of multi-storey multi-mode structures. Several authors [86, 158] highlight the fact that SSI affects primary to the fundamental mode of vibration of multi-storey structures, justifying this way the use of this simplified approach. This way, their dynamic behaviour can be defined by their fixed-base fundamental period T, the height h of the resultant of the inertia forces for the first mode, the mass m participating in this mode, and the corresponding structural damping ratio ζ (see fig. 6.1). The horizontal stiffness of the structure is $k = 4\pi^2 m/T^2$, and hysteretic material damping is considered for the structural piers through a complex valued stiffness of the type $k = Re[k](1 + 2i\zeta)$.

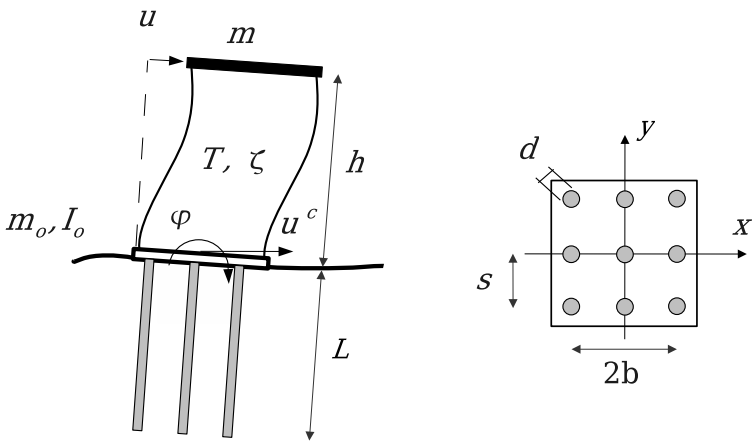

Figure 6.1: *Problem definition.*

Simultaneously, these super-structures are considered to be founded on a square pile group embedded in a viscoelastic half-space, as depicted in fig. 6.1, being the pile group defined by length L and sectional diameter d of piles, centre-to-centre spacing between adjacent piles s, cap mass m_o, and cap moment of

inertia about a horizontal axis passing through the centre of gravity of the cap I_o. b is the foundation halfwidth.

If soil-structure interaction is taken into account, the system behaviour can be approximated by that of a three-degree-of-freedom system, defined by the foundation horizontal displacement u^c and rocking φ, together with the structural horizontal deflection u. (Note that rocking of pile cap and structure are identical). Vertical motions are neglected in this study.

6.3 Substructure model

This problem can be studied by means of a substructure approach, in which the system is subdivided into *building-cap* substructure and *soil-foundation* stiffness and damping, represented by means of springs and dashpots, as shown in fig. 6.2. The system is then subjected to the kinematic pile cap motion, *i.e.* the response of the foundation alone, considering a massless cap, to the incident seismic waves, as computed in chapter 5. Note that the horizontal u_r^c and rocking φ_r motions of the foundation are here defined as relative to the foundation input motions.

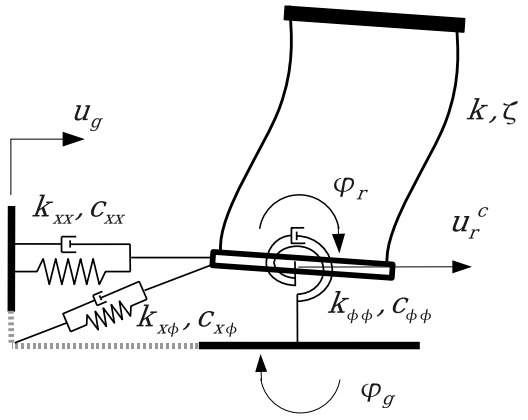

Figure 6.2: *Substructure model of a one-storey structure.*

The complex-valued frequency-dependent functions (k_{xx}, c_{xx}), $(k_{\phi\phi}, c_{\phi\phi})$ and $(k_{x\phi}, c_{x\phi})$ represent the stiffness and damping of the soil in the horizontal, rocking and cross-coupled horizontal-rocking vibration modes, respectively. Even though the cross-coupled terms $(k_{x\phi}, c_{x\phi})$ and $(k_{\phi x}, c_{\phi x})$, which should be identical, are not exactly equal to one another when computed numerically, the difference is small for practical purposes, and they are considered identical in this approach. $(k_{x\phi}, c_{x\phi})$ functions usually show oscillations of numerical nature, while $(k_{\phi x}, c_{\phi x})$

functions tend to be smoother. For this reason, these last terms are the ones usually selected for the analyses presented in this chapter.

As for the seismic input, incident fields produce, in general, both horizontal and rocking motions in any foundation element. In the present case of deep foundations, even vertically incident S waves in a half-space (for which the free-field motion at the ground surface is exclusively horizontal) generate rocking kinematic response at the pile cap. For this reason, both horizontal u_g and rocking φ_g foundation input motions are specified at the base of the structure and, unless otherwise specified, they will be always computed taking kinematic interaction effects into account.

Hence, the equations of motion of the system shown in fig. 6.2, assuming small displacements, can be written in terms of relative motions as

$$m(\ddot{u} + \ddot{u}_r^c + \ddot{u}_g + h(\ddot{\varphi}_r + \ddot{\varphi}_g)) + k\,u = 0 \quad (6.1)$$

$$m(\ddot{u} + \ddot{u}_r^c + \ddot{u}_g + h(\ddot{\varphi}_r + \ddot{\varphi}_g)) + k_{xx}\,u_r^c + k_{x\phi}\varphi + m_o(\ddot{u}_r^c + \ddot{u}_g) = 0 \quad (6.2)$$

$$h\,m(\ddot{u} + \ddot{u}_r^c + \ddot{u}_g + h(\ddot{\varphi}_r + \ddot{\varphi}_g)) + k_{\phi x}\,u_r^c + k_{\phi\phi}\varphi + I_o(\ddot{\varphi}_r + \ddot{\varphi}_g) = 0 \quad (6.3)$$

where eq. (6.1) represents the horizontal force equilibrium of the structure, eq. (6.2) the horizontal force equilibrium of the structure-foundation system and eq. (6.3) the moment equilibrium of the structure-foundation system about a horizontal axis passing through the centre of gravity of the pile cap. This set of equations can be expressed in a matrix form as

$$\begin{bmatrix} k-\omega^2 m & -\omega^2 m & -\omega^2 m\,h \\ -\omega^2 m & k_{xx}-\omega^2(m+m_o) & k_{x\phi}-\omega^2 m\,h \\ -\omega^2 m\,h & k_{\phi x}-\omega^2 m\,h & k_{\phi\phi}-\omega^2 m\,h^2 - I_o \end{bmatrix} \begin{bmatrix} u \\ u_r^c \\ \varphi_r \end{bmatrix} = \omega^2 \begin{bmatrix} m \\ m+m_o \\ m\,h \end{bmatrix} u_g + \omega^2 \begin{bmatrix} m\,h \\ m\,h \\ m\,h^2 + I_o \end{bmatrix} \varphi_g \quad (6.4)$$

where ω is the excitation frequency and motions have been assumed to be time-harmonic of the type $u(t) = u\,e^{\mathrm{i}\omega t}$. Once the foundation input motion is computed, the right-hand vector and the coefficient matrix are known, and structural deflection and foundation relative motions can be computed for every frequency.

6.4 Dimensionless parameters

A specific set of dimensionless parameters, covering the main features of SSI problems, has been repeatedly used in the related literature to perform parametric

analyses [82, 86, 87, 159]. Following these authors, the parameters that will be used herein to characterize the soil-foundation-structure system are:

1. The wave parameter $\tau = h/(c_s T)$, measuring the structure-soil relative stiffness.

2. The slenderness ratio h/b, measuring the relation between structure height and foundation half-width.

3. The mass density ratio $\gamma = m/(4\rho b^2 h)$ between structure and supporting soil.

4. The foundation-structure mass ratio m_o/m.

5. The foundation-structure mass moment of inertia ratio $I_o/(m\,h^2)$.

6. The fixed-base structure damping ratio ζ.

7. Poisson's ratio ν_s and damping ratio β of the soil.

8. The excitation frequency, that can be expressed by means of the ratio T/T_o, where T_o is the excitation period.

On the other hand, the pile foundations are defined using the dimensionless parameters already explained in the previous chapters. Most results presented in this chapter correspond to the following values: pile-soil stiffness ratios $E_p/E_s = 100$ and 1000; soil-pile density ratio $\rho_s/\rho_p = 0.7$; piles aspect ratio $L/d = 15$; soil damping coefficient $\beta = 0.05$; and Poisson's ratio of the soil $\nu_s = 0.4$.

6.5 Solution procedure

Harmonic response spectra of the soil-structure system can be obtained by solving the system of equations (6.4) for several values of the excitation frequency within a certain range. One example is shown in fig. 6.3, where the fixed-base and flexible-base response of a soil-foundation-structure system, subjected to vertically incident S waves, are shown. Apart from those defined before, the system properties are: $\tau = 0.1$, $h/b = 1$, $\gamma = 0.2$, $m_o/m = 0.25$, $\zeta = 0.05$, $I_o/(mh^2) = 0.05$, $E_p/E_s = 10^3$ and $s/d = 2$. The seismic response of the structures is presented in terms of its lateral deformation response spectra Q, defined as $\mathrm{Abs}[\Omega^2 u/\omega^2 u_{ff}]$, where $\Omega = 2\pi/T$ is the fundamental frequency of the fixed-base structure, ω is the excitation frequency and u_{ff} is the horizontal free-field motion at the ground surface. The usefulness of this variable comes from the fact that the product of this value with the structural mass and the corresponding free-field horizontal

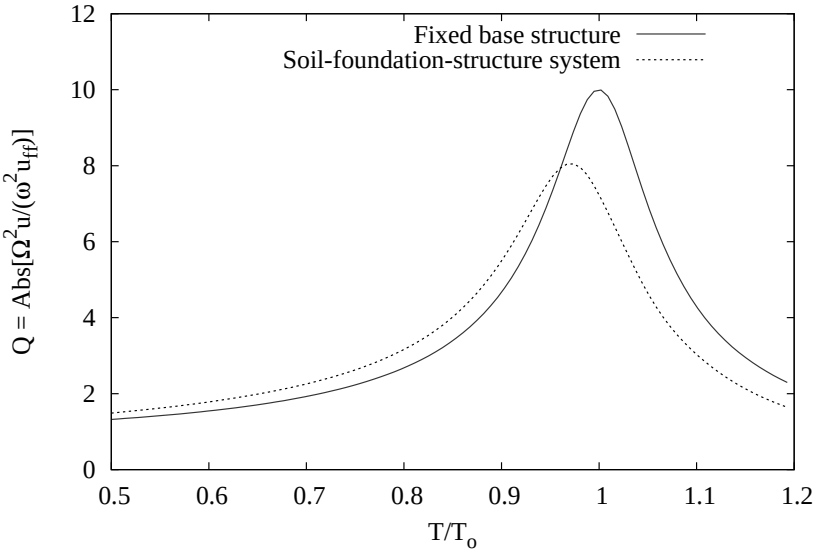

Figure 6.3: *Harmonic response spectra of fixed-base and flexible-base structures founded on a* 2×2 *pile group*

acceleration at ground surface level yields the amplitude of the shear force at the base of the structure.

Relevant information about the influence of soil compliance and foundation configuration on the seismic behaviour of the system can be inferred from this kind of spectra. Consider the harmonic response spectra of a flexible-base one-storey shear structure for different values of τ, as shown in fig. 6.4. The values of all system parameters are identical to those of the previous example, except that a 3×3 pile group with $s/d = 5$ is now used, and that two slenderness ratios, $h/b = 2$ and 3, are presented. It can be seen that the system response changes for different structure-soil relative stiffness ratios τ. However, while the variation of the system resonant period is similar in both cases, the variation of the maximum value of Q is quite different. For $h/b = 3$, the magnitude of the maximum response tends to grow as τ increases, while for $h/b = 2$, the tendency is just the opposite, except for $\tau = 0.2$. As the magnitude of the maximum response can be related to the system damping, it can be inferred that the overall system damping at the resonant period increases with τ for $h/b = 2$ but decreases for $h/b = 3$. As already pointed out by Veletsos and Meek [82], this fact can be understood in terms of the existence of two opposite phenomena:

- On the one hand, the higher the structure-soil relative stiffness ratio τ, the more the soil deformation around the foundation and the mass of soil

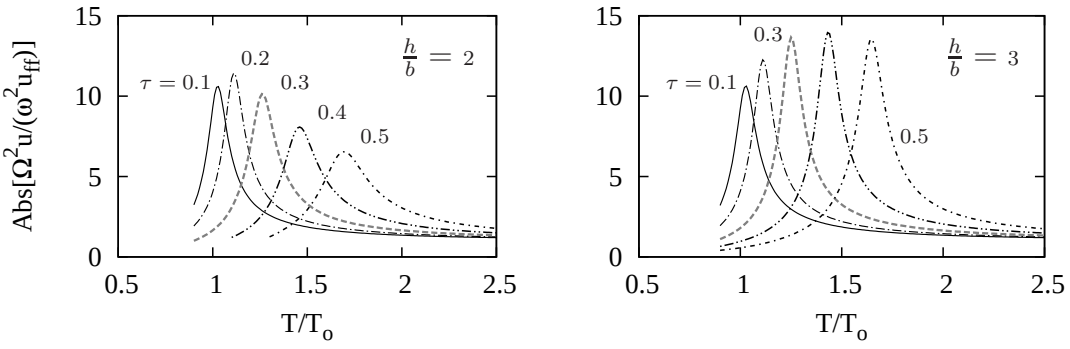

Figure 6.4: *Harmonic response spectra of a single-degree-of-freedom system on a* 3×3 *pile group*

affected by the scattered field produced by the structure. Consequently, more energy from the structure vibration will be dissipated in terms of internal and radiation damping in the soil, leading to a decrease in the structural response.

- On the other hand, the higher the parameter τ, the higher the foundation rocking and, therefore, the inertia forces at mass m, leading to an increase in the structural response. Obviously, the higher the structure, the more important this effect becomes in the overall behaviour of the system, explaining why equivalent damping ratios tend to be smaller for higher structures.

In short, the most important pieces of information offered by harmonic response spectra are:

- the variation of the system resonant period, and
- the magnitude of the system maximum response.

The first parameter can be expressed by the ratio $\tilde{T}/T$, where $\tilde{T}$ is the soil-foundation-structure system fundamental period, while the second piece of information can be related to the damping ratio $\tilde{\zeta}$ of an equivalent single-degree-of-freedom oscillator, as that shown in fig. 6.5 (see *e.g.* [82, 87]). Consequently, one main goal of SSI analyses must be finding the evolution of parameters $\tilde{T}/T$ and $\tilde{\zeta}$ with τ. To this end, several simplified procedures for practical purposes have been derived by different authors by making the resonant period and peak pseudo-acceleration of a replacement oscillator equal to those of the interacting system [82, 83, 86, 159]. However, among other simplifying assumptions, all these solutions neglect the cross-coupled stiffness and damping terms, $k_{x\phi}$ and $c_{x\phi}$, which

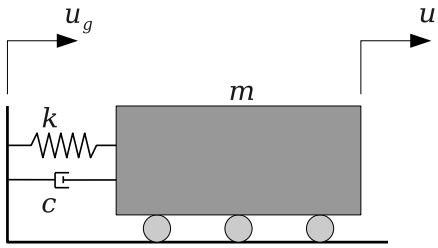

Figure 6.5: *Equivalent single-degree-of-freedom oscillator.*

is not acceptable for pile foundations. For this reason, Maravas et al. [160] presented an approximate iterative procedure based on the same analogy but placing the reference system at a depth $e = k_{x\phi}/k_{xx}$ such that the cross-coupled terms can be neglected. Making use of this procedure, Maravas et al. were able to study SSI effects on single-pile supported one-storey shear structures. However, a different methodology will be used herein.

To be able to address the problem for a general pile foundation configuration, a more complex but more accurate procedure has been employed in this work. It is an iterative procedure that searches the maximum of the harmonic spectrum for different values of τ, following algorithm 6.1. It starts in $\tau = \tau_{min}$, with $\tau_{min} \to 0$, *i.e.* for very soft structures (or very hard soils), when $\tilde{T} \to T$. Then, with the assumption that $\tilde{T}^{(i)} = T$, values of Q are computed at $\tilde{T}^{(i)} - \Delta T$, $\tilde{T}^{(i)}$ and $\tilde{T}^{(i)} + \Delta T$, being $\Delta T \to 0$. As these curves are known to be smooth, the search point is then moved in the direction of increasing Q (usually, but not always, increasing T), until a maximum is reached, moment in which the corresponding $\tilde{T}^{(i)}$ is stored as the system resonant period $\tilde{T}$ for this value of τ. Afterwards, as τ grows until $\tau = \tau_{max}$, the iterative procedure is repeated, this time starting at the last computed value of $\tilde{T}$.

The equivalent damping ratio $\tilde{\zeta}$ is computed for each point, once the corresponding $\tilde{T}/T$ is known. If the damping mechanism of the equivalent single-degree-of-freedom oscillator is assumed to be of hysteretic nature, it can be easily shown that the relationship between the maximum value of Q and the damping ratio is

$$\tilde{\zeta} = \frac{1}{2Q_m} \tag{6.5}$$

On the contrary, if the damping mechanism of the oscillator is of viscous nature, this relationship is [140]

$$\tilde{\zeta}^2 = \frac{1}{2}\left(1 - \sqrt{\frac{Q_m^2 - 1}{Q_m^2}}\right) \tag{6.6}$$

Algorithm 6.1 Pseudocode for the computation of $\tilde{T}/T = f(\tau)$ and $\tilde{\zeta} = g(\tau)$

INPUT: Set of parameters defining the system: h/b, γ, ζ, m_o/m, $I_o/(mh^2)$, ρ_s, d, c_s, foundation dynamic stiffnesses and foundation kinematic interaction factors; and algorithm parameters τ_{min}, τ_{max}, $\Delta\tau$ and Δa_o

$\Delta T \leftarrow 2\pi d/(c_s \Delta a_o)$

for $\tau^{(i)} = \tau_{min}$ to τ_{max}, in steps of $\Delta\tau$ **do**

  compute corresponding structural properties

  if $\tau^{(i)} = \tau_{min}$ **then**

    $\tilde{T}^{(i)} \leftarrow T$

  else

    $\tilde{T}^{(i)} \leftarrow \tilde{T}^{(i-1)}$

  end if

  $Q_1^{(i)} = Q(\tilde{T}^{(i)} - \Delta T)$

  $Q_2^{(i)} = Q(\tilde{T}^{(i)})$

  $Q_3^{(i)} = Q(\tilde{T}^{(i)} + \Delta T)$

  do

    if $Q_3^{(i)} \geqslant Q_2^{(i)}$ **then**

      $\tilde{T}^{(i)} \leftarrow \tilde{T}^{(i)} + \Delta T$

      $Q_1^{(i)} \leftarrow Q_2^{(i)}$

      $Q_2^{(i)} \leftarrow Q_3^{(i)}$

      $Q_3^{(i)} = Q(\tilde{T}^{(i)})$

    else if $Q_1^{(i)} \geqslant Q_2^{(i)}$ **then**

      $\tilde{T}^{(i)} \leftarrow \tilde{T}^{(i)} - \Delta T$

      $Q_3^{(i)} \leftarrow Q_2^{(i)}$

      $Q_2^{(i)} \leftarrow Q_1^{(i)}$

      $Q_1^{(i)} = Q(\tilde{T}^{(i)})$

    end if

  while $(Q_1^{(i)} \geqslant Q_2^{(i)})$.OR.$(Q_3^{(i)} \geqslant Q_2^{(i)})$

  compute $(\tilde{T}/T)^{(i)}$ and $\tilde{\zeta}$

end for

OUTPUT: $\tau^{(i)}$, $(\tilde{T}/T)^{(i)}$, $\tilde{\zeta}^{(i)}$

Throughout this work, equivalent damping will be computed with eq. (6.5), assuming hysteretic damping. It is worth noting, however, that for usual values of $\tilde{\zeta}$, both models produce very close results.

This technique may appear to be inefficient, but the resolution of the system of equations is so cheap that obtaining a whole set of curves using this simple algorithm in a normal PC is just a matter of a few seconds. As said above, the most difficult and time consuming tasks in these kinds of analyses are the previous computation of foundation impedances and kinematic interaction factors.

6.5.1 Comparison results

Fig. 6.6 compares results obtained by this methodology (left) with those published by Veletsos and Meek [82] (right). Parameters $T/\tilde{T}$ and $\tilde{\zeta}$ are plotted as a function of $\sigma = c_s T/h = 1/\tau$. Note that Veletsos and Meek's plot has been taken directly from their article for comparison, and that they use frequency f (in Hz) rather than periods T. The example corresponds to three one-storey shear structures with slenderness ratios $h/r = 1$, 2 and 5, being r the radius of the rigid circular plate foundation of negligible thickness. The stiffness and damping functions of this foundation mat, resting on an elastic half-space with no material damping, are specified in the cited work in terms of simple expressions which are a function of a series of dimensionless parameters given in plots. Such impedance functions have been approximated in this work as

$$k_{xx} = k_s \tag{6.7}$$

$$c_{xx} = 0.5\, k_s\, a_o\, \frac{r}{c_s} \tag{6.8}$$

$$k_{\phi\phi} = 0.95\, k_s\, (1 - a_o/5) \tag{6.9}$$

$$c_{\phi\phi} = 0.90\, k_x\, a_o^2\, \frac{r}{8c_s} \tag{6.10}$$

where $k_s = 8\,\mu\, r/(2 - \nu_s)$ and $a_o = \omega\, r/c_s$. The rest of properties used in this example are $\gamma = 0.15$, $m_o/m = 0$, $I_o/(m\, h^2) = 0$, $\zeta = 0.02$ and $\nu_s = 0.45$. It can be seen that there exists a good agreement between both sets of results. Differences are thought to be due to small errors in the computation of foundation impedances and to the simplifying assumptions introduced by Veletsos and Meek in the computation of $\tilde{\zeta}$.

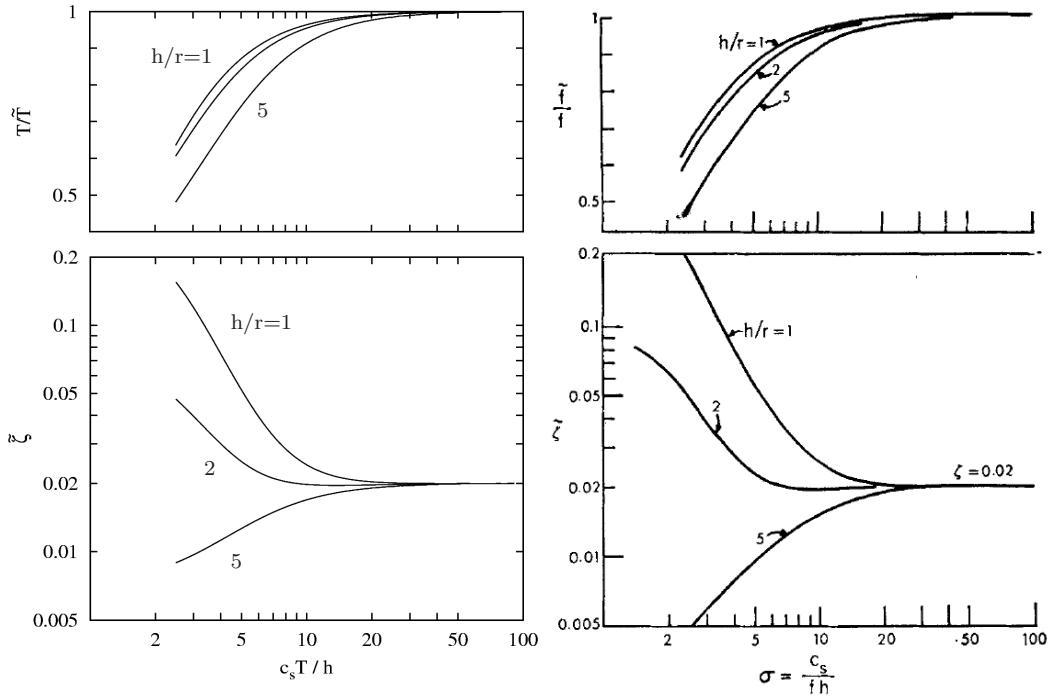

Figure 6.6: *Comparison between proposed method (left) and Veletos and Meek's solution (right) extracted directly from the original paper [82]*

6.6 Results

In this section, the substructure approach described above is going to be used to investigate the influence of SSI on the response of pile supported one-storey shear buildings subjected to vertically incident S waves. The considered foundation configurations are: 2×2 and 3×3 pile groups, $s/d = 2$ and 5, and $E_p/E_s = 1000$ and 100.

Horizontal, rocking and cross-coupled horizontal-rocking impedances, together with the horizontal and rocking kinematic interaction factors, are needed to perform the parametric analyses. The two first impedance functions corresponding to the chosen foundations were already presented in chapter 4, while the rest of functions are given herein before showing the SSI results.

Figs. 6.7 to 6.10 present the cross-coupled horizontal-rocking stiffness and damping functions corresponding to the considered pile groups. They are normalized by the addition of the products of the vertical static stiffness of a single pile ($k^s_{zz_o}$) times the horizontal distance of each pile to the rotation axis of the cap (x_i). Note that both stiffness and damping have negative values for the reference

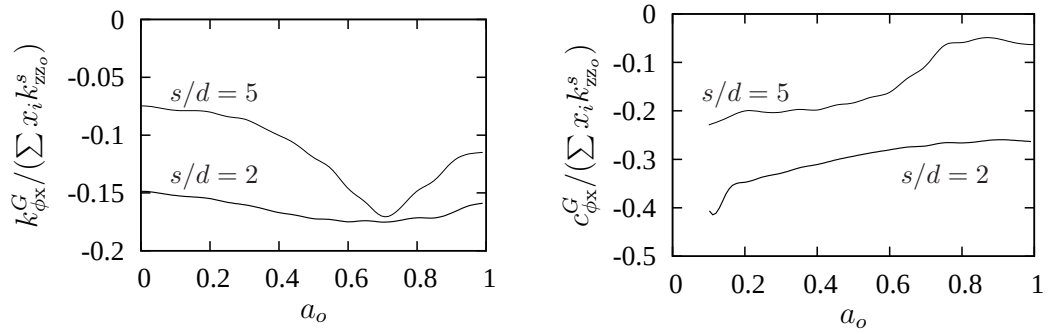

Figure 6.7: *Cross-coupled horizontal-rocking impedance of a* 2×2 *pile group.* $E_p/E_s = 1000$

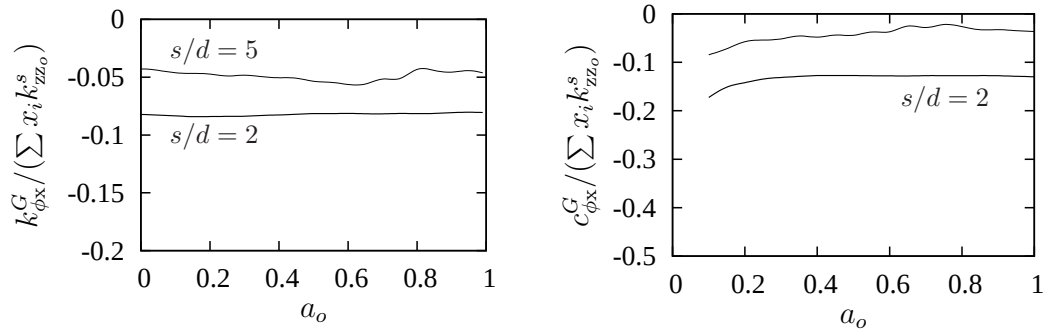

Figure 6.8: *Cross-coupled horizontal-rocking impedance of a* 2×2 *pile group.* $E_p/E_s = 100$

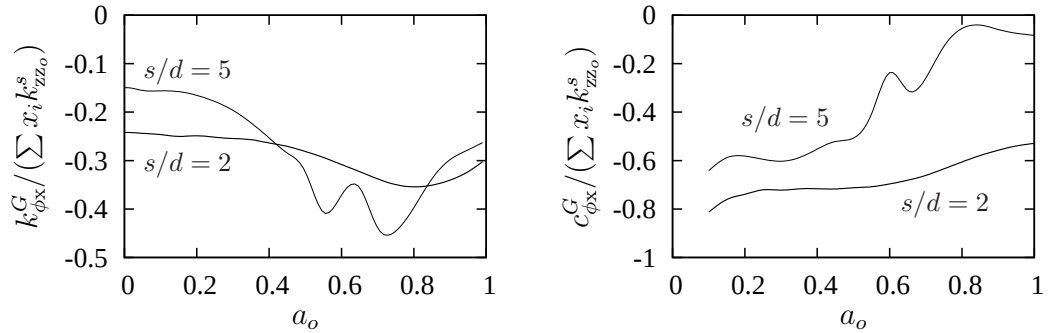

Figure 6.9: *Cross-coupled horizontal-rocking impedance of a* 3×3 *pile group.* $E_p/E_s = 1000$

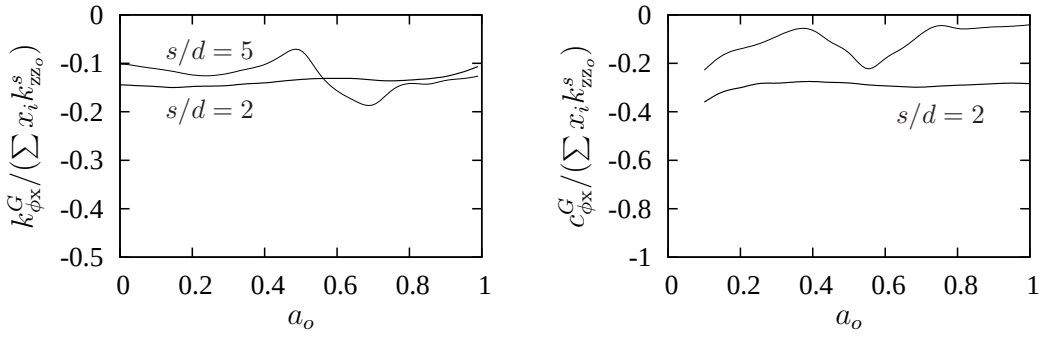

Figure 6.10: *Cross-coupled horizontal-rocking impedance of a* 3×3 *pile group.* $E_p/E_s = 100$

system shown in fig. 6.2.

Time-harmonic horizontal displacement and rocking transfer functions, at the pile cap of the different foundations subjected to vertically incident S waves, are presented from fig. 6.11 to 6.14. Both functions are normalized by the free-field horizontal motion at the ground surface u_{ff}, and the rocking response at the pile cap ϕ_{cap} is multiplied by the piles diameter d. Note that the kinematic behaviour is almost independent of the pile-soil stiffness ratio E_p/E_s and that rocking is much smaller for widely spaced piles.

Once all these frequency-dependant functions have been computed, the influence of SSI effects on the dynamic behaviour of one-storey shear structures can be assessed as explained in the previous sections. Figs. 6.15 to 6.18 present the evolution of the system fundamental period and equivalent damping with τ. Results for three different slenderness ratios $h/b = 2$, 3 and 6, and two different separation ratios $s/d = 2$ and 5 are shown in each figure. As $s/d = 2$ foundations are narrow, and also in order to make results comparable for different separation ratios, the halfwidth of the foundation has always been taken to be that corresponding to the $s/d = 5$ pile group, *i.e.* $b = s_{(s/d=5)}$ for 3×3 pile groups and $b = 0.5\, s_{(s/d=5)}$ for 2×2 pile groups. In all cases $\gamma = 0.15$, $m_o/m = 0.25$, $I_o/(m\, h^2) = 0.05$ and $\zeta = 0.05$.

It can be seen that the parameter $\tilde{T}/T$ tends to increase with both τ and the slenderness ratio h/b, while the equivalent damping ratio $\tilde{\zeta}$ decreases with h/b, as already explained above. On the other hand, $\tilde{T}/T$ is always smaller for $s/d = 5$ pile groups because of the higher stiffness of these foundations. It is shown that, in general, SSI phenomena can be of great importance on the dynamic response of pile supported structures.

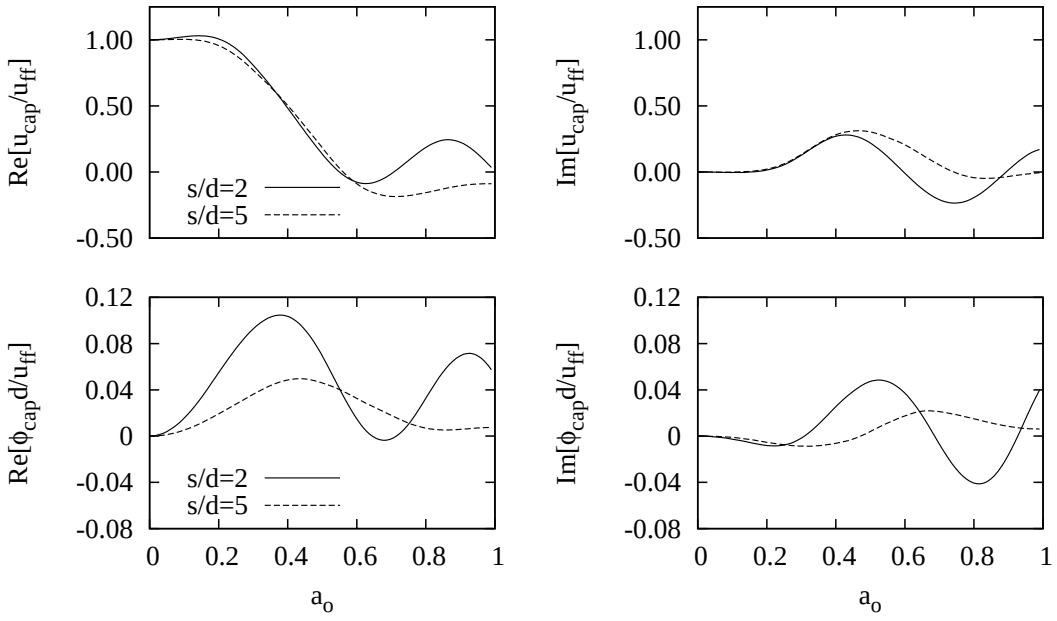

Figure 6.11: *Time-harmonic horizontal displacement and rocking transfer functions, at the pile cap, of a* 2×2 *pile group under vertically incident S waves.* $E_p/E_s = 1000$

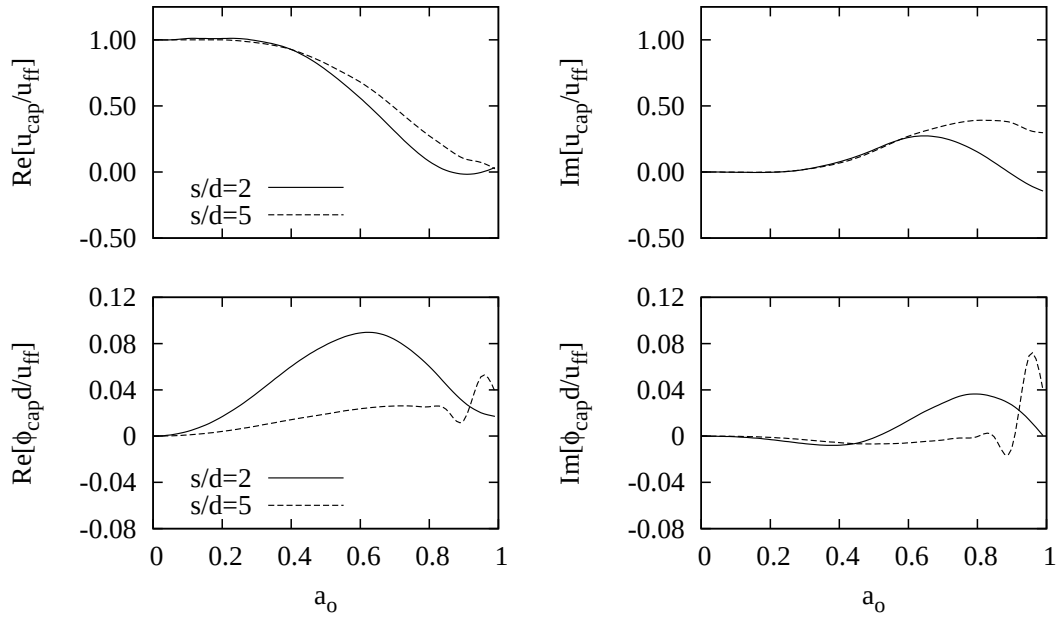

Figure 6.12: *Time-harmonic horizontal displacement and rocking transfer functions, at the pile cap, of a* 2×2 *pile group under vertically incident S waves.* $E_p/E_s = 100$

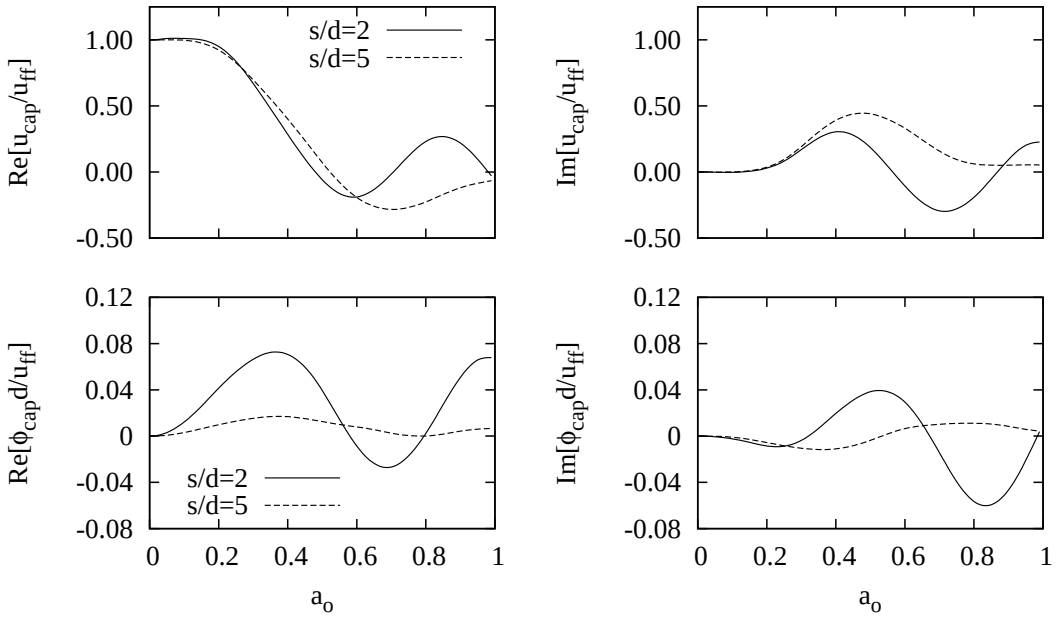

Figure 6.13: *Time-harmonic horizontal displacement and rocking transfer functions, at the pile cap, of a* 3×3 *pile group under vertically incident S waves.* $E_p/E_s = 1000$

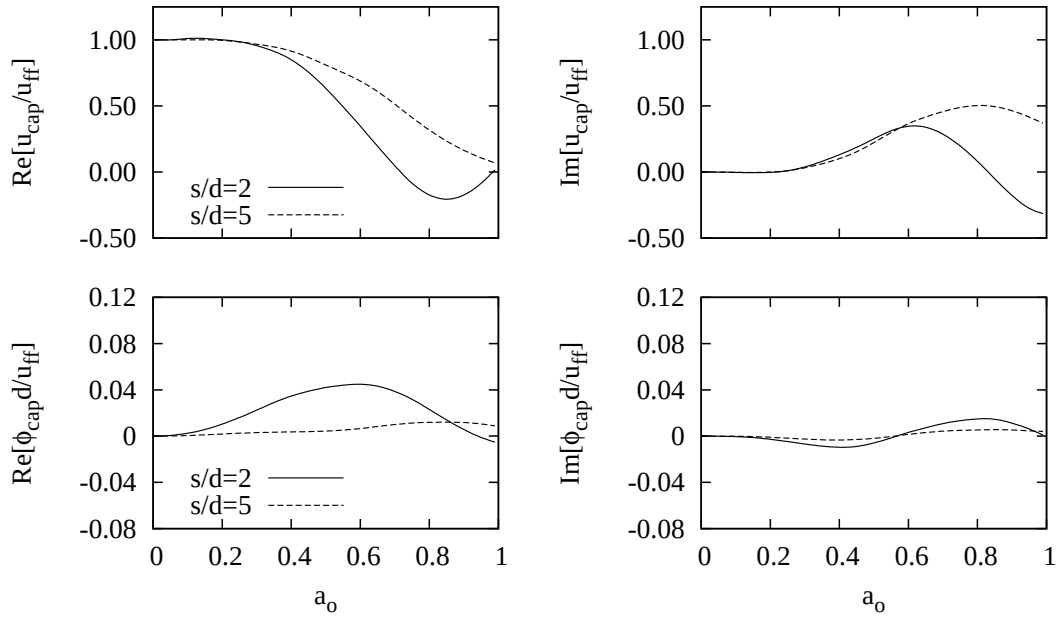

Figure 6.14: *Time-harmonic horizontal displacement and rocking transfer functions, at the pile cap, of a* 3×3 *pile group under vertically incident S waves.* $E_p/E_s = 100$

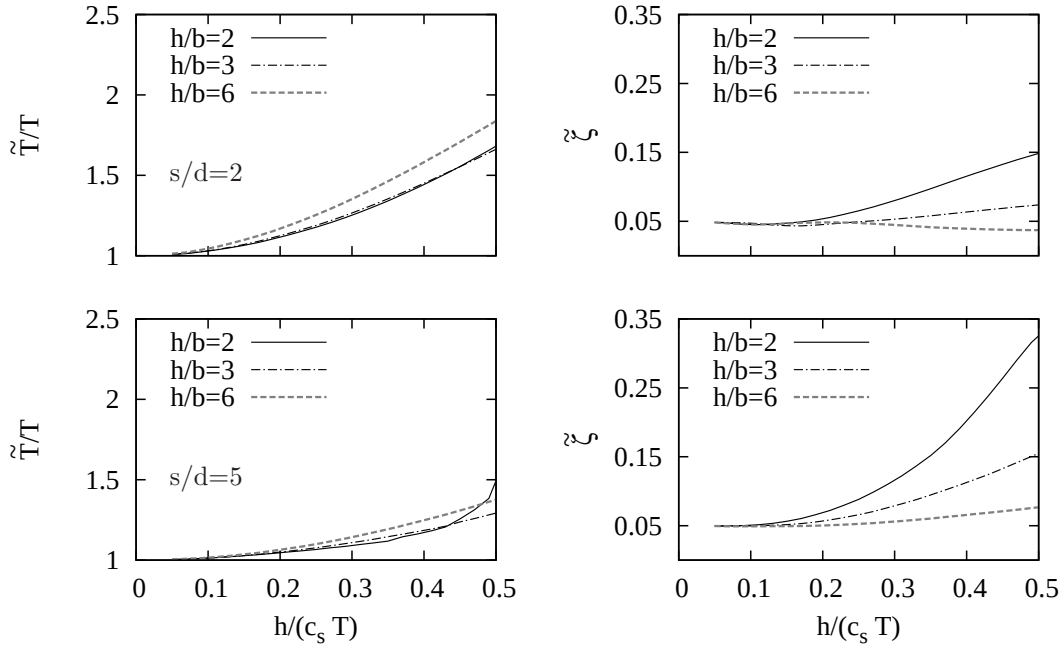

Figure 6.15: *System fundamental period and equivalent damping taking SSI into account.* 2×2 *pile group.* $E_p/E_s = 1000$

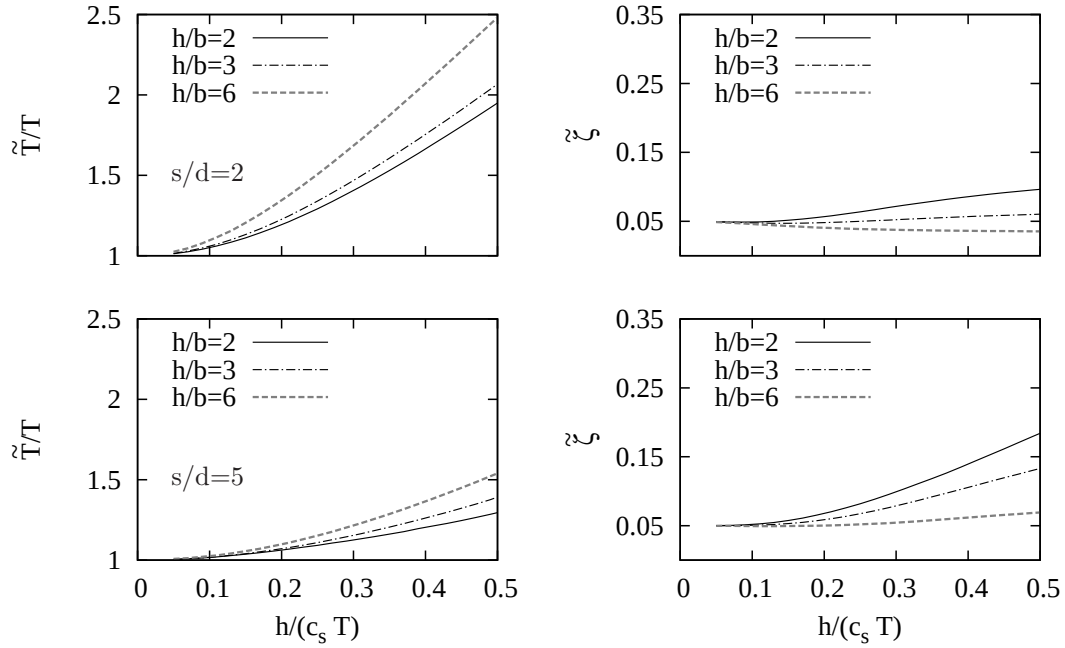

Figure 6.16: *System fundamental period and equivalent damping taking SSI into account.* 2×2 *pile group.* $E_p/E_s = 100$

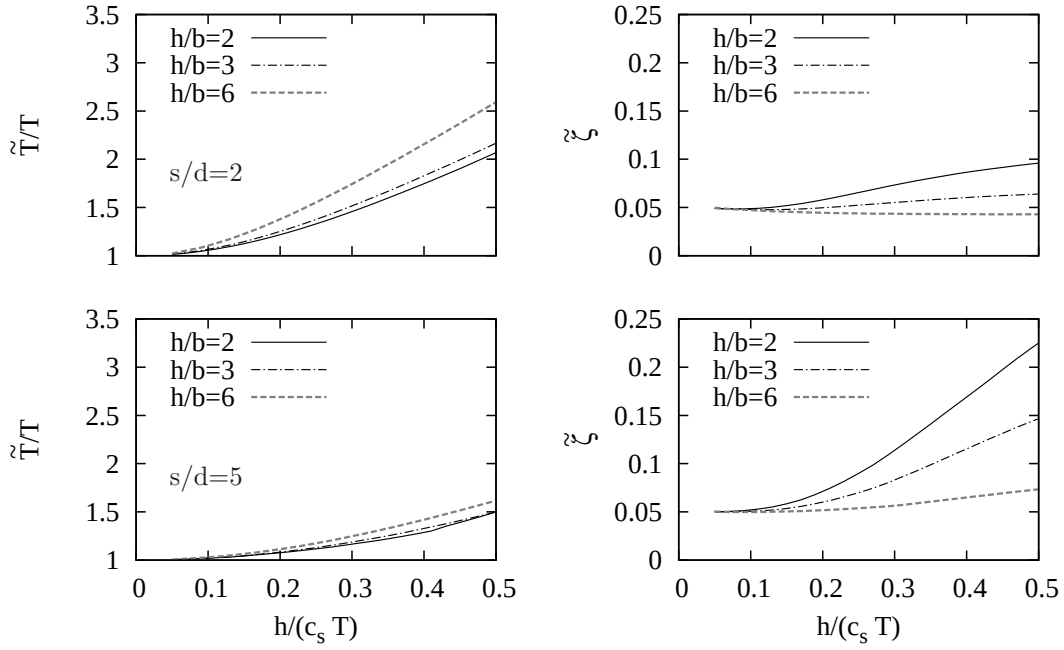

Figure 6.17: *System fundamental period and equivalent damping taking SSI into account.* 3×3 *pile group.* $E_p/E_s = 1000$

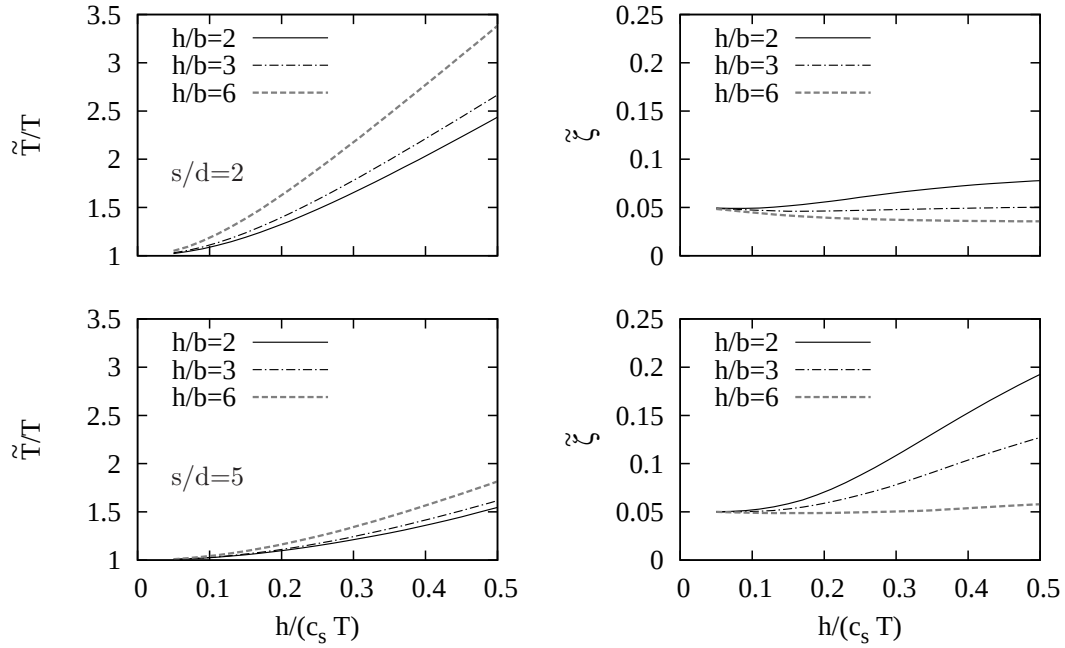

Figure 6.18: *System fundamental period and equivalent damping taking SSI into account.* 3×3 *pile group.* $E_p/E_s = 100$

Veletsos and Meek [82] and Avilés and Pérez-Rocha [86] have already pointed out that the system response is not sensitive to variations of parameters γ, m_o/m and $I_o/(m\,h^2)$ within the ranges corresponding to usual buildings and soils. However, it may be of interest to measure the sensitivity of the system response to these parameters. To this end, figs. 6.19, 6.20 and 6.21 present the dynamic response of structures founded on a 2×2, $s/d = 5$, $E_p/E_s = 100$ pile group for different values of γ, m_o/m and $I_o/(m\,h^2)$, respectively. It is shown that both system fundamental period and equivalent damping are completely insensitive to variations of foundation-structure mass and mass moment of inertia ratios (figs. 6.20 and 6.21). However, the dynamic response of the system is affected to variations of the structure-soil mass ratio γ within the range of practical values $0.1 < \gamma < 0.2$. As expected, larger values of γ tend to increase both the system resonant period and equivalent damping, and viceversa. Within the above mentioned range, and for this representative case, parameters $\tilde{T}/T$ and $\tilde{\zeta}$ can vary up to 20%, though equivalent damping ratio of short structures is little affected.

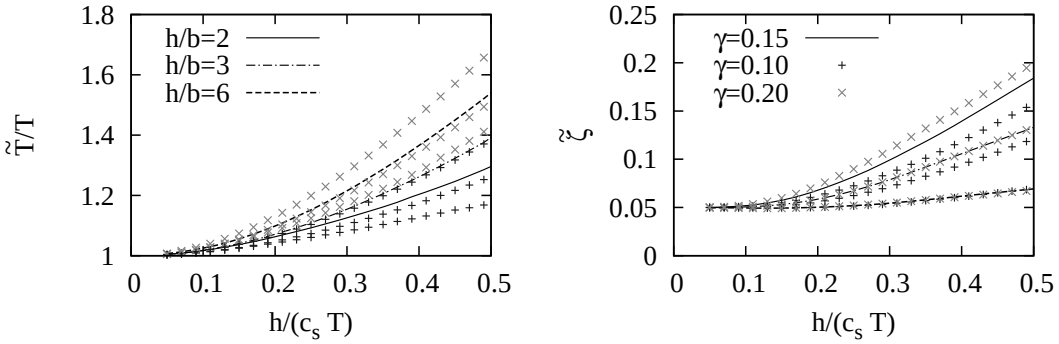

Figure 6.19: *Sensitivity of parameters $\tilde{T}/T$ and $\tilde{\zeta}$ to variations in mass density ratio γ. $s/d = 5$, $E_p/E_s = 100$, 2×2 pile group.*

Another parameter whose influence on the seismic response is worth studying is the assumed structural damping ratio. As all results presented herein have been obtained for $\zeta = 0.05$, fig. 6.22 presents the dynamic behaviour of the case studied above for three different structural damping ratios: $\zeta = 0.02$, 0.05 and 0.10. It can be seen that the evolution of $\tilde{T}/T$ is not sensitive to this parameter, especially for tall structures. Obviously, the evolution of equivalent damping ratios $\tilde{\zeta}$ is more sensitive to the structural damping value. However, relative differences for $\tau \to 0.5$ are much smaller than for $\tau \to 0$. Hence, while the equivalent damping ratio $\tilde{\zeta}$ is governed by the assumed structural damping ratio ζ in case of very hard soils (or very soft structures), for relatively soft soils (or stiff structures), the

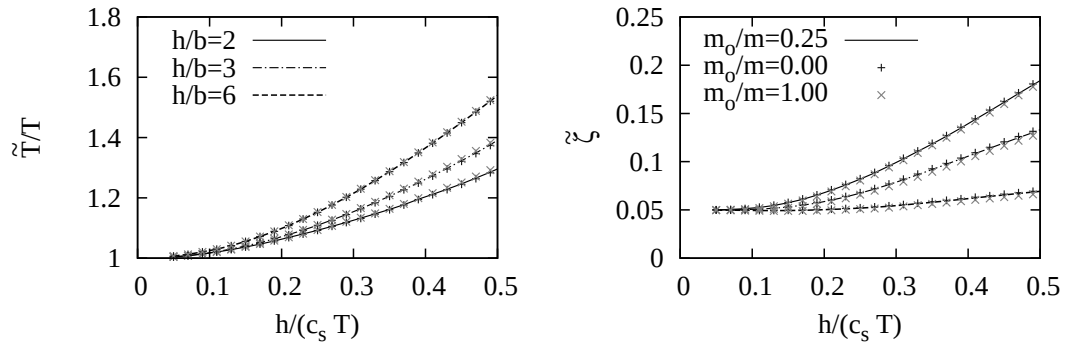

Figure 6.20: *Sensitivity of parameters $\tilde{T}/T$ and $\tilde{\zeta}$ to variations in foundation-structure mass ratio m_o/m. $s/d = 5$, $E_p/E_s = 100$, 2×2 pile group.*

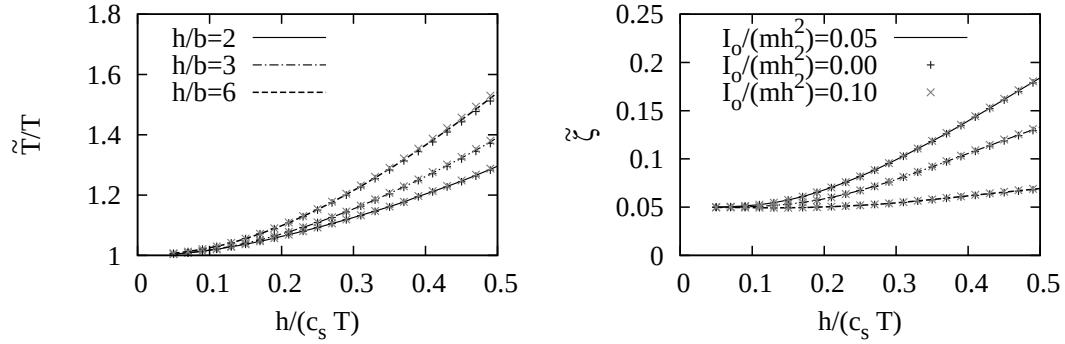

Figure 6.21: *Sensitivity of parameters $\tilde{T}/T$ and $\tilde{\zeta}$ to variations in foundation-structure mass moment of inertia ratio $I_o/(mh^2)$. $s/d = 5$, $E_p/E_s = 100$, 2×2 pile group.*

dissipative mechanisms of the soil (both radiation and material damping) are of major importance.

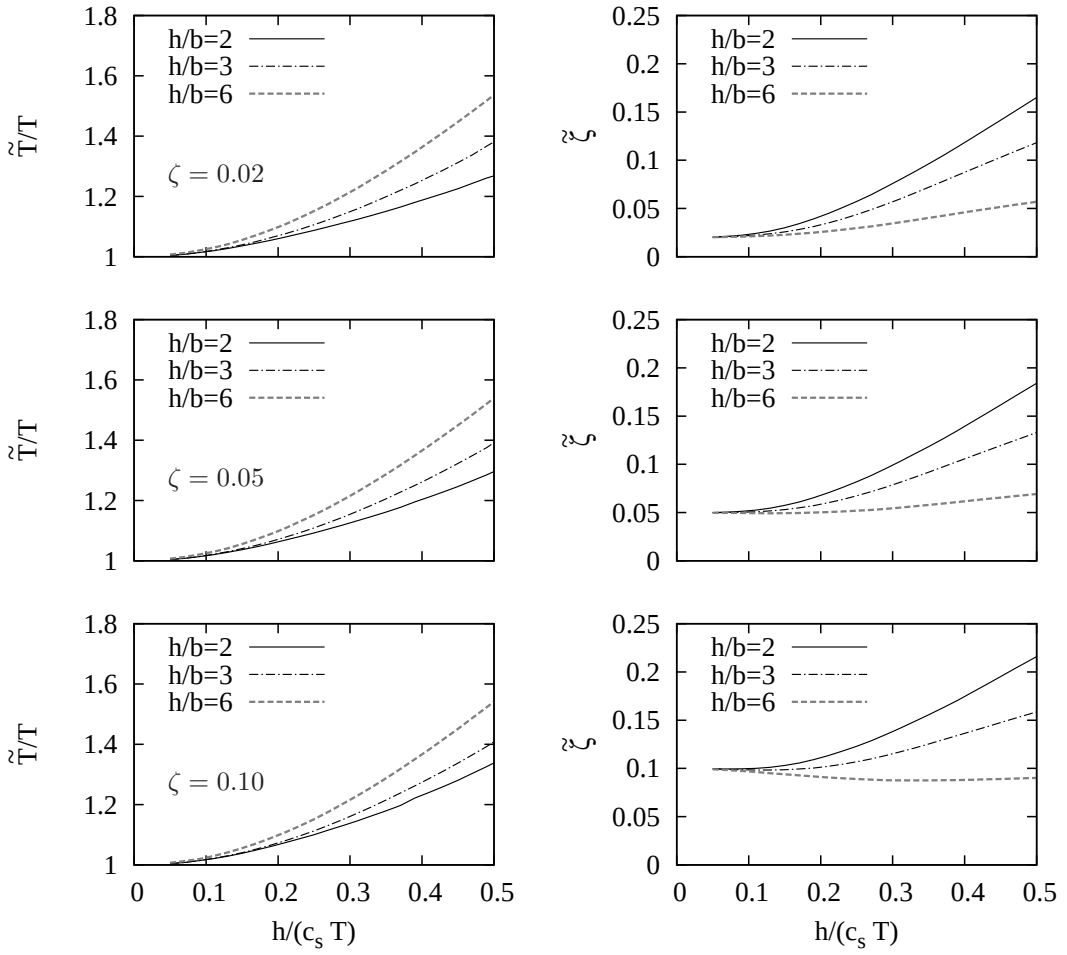

Figure 6.22: *Sensitivity of parameters $\tilde{T}/T$ and $\tilde{\zeta}$ to variations in fixed-base structure damping ζ. $s/d = 5$, $E_p/E_s = 100$, 2×2 pile group.*

As for the foundation input motions, much of the literature on SSI effects exclude the kinematic interaction effects. Therefore, it may be of interest to assess its influence on the system dynamic response. To this end, figs. 6.23 and 6.24 (corresponding to two of the cases studied before) compare the responses considering the foundation input motion to be either the transfer functions of the specific foundation, or the free-field ground motion (no k.i.). It can be seen that the system fundamental period is not affected by this parameter. However, when kinematic interaction effects are considered, equivalent damping ratios are

greater in comparison to the case where only the free-field ground motion is used. Consequently, kinematic interaction phenomena produce smaller structural response, while neglecting it would lead to an overestimation of the magnitude of the response. These conclusions are in accord with those reported by Avilés and Pérez-Rocha [87] for one-storey structures supported by a rigid square foundation embedded in a homogeneous elastic half-space.

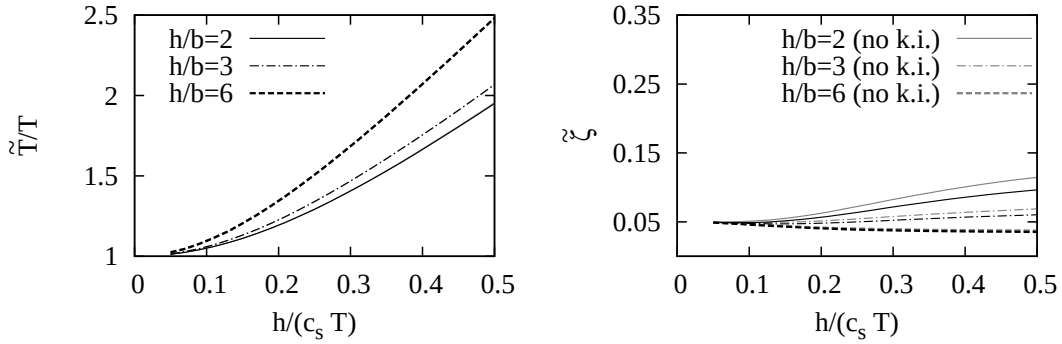

Figure 6.23: *Influence of kinematic interaction (k.i.) on system response. Comparison between parameters $\tilde{T}/T$ and $\tilde{\zeta}$ computed taking k.i. into account or neglecting it (no k.i.). $s/d = 5$, $E_p/E_s = 100$, 2×2 pile group.*

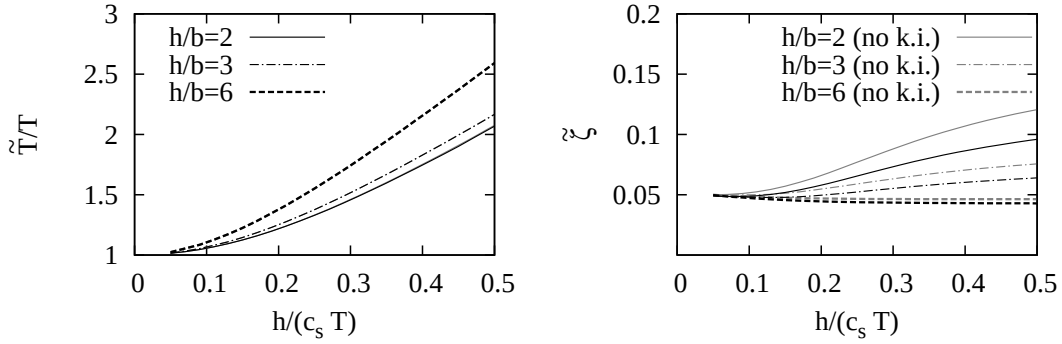

Figure 6.24: *Influence of kinematic interaction (k.i.) on system response. Comparison between parameters $\tilde{T}/T$ and $\tilde{\zeta}$ computed taking k.i. into account or neglecting it (no k.i.). $s/d = 2$, $E_p/E_s = 1000$, 3×3 pile group.*

6.7 Conclusions

The main motivation in obtaining the impedance functions and kinematic interaction factors of foundations lies in the fact that they are a key part of the substructure models for SSI problems that are generally used in design. For this reason, the substructure approach has been used in this chapter to address the analysis of soil-structure interaction effects on the dynamic response of pile supported structures. The equations of motion have been derived for a three-degree-of-freedom substructure model for the horizontal and rocking behaviour of shear linear one-storey structures. The cross-coupled horizontal-rocking impedance terms, together with the horizontal and rocking foundation input motions, are considered. A simple algorithm, that finds the resonant frequency and equivalent damping of the system, has been presented and employed to perform several parametric analyses. Here is where the use of a substructure model is justified in front of the direct model presented in chapter 3, because once impedance functions and transfer functions have been computed, the substructure approach allows performing parametric analyses with very little computational effort.

The influence of SSI on the dynamic response of pile supported structures was studied by means of parametric analyses in which foundation configuration, slenderness ratio and structure-soil relative stiffness were taken into account. It has been proved that SSI effects can be of importance for pile supported structures founded on relatively soft soils or for relatively stiff structures, and that this influence can be both beneficial or detrimental, depending mainly on the structural slenderness ratio. Afterwards, the sensitivity of these results to variations of some other parameters, usually considered to be of minor importance, was assessed, finding such assumption to be valid. The influence of kinematic interaction effects on the dynamic response of pile supported structures was also studied, finding that it only affects to the system equivalent damping.

A very interesting extension of this work would be a comparative study of the influence of SSI on the dynamic response of similar structures founded with different types of foundations. A comprehensive analysis of this kind would enable the practioner to evaluate, from the structural point of view, the relative seismic performance of different foundation systems (pile foundations, shallow foundations, embedded footings, embedded pile footings ...) in a specific case.

Chapter 7

Dynamic structure-soil-structure interaction between nearby piled buildings under seismic excitation

7.1 Introduction

In the last chapter, the substructure method was used to assess the influence of soil compliance and foundation configuration on the dynamic response of structures under seismic excitation. The use of a substructure approach, instead of a direct methodology, was justified in that case by the good accuracy of the results and the little computational effort required to perform parametric analyses when impedance and kinematic interaction functions are already known.

The substructure method can be an accurate, simple and efficient tool for the analysis of some soil-structure interaction problems, such as that of a single building-type structure founded on a single foundation. However, this methodology is not as suitable for many other SSI problems such as, for instance, long structures with multiple foundations (long-span bridges), large massive structures (dams) or groups of structures or elements that may interact with each other.

For this reason, the BEM-FEM code presented in chapter 3 for the dynamic analysis of pile supported structures is used herein to study the effects of through-soil interaction between neighbouring pile supported structures three-dimensionally distributed, as those shown in fig. 7.1. In a first step, the problem has been deliberately simplified in order to: first, concentrate on structure-soil-structure interaction (SSSI) phenomena; and second, establish a link to previous works on the matter. To this end, all buildings have been considered as one-storey shear structures founded on 3×3 similar pile caps in a viscoelastic half-space, and a reduced set of problem configurations has been chosen to perform the analysis,

whose intention is not to be a comprehensive study.

Figure 7.1: *Group of neighbouring pile supported buildings.*

The problem is first stated in section 7.2. Then, the problem parameters and properties are defined in section 7.3. Afterwards, a set of numerical results in the frequency domain is presented in section 7.4.1 to assess the effects of structure-soil-structure interaction on the seismic response of buildings in terms of its spectral deflection, fundamental frequency, vertical and rotational response and shear forces at pile heads. Maximum response spectra are also presented for an artificial seismic input in section 7.4.2. Some of these results have previously been presented in a conference paper [161].

7.2 Problem definition

The system under investigation is composed of several neighbouring one-storey linear shear structures, three-dimensionally distributed, founded on 3×3 fixed-head pile groups embedded on a viscoelastic half-space. A plane sketch of the problem is depicted in fig. 7.2, where the geometric properties of buildings and piles are labelled. Pile groups are defined by length L and sectional diameter d of piles, centre-to-centre spacing between adjacent piles s and foundation halfwidth b, being in this specific case $b = s$. The rest of parameters are: centre-to-centre spacing between adjacent foundations D, fixed-base fundamental period T and structural damping ratio ζ, cap mass m_o and moment of inertia I_o, structure effective height h and structure effective mass m.

In this work, as a first approximation and also in order to focus on SSSI, superstructures are modelled as one-degree-of-freedom shear buildings in its fixed-base condition. However, these may represent either one-storey constructions or the fundamental mode of multi-mode structures (see section 6.2). Subsequently, h, m and ζ must be generally understood as first-mode equivalent height, mass and damping ratio. On the other hand, note that fig. 7.2 is a two-dimensional representation of the three-dimensional model used herein. This way, eight degrees of freedom are considered on each foundation-superstructure subsystem: two lateral deformations of the structure u and two foundation translations u^c along axes x and y, one vertical displacement u_z, two rocking motions φ around horizontal axes and one rotational motion ϕ around the vertical axis. Note that vertical motions of cap and storey have been forced to be identical because buildings are modelled as purely shear structures.

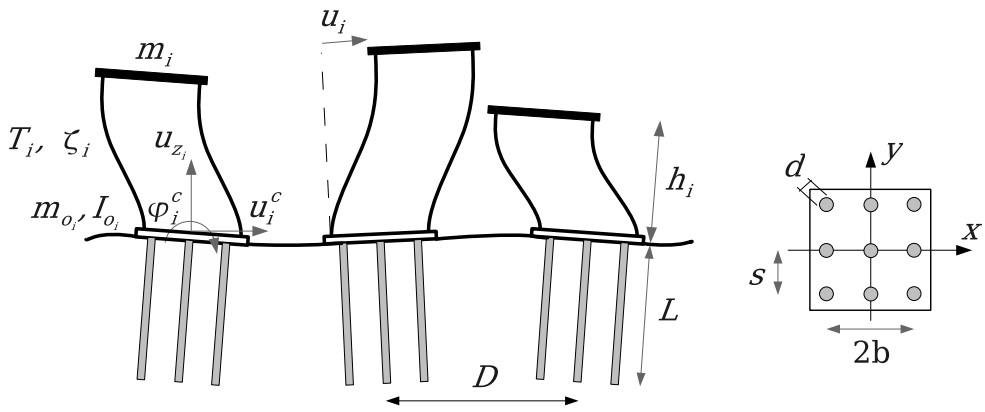

Figure 7.2: *Geometric definition of the problem.*

The dynamic behaviour of several problems (of which the different relative arrangements of structures are shown in fig. 7.3) under vertically incident plane S waves (producing motions on the y axis) or Rayleigh waves (moving along the y axis from $y < 0$ to $y > 0$), is analysed. To this end, the response of each structure in the group is compared to that of the single-structure-soil system in order to find out whether or not structure-soil-structure interaction effects between two or more buildings can be of importance. Note that in all configurations the distance D between adjacent structures is measured in parallel to x and y axes, and is the same between all structures in the same problem.

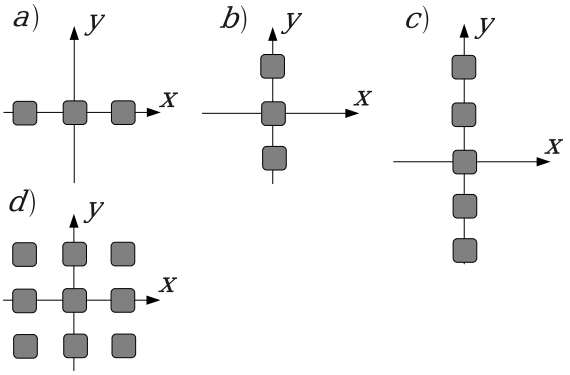

Figure 7.3: *Different relative arrangements of structures considered in this work.*

7.3 Problem parameters

The mechanical and geometrical properties of pile foundations and soil are defined by the following parameters: piles separation ratio $s/d = 5$, pile-soil modulus ratios $E_p/E_s = 100$ and 1000, soil-pile density ratio $\rho_s/\rho_p = 0.7$, piles aspect ratio $L/d = 15$, soil damping coefficient $\beta = 0.05$ and Poisson ratio $\nu_s = 0.4$.

On the other hand, the most important parameters to define the superstructure dynamic behaviour are: structural aspect ratios $h/b = 2$, 3 and 4; structure-soil stiffness ratio $h/(T\,c_s) = 0.3$, being c_s the soil shear wave velocity; and structural damping ratio $\zeta = 0.05$. The choice of the structure-soil stiffness ratio is justified below. Other parameters are: foundation mass moment of inertia $I_o = 5\%$, 2.2% and 1.25% of mh^2 for $h/b = 2$, 3 and 4, respectively; structure-soil mass ratio $m/4\rho_s b^2 h = 0.20$; and foundation-structure mass ratio $m_o/m = 0.25$. The values chosen for these three last parameters are considered to be representative for typical constructions, and similar values have been used by other authors before [82, 83, 86]. In any case, SSI and SSSI results are not significantly sensitive to its variation (see section 6.6).

Soil-structure interaction effects on a single building can be measured by parameters $\tilde{T}/T$ and $\tilde{\zeta}$, where $\tilde{T}$ is the fundamental period of the soil-structure system and $\tilde{\zeta}$ its equivalent structural damping (see section 6.5). The first parameter accounts for the shifting in the system fundamental frequency, while the effective damping is related to the absolute maximum value of the pseudo-acceleration in the structure, *i.e.* if $\tilde{\zeta} > \zeta$, the maximum structural response of the soil-structure system is smaller than the fixed-base response, and viceversa. In order to be able to relate the SSSI effects that are studied herein with the specific level of SSI effects of the isolated soil-structure system, fig. 7.4 shows the evolution of $\tilde{T}/T$ and $\tilde{\zeta}$ with the structure-soil stiffness ratio $h/(T\,c_s)$, being c_s the soil shear

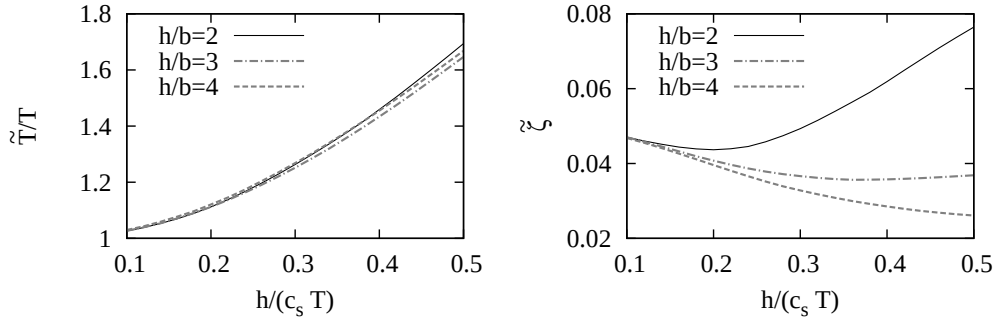

Figure 7.4: *SSI effects measurement for shear structures founded on* $s/d = 5$, $L/d = 15$, 3×3 *pile groups.* $E_p/E_s = 1000$.

wave velocity, for the problem defined above with $E_p/E_s = 1000$. Since this is the case of a single structure founded on only one pile group with a rigid cap, the study has been performed by the substructure method, which requires less computational effort in comparison to the direct approach. Therefore, fig. 7.4 has been obtained with the model presented in chapter 6, and making use of complex impedance functions and kinematic factors, computed as explained in chapters 3 and 4. As mentioned above, the present study has been performed for $h/(T\,c_s) = 0.3$, which is within the range of realistic values and yet soil-structure interaction effects become apparent. Obviously, for $h/(T\,c_s) \to 0$ (relatively stiff soil or soft/tall structure), the structure behaviour is that of the fixed-base system, and consequently, no SSSI effects would appear.

7.4 Numerical results

7.4.1 Steady-state response

The influence of structure-soil-structure interaction on the dynamic response of piled structures is addressed in this section. Here, the horizontal seismic behaviour of buildings is analysed in terms of its lateral deformation response spectra, defined as $\mathrm{Abs}[\Omega^2 u/\omega^2 u_{ff}]$, where Ω is the fundamental frequency of the fixed-base structure, ω is the excitation frequency and u_{ff} is the horizontal free-field motion at the ground surface. The product of this value with the structural mass and the corresponding free-field horizontal acceleration at ground surface level yields the amplitude of the shear force at the base of the structure. On the other hand, the harmonic vertical motion of structures u_z is obtained in terms of transfer func-

tions defined as Abs$[u_z/u_{ff}]$ or Abs$[u_z/u_{z_{ff}}]$ when the system is impinged by S or Rayleigh waves, respectively, and where $u_{z_{ff}}$ is the vertical free-field motion at the ground surface for Rayleigh waves. The harmonic rotational motion of structures ϕ around its vertical axis is also analysed in terms of transfer functions defined as Abs$[\phi \cdot b/u_{ff}]$. All figures in this section are plotted against the dimensionless frequency $a_o = \omega d/c_s$.

Distance D between adjacent foundations is expressed either proportionally to the foundation halfwidth b or as a fraction of the soil wave length at the soil-structure fundamental frequency $\lambda = c_s\tilde{T}$. The goal of relating D and λ is linking the separation between dynamically similar structures to one of the system's main dynamic properties.

Fig. 7.5 shows the dynamic response of single soil-structure systems (solid lines) together with the response of groups of three identical buildings (non-solid lines) under vertically incident S waves in terms of their lateral deformation response spectra for $E_p/E_s = 1000$. Three different structural aspect ratios ($h/b =$ 2, 3 and 4) and distances between adjacent buildings ($D = \lambda/2$, $3\lambda/4$ and $\lambda/4$) are considered. Shaking direction is assumed to be either parallel or perpendicular to the direction of alignment of the structures (as shown in figs. 7.3*a* and *b*, respectively). It can be seen that the lateral response of a structure may vary significantly due to the presence of neighbouring buildings. A slight shift in the fundamental period of the system takes place, but the peak value of the lateral shear force at the base of the structure can be considerably amplified. For instance, when $D = \lambda/2$, the lateral response of the central building of three aligned along the direction of shaking is increased by 40, 35 and 25 per cent for $h/b = 2$, 3 and 4, respectively. The influence of SSSI varies from one position to another, as well as for different distances between structures and for different aspect ratios, and the response may even increase or decrease depending on the configuration. However, it appears that the central construction is usually subject to the strongest shaking. It is also worth noting that even though problems with different h/b and the same D are not dimensionally equivalent, the same trends can be observed when D remains constant, in terms of λ.

The relation between the seismic response of different structures in a group configuration and the single soil-structure problem is also approximately the same for different pile-soil modulus ratios E_p/E_s. To show this, fig. 7.6 presents the dynamic response of single soil-structure systems (solid lines) together with the response of groups of three identical buildings (non-solid lines) under vertically incident S waves, now for $E_p/E_s = 100$. Only results for $h/b = 4$ and distances between adjacent buildings $D = \lambda/2$ and $\lambda/4$ are presented. Indeed, comparing these plots with those of fig. 7.5 for the same structural aspect ratio, it is observed that the system behaviour is qualitatively equivalent for both E_p/E_s values.

The influence of distance on the interaction between identical structures of

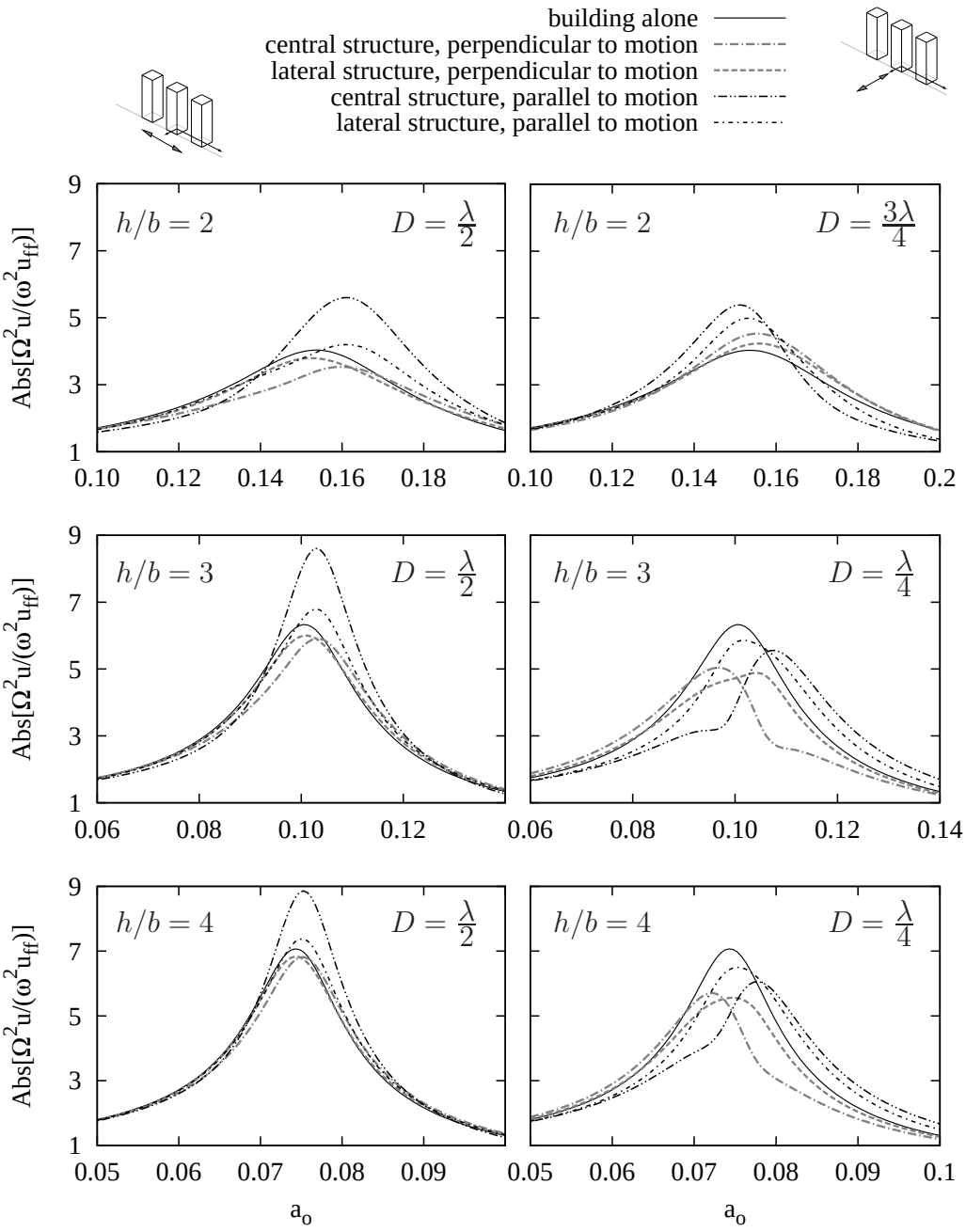

Figure 7.5: *Interaction between three structures of identical fundamental frequencies in terms of their harmonic response spectra for different configurations under S waves.* $E_p/E_s = 1000$

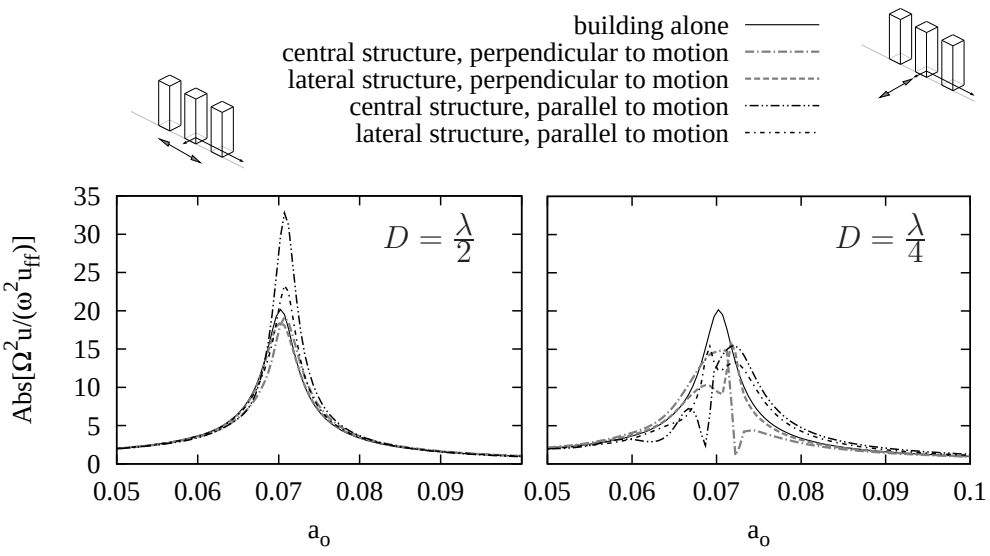

Figure 7.6: *Interaction between three structures of similar fundamental frequencies in terms of their harmonic response spectra under S waves.* $E_p/E_s = 100$. $h/b = 4$. *To be compared with bottom plots of fig. 7.5.*

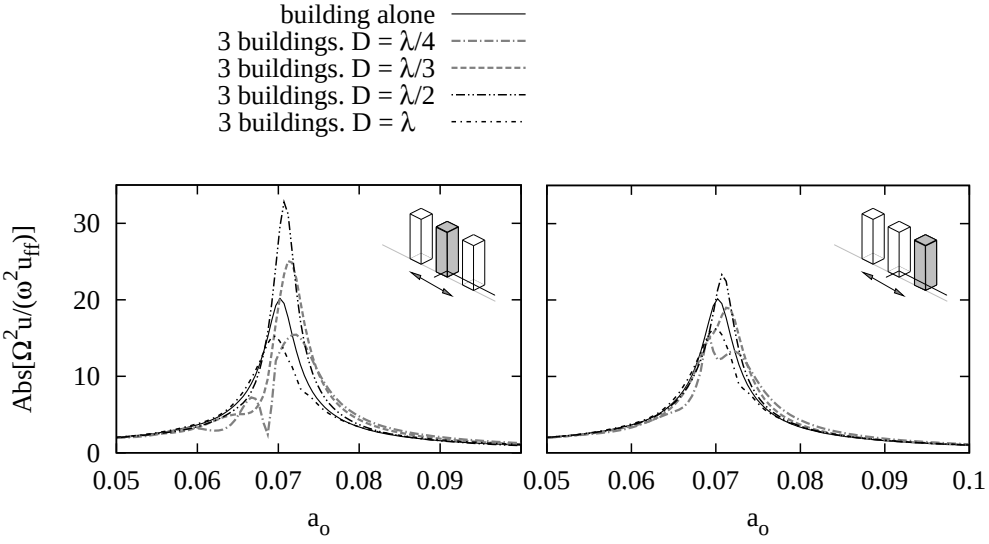

Figure 7.7: *Influence of distance on the interaction between three structures of identical fundamental frequencies under S waves.* $h/b = 4$, $E_p/E_s = 100$

aspect ratio $h/b = 4$ is investigated in fig. 7.7 for $E_p/E_s = 100$. The structures are aligned along the direction of shaking, produced by vertically incident S waves. Results for the central and lateral buildings are presented for $D = \lambda/4$, $\lambda/3$, $\lambda/2$ and λ. Once again it is observed that the central structure is the most influenced one by the presence of neighbouring constructions, and that, for the properties used in this work, $D = \lambda/2$ yields the highest lateral deformations, up to 65 per cent larger than those of the single soil-structure system. On the contrary, $D = \lambda/4$ and λ produce an attenuation of the response of 25 per cent.

Figs. 7.8 and 7.9 show the dynamic response of single soil-structure systems (solid lines) together with the response of groups of three dissimilar buildings (non-solid lines) under vertically incident S waves producing motions parallel or perpendicularly to the direction of alignment of the structures, respectively. In this case, adjacent buildings are considered to have different structural aspect ratios ($h/b = 2$ and 4) and, regarding the rest of constraints, their fixed-based fundamental period differ by a factor of 2. Two distances between adjacent buildings ($D = 4b$ and $6b$) are considered, and $E_p/E_s = 100$. It is observed that, under these assumptions, SSSI effects appear to be generally negligible, though when a short-period building is placed among two identical long-period structures, the response of both types of constructions increases by 20 and 30 per cent, respectively.

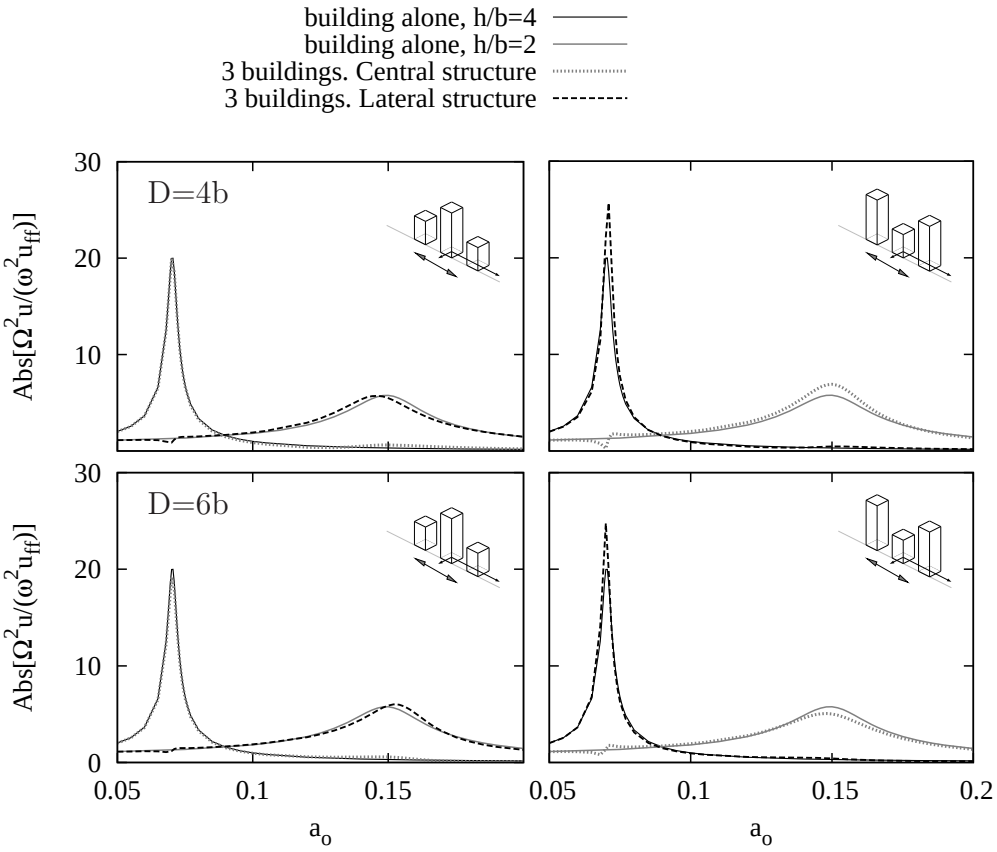

Figure 7.8: *Interaction between three structures of dissimilar fundamental frequencies in terms of their harmonic response spectra for different configurations under S waves. Structures aligned along direction of shaking.* $h/b = 2$ *and* 4. $E_p/E_s = 100$.

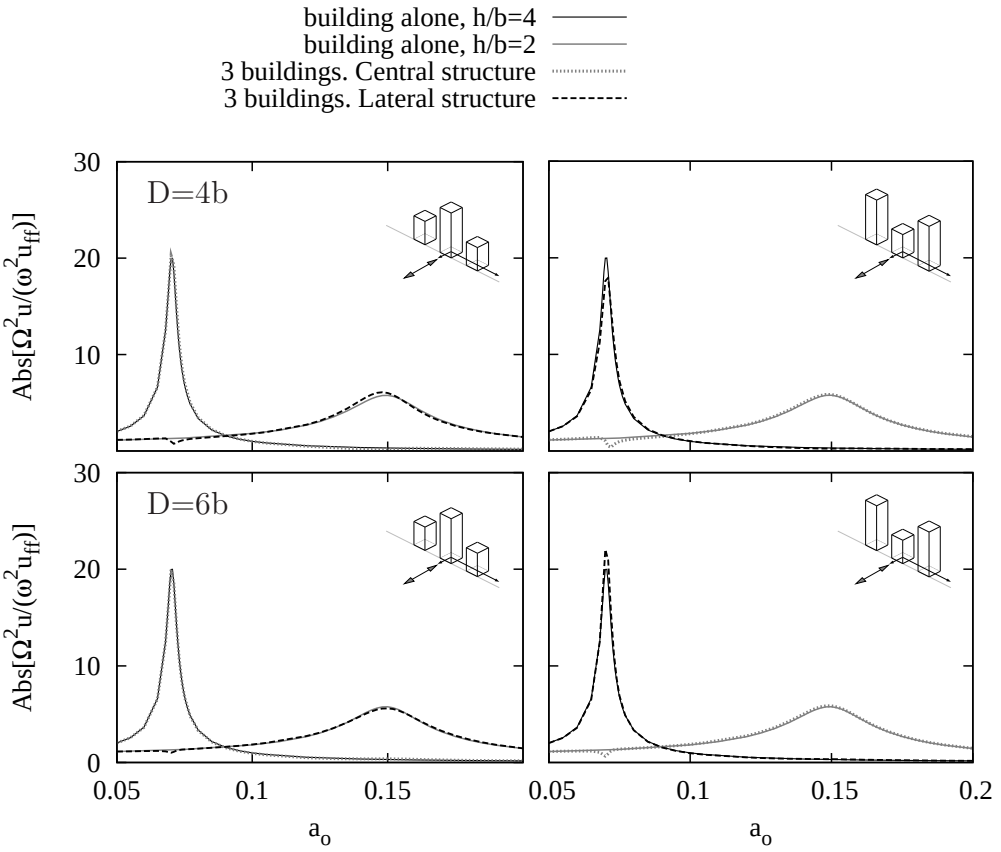

Figure 7.9: *Interaction between three structures of dissimilar fundamental frequencies in terms of their harmonic response spectra for different configurations under S waves. Structures aligned perpendicularly to the direction of shaking.* $h/b = 2$ *and* 4. $E_p/E_s = 100$.

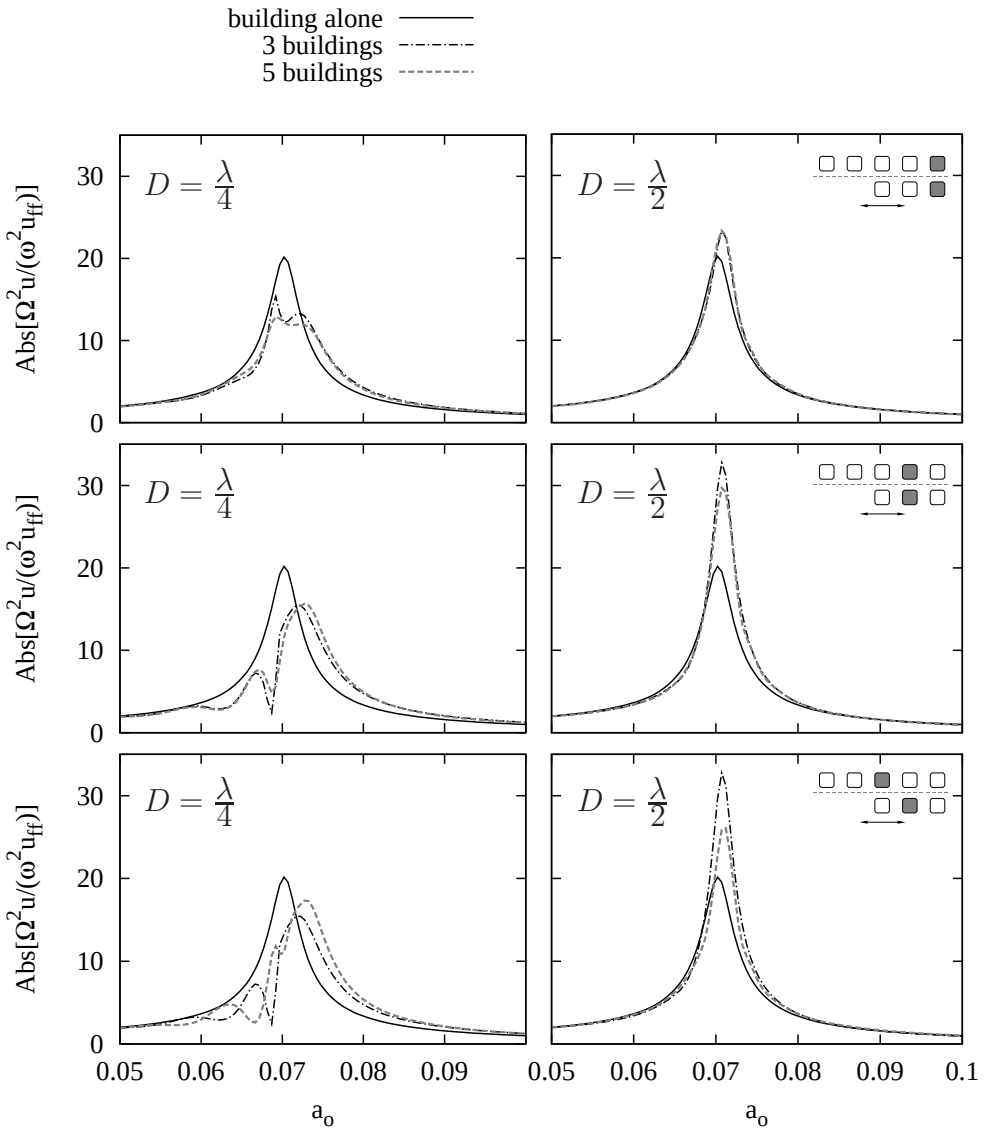

Figure 7.10: *Interaction between three or five structures of similar fundamental frequencies in terms of their harmonic response spectra under S waves. Structures aligned along direction of shaking. Comparison of behaviour of structures according to their position in the row.* $h/b = 4$. $E_p/E_s = 100$.

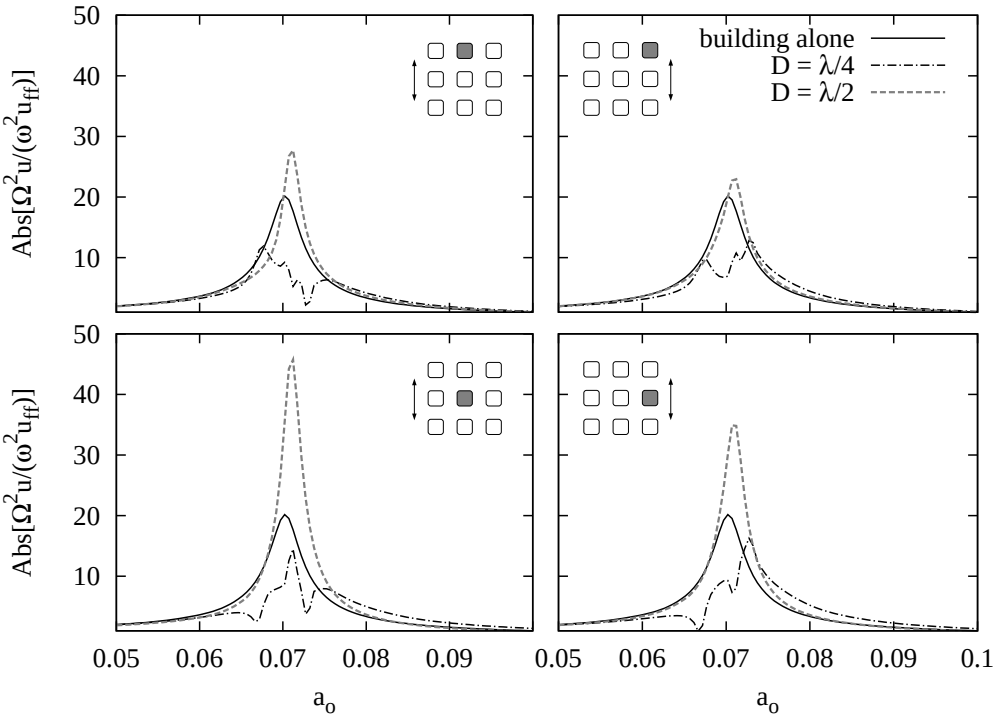

Figure 7.11: *Interaction between nine structures of similar fundamental frequencies in terms of their harmonic response spectra under S waves.* $h/b = 4$. $E_p/E_s = 100$.

The dynamic response of a group of five structures under vertically incident S waves is presented and compared to that of a group of three in fig. 7.10 for $E_p/E_s = 100$ and two values of D: $\lambda/4$ and $\lambda/2$. Buildings are aligned along the direction of shaking (arranged as shown in figs. 7.3*b* and *c*), and both cases are compared according to their position in the row. It becomes apparent how the dynamic behaviour of the structures is significantly similar when compared by pairs starting by the end positions. However, the responses of the respective central constructions are considerably different. Besides, the configuration of five structures appears to be slightly less unfavorable than that of three.

Now, a case of nine similar $h/b = 4$ structures arranged as shown in fig. 7.3d is analysed. To this end, fig. 7.11 shows the dynamic response of the single soil-structure system (solid lines), together with the response of similar buildings in a group of nine (non-solid lines), under vertically incident S waves in terms of their lateral deformation response spectra for $E_p/E_s = 100$. Two different distances between adjacent buildings ($D = \lambda/2$ and $\lambda/4$) are considered. This plot can be

compared with fig. 7.6, where the same problem but with only three structures is presented. It can be seen that, again, the general trend remains, *i.e.*, that the $D = \lambda/2$ configuration is much more unfavorable than the $D = \lambda/4$ situation, and that structures in central positions show significantly larger maximum response values. In this case, the central building increases its response by 130 per cent with respect to the response of the isolated soil-structure system.

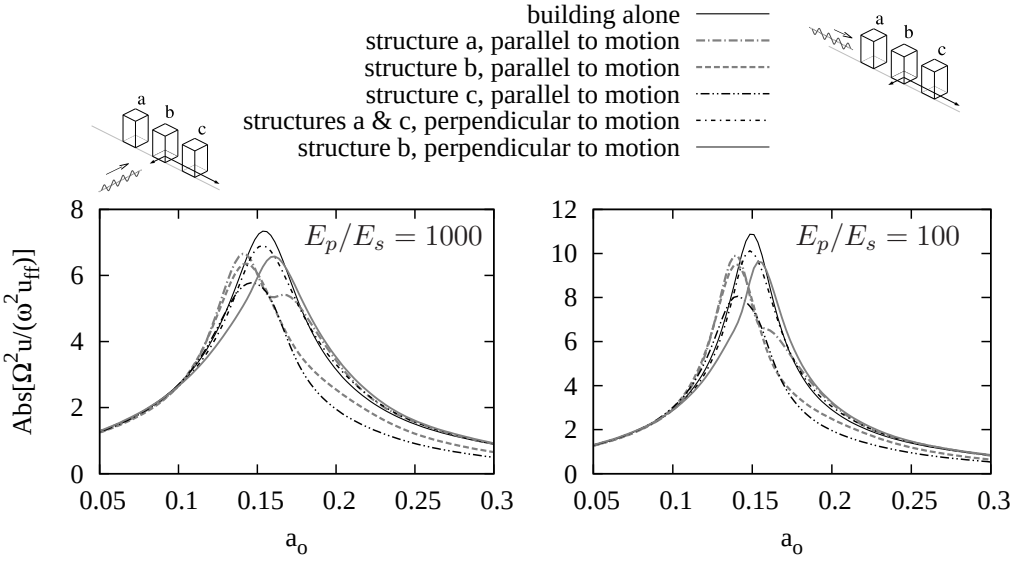

Figure 7.12: *Interaction between three structures of similar fundamental frequencies in terms of their harmonic response spectra under Rayleigh waves.* $h/b = 2$. $D = \lambda/2$.

The next three figures show the response of several groups of structures subject to incident Rayleigh waves. Fig. 7.12 presents the dynamic response of the single soil-structure system together with the response of groups of three similar $h/b = 2$ buildings in terms of their lateral deformation response spectra, for $D = \lambda/2$. Fig. 7.13 presents the same information for three identical $h/b = 4$ buildings and two distances ($D = \lambda/2$ and $\lambda/4$). Results for $E_p/E_s = 100$ and 1000 are presented for Rayleigh waves impinging parallel or perpendicularly to the direction of alignment of the structures. Firstly, it is worth noting that, when the system is impinged by Rayleigh waves, the most unfavorable separation, for the properties used in this work and among the considered distances, is $D = \lambda/4$, contrary to what happened with the vertically incident S waves. In fact, in this case, the grouping of the structures at distance $D = \lambda/2$ makes the seismic response smaller.

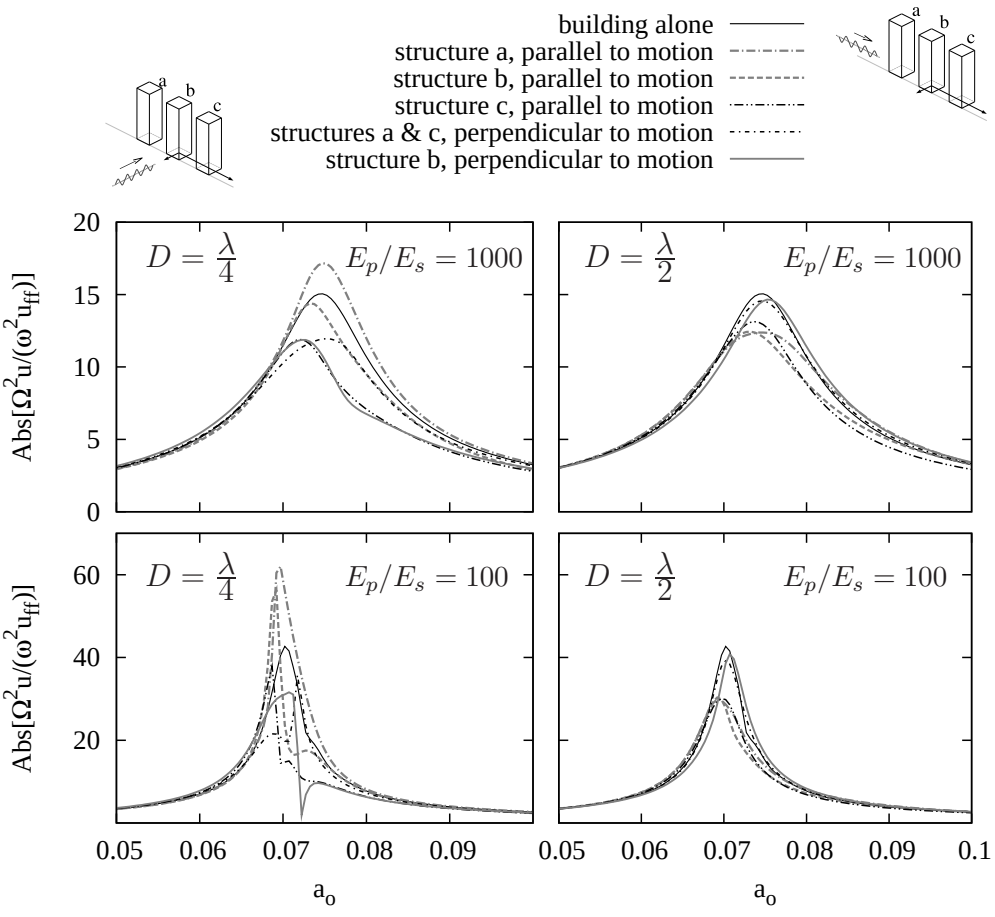

Figure 7.13: *Interaction between three structures of similar fundamental frequencies in terms of their harmonic response spectra under Rayleigh waves.* $h/b = 4$.

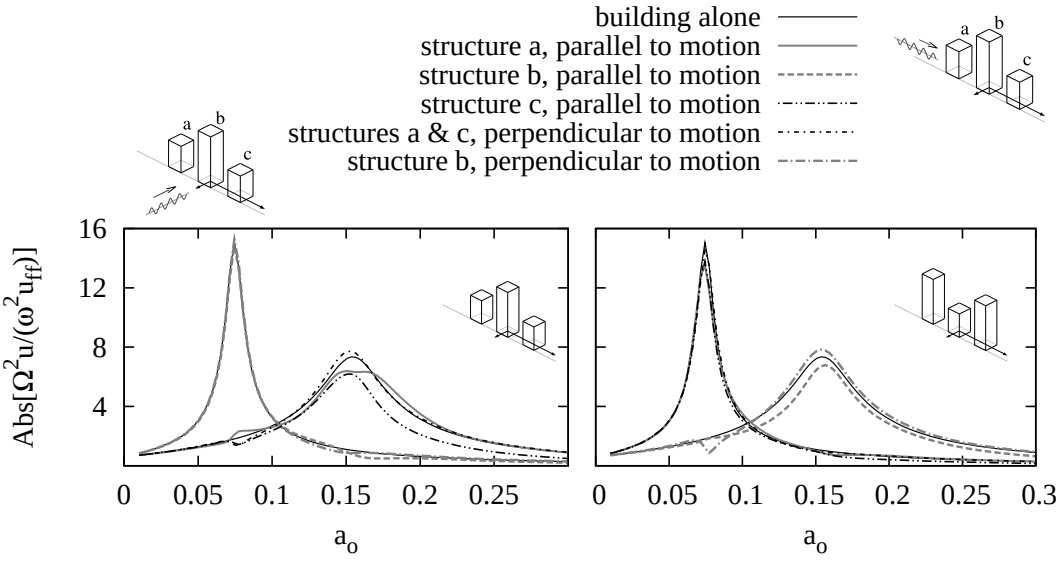

Figure 7.14: *Interaction between three structures of dissimilar fundamental frequencies in terms of their harmonic response spectra under Rayleigh waves.* $h/b = 2$ *and* 4. $E_p/E_s = 1000$. $D = 4b$.

Secondly, when seismic waves impinge in the direction of alignment of structures, a slight shifting in the fundamental period of the overall system is observed: up to 8 per cent smaller than that corresponding to the single soil-structure system. Also, shielding effects become apparent in this case. Around the overall system fundamental frequency, seismic response of the first structure to be impinged by the incident Rayleigh waves (labelled "a" in the figures) is significantly above the seismic response of the other two. The last structure (labelled "c") is usually the weakliest excited by the impinging waves, being its seismic response up to a 50 per cent smaller. Finally, both figures show that the overall behaviour of the system is independent of E_p/E_s (though, obviously, magnitudes change from one to another). The last of this set is fig. 7.14, where the response of three different structures $h/b = 2$ and 4 is presented for $E_p/E_s = 1000$ and $D = 4b$. In this case, similarly to what happened for the S waves, the interaction effects are negligible, except for the existent shielding effects.

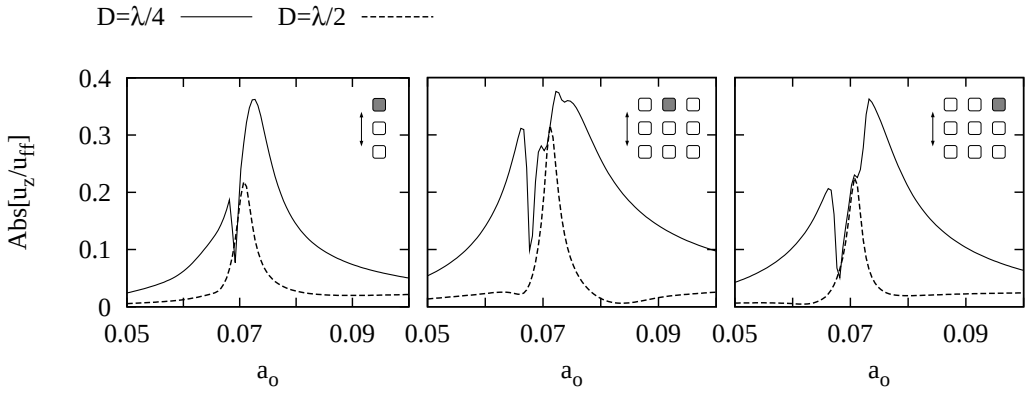

Figure 7.15: *Vertical displacement transfer functions of piled structures under vertically incident S waves due to SSSI.* $h/b = 4$. $E_p/E_s = 100$.

Vertical and rotational behaviour of adjacent pile supported structures is presented in terms of transfer functions in figs. 7.15 and 7.16 for vertically incident S waves, and in fig. 7.17 for incident Rayleigh waves. All results correspond to parameters $E_p/E_s = 100$ and $h/b = 4$. For incident S waves, results for groups of three and nine piled structures are shown, while for Rayleigh waves, only the response of three adjacent buildings is presented. In all cases, only the positions and configurations whose transfer functions are not zero are specified. Vertical displacements, measured at the centre of gravity of the caps, are normalized by the free-field horizontal or vertical motion for incident S or Rayleigh waves, respectively, while rotation is multiplied to the foundation halfwidth and normalized

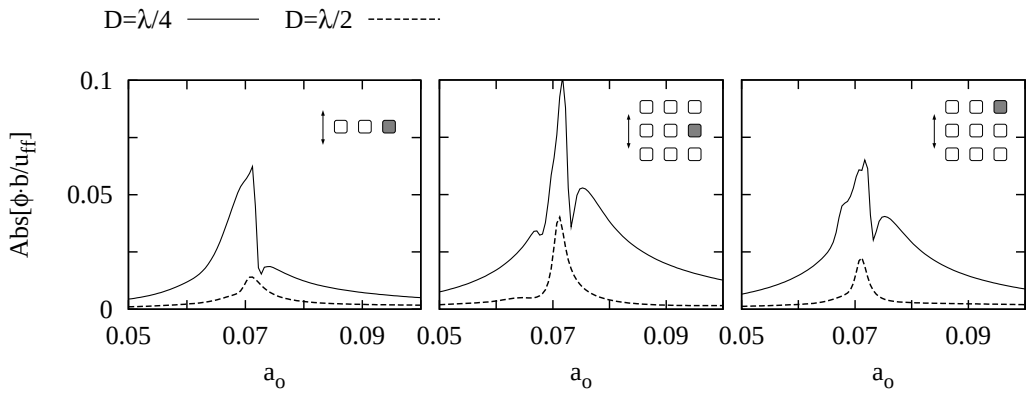

Figure 7.16: *Rotation transfer functions of piled structures under vertically incident S waves due to SSSI.* $h/b = 4$. $E_p/E_s = 100$.

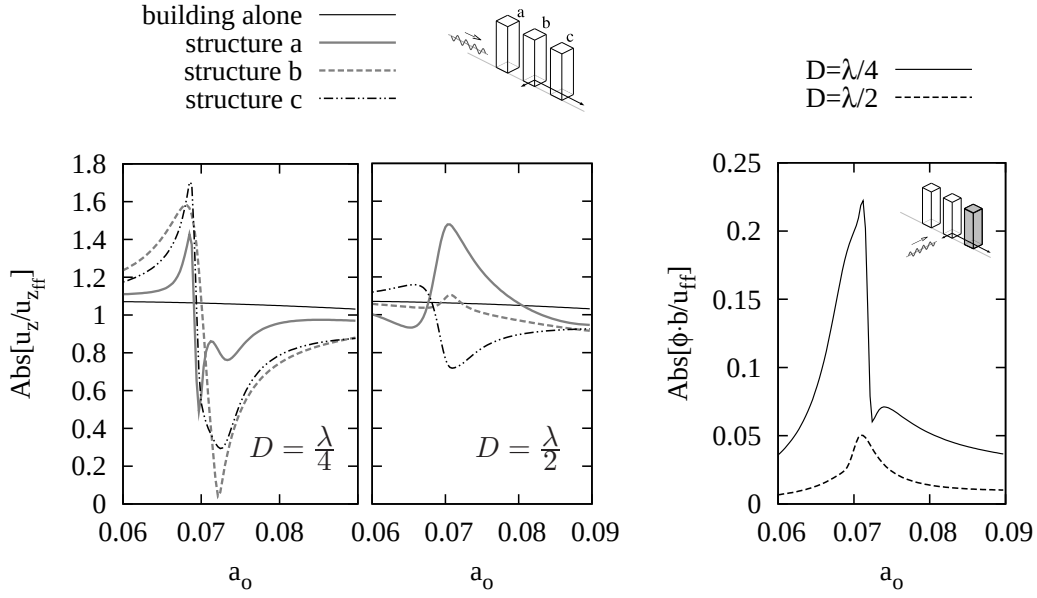

Figure 7.17: *Vertical motion and rotation transfer functions of piled structures under Rayleigh waves due to SSSI.* $h/b = 4$. $E_p/E_s = 100$.

by the free-field horizontal motion, so that the magnitude is indicative of the horizontal displacements at the external pile heads due to rotation. Fig. 7.15 shows that vertical displacements under incident S waves are greater for the shortest of the tested distances between adjacent buildings. For $D = \lambda/4$, vertical motions arising from structure-soil-structure interaction effects are above 35 per cent of horizontal motions at free-field ground level produced by the incident S waves, and for $D = \lambda/2$ they reach values between 20 and 30 per cent. The rotational response, shown in fig. 7.16, seems to be also of importance, as it produces horizontal displacements on piles of the order of 5 to 10 per cent of horizontal motions at free-field ground level. The system exhibits similar trends under the action of incident Rayleigh waves. In this case (fig. 7.17), SSSI can produce vertical motions up to 70 per cent larger than those presented by a single structure. At the same time, horizontal displacements on piles due to rotational response of buildings are above 20 per cent of horizontal motions at free-field ground level.

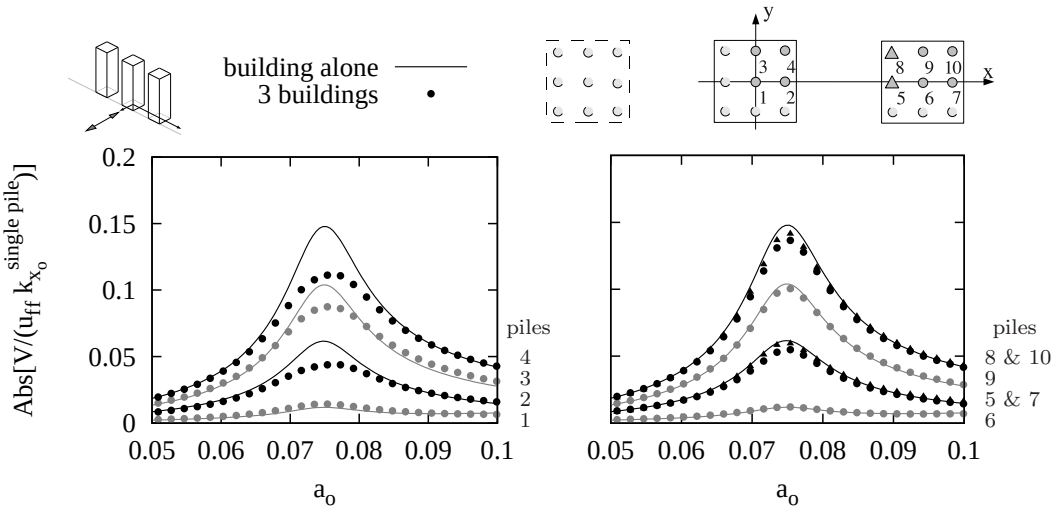

Figure 7.18: *Shear forces on pile heads under S waves. Three buildings aligned perpendicularly to shaking direction.* $h/b = 4$. $E_p/E_s = 1000$. $D = \lambda/3$.

Finally, figs. 7.18 and 7.19 compare shear forces at pile heads due to vertically incident S waves under $h/b = 4$ structures alone or when three identical buildings are separated $D = \lambda/3$ and aligned either perpendicularly or parallel to shaking direction. Shear forces are normalized by the static horizontal stiffness of a single pile and the free-field horizontal motion due to the incident seismic waves. When structures are aligned perpendicularly to shaking direction, shear forces at pile heads of lateral buildings are almost identical to those corresponding to a single building, while at the central cap, shear forces decrease with respect to the single

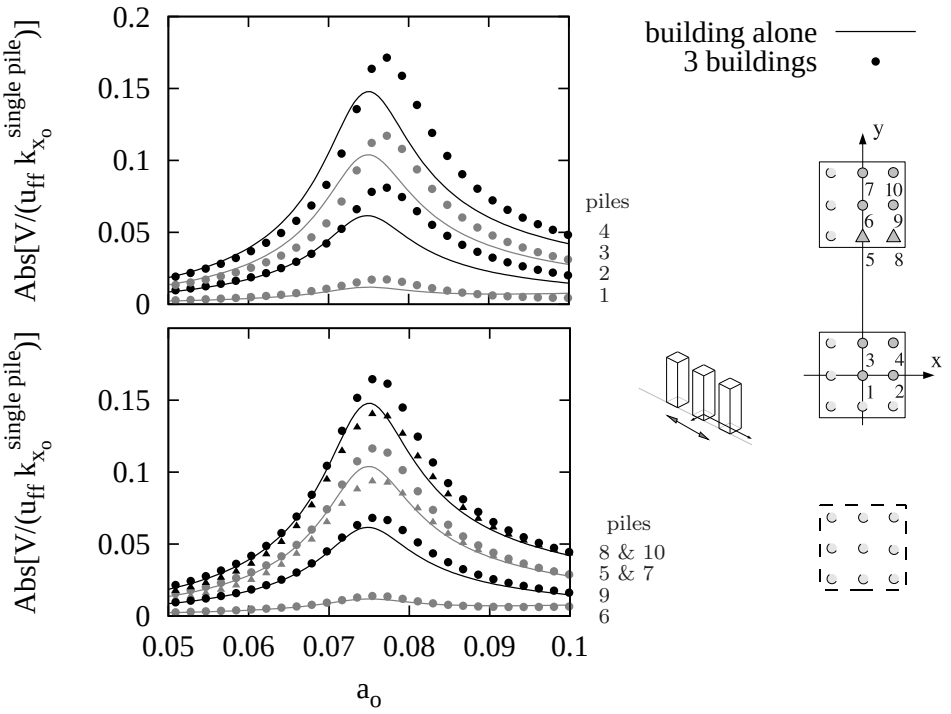

Figure 7.19: *Shear forces on pile heads under S waves. Three buildings aligned parallel to shaking direction.* $h/b = 4$. $E_p/E_s = 1000$. $D = \lambda/3$.

building case. On the contrary, when structures are aligned parallel to shaking direction, shear forces increase both under lateral and central buildings. More precisely, in this case corner piles are subject to forces up to 16 per cent greater.

7.4.2 Earthquake response

In this section, selected acceleration response spectra are presented in order to measure the influence of SSSI on the seismic response of structures. Results in the time domain are obtained by Fourier transformation, using the fast Fourier transform (FFT) algorithm. An artificial accelerogram, compatible with AFPS-90 [162] chapter 5.7 normalized response spectrum (shown in fig. 7.20), has been produced making use of SIMQKE [163]. Signal's total length and peak acceleration are 18 seconds and 0.17 g, respectively. Five per cent damped peak spectral response acceleration of artificial signal and target spectrum are 0.463 g and 0.425 g, respectively. The reason why a synthetic accelerogram has been used instead of a recorded one is the greater smoothness of the target response spectra, which clarifies the results. Two kinds of soils has been chosen, and the system properties used to compute these results are summarized in table 7.1, being $h/b = 4$. It is worth saying that the soil-structure system fundamental periods are $\tilde{T} \simeq 0.40$ and 0.67 s for the first and second soils, respectively.

Soil	**Piles**	**Structures**
$c_s^{(1)} = 239\ m/s$	$E_p = 2.76 \cdot 10^{10}\ N/m^2$	$T^{(1)} = 0.28\ s$
$c_s^{(2)} = 134\ m/s$	$E_p = 2.76 \cdot 10^{10}\ N/m^2$	$T^{(2)} = 0.50\ s$
$\rho_s = 1750\ kg/m^3$	$\rho_p = 2500\ kg/m^3$	$m = 7 \cdot 10^5\ kg$
$\nu_s = 0.4$	$d = 1\ m$	$h = 20\ m$
$\beta_s = 0.05$	$L = 15\ m$	$\zeta = 0.05$

Table 7.1: *Soil, piles and structures properties.*

Five per cent damped acceleration response spectra, corresponding to an isolated structure and to the central building of three adjacent constructions separated either $D = \lambda/4$ or $D = \lambda/2$, and aligned along the direction of shaking, are presented. They have been obtained assuming that the system is subject to the input accelerogram that was described above, prescribed at free-field surface, and that the seismic motion is caused by vertically incident S waves. The system transfer functions are part of those used to compute the results shown in fig.7.7.

Fig. 7.20 shows the system response measured at pile caps together with the free-field and target response spectra, while fig. 7.21 shows the response measured

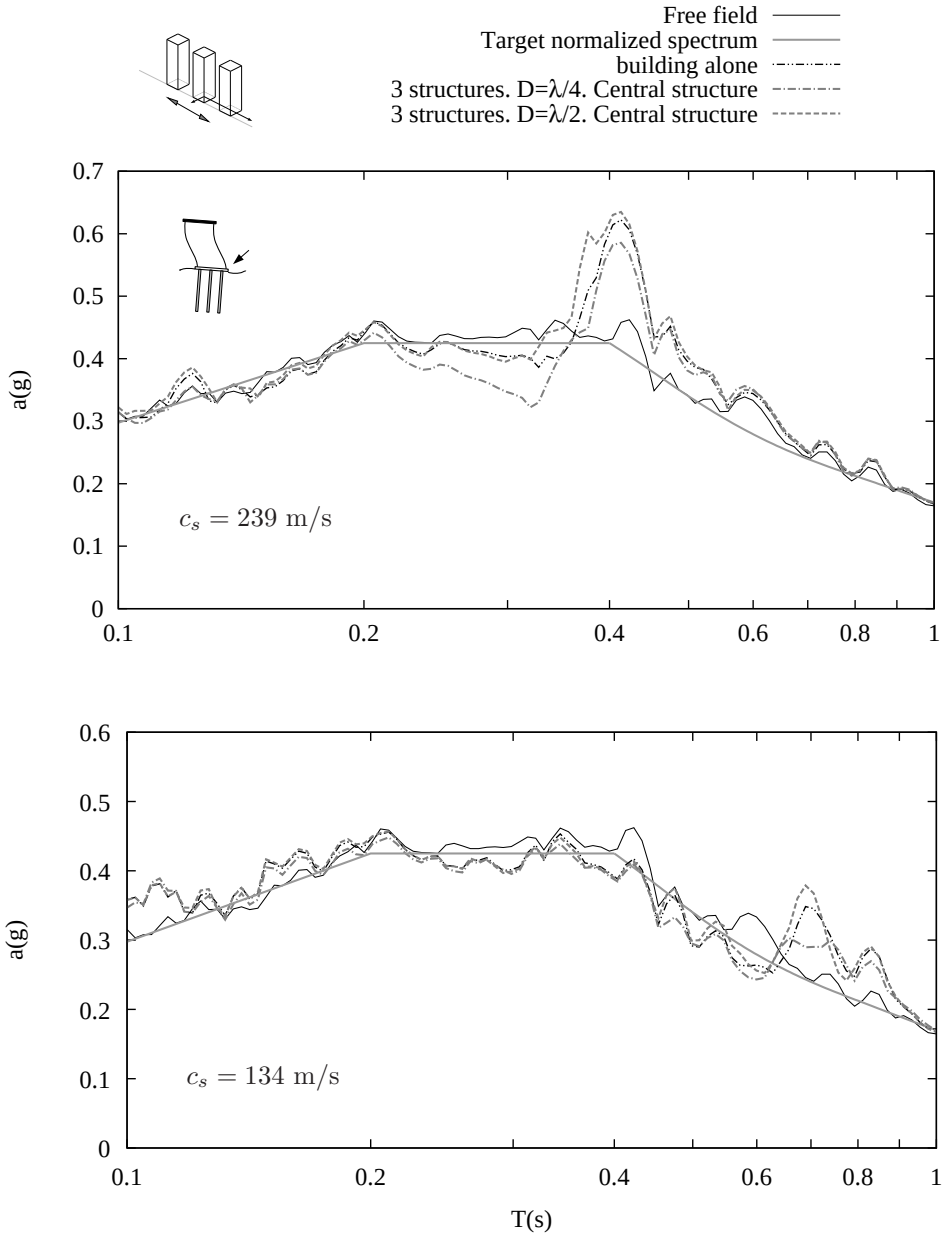

Figure 7.20: *Five per cent-damped acceleration response spectra. Group of three $h/b = 4$ structures under S waves. Response at the pile cap.*

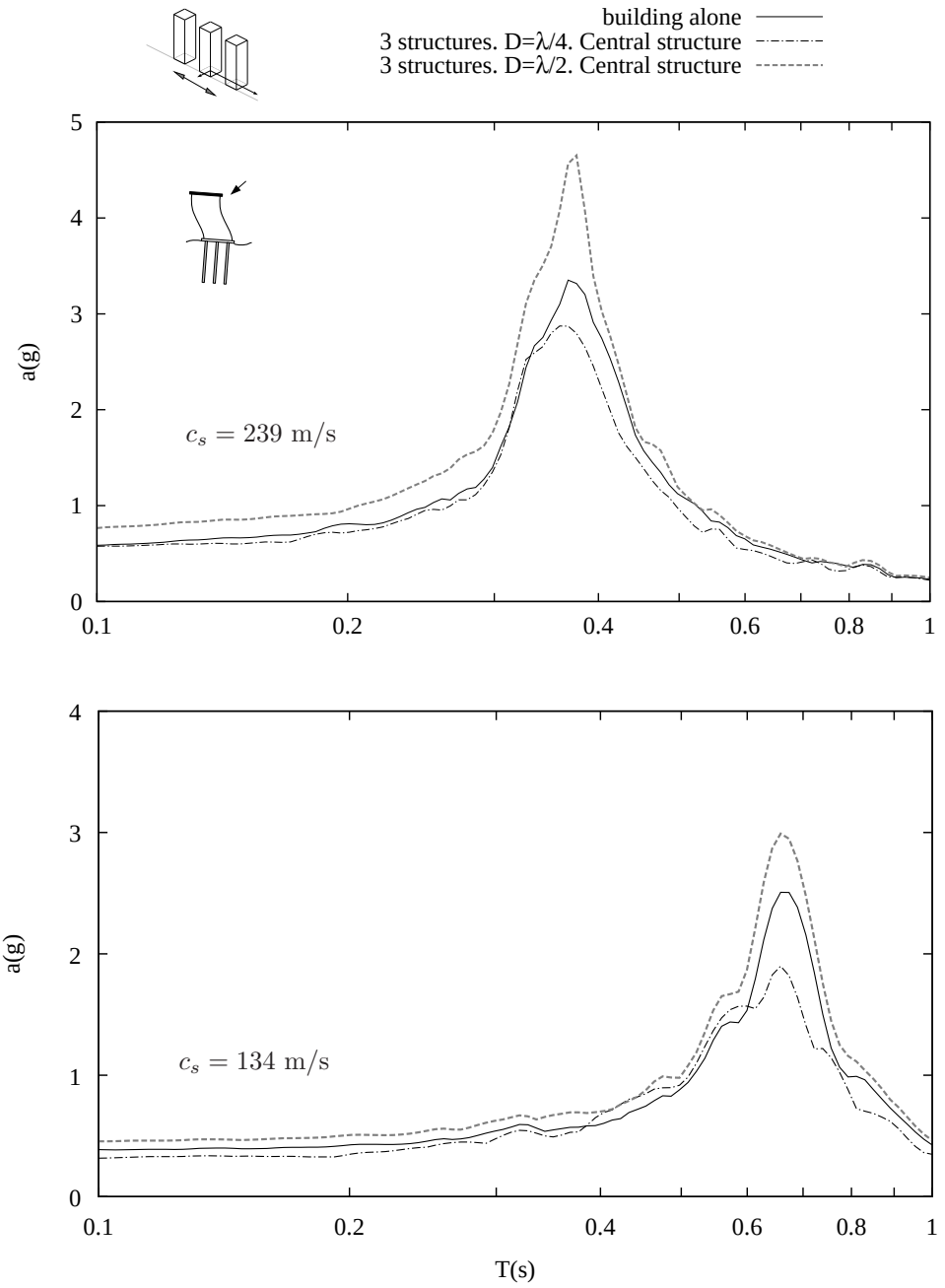

Figure 7.21: *Five per cent-damped acceleration response spectra. Group of three $h/b = 4$ structures under S waves. Response at the slab at height h.*

at slabs at height h. Obviously, peak spectral response acceleration at pile caps is highly influenced by the presence of the superstructure at periods around soil-structure system fundamental frequency. On the contrary, in this range, it is little influenced by the presence of other structures in the neighbourhood, being the increment in the response not larger than 8 per cent in any case. However, for periods around 0.32 seconds, differences due to SSSI reach 20 per cent for $c_s = 239$ m/s. On the other hand, peak spectral response acceleration measured at height h is significantly influenced by the presence of nearby structures. In comparison to the peak response of a single structure, the one corresponding to the central building of a group is 15 per cent lower for $D = \lambda/4$ and 38 per cent higher for $D = \lambda/2$, in the case of $c_s = 239$ m/s, and 25 per cent lower for $D = \lambda/4$ and 18 per cent higher for $D = \lambda/2$, in the case of $c_s = 134$ m/s. Consequently, neighbouring pile supported structures can significantly increase the seismic response of a structure.

7.5 Conclusions

The 3D numerical procedure for the dynamic analysis of pile supported linear structures proposed in this work has been used to address the problem of through-soil interaction between neighbouring one-storey shear buildings. A particular set of parameters and problem configurations was chosen to perform the analysis, which obviously does not intend to be a comprehensive study. One-storey shear buildings, founded on 3×3 pile groups in a viscoelastic half-space, with different aspect ratios and separations between adjacent structures, were considered. Lateral spectral deformation, vertical and rotational transfer functions, harmonic shear forces at pile heads, and maximum response spectra are presented in order to assess the influence of structure-soil-structure interaction phenomena on the structural seismic response of neighbouring buildings subject to incident S or Rayleigh waves.

SSSI effects have been found to be of importance in the case of groups of structures with similar dynamic characteristics, chiefly in the structural response around the overall system fundamental frequency. Depending on the distance between adjacent buildings, which is expressed in terms of the soil wave length $\lambda = c_s\tilde{T}$ at the soil-structure fundamental period $\tilde{T}$, the seismic response of each member of the group can increase or decrease. For vertically incident S waves, and for the set of properties and configurations selected for this work, the most unfavorable distance appears to be $D = \lambda/2$. For this separation between adjacent buildings, large amplifications have been observed in the response of groups of three and five aligned structures, and even larger motions for a square group of nine similar constructions. The highest amplifications occur at central constructions

and when the impinging waves produce motions in the direction of alignment of the structures. On the other hand, in the case of groups of dissimilar structures, SSSI effects are not that important, being the situation of short-period buildings placed among long-period constructions the most unfavorable configuration.

On the other hand, when Rayleigh waves impinge in the same direction of alignment of the structures, the first building to be hit suffers the largest displacements and, at the same time, shielding effects become apparent. In this case, contrary to what happened for S waves, the most unfavorable of the tested distances is $D = \lambda/4$. For Rayleigh waves impinging perpendicularly to the direction of alignment of the structures, the overall response is usually attenuated.

Vertical and rotational motions induced by SSSI have been found to be also of importance for both S and Rayleigh waves. For instance, vertical displacement amplitudes of lateral structures of groups impinged by S waves can reach values of 35 per cent of horizontal motions at free-field ground level. In addition, shear forces at pile heads can also be amplified due to SSSI.

In view of the results, it is apparent that further studies about structure-soil-structure interaction phenomena and their influence on structural seismic risk are mandatory, as it has been shown that nearby buildings can significantly increase the seismic response of a structure. Influence on the system response of foundation characteristics, structural configuration and design, relationships between dynamic properties of neighbouring structures, subsoil properties and stratigraphy, and characteristics of the seismic excitation, should be addressed.

Chapter 8

Summary, conclusions and future research directions

8.1 Summary and conclusions

This dissertation proposes a new three-dimensional boundary element – finite element coupling model for the dynamic analysis of pile foundations and pile supported structures, in which each region of the soil is modelled by the BEM as a linear, homogeneous, isotropic, viscoelastic domain, and each pile is modelled by the FEM as a vertical Euler-Bernoulli beam. This approach considers the tractions at the pile-soil interfaces as body forces acting within the domain, while the stiffness of the pile is taken into account by introducing longitudinal finite elements, without the need of discretizing the pile-soil interfaces by boundary elements. This means that, in the model, the presence of the piles does not imply the existence of a hollow in the domain that represents the soil. On the contrary, the soil region is continuous at the positions of the piles. At first, this fact could give the impression that the model cannot represent correctly the effects of the multiple interaction phenomena that take place in the pile-soil system, including reflection and refraction of waves. However, it has been shown that the formulation is able to produce accurate results involving multiple piles and incident seismic waves.

Body forces are considered to be zero in most of the applications of the boundary element method to the elastodynamic problem. This way, the domain integral that appears in the general expression of the corresponding integral equation vanishes. Here, on the contrary, body forces are different from zero at the pile-soil interface and, consequently, the domain integral must be evaluated in that region. In general, however, this new integral is evaluated along a line defined by the pile axis without loss of accuracy. The exception appears when the collocation point belongs to the integrated element, case in which there exists a singularity.

This situation is solved by integrating that element over the pile-soil interface geometry, although it was shown that this procedure is completely equivalent to a non-nodal collocation strategy.

This coupling model was succesfully formulated and implemented in a previously existent 3D BEM code belonging to the research group of continuum mechanics and structures of the University of Las Palmas de Gran Canaria. In fact, this dissertation is just another step in the research line on soil-structure interaction problems that is being carried out in collaboration between the University of Las Palmas de Gran Canaria and the University of Seville, and under the supervision of Professors José Domínguez and Orlando Maeso. The work of the group of Las Palmas de Gran Canaria has been focused mainly, but not only, on the development of numerical tools for the analysis of the seismic response of arch dams [111–113, 116]. This determination resulted in the dissertation of Prof. Juan José Aznárez [114], who enhanced the previous code by, among many other improvements, including the possibility of modelling poroelastic regions according to Biot's theory. Making use of this multidomain code for three-dimensional problems, several works on the dynamic analysis of arch dams with porous sediments have been presented [115, 117, 118]. Such program was also used to obtain impedance functions of piles and pile groups in viscoelastic and poroelastic soils [63, 64], and was subsequently the basis of the code developed for the work presented in this dissertation.

Obviously, the fact that pile-soil interfaces are not discretized, results in a significant saving in degrees of freedom, which was one of the aims of the work. The other objectives have also been fulfilled. The code allows general and relatively simple modelling of multiple pile foundations made up by vertical piles and rigid caps. The soil discretization, able to model the topography and stratigraphy of the site, is completely independent of the foundation discretization. Consequently, several analysis, involving different foundation configurations, can be performed with little extra effort in the generation of the data files. Also, the presence of multiple pile supported superstructures has been formulated and implemented, and a wide set of boundary conditions are available to the user. Finally, the whole formulation is relatively easy to implement in a previously existent BEM code, which may increment its interest to the scientific community.

This BEM-FEM scheme has been used to study several problems related to the seismic response of pile foundations and pile supported structures. In order to make the exposition clear, and due to the fact that most of these cases are of different nature, the author has opted for reproducing here the conclusions of each section, instead of summarizing them.

Analysis of the distribution of shear forces along piles in a group

An analysis of the distribution of shear forces along some of the piles in a 5×5 pile group has been performed. Some results have been presented for a unitary horizontal displacement imposed at the pile cap, and the conclusions that can be drawn from them are:

- In the quasi-static state,
  - the distribution of shear forces is approximately exponential with depth, being the lateral loads withstood mainly by the upper part of the piles.
  - the *active length* of the piles is shorter for $E_p/E_s = 10^2$ (stiffest soil)
  - the central pile a and corner pile d are the ones withstanding, respectively, the lowest and the highest fraction of load.
- For intermediate and high frequencies,
  - the distribution of shear forces at a certain time t fluctuates around zero and, the higher the frequency, the shorter the 'wave length'.
  - the magnitude of the shear forces is maximum at pile heads, but it can also reach relatively high values in the bottom half of the pile.
  - significant shear forces may appear along the whole length of the pile, and not only along its *active length*.
  - the fraction of load withstood by each pile in the group, as well as the position of the pile resisting the highest fraction, depends on the frequency.

Dynamic stiffness of pile foundations in homogeneous strata

The BEM-FEM coupling model presented in this work has been used to compute time-harmonic impedance functions of piled foundations embedded in viscoelastic homogeneous strata resting on a rigid bedrock. Several results of vertical, horizontal and rocking impedances for single piles and three different configurations of 2×2 pile groups have been presented. Several depths of the stratum and two different ratios between the Young's moduli of pile and soil have been studied, and the effects associated to each of these parameters have been highlighted. From the analysis of these results, the following conclusions can be drawn:

- The pile-soil system presents small peaks associated to the stratum natural frequencies that the numerical model is able to predict adequately.

- The vertical impedance functions of a pile foundation embedded in strata of the analysed depths are equivalent to those embedded in a half-space at frequencies above 1.5 times the fundamental frequency of the stratum in the dilatational mode. Besides, the foundation vertical behaviour is only influenced by this natural frequency.

- The influence of the stratum depth over the horizontal impedance functions of a pile foundation is significant over a broader band of frequencies. Thus, several peaks associated to both the shear and the dilatational modes appear in the foundation response.

- This influence is even more evident in the damping functions, which at low frequencies are much smaller than those corresponding to the half-space. On the contrary, their values are similar at higher frequencies, which reveals that the main damping mechanism at intermediate and high frequencies is the energy dissipation through surface waves for both the half-space and the strata.

- The influence of the presence of the rigid bedrock is still noticeable for a stratum depth five times the pile length.

- The group effect is predominant over the influence of the presence of the rigid bedrock, especially in vertical and rocking impedances, in which the peaks associated to the natural frequencies of the stratum are of small magnitude. However, the effects of the presence of the bedrock on the horizontal behaviour are stronger and become evident along a broader frequency band. In all cases, the influence of the rigid bedrock increases with the ratio s/d.

- The frequency band in which the foundation response is influenced by the rigid bedrock broadens with the increase of the soil stiffness and, at the same time, a larger number of natural frequencies of the stratum in both the shear and the dilatational modes becomes evident for the horizontal and rocking cases.

- The group effect becomes more evident as the ratio E_p/E_s increases.

- The rocking behaviour is the less influenced by the presence of a rigid bedrock.

- The difference between the vertical response of floating and hinged pile foundations increases with the ratio E_p/E_s, and is always noticeable.

- The group effect becomes apparent in the case of hinged pile groups. In fact, for hinged pile groups embedded in a stiff stratum, the vertical stiffness

functions tend to be equivalent to those of floating pile groups above a certain frequency which decreases when the ratio s/d increases. Thus, in these cases, the active pile length is far shorter than the stratum depth.

As can be seen from the foregoing discussion, the effect of the presence of the rigid bedrock is vital for the horizontal behaviour of single piles and pile groups, and also for the rocking behaviour of single piles, while it is almost negligible for the rocking behaviour of pile groups. Regarding the vertical behaviour of floating pile foundations, the effect of the bedrock is not important except for frequencies below 1.5 times the fundamental frequency of the stratum. At the same time, the influence of the surrounding soil is of great importance even for hinged pile foundations, due to the fact that the influence of the boundary condition at the piles tips becomes less significant as the ratio E_p/E_s decreases.

Seismic response of pile groups to vertically-incident shear waves

The seismic response of a square 3×3 hinged pile group embedded in different soil profiles and under vertically-incident plane time-harmonic shear waves and two different strong ground motions, has been studied. General conclusions cannot be drawn without more and deeper analysis on the subject but, as for the presented case, it has been shown that:

- the presence of a soft layer atop the soil yields to much more rapidly decreasing displacement transfer functions than those corresponding to foundations in the reference homogeneous soil. In fact, two different trends are clearly defined, depending on whether the soft layer is considered or not.

- the addition of further intermediate shear wave velocity layers in between is of minor importance.

- the incident field at the free surface is perturbed by the presence of the pile foundation, being the magnitude of this perturbation larger when a soft layer exists atop. The maximum value of this perturbation is of similar order in both the direction of motions induced by the S waves and its perpendicular.

- pile-to-pile interaction under seismic excitation is almost non-existent.

- pile foundations embedded in the non-homogeneous soil profiles studied here filter out a great part of the harmonic components of the seismic input, in such a way that the resulting acceleration response spectra are significantly lower than those corresponding to the free field.

- the simplification of the soil profile to just one stratum or to a half-space would lead to over- or underestimating, depending on the chosen properties, the excitation at the base of a superstructure in a substructuring analysis.
- these conclusions are valid for earthquake motions specified at either the free surface or at the bedrock.

Dynamic analysis of piled embedded footings

The steady-state dynamic behaviour of piled embedded footings was investigated in order to: first, find out if its seismic response can be estimated from that of their components analysed separately; and second, to study the influence, on dynamic stiffness and damping, of loss of contact between soil and the underside of an embedded footing reinforced with piles, due to soil consolidation effects. To this end, a set of numerical parametric analyses were carried out.

It was shown that the impedances obtained by superposition of pile group and footing stiffness functions are generally higher than that arising from the analysis of the system as a single problem. This difference can be attributed to interaction phenomena between the pile group and the embedded footing, which are neglected in the superposition approach. More precisely, vertical, horizontal, rocking and cross-coupled terms can be up to 100%, 50%, 20% and 20% higher, respectively, though differences decrease rapidly with frequency. On the other hand, phase differences are normally below 20^o and denote that the damping capacity of the system acting as a whole is greater than that estimated from the superposition. This effect is particularly apparent in the vertical and horizontal mode and at low frequencies. Besides, the dependence of the response to parameters such as separation between adjacent piles and pile-soil stiffness ratio was elucidated. The effect of embedment was shown to be particularly important, for it was observed that the more embedment, the smaller the difference between rigorous and superposition-based estimates. This trend can be understood given the omission of embedment effects in the assessment of pile group impedance. Overall, the superposition approach was found to be sound as an engineering tool, with average discrepancies not exceeding 20%.

Regarding kinematic effects, piled embedded footings were found to be less compliant to the soil movement than their parts analysed separately. Translational kinematic response factors decrease faster with frequency than those corresponding to pile groups or footings alone, while rotational kinematic interaction factors were found to increase more rapidly. Overall, kinematic response of embedded footings has been found to provide suitable estimates of the piled embedded footings behaviour.

As for the importance of footing-soil separation on dynamic stiffness functions of piled embedded footings, it was demonstrated that

- The influence of separation is negligible for frequencies below those for which dynamic group effects start becoming apparent.
- The effect of separation is more noticeable in the vertical mode and may decrease the stiffness of the system by 50% beyond $a_o = 0.5$. On the other hand, the change in stiffness is minimized in the lateral mode and does not exceed 20%.
- The overall stiffness of the foundation when no separation exists is not necessarily higher than that corresponding to the system after soil consolidation. The relationship between the dynamic stiffness in both cases depends on the constructive and destructive interference of the waves generated at the pile-soil and the footing-soil interfaces, and, therefore, is frequency-dependent.
- A counterbalance between footing and pile group stiffness contributions was found to exist under loss of soil-pile cap contact.
- The contribution of the pile group to the overall stiffness of the system is independent of embedment, although it depends on the ground-cap contact condition, i.e., changes between ground-raised and ground-contacting caps. This property can be used to simplify the models when estimating the impedance functions of piled footings by superposition approaches.

SSI analysis of pile supported structures by substructuring

The influence of SSI on the dynamic response of pile supported structures was studied by means of parametric analyses in which foundation configuration, slenderness ratio and structure-soil relative stiffness were taken into account. It has been proved that SSI effects can be of importance for pile supported structures founded on relatively soft soils or for relatively stiff structures, and that this influence can be both beneficial or detrimental, depending mainly on the structural slenderness ratio. Afterwards, the sensitivity of these results to variations of some other parameters, usually considered to be of minor importance, was assessed, finding such assumption to be valid. The influence of kinematic interaction effects on the dynamic response of pile supported structures was also studied, finding that it only affects to the system equivalent damping.

Dynamic structure-soil-structure interaction between nearby piled buildings under seismic excitation

The 3D numerical procedure for the dynamic analysis of pile supported linear structures proposed in this work has been used to address the problem of through-soil interaction between neighbouring one-storey shear buildings. A particular set

of parameters and problem configurations was chosen to perform the analysis, which obviously does not intend to be a comprehensive study. One-storey shear buildings, founded on 3×3 pile groups in a viscoelastic half-space, with different aspect ratios and separations between adjacent structures, were considered. Lateral spectral deformation, vertical and rotational transfer functions, harmonic shear forces at pile heads, and maximum response spectra are presented in order to assess the effects of structure-soil-structure interaction phenomena on the structural seismic response of neighbouring buildings subject to incident S or Rayleigh waves.

SSSI effects have been found to be of importance in groups of structures with similar dynamic characteristics, around the overall system fundamental frequency. Depending on the distance between adjacent buildings, which is expressed in terms of the soil wave length $\lambda = c_s\tilde{T}$ at the soil-structure fundamental period $\tilde{T}$, the seismic response of each member of the group can increase or decrease. For vertically incident S waves, and for the set of properties and configurations selected for this work, the most unfavorable distance appears to be $D = \lambda/2$. For this separation between adjacent buildings, large amplifications have been observed in the response of groups of three and five aligned structures, and even larger motions for a square group of nine similar constructions. The highest amplifications occur at central constructions and when aligned structures are placed in parallel to shaking direction. On the other hand, in the case of groups of dissimilar structures, SSSI effects are not that important, being the situation of short-period buildings placed among long-period constructions the most unfavorable configuration.

On the other hand, when Rayleigh waves impinge in the same direction of alignment of the structures, the first building to be hit suffers the largest effects while shielding effects become apparent. In this case, contrary to what happened for S waves, the most unfavorable of the tested distances is $D = \lambda/4$. For Rayleigh waves impinging perpendicularly to the direction of alignment of the structures, the overall response is usually attenuated.

Vertical and rotational motions induced by SSSI have been found to be also of importance for both S and Rayleigh waves. For instance, vertical displacement amplitudes of lateral structures of groups impinged by S waves can reach values of 35 per cent of horizontal motions at free-field ground level. In addition, shear forces at pile heads can also be amplified due to SSSI.

8.2 Future research directions

The BEM-FEM formulation presented in this work has been used to perform several studies involving the dynamic and seismic response of pile foundations and pile supported structures. Using the code in its present form, some other interesting analyses that may be carried out are:

- A parametric study on the seismic response of pile groups to vertically-incident S and P waves, and to incident Rayleigh waves. Consequently, the analysis presented in chapter 4 should be enhanced in order to include a wider set of foundation configurations, subsoil configuration and site characteristics. Different types of seismic waves, as well as different directions of incidence, should also be considered. Results should be also obtained in the time domain for groups of recorded and synthesized earthquake motions coherent with the site characteristics. This way, the magnitude of the influence of each parameter could be assessed, not only in terms of transfer functions, but also in terms of time responses.

- A comprehensive analysis of the influence of neighbouring constructions on the seismic response of pile supported structures. This would be an extension of the work presented in chapter 7, and should include the influence on the system response of parameters such as foundation characteristics, structural configuration and design, subsoil properties and stratigraphy, type and direction of the incident seismic waves, and relationships between dynamic properties of neighbouring structures.

- Analysis of the shear forces and bending moments induced in the pile foundations of pile supported structures subjected to seismic excitation. In linear soil-structure models, these forces can be considered to be a result of two different phenomena: *(i)* the motion of the superstructure, and *(ii)* the motion of the soil due to the incident seismic waves. The first component produces what is called *inertial-interaction* forces, while the second component produces *kinematic-interaction* forces. In common engineering practice, inertial-interaction forces, that can be more easily estimated with the available simplified procedures, are given much importance in design. Kinematic-interaction forces, on the contrary, are usually considered to be of minor importance. However, recent papers (see e.g. [75–77]) have shown the importance of this last component on the seismic performance of pile foundations. For this reason, it is of interest to analyse the seismic shear forces and bending moments in pile foundations as a function of different parameters such as: superstructure slenderness ratio, soil-structure stiffness ratio, soil-structure mass ratio, number and position of pile foundations,

pile foundation configuration, pile-soil stiffness ratio, stratigraphy of the soil, presence of neighbouring structures, type of the incident waves and direction of incidence.

On the other hand, the code could be improved, from the point of view of the implementation, or from the purely numerical point of view, in a number of ways, some of which are:

- The implementation of a sparse matrix storage format, which would make it possible to store and use only the non-zero terms of the system matrix, with the subsequent saving in memory requirements. It is worth remembering here that blocks of zeros are generated in the system matrix, not only due to the pile-soil coupling, but also due to the coupling between different BEM regions.
- The parallel implementation of iterative solvers, in conjunction with suitable preconditioners and a sparse matrix storage format, as said above.
- The parallelization of the code, even in its present form, which would imply a very important reduction in the required computing times.
- In order to simplify the meshing work and increase the accuracy in the solution, mesh refinement and smoothing techniques could be implemented (see e.g. [164, 165]).
- The reformulation of the model and its implementation into a fast multipole boundary element code, which would allow the solution of large-scale problems with extremely low memory requirements and computing times.

Finally, both the formulation and the code can be enhanced in a number of different ways, some of which are listed below:

- Formulation of inclined piles, which are receiving increasing attention in the geotechnical community. In fact, the problem can be generalized by considering general curvilinear finite elements, also with the possibility of modelling different structural elements with multiple common points. This way, the code could be applied to the analysis of inclined piles, pile foundations with a tree configuration within the soil and other buried structures different from piles, such as tunnels.
- Implementation of incident S and P waves with any direction of incidence, in such a way that the effects of this parameter on the seismic response of pile foundations and pile supported structures could be assessed. It would

also allow the evaluation of the content of the most unfavorable earthquake with respect to a certain parameter, such as the magnitude of motions at the ground surface.

- Formulation of a new model, based on the same idea of the scheme presented herein, for the dynamic analysis of walls embedded in soils. Walls would be discretized with thin plate/shell finite elements.

- Formulation of a BEM-FEM scheme able to model the interaction between a pile and surrounding water, i.e. between a pile and a potential region. This would lead to a more general formulation able to model the dynamic behaviour of a pile embedded in a poroelastic soil.

- Formulation of pile raft foundations by means of thin plate/shell finite elements. This would allow the analysis of very large pile groups, case in which the assumption of rigidness of the pile cap is not generally acceptable, and would imply establishing equilibrium and compatibility conditions between the raft (modelled by finite elements) and the soil surface (modelled by boundary elements), with the obvious associated difficulties.

- Formulation of a fundamental solution for the half-space, with which the discretization of both the free surface and the horizontal interfases, in case of horizontally-layered soils, are avoided.

Bibliography

[1] Hall, W. S. and Oliveto, G. (eds.) (2003) *Boundary element methods for soil-structure interaction*. Kluwer Academic Publishers, The Netherlands.

[2] Beskos, D. E. (1987) Boundary element methods in dynamic analysis. *Appl Mech Rev*, **40**, 1–23.

[3] Beskos, D. E. (1997) Boundary element methods in dynamic analysis: Part II (1986-1996). *Appl Mech Rev*, **50**, 149–197.

[4] Domínguez, J. (1978) Dynamic stiffness of rectangular foundations. Report R78-20, Massachusetts Institute of Technology, Cambridge, MA.

[5] Alarcón, E. and Domínguez, J. (1980) Impedance of foundations using the boundary integral equation method. *In Proc. of 2nd Int Symposium on innovative numerical analysis in applied Engineering Sciences*, Montreal.

[6] Alarcón, E., Del Caño, F., and Domínguez, J. (1981) Dynamic stiffness matrices for layered viscoelastic halfspaces and rectangular embedded foundations. *In Proc. of the Annual Meeting of the Seismological Society of America.*, Bechtel Engineering Center. University of California, USA.

[7] Abascal, R. and Domínguez, J. (1986) Vibrations of footings on zoned viscoelastic soils. *J Eng Mech ASCE*, **112**, 433–447.

[8] Apsel, R. J. and Luco, J. E. (1987) Impedance functions for foundations embedded in a layered medium: an integral equation approach. *Earthquake Eng Struct Dyn*, **12**, 213–231.

[9] Luco, J. E. and Wong, H. L. (1987) Seismic response of foundations embedded in a layered half-space. *Earthquake Eng Struct Dyn*, **15**, 233–247.

[10] Gazetas, G. and Tassoulas, J. L. (1987) Horizontal stiffness of arbitrarily shaped embedded foundations. *J Geotech Eng ASCE*, **113**, 440–457.

[11] Gazetas, G. and Tassoulas, J. L. (1987) Horizontal damping of arbitrarily shaped embedded foundations. *J Geotech Eng ASCE*, **113**, 458–475.

[12] Luco, J. E. and Mita, A. (1987) Response of a circular foundation on a uniform half-space to elastic waves. *Earthquake Eng Struct Dyn*, **15**, 105–118.

[13] Rajapakse, R. K. N. D. and Shah, A. H. (1988) Impedances of embedded rigid strip foundations. *Earthquake Eng Struct Dyn*, **16**, 255–273.

[14] Emperador, J. M. (1988) *El Método de los elementos de contorno en problemas elastodinámicos con simetría de revolución*. Ph.D. thesis, Universidad de Las Palmas de Gran Canaria, Las Palmas de G.C., Spain.

[15] Emperador, J. M. and Domínguez, J. (1989) Dynamic response of axisymetric embedded foundations. *Earthquake Eng Struct Dyn*, **18**, 1105–1117.

[16] Alarcón, E., Cano, J. J., and Domínguez, J. J. (1989) Boundary element approach to the dynamic stiffness functions of circular foundations. *Int J Num Meth Geomech*, **13**, 645–664.

[17] Domínguez, J. and Abascal, R. (1989) Seismic response of strip footings on zoned viscoelastic soils. *J Eng Mech ASCE*, **115**, 913–934.

[18] Israil, A. S. M. and Ahmad, S. (1989) Dynamic vertical compliance of strip foundations in layered soils. *Earthquake Eng Struct Dyn*, **18**, 933–950.

[19] Gonsalves, I. R., Shippy, D. J., and Rizzo, F. J. (1990) Direct boundary integral equations for elastodynamics in 3-D half-spaces. *Comput Mech*, **6**, 279–292.

[20] Israil, A. S. M. and Banerjee, P. K. (1990) Effects of geometrical and material properties on the vertical vibration of three-dimensional foundations by BEM. *Int J Num Anal Meth Geomech*, **14**, 49–70.

[21] Ahmad, S. and Bharadwaj, A. (1991) Horizontal impedance of embedded strip foundations in layered soil. *J Geotech Eng ASCE*, **117**, 1021–1041.

[22] Ahmad, S. and Gazetas, G. (1992) Torsional stiffness of arbitrarily shaped embedded foundations. *J Geotech Eng ASCE*, **118**, 1168–1185.

[23] Ahmad, S. and Gazetas, G. (1992) Torsional radiation damping of arbitrarily shaped embedded foundations. *J Geotech Eng ASCE*, **118**, 1186–1199.

[24] De Barros, F. C. P. and Luco, J. E. (1995) Dynamic response of a two-dimensional semi-circular foundation embedded in a layered viscoelastic half-space. *Soil Dyn Earthquake Eng*, **14**, 45–57.

[25] Poulos, H. G. and Davis, E. H. (1980) *Pile foundation analysis and design*. John Wiley & Sons, NY.

[26] Novak, M. (1991) Piles under dynamic loads. *Proc. of the 2nd Int Conf Recent Adv Geotech Earthquake Eng Soil Dyn*, St Louis, Missouri, vol. 3, pp. 250–273.

[27] Pender, M. (1993) Aseismic pile foundation design analysis. *Bull New Zealand Nat Soc Earthquake Eng*, **26**, 49–160.

[28] Pak, R. S. Y. and Jennings, P. C. (1987) Elastodynamic response of the pile under transverse excitation. *J Eng Mech, ASCE*, **113**, 1101–1116.

[29] Rajapakse, R. K. N. D. and Shah, A. H. (1987) On the longitudinal harmonic motion of an elastic bar embedded in an elastic half-space. *Int J Solids Struct*, **23**, 267–285.

[30] Rajapakse, R. K. N. D. and Shah, A. H. (1987) On the lateral harmonic motion of an elastic bar embedded in an elastic half-space. *Int J Solids Struct*, **23**, 287–303.

[31] Abedzadeh, F. and Pak, R. Y. S. (2004) Continuum mechanics of lateral soil-pile interaction. *J Eng Mech ASCE*, **130**, 1309–1318.

[32] Matlock, H. and Reese, L. C. (1960) Generalized solutions for laterally loaded piles. *J Soil Mech Found Div*, **85**, 63–91.

[33] Penzien, J., Scheffley, C. F., and Parmelee, R. A. (1964) Seismic analysis of bridges on long piles. *J Eng Mech Div ASCE*, **90**, 223–254.

[34] Dobry, R., O'Rourke, M. J., Roesset, J. M., and Vicente, E. (1982) Horizontal stiffness and damping of single piles. *J Geotech Eng Div, ASCE*, **108**, 439–459.

[35] Nogami, T. (1985) Flexural responses of grouped piles under dynamic loading. *Earthquake Eng Struct Dyn*, **13**, 321–336.

[36] Dobry, R. and Gazetas, G. (1988) Simple method for dynamic stiffness and damping of floating pile groups. *Géotechnique*, **38**, 557–574.

[37] Gazetas, G. and Makris, N. (1991) Dynamic pile-soil-pile interaction. Part I: Analysis of axial vibration. *Earthquake Eng Strutc Dyn*, **20**, 115–132.

[38] Gazetas, G., Fan, K., Kaynia, A. M., and Kausel, E. (1991) Dynamic interaction factors for floating pile groups. *J Geotech Eng Div, ASCE*, **117**, 1531–1548.

[39] Makris, N. and Gazetas, G. (1992) Dynamic pile-soil-pile interaction. Part II: Lateral and seismic response. *Earthquake Eng Strutc Dyn*, **21**, 145–162.

[40] Guo, W. and Randolph, M. F. (1997) Vertically loaded piles in nonhomogeneous media. *Int J Numer Analyt Meth Geomech*, **21**, 507,532.

[41] Mylonakis, G. and Gazetas, G. (1999) Lateral vibration and internal forces of grouped piles in layered soil. *J Geotech Geoenviron Eng ASCE*, **125**, 16–25.

[42] Cairo, R., Conte, E., and Dente, G. (2005) Interaction factors for the analysis of pile groups in layered soils. *J Geotech Geoenviron Eng ASCE*, **131**, 525–528.

[43] Cairo, R., Conte, E., and Dente, G. (2005) Analysis of pile groups under vertical harmonic vibration. *Comput Geotech*, **32**, 545–554.

[44] Kausel, E. and Roesset, J. M. (1974) Soil-structure interaction for nuclear containment. *Power Div. ASCE Specialty Conf*, Boulder, Colorado, pp. 469–498.

[45] Blaney, G. W., Kausel, E., and Roesset, J. M. (1976) Dynamic stiffness of piles. *Proc. of 2nd Int Conf Num Meth Geomech*, Virginia Polytech Inst and State Un Blacksburg, VA, pp. 1010–1012.

[46] Kuhlemeyer, R. L. (1979) Static and dynamic laterally loaded floating piles. *J Geotech Eng, ASCE*, **105**, 289–304.

[47] Wolf, J. P. and von Arx, G. A. (1978) Impedance functions of a group of vertical piles. *Proc of ASCE Specialty Conf Earthquake Eng Soil Dyn*, Pasadena, CA.

[48] Velez, A., Gazetas, G., and Krishnan, R. (1983) Lateral dynamic response of constrained-head piles. *J Geotech Eng, ASCE*, **109**, 1063–1081.

[49] Blaney, G. W. and El Naggar, M. H. (2000) Numerical analysis of kinematic response of single piles. *Can Geotech J*, **37**, 1368–1382.

[50] Tuladhar, R., Maki, T., and Mutsuyoshi, H. (2007) Cyclic behavior of laterally loaded concrete piles embedded into cohesive soil. *Earthquake Eng Struct Dyn*, **37**, 43–59.

[51] Kaynia, A. M. (1982) Dynamic stiffness and seismic response of pile groups. Report R83-03, Massachusetts Institute of Technology, Cambridge, MA.

[52] Kaynia, A. M. and Kausel, E. (1982) Dynamic behavior of pile groups. *2nd Int Conf on Numerical Methods for offshore piling*, Austin, Texas.

[53] Sen, R., Davies, T. G., and Banerjee, P. K. (1985) Dynamic analysis of piles and pile groups embedded in homogeneous soils. *Earthquake Eng Struct Dyn*, **13**, 53–65.

[54] Sen, R., Kausel, E., and Banerjee, P. K. (1985) Dynamic analysis of piles and pile groups embedded in non-homogeneous soils. *Int J Numer Anal Geomech*, **9**, 507–524.

[55] Davies, T. G., Sen, R., and Banerjee, P. K. (1985) Dynamic behavior of pile groups in inhomogeneous soil. *J Geotech Eng*, **111**, 1365–1379.

[56] Mamoon, S. M., Kaynia, A. M., and Banerjee, P. K. (1990) Frequency domain dynamic analysis of piles and pile groups. *J Eng Mech, ASCE*, **116**, 2237–2257.

[57] Kaynia, A. M. and Kausel, E. (1991) Dynamics of piles and pile groups in layered soil media. *Soil Dyn Earthquake Eng*, **10**, 386–401.

[58] Miura, K., Kaynia, A. M., Masuda, K., Kitamura, E., and Seto, Y. (1994) Dynamic behaviour of pile foundations in homogeneous and non-homogeneous media. *Earthquake Eng Struct Dyn*, **23**, 183–192.

[59] Guin, J. and Banerjee, P. K. (1998) Coupled soil-pile-structure interaction analysis under seismic excitation. *J Struct Eng*, **124**, 434–444.

[60] Millán, M. A. and Domínguez, J. (2008) Simplified BEM/FEM model for dynamic analysis of structures on piles and pile groups in viscoelastic and poroelastic soils. *Eng Anal Bound Elem*, p. doi:10.1016/j.enganabound.2008.04.003.

[61] Kattis, S. E., Polyzos, D., and Beskos, D. E. (1999) Vibration isolation by a row of piles using a 3-D frequency domain BEM. *Int J Numer Meth Eng*, **46**, 713–728.

[62] Kattis, S. E., Polyzos, D., and Beskos, D. E. (1999) Modelling of pile wave barriers by effective trenches and their screening effectiveness. *Soil Dyn Earthquake Eng*, **18**, 1–10.

[63] Vinciprova, F., Aznárez, J. J., Maeso, O., and Oliveto, G. (2003) *Problems in structural identification and diagnostic: General aspects and applications*, chap. Interaction of BEM analysis and experimental testing on pile-soil systems, pp. 195–227. Springer-Verlag.

[64] Maeso, O., Aznárez, J. J., and García, F. (2005) Dynamic impedances of piles and groups of piles in saturated soils. *Comput Struct*, **83**, 769–782.

[65] Wolf, J. P., von Arx, G. A., de Barros, F. C. P., and Kakubo, M. (1981) Seismic analysis of the pile foundation of the reactor building of the NPP Angra 2. *Nuclear Eng Design*, **65**, 329–341.

[66] Flores-Berrones, R. and Whitman, R. V. (1982) Seismic response of end-bearing piles. *J Geotech Eng Div ASCE*, **108**, 554–569.

[67] Mamoon, S. M. and Banerjee, P. K. (1990) Response of piles and pile groups to travelling SH-waves. *Earthquake Eng Struct Dyn*, **19**, 597–610.

[68] Mamoon, S. M. and Ahmad, S. (1990) Seismic response of piles to obliquely incident SH, SV and P waves. *J Geotech Eng, ASCE*, **116**, 186–204.

[69] Fan, K., Gazetas, G., Kaynia, A. M., Kausel, E., and Ahmad, S. (1991) Kinematic seismic response of single piles and pile groups. *J Geotech Eng, ASCE*, **117**, 1860–1879.

[70] Kaynia, A. M. and Novak, M. (1992) Response of pile foundations to Rayleigh waves and obliquely incident body waves. *Earthquake Eng Struct Dyn*, **21**, 303–318.

[71] Gazetas, G., Fan, K., Tazoh, T., Shimizu, K., Kavvadas, M., and Makris, N. (1992) Seismic pile-group-structure interaction. *Geotech Spec Publ, ASCE*, **34**, 56–93.

[72] Kavvadas, M. and Gazetas, G. (1993) Kinematic seismic response and bending of free-head piles in layered soil. *Géotechnique*, **43**, 207–222.

[73] Ji, F. and Pak, R. Y. S. (1996) Scattering of vertically-incident P-waves by an embedded pile. *Soil Dyn Earthquake Eng*, **15**, 211–222.

[74] Masayuki, H. and Shoichi, N. (1991) A study on pile forces of a pile group in layered soil under seismic loadings. *Proc. of the II Int Conf on Recent Advances in Geotech Earthquake Eng and Soil Dyn*, St Louis, Missouri.

[75] Kaynia, A. M. and Mahzooni, S. (1996) Forces in pile foundations under seismic loading. *J Eng Mech, ASCE*, **122**, 46–53.

[76] Nikolaou, S., Mylonakis, G., Gazetas, G., and Tazoh, T. (2001) Kinematic pile bending during earthquakes: analysis and field measurements. *Géotechnique*, **51**, 425–440.

[77] Mylonakis, G. (2001) Simplified model for seismic pile bending at soil layer interfaces. *Soils Found, Jap Geotech Soc*, **41**, 47–58.

[78] Parmelee, R. A. (1967) Building-foundation interaction effects. *J Eng Mech Div, ASCE*, **93**, 131–152.

[79] Perelman, D. S., Parmelee, R. A., and Lee, S. L. (1968) Seismic response of single-storey interaction systems. *J Struct Div, ASCE*, **94**, 2597–2608.

[80] Parmelee, R. A., Perelman, D. S., and Lee, S. L. (1969) Seismic response of multiple-storey structures on flexible foundation. *Bull Seism Soc Ame*, **59**, 1061–1070.

[81] Sarrazin, M. A., Roesset, J. M., and Whitman, R. V. (1972) Dynamic soil-structure interaction. *J Struct Div, ASCE*, **98**, 1525–1544.

[82] Veletsos, A. S. and Meek, J. W. (1974) Dynamic behaviour of building-foundation systems. *Earthquake Eng Struct Dyn*, **3**, 121–138.

[83] Bielak, J. (1975) Dynamic behavior of structures with embedded foundations. *Earthquake Eng Struct Dyn*, **3**, 259–274.

[84] Wolf, J. P. (1985) *Dynamic soil-structure interaction*. Prentice-Hall, Englewood Cliffs, NJ.

[85] Todorovska, M. I. (1992) Effects of the depth of the embedment on the system response during building-soil interaction. *Soil Dyn Earthquake Eng*, **11**, 111–123.

[86] Avilés, J. and Pérez-Rocha, L. E. (1996) Evaluation of interaction effects on the system period and the system damping due to foundation embedment and layer depth. *Soil Dyn Earthquake Eng*, **15**, 11–27.

[87] Avilés, J. and Pérez-Rocha, L. E. (1998) Effects of foundation embedment during building-soil interaction. *Earthquake Eng Struct Dyn*, **27**, 1523–1540.

[88] Avilés, J. and Suárez, M. (2002) Effective periods and dampings of building-foundation systems including seismic wave effects. *Eng Struct*, **24**, 553–562.

[89] Takemiya, H. and Yamada, Y. (1981) Layered soil-pile-structure dynamic interaction. *Earthquake Eng Struct Dyn*, **9**, 437–457.

[90] Mylonakis, G. (1995) *Contributions to static and seismic analysis of piles and pile-supported bridge piers*. Ph.D. thesis, State University of New York at Buffalo.

[91] Mylonakis, G. and Nikolaou, A. (1997) Soil-pile-bridge seismic interaction: kinematic and inertial effects. Part I. *Earthquake Eng Struct Dyn*, **26**, 337–359.

[92] Kumar, S. and Prakash, S. (1997) Effect of type of foundation on period and base shear response of structures. *Geotech Spec Publ, ASCE*, **70**, 52–68.

[93] Han, Y. and Cathro, D. (1997) Seismic behavior of tall buildings supported on pile foundations. *Geotech Spec Publ, ASCE*, **70**, 36–51.

[94] Koo, K. K., Chau, K. T., Yang, X., Lam, S. S., and Wong, Y. L. (2003) Soil-pile-structure interaction under SH wave excitation. *Earthquake Eng Struct Dyn*, **32**, 395–415.

[95] Stewart, J. P., Fenves, G. L., and Seed, R. B. (1999) Seismic soil-structure interaction in buildings. I: Analytical Methods. *J Geotech Geoenviron Eng ASCE*, **125**, 26–37.

[96] Stewart, J. P., Fenves, G. L., and Seed, R. B. (1999) Seismic soil-structure interaction in buildings. II: Empirical Findings. *J Geotech Geoenviron Eng ASCE*, **125**, 38–48.

[97] Lee, T. H. and Wesley, D. A. (1973) Soil-structure interaction of nuclear reactor structures considering through-soil coupling between adjacent structures. *Nuclear Eng Design*, **24**, 374–387.

[98] Luco, J. E. and Contesse, L. (1973) Dynamic structure-soil-structure interaction. *Bull Seism Soc Ame*, **63**, 1289–1303.

[99] Wong, H. L. and Trifunac, M. D. (1975) Two-dimensional, antiplane, building-soil-building interaction for two or more buildings and for incident plane SH waves. *Bull Seism Soc Ame*, **65**, 1863–1885.

[100] Wang, S. and Schmid, G. (1992) Dynamic structure-soil-structure interaction by FEM and BEM. *Comput Mech*, **9**, 347–357.

[101] Lehmann, L. and Antes, H. (2001) Dynamic structure-soil-structure interaction applying the Symmetric Galerkin Boundary Element Method (SGBEM). *Mech Research Comm*, **3**, 297–304.

[102] Clouteau, D. and Aubry, D. (2001) Modifications of the ground motion in dense urban areas. *J Comput Acoustics*, **9**, 1659–1675.

[103] Tsogka, C. and Wirgin, A. (2003) Simulation of seismic response in an idealized city. *Soil Dyn Earthquake Eng*, **23**, 391–402.

[104] Kham, M., Semblat, J. F., Bard, P. Y., and Dangla, P. (2006) Seismic site-city interaction: main governing phenomena through simplified numerical models. *Bull Seism Soc Ame*, **96**, 1934–1951.

[105] Bard, P. Y., Guéguen, P., Chazelas, J. L., Kham, M., and Semblat, J. F. (2007) Seismic hazard in urban environments: Can man modify the hazard? Martínez-Guevara, J.-B. (ed.), *Proc. of 3ed Congreso Nacional de Ingeniería sísmica*, CIMNE.

[106] Boulanger, R. W., Curras, C. J., Kutter, B. L., Wilson, D. W., and Abghari, A. (1999) Seismic soil-pile-structure interaction experiments and analyses. *J Geotech Geoenviron Eng ASCE*, **125**, 750–759.

[107] Rollins, K. M., Olsen, R. J., Egbert, J. J., Olsen, K. G., Jensen, D. H., and Garrett, B. H. (2003) Response, analysis and design of pile groups subjected to static and dynamic lateral loads. Report UT-03.03, Utah Deparment of Transportation Research and Development Division.

[108] Finn, W. D. L. (2005) A study of piles during earthquakes: issues of design and analysis. *Bull Earthquake Eng*, **3**, 141:234.

[109] Domínguez, J. and Alarcón, E. (1981) *Elastodynamics*. Progress in Boundary Element Methods, Pentech Press Ltd., London, UK.

[110] Medina, F. and Domínguez, J. (1989) Boundary elements for the analysis of the seismic response of dams including dam-water-foundation interaction effects. *Eng Anal Bound Elem*, **6**, 152–157.

[111] Maeso, O. (1992) *Modelo para el análisis sísmico de presas bóveda incluyendo los efectos de interacción suelo-agua-estructura*. Ph.D. thesis, University of Las Palmas de Gran Canaria, Las Palmas de G.C., Spain.

[112] Maeso, O. and Domínguez, J. (1993) Earthquake analysis of arch dams. I: dam-foundation interaction. *J Eng Mech ASCE*, **119**, 496–512.

[113] Domínguez, J. and Maeso, O. (1993) Earthquake analysis of arch dams. II: dam-water-foundation interaction. *J Eng Mech ASCE*, **119**, 513–530.

[114] Aznárez, J. J. (2002) *Efectos de los fenómenos de interacción incluyendo los factores espaciales y sedimentos de fondo en la respuesta sísmica de presas bóveda*. Ph.D. thesis, University of Las Palmas de Gran Canaria, Las Palmas de G.C., Spain.

[115] Aznárez, J. J., Maeso, O., and Domínguez, J. (2001) A 3-D boundary element model for the dynamic analysis of arch dams with porous sediments. *Advan Earthquake Eng*, **9**, 713–722.

[116] Maeso, O., Aznárez, J. J., and Domínguez, J. (2002) Effects of space distribution of excitation on seismic response of arch dams. *J Eng Mech*, **128**, 759–768.

[117] Maeso, O., Aznárez, J. J., and Domínguez, J. (2004) Three-dimensional models of reservoir sediment and effects on the seismic response of arch dams. *Earthquake Eng Struct Dyn*, **33**, 1103–1123.

[118] Aznárez, J. J., Maeso, O., and Domínguez, J. (2006) BE analysis of bottom sediments in dynamic fluid-structure interaction problems. *Eng Anal Bound Elem*, **30**, 124–136.

[119] Matos Filho, R., Mendonça, A. V., and Paiva, J. B. (2005) Static boundary element analysis of piles submitted to horizontal and vertical loads. *Eng Anal Boundary Elem*, **29**, 195–203.

[120] Domínguez, J. (1993) *Boundary elements in dynamics*. Computational Mechanics Publications & Elsevier Applied Science, Southampton, NY.

[121] Achenbach, J. D. (1973) *Wave propagation in elastic solids*. North-Holland, Amsterdam.

[122] Eringen, A. C. and Suhubi, E. S. (1975) *Elastodynamics*, vol. 2 - Linear Theory. Academic Press, NY.

[123] Graffi, D. (1946) Sul teorema di reciprocitá nella dinamica dei corpi elastici. *Mem Accad Sci, Bologna*, **4**, 103–111.

[124] Wheeler, L. T. and Sternberg, E. (1968) Some theorems in classical elastodynamics. *Arch Rat Mech Anal*, **31**, 51–90.

[125] Stokes, G. G. (1849) On the dynamical theory of diffraction. *Trans Cambridge Filos Soc*, **9**, 1–62.

[126] Cruse, T. A. and Rizzo, F. J. (1968) A direct formulation and numerical solution of the general transient elastodynamic problem. *J Math Anal Appl*, **22**, 244–259.

[127] Kupradze, V. D. (1963) *Dynamical problems in elasticity*. Progress in solid mechanics, North-Holland, Amsterdam.

[128] Hartmann, F. (1981) *Elastostatics*. Progress in boundary element methods, Pentech Press, London.

[129] Medina, F. (1987) *Análisis de la respuesta sísmica de presas incluyendo efectos de interacción suelo-fluido-estructura*. Ph.D. thesis, University of Seville, Spain.

[130] Stroud, A. H. and Secrest, D. (1966) *Gaussian quadrature formulas*. Prentice-Hall, NY.

[131] Abramowitz, M. and Stegun, I. A. (1964) *Handbook of Mathematical Functions with Formulas, Graphs, and Mathematical Tables*. Dover, NY.

[132] Telles, J. C. (1987) A selfadaptative coordinate transformation for efficient evaluation of general boundary element integrals. *Int J Numer Meth Eng*, **24**, 937–959.

[133] Li, H. B., Han, G. M., and Mang, H. A. (1985) A new method for evaluating singular integrals in stress analysis of solids by the direct boundary element method. *Int J Numer Meth Eng*, **21**, 2071–2098.

[134] Cerrolaza, M. and Alarcón, E. (1989) A bicubic transformation for the numerical evaluation of the Cauchy principal value integrals in boundary elements. *Int J Numer Meth Eng*, **28**, 987–999.

[135] Chirino, F., Maeso, O., and Aznárez, J. J. (2000) Una técnica simple para el cálculo de las integrales en el sentido del valor principal de Cauchy en el MEC 3D. *Rev Int Met Num para Cálculo y Diseño en Ing*, **16**, 77–95.

[136] Cruse, T. A. (1969) Numerical solutions in three dimensional elastostatics. *Int J Numer Meth Eng*, **5**, 1259–1274.

[137] Christensen, R. M. (1982) *Theory of viscoelasticity*. Academic Press Inc., NY.

[138] Padrón, L. A., Aznárez, J. J., and Maeso, O. (2006) A BEM-FEM model for studying dynamic impedances of piles in elastic soils. Topping, B. H. V., Montero, G., and Montenegro, R. (eds.), *Proc. of the Fifth Int Conf on Eng Comput Technology*, Stirlingshire, UK, no. 163, Civil-Comp Press.

[139] Padrón, L. A., Aznárez, J. J., and Maeso, O. (2007) BEM-FEM coupling model for the dynamic analysis of piles and pile groups. *Eng Anal Bound Elem*, **31**, 473–484.

[140] Clough, R. W. and Penzien, J. (1982) *Dynamics of structures*. McGraw-Hill.

[141] Padrón, L. A., Aznárez, J. J., and Maeso, O. (2007) Modelo numérico para el cálculo de impedancias dinámicas de pilotes y grupos de pilotes. Rodríguez Ferrán, A., Oliver, J., Lyra, P., and Álves, J. (eds.), *Proc. of VIII Congresso de Metodos Numericos e Computacionais em Enghenaria CMNE/CILAMCE*, Porto, Portugal.

[142] Padrón, L. A., Aznárez, J. J., and Maeso, O. (2008) Dynamic analysis of piled foundations in stratified soils by a BEM-FEM model. *Soil Dyn Earthquake Eng*, **28**, 333–346.

[143] Nogami, T. (1979) Dynamic group effect of multiple piles under vertical vibration. *Proc. of ASCE Engineering Mechanics Division Specialty Conference*, Austin, Texas, pp. 750–754.

[144] Gazetas, G. and Mylonakis, G. (1998) Seismic soil-structure interaction: new evidence and emerging issues. *Geotech Spec Publ, ASCE*, **75**, 1119–1174.

[145] Mylonakis, G., Nikolaou, S., and Gazetas, G. (2006) Footings under seismic loading: Analysis and design issues with emphasis on bridge foundations. *Soil Dyn Earthquake Eng*, **26**, 824–853.

[146] Stewart, J. P. and Stewart, A. F. (1997) Analysis of soil-structure interaction effects on building response from earthquake strong motion recordings at 58 sites. Report UCB/EERC-97/01, Earthquake engineering research center, University of California at Berkeley, CA.

[147] Combarieu, O. and Evrard, H. (1979) Combination of footing-pile foundations. *Bull de liaison des laboratoires des ponts et chausses*, **102**, 49–58.

[148] Combarieu, O. and Morbois, A. (1982) Combined footing-pile foundations. *Annales de l'institut technique du batiment et des travaux publics*, **410**, 1–34.

[149] Cooke, R. W. (1986) Piled raft foundations on stiff clays - a contribution to design philosophy. *Géotechnique*, **36**, 169–203.

[150] Poulos, H. (2001) Pile raft foundations: Design and applications. *Géotechnique*, **51**, 95–113.

[151] Reul, O. and Randolph, M. F. (2003) Piled rafts in overconsolidated clay: a comparison of in situ measurements and numerical analyses. *Géotechnique*, **53**, 301–315.

[152] Small, J. C. and Poulos, H. G. (2007) Non-linear analysis of piled raft foundations. *Geotech Spec Publ, ASCE*, **158**.

[153] Butterfield, R. and Banerjee, P. K. (1971) The problem of pile group-pile cap interaction. *Géotechnique*, **21**, 135–142.

[154] Akinmusuru, J. O. (1980) Interaction of piles and cap in piled footings. *J Geotech Eng Div, ASCE*, **106**, 1263–1268.

[155] Chow, Y. K. and Teh, C. I. (1991) Pile-cap-pile-group interaction in nonhomogeneous soil. *J Geotech Eng, ASCE*, **117**, 1655–1668.

[156] Buckingham, E. (1914) On physically similar systems: illustration of the use of dimensional equations. *Phys Rev*, **4**, 345–376.

[157] Randolph, M. F. (1981) Response of flexible piles to lateral loading. *Géotechnique*, **31**, 247–259.

[158] Jennings, P. C. and Bielak, J. (1973) Dynamics of building-soil interaction. *Bull Seism Soc Ame*, **63**, 9–48.

[159] Veletsos, A. S. and Nair, V. V. D. (1975) Seismic interaction of structures on hysteretic foundations. *J Struct Div, ASCE*, **101**, 109–129.

[160] Maravas, A., Mylonakis, G., and Karabalis, D. L. (2007) Dynamic characteristics of simple structures on piles and footings. *Proc. of 4th Int Conf on Earthquake Geotech Eng*, Thessaloniki, Greece, June, no. 1672.

[161] Padrón, L. A., Aznárez, J. J., and Maeso, O. (2008) BEM-FEM coupling model for the analysis of soil-pile-structure interaction in the frequency domain. *Proc. of the Int Conf on Boundary Element Techniques XI*, Seville, Spain.

[162] AFPS (1990) *Récommandations AFPS 90*. Association Française du Génie Parasismique, Presses des Ponts et Chaussées, Paris, France.

[163] Vanmarcke, E. H. (1976) SIMQKE: A program for artificial motion generation. Report, Massachusetts Institute of Technology, Cambridge, MA.

[164] Escobar, J. M., Rodríguez, E., Montenegro, R., Montero, G., and González-Yuste, J. M. (2003) Simultaneous untangling and smoothing of tetrahedral meshes. *Comput Meth Appl Mech Eng*, **192**, 2775–2787.

[165] González-Yuste, J. M., Montenegro, R., Escobar, J. M., Montero, G., and Rodríguez, E. (2004) Local refinement of 3-D triangulations using object-oriented methods. *Adv Eng Software*, **35**, 693–702.

Appendices: Summary of the dissertation in Spanish

Índice general

Apéndice A

Introducción y antecedentes

En muchas ocasiones, durante el proceso de diseño de una obra civil, las características del emplazamiento, o la magnitud de las cargas a las que va a estar sometida la estructura, hacen aconsejable la elección de cimentaciones pilotadas. Esto ocurre, especialmente, en los siguientes casos: *a*) cuando el suelo posee una baja capacidad portante o no es lo suficientemente estable, *b*) cuando existen rocas o suelos más resistentes a cotas más bajas, *c*) cuando la magnitud de las cargas de diseño es muy grande, *d*) cuando se prevén cargas horizontales relativamente grandes o la existencia de cargas verticales ascendentes, o *e*) cuando el asentamiento estimado para otros sistemas de cimentación es inaceptable. Además, el uso de cimentaciones pilotadas puede mejorar la respuesta sísmica de las estructuras, dado que puede disminuir la magnitud de la solicitación sísmica en la base de la estructura y, al mismo tiempo, aumentar el amortiguamiento del sistema. Por todas estas razones, los pilotes son a menudo utilizados para cimentar edificios altos, estructuras y plataformas marinas, grandes pilas de puentes y centrales nucleares.

En la práctica común, tales cimentaciones pilotadas son generalmente diseñadas haciendo uso de procedimientos simplificados que están basados en resultados experimentales, en estudios paramétricos analíticos y/o numéricos, en la experiencia y en aproximaciones de tipo ingenieril. Estas metodologías simplificadas son capaces de predecir adecuadamente la respuesta estática o pseudo-estática de la cimentación, incluso en casos influidos por fenómenos no lineales. Por contra, no son, a día de hoy, capaces de modelar con suficiente precisión el comportamiento dinámico de las cimentaciones pilotadas, que además es, en general, altamente dependiente de la frecuencia. Un problema de especial dificultad, debido al gran número de fenómenos implicados, es el de la respuesta sísmica de cimentaciones pilotadas y de estructuras cimentadas sobre pilotes.

Por todo ello, y a pesar del gran número de investigaciones que han sido llevadas a cabo durante las últimas tres décadas sobre el comportamiento dinámico de pilotes, existe aún la necesidad de alcanzar una mejor comprensión acerca

de este problema. En relación con este asunto, otros problemas de interés son aquellos que tienen que ver con la influencia, en la respuesta dinámica de las estructuras, de la flexibilidad del sistema cimentación-suelo (efectos de interacción suelo-estructura) y de la presencia de construcciones cercanas (efectos de interacción estructura-suelo-estructura). En consecuencia, diferentes líneas de investigación, basadas tanto en técnicas experimentales como en métodos numéricos o analíticos, están actualmente en marcha. Una de estas corrientes de investigación se centra en la formulación de herramientas numéricas capaces de modelar el comportamiento dinámico del sistema suelo-cimentación-estructura de modo riguroso, siendo esta línea el marco en el que se encuadra este trabajo.

Más concretamente, se ha formulado y desarrollado un modelo acoplado de elementos de contorno y elementos finitos para el análisis dinámico tridimensional de cimentaciones pilotadas y de estructuras cimentadas sobre pilotes. Se trata de una aproximación directa al problema formulado en el dominio de la frecuencia, capaz de analizar la respuesta de múltiples estructuras de varias plantas cimentadas sobre pilotes en suelos de estratigrafía y topografía genéricas. En dicho modelo acoplado, el Método de los Elementos Finitos (FEM) se utiliza para modelar los pilotes y las superestructuras, mientras que los suelos estratificados son modelados a través del Método de los Elementos de Contorno (BEM), en el que cada estrato es considerado como un medio continuo, semi-infinito, isótropo y viscoelástico.

Tal y como se ha dicho anteriormente, el modelo presentado en este trabajo constituye una formulación lineal del problema. Obviamente, los efectos no lineales pueden jugar un papel primordial en la respuesta dinámica de las cimentaciones pilotadas. Por ejemplo, fenómenos de licuefacción, o de desprendimiento de tierras en un talud, pueden ocasionar grandes esfuerzos cortantes y momentos flectores en los pilotes. También los fenómenos de despegue o de deslizamiento en la interfase pilote-suelo, o las variaciones en las características resistentes de los suelos debidas a la solicitación sísmica, pueden influir considerablemente en la respuesta. Sin embargo, los efectos de interacción suelo-estructura, incluso en el rango lineal, no están aún completamente comprendidos, y por lo tanto, el desarrollo de modelos directos lineales como el que se presenta aquí está completamente justificado.

A.1. Revisión bibliográfica

Gracias a su habilidad para modelar el comportamiento dinámico de regiones no acotadas, el método de los elementos de contorno está especialmente indicado para el estudio de problemas de interacción suelo-estructura, entre otra razones, porque las condiciones de radiación de energía hacia el infinito están recogidas de manera implícita en la representación integral utilizada, y también porque no es necesario discretizar el dominio. Existe un gran número de problemas ingenieriles

que pueden encuadrarse dentro de este campo de la interacción suelo-estructura. Algunas revisiones bibliográficas de interés sobre la aplicación del método de los elementos de contorno a este tema pueden encontrarse, por ejemplo, en una obra reciente editada por Hall y Oliveto [1], con contribuciones de distintos expertos en la materia. También, una revisión exhaustiva hasta 1997 es la ofrecida por Beskos en [2] y [3].

El análisis dinámico de cimentaciones embebidas en semi-espacios uniformes o estratificados ha sido objeto de numerosos estudios. El método de los elementos de contorno, en sus formas directa e indirecta, ha sido utilizado con asiduidad para estimar el comportamiento dinámico de cimentaciones superficiales y embebidas en el dominio de la frecuencia, tanto en dos como en tres dimensiones [4–24]. Por otro lado, y centrándonos en el análisis de cimentaciones profundas, tema central de esta tesis doctoral, los primeros trabajos relacionados con el análisis dinámico de pilotes aparecieron durante los años sesenta, muchos de los cuales fueron recogidos por Poulos y Davis en su libro [25]. Dos revisiones más recientes en esta materia son las de Novak [26] y Pender [27], pero más referencias pueden encontrarse en los trabajos de Beskos anteriormente citados [2] y [3].

El problema de la obtención de la respuesta dinámica en el dominio de la frecuencia de cimentaciones pilotadas ha sido tratado a través de soluciones analíticas rigurosas [28–31], de procedimientos simplificados de tipo semi-analítico (incluyendo los modelos tipo Winkler) [32–43] y de diferentes técnicas numéricas: modelos de elementos finitos [44–50]; esquemas acoplados BEM-FEM, o elementos de contorno combinados con diferentes funciones de Green para el semiespacio, y elementos estructurales monodimensionales para los pilotes [51–60]; y formulaciones multi-dominio de elementos de contorno [61–64].

Si bien es cierto que un gran número de estos trabajos están centrados en el problema de vibración forzada, muchos de ellos, como por ejemplo los recogidos en [65–73], abordan también la respuesta cinemática de las cimentaciones pilotadas. Entre dichos trabajos se encuentran algunos estudios paramétricos sobre la respuesta sísmica de pilotes simples y grupos de pilotes ante ondas de Rayleigh y ondas volumétricas. Otros trabajos han analizado también, de forma específica, los cortantes y flectores que aparecen en los pilotes debido, exclusivamente, a los fenómenos de interacción cinemática [74–77].

Cada una de las metodologías propuestas para el análisis dinámico de cimentaciones pilotadas tiene sus propias ventajas e inconvenientes. Las soluciones analíticas rigurosas permiten analizar de forma exhaustiva los fenómenos físicos que tienen lugar en el modelo, y permiten la obtención de resultados con un bajo esfuerzo computacional. Sin embargo, su alto grado de complejidad, junto al hecho de que están orientadas hacia un problema específico, las hace inflexibles y difíciles de ampliar. Por otro lado, las principales ventajas de los procedimientos semi-analíticos simplificados son sus bajos requerimientos computacionales y su

relativa simplicidad, pero por contra, la mayoría de ellos, en tanto que modelos discretos que no incluyen el suelo como medio continuo, no son capaces de modelar rigurosamente algunos mecanismos, como son los amortiguamientos interno y por radiación, los efectos inerciales en el suelo, y los fenómenos de interacción entre pilotes. En cuanto a los esquemas numéricos, el Método de los Elementos Finitos, con sus limitaciones intrínsecas a la hora de modelar dominios no acotados, necesita especial atención a la hora de elaborar las discretizaciones y también en el tratamiento de la energía radiada hacia el exterior, pero su flexibilidad ha favorecido el desarrollo de numerosas técnicas para abordar el problema, tanto en régimen lineal como no lineal. Por otro lado, las formulaciones acopladas de elementos de contorno y elementos finitos, incluyendo las que están basadas en funciones de Green específicas para modelar la interacción pilote-suelo, constituyen generalmente, debido a su rigurosidad y sus relativamente bajos requerimientos computacionales, la mejor opción para abordar el problema . Finalmente, el Métodos de los Elementos de Contorno, implementado con características multi-dominio, es altamente flexible y riguroso, pero requiere de mucho tiempo de cálculo y de importantes esfuerzos a la hora de preparar las mallas y los ficheros de datos.

En cuanto a la respuesta de la superestructura, los efectos de interacción suelo-estructura (SSI) en edificios han sido objeto de estudio durante más de treinta años. Los trabajos pioneros en este área, que investigaron la influencia de la flexibilidad del suelo en el comportamiento dinámico de estructuras a cortante de una sola altura, fueron presentados por Parmelee [78], Perelman et al [79], Parmelee et al [80] y Sarrazin et al [81]. A partir de estos trabajos, Veletsos y Meek [82], y Bielak [83], propusieron, por separado, aproximaciones basadas en modelos monodimensionales dirigidos a ofrecer pautas para el diseño de estructuras. Estos autores utilizaron las funciones de impedancia que estaban disponibles en aquel momento, y que correspondían a placas rígidas superficiales de forma circular. Una década más tarde, Wolf presentó una recopilación de problemas de interacción suelo-estructura en su libro [84]. Algunos trabajos posteriores ampliaron estos estudios y analizaron la influencia del grado de embebimiento de la cimentación, y de los fenómenos de interacción cinemática (*e.g.* [85–88]).

Tal y como se ha venido diciendo, existen múltiples resultados de rigideces dinámicas y de respuesta sísmica de pilotes y grupos de pilotes. Tales resultados pueden ser utilizados para abordar problemas de interacción suelo-estructura, para estructuras pilotadas, haciendo uso de modelos de subestructuración, tal y como se ha hecho, por ejemplo, en [65, 75, 89–93]. Otra forma de afrontar el problema es mediante formulaciones directas que contemplan, de forma implícita, los efectos de interacción suelo-estructura. Algunas formulaciones de este tipo han sido propuestas e implementadas para, por ejemplo, analizar puentes y edificios pilotados de múltiples plantas [59, 60, 94]. Una comparación entre mediciones experimentales y resultados numéricos, obtenidos mediante los procedimientos de uso común en la

práctica para la evaluación de los efectos de la interacción suelo-estructura, puede encontrarse en el estudio presentado por Stewart et al [95, 96].

El problema de la interacción entre estructuras adyacentes a través del suelo ha recibido menos atención. Lee y Wesley, en su trabajo pionero [97], investigaron la influencia de la interacción estructura-suelo-estructura (SSSI) sobre la respuesta sísmica de varios reactores nucleares adyacentes, para lo cual utilizaron una aproximación tridimensional y una solución aproximada para la interacción dinámica entre placas rígidas superficiales de geometría circular. Poco después, Luco y Contesse [98], seguidos por Wong y Trifunac [99], abordaron el problema antiplano bidimensional de la interacción entre muros infinitos sometidos a ondas incidentes de tipo SH, para lo cual utilizaron una solución para la interacción entre cimentaciones semi-infinitas de sección semi-circular. Posteriormente, dos modelos acoplados diferentes de elementos finitos y elementos de contorno fueron utilizados por Wang y Schmid [100], y por Lehmann y Antes [101], para investigar la interacción dinámica entre estructuras tridimensionales cimentadas sobre zapatas rectangulares, para los casos de una carga puntual aplicada sobre uno de los nodos de una de las estructuras, en el primer trabajo, y de una carga vertical sobre el suelo situado entre ambas estructuras, en el segundo trabajo. Más recientemente, se han realizado estudios numéricos y experimentales con el objetivo de investigar cómo influye la presencia de grandes grupos de edificios sobre la respuesta sísmica del sistema en su conjunto, teniendo en cuenta las características geológicas y topográficas del emplazamiento (efecto local) [102–105].

Finalmente, recordar que este trabajo está centrado principalmente en el modelado numérico del comportamiento dinámico, en el dominio de la frecuencia, de cimentaciones pilotadas y de edificios cimentados sobre pilotes en suelo viscoelásticos. Por lo tanto, el estudio se realiza asumiendo un comportamiento lineal del sistema, a pesar de que, como fue ya comentado anteriormente, se trata de un problema ingenieril complejo en el que deben tenerse en cuenta numerosos factores diferentes. Es por esto por lo que tanto los estudios experimentales, como los trabajos computacionales sobre los aspectos no lineales del problema, han sido excluidos de esta revisión bibliográfica. Más información sobre estos temas puede encontrarse, por ejemplo, en los trabajos de Boulanger et al [106], Rollins et al [107] y Finn [108].

A.2. Objetivos

Esta tesis pretende ser un paso más en una línea de investigación que comenzó con los trabajos pioneros de los profesores Enrique Alarcón Álvarez y José Domínguez Abascal, quienes aplicaron el método directo de los elementos de contorno a problemas de la elastodinámica [4, 7, 16, 109, 110]. Posteriormente, se estableció una

fructífera línea de colaboración entre la Universidad de Sevilla y la Universidad de Las Palmas de Gran Canaria, que dio lugar a la elaboración de un código de elementos de contorno multidominio y tridimensional en el dominio de la frecuencia [111–113]. Dicho código continuó siendo desarrollado en los años posteriores, y alcanzó su última etapa durante la elaboración de la tesis doctoral del profesor Juan J. Aznárez [114] quien, bajo la dirección del profesor Orlando Maeso, formuló e implementó, entre otras características, la posibilidad de modelar subdominios de naturaleza poroelástica. Este código fue utilizado para llevar a cabo diversos estudios sobre el análisis dinámico de presas bóveda en presencia de sedimentos porosos [115–118], y también para obtener impedancias de pilotes y grupos de pilotes en suelos viscoelásticos y poroelásticos [63, 64]. Tal y como se dijo anteriormente, los mayores inconvenientes de este tipo de enfoques son su alto coste computacional y el tiempo requerido en la preparación de las mallas y los ficheros de datos, lo que hace inabordable el análisis de grandes grupos de pilotes con esta herramienta. Por lo tanto, se hizo necesario desarrollar, e implementar en el código de elementos de contorno previamente existente, una formulación simplificada pero rigurosa que permitiera reducir el número de grados de libertad necesarios para el análisis de este tipo de problemas.

Por todo esto, el objetivo principal de este trabajo es la formulación e implementación de un modelo acoplado de elementos de contorno y elementos finitos para el análisis dinámico de cimentaciones pilotadas embebidas en suelos viscoelásticos, y de estructuras pilotadas, todo ello en el dominio de la frecuencia. La idea básica del enfoque planteado en este trabajo reside en la consideración de que las tracciones en la interfase pilote-suelo pueden ser consideradas, en la ecuación integral del problema, como fuerzas de volumen, y que el suelo puede modelarse como un medio continuo a pesar de la presencia de los pilotes. Esto conlleva la necesidad de evaluar las integrales de dominio en las que intervienen las fuerzas de volumen, cuyo valor es nulo en gran número de aplicaciones. Sin embargo, estas nuevas integrales habrán de evaluarse tan solo a lo largo de las interfases pilote-suelo, de modo que no habrá necesidad de discretizar el dominio completo. Esta idea es similar a la que subyace a un modelo estático previo presentado por Matos Filho et al [119]. El esquema de acoplamiento debe permitir un modelado relativamente simple y genérico de múltiples cimentaciones pilotadas compuestas por pilotes verticales y encepados rígidos. Ha de ser también posible modelar la topografía y la estratigrafía del emplazamiento, incluyendo depósitos e inclusiones, capas de material y lechos rocosos. El esfuerzo necesario para generar las mallas debería ser considerablemente menor que el requerido para un análisis equivalente realizado con el código de elementos de contorno multidominio previamente existente. Además, la formulación debe incluir la posibilidad de estudiar diversas estructuras lineales de varias alturas cimentadas sobre una o varias cimentaciones pilotadas.

Por otro lado, el código debe permitir el establecimiento de un amplio abanico de condiciones de contorno. Por ejemplo, debe ser posible imponer tensiones y desplazamientos armónicos en distintos contornos, así como cargas y movimientos armónicos en las cabezas de los pilotes, en los encepados o en las plantas de las superestructuras. De este modo será posible obtener funciones de impedancia o factores de interacción cinemática de pilotes y grupos de pilotes. Además, la obtención de la respuesta dinámica del sistema ante ondas S, P o de Rayleigh es también de interés, por lo que cualquier aspecto relacionado con su implementación deberá ser abordado. Así, no sólo podrán evaluarse los factores de interacción cinemática de las cimentaciones, sino también la respuesta sísmica de una o varias estructuras pilotadas.

Cuando el modelo haya sido formulado y validado, deberá ser aplicado a tres tipos distintos de problemas: *(i)* la obtención de funciones de impedancia y de factores de interacción cinemática de cimentaciones pilotadas; *(ii)* la evaluación de la importancia de los efectos de interacción suelo-estructura en la respuesta de estructuras pilotadas, haciendo uso de las funciones obtenidas en el punto anterior a través de un modelo de subestructuración; y *(iii)* la evaluación de la influencia de la presencia de estructuras cercanas en la respuesta sísmica de estructuras pilotadas.

A.3. Contenidos

Esta tesis doctoral ha sido redactada en inglés. Por esta razón, y siguiendo lo establecido en el *reglamento para la elaboración, tribunal, defensa y evaluación de tesis doctorales de la Universidad de Las Palmas de Gran Canaria* del año 2005, se incluye este apartado, redactado en castellano, que recoge los antecedentes y objetivos de la investigación, la metodología utilizada, aportaciones originales, las conclusiones obtenidas y las futuras líneas de investigación.

Dado que este anexo recoge tan solo una parte del material presentado en la tesis doctoral, se ha optado por comentar a continuación la estructura y contenidos de la parte principal del documento de tesis, con el objetivo de ofrecer al lector una visión completa de los temas tratados en esta tesis.

Los conceptos básicos necesarios para abordar el problema que nos ocupa son expuestos de manera breve en el capítulo 2. Al principio del capítulo se presentan las ecuaciones de gobierno de la elastodinámica, seguidas de algunos comentarios sobre los fenómenos de propagación de ondas en medios elásticos, haciendo hincapié en el caso de las ondas armónicas planas. A partir de ahí, y haciendo uso del teorema de reciprocidad de la elastodinámica, se obtiene la representación integral del problema, lo cual permite la posterior formulación del método de los elementos de contorno, que es presentado hacia el final del capítulo. Finalmente

se comenta brevemente cómo puede utilizarse la misma formulación para estudiar materiales viscoelásticos.

El núcleo de este trabajo reside en la formulación de un método acoplado BEM-FEM para el análisis dinámico de cimentaciones pilotadas, el cual es presentado en el capítulo 3. Este capítulo comienza con la obtención de las ecuaciones de elementos de contorno y de elementos finitos que son utilizadas para modelar, respectivamente, el suelo y los pilotes. El acoplamiento es realizado entonces a través de la imposición de las condiciones de equilibrio y compatibilidad en la interfase pilote-suelo. Posteriormente, y tras definir los encepados rígidos, se presenta el modelo que es utilizado para modelar las estructuras lineales, en el que todos los grados de libertad correspondientes a la superestructura son condensados al centro de gravedad de forjados y encepados. El capítulo termina con algunos comentarios acerca de la evaluación numérica de las integrales a lo largo de los pilotes.

El método acoplado de elementos de contorno y elementos finitos presentado en el capítulo 3 es utilizado en el capítulo 4 para analizar la respuesta dinámica de cimentaciones pilotadas. Antes de eso, el modelo es validado a través de distintas comparaciones con resultados obtenidos por otros autores. Posteriormente, se presentan tres grupos distintos de resultados: en primer lugar se estudia la distribución de esfuerzos cortantes a lo largo de algunos de los pilotes de un grupo cuadrado de 5×5, sujeto a vibración forzada; en segundo lugar se obtienen funciones de impedancia de cimentaciones pilotadas en estratos homogéneos, estudiando la influencia de parámetros tales como la relación de rigideces entre el pilote y el suelo, la profundidad del estrato y la configuración de la cimentación; finalmente, en la última sección del capítulo, se estudia la sensibilidad de la respuesta sísmica de un grupo de 3×3 pilotes a la estratigrafía del suelo, cuando la cimentación es sometida a ondas de corte de incidencia vertical.

En el capítulo 5 se estudia la respuesta sísmica de zapatas embebidas cimentadas sobre pilotes (denominadas de aquí en adelante *zapatas pilotadas*), problema que, sorprendentemente, ha recibido muy poca atención de la comunidad científica. La primera parte del capítulo presenta un procedimiento simple de tipo ingenieril para obtener las funciones de impedancia de este tipo de cimentaciones a partir de las correspondientes a la zapata embebida y al grupo de pilotes, obtenidas por separado y combinadas por superposición. A continuación se investiga cuál es la mejor forma de estimar los factores de interacción cinemática de las zapatas pilotadas a partir de los factores de sus partes constitutivas. El capítulo termina analizando los efectos que, sobre las funciones de impedancia, pueda tener la separación que puede llegar a existir entre la cara inferior de la zapata y el suelo debido a la consolidación de éste.

La principal utilidad de las funciones de rigidez dinámica y de los factores de interacción cinemática que fueron obtenidos en los capítulos 4 y 5 reside en

su utilización en modelos de subestructuración para analizar los efectos de interacción suelo-estructura a la hora de diseñar una estructura. Por este motivo, el capítulo 6 propone un modelo de subestructuración para el análisis de los efectos dinámicos de interacción suelo-estructura en estructuras pilotadas. Dicho modelo se utiliza para analizar la influencia de dichos efectos en el período fundamental y en el amortiguamiento equivalente del sistema, para diferentes configuraciones estructurales y de la cimentación. A pesar de que este tipo de análisis podría ser realizado a través del método directo presentado en el capítulo 3, las características del estudio hacen aconsejable el uso de un modelo de subestructuración, el cual es capaz de ofrecer resultados suficientemente precisos con muy poco esfuerzo computacional. El capítulo comienza con la presentación del problema, del modelo de subestructuración y del procedimiento de resolución. A continuación, se presenta un estudio paramétrico de la respuesta dinámica de estructuras cimentadas sobre grupos de 2×2 y 3×3 pilotes. El capítulo concluye con un análisis de la sensibilidad de los resultados ante variaciones de parámetros tales como la relación de densidades entre el suelo y la estructura, la relación de masas de la cimentación y la estructura, y el amortiguamiento estructural sobre base rígida.

Las virtudes y las posibilidades de la formulación directa son explotadas en el capítulo 7, donde los efectos de interacción dinámica a través del suelo entre edificios pilotados cercanos son investigados haciendo uso de la formulación presentada en el capítulo 3. Después de definir el problema, se evalúa la influencia de los fenómenos de interacción en casos de grupos de tres, cinco y nueve estructuras cercanas de características dinámicas similares o no. El estudio tiene en cuenta parámetros como, por ejemplo, la esbeltez estructural, la relación entre las rigideces de pilotes y suelo, o la distancia entre estructuras adyacentes. El capítulo termina presentando varios espectros de respuesta máxima con el fin de ilustrar la influencia de los efectos de interacción estructura-suelo-estructura en la respuesta sísmica de estructuras que son sometidas a un movimiento sísmico.

Por último, el capítulo 8 contiene una revisión de las aportaciones originales del trabajo y de las conclusiones más interesantes que pueden derivarse de él. La tesis concluye comentando posibles líneas de investigación futuras y algunos desarrollos que podrían realizarse en breve a partir de aquí.

Apéndice B

Modelo BEM-FEM para el análisis dinámico de cimentaciones y estructuras pilotadas

B.1. Introducción

A la hora de plantear el método directo de los elementos de contorno aplicado al problema elastodinámico en el dominio de la frecuencia, la ecuación integral en el contorno es generalmente obtenida a partir del teorema de reciprocidad de la elastodinámica, teniendo en cuenta la fuerzas por unidad de volumen. Sin embargo, antes del proceso de discretización que permite plantear el sistema lineal de ecuaciones del método de los elementos de contorno, se asume, en la mayor parte de las aplicaciones, que dichas fuerzas por unidad de volumen son nulas en todo el dominio, lo que permite cancelar el último término de la ecuación integral.

Por contra, el enfoque utilizado en este trabajo, similar al presentado por Matos Filho et al [119] en un modelo estático previo, incluye este término al considerar que las tensiones que aparecen en la interfase pilote-suelo pueden entenderse como fuerzas de volumen que actúan en el interior del dominio. Por otro lado, la rigidez aportada por los pilotes es tenida en cuenta a través de elementos finitos longitudinales que relacionan los desplazamientos de distintos puntos internos del suelo alineados a lo largo del eje del pilote. De este modo, no hay necesidad de discretizar la interfase pilote-suelo utilizando elementos de contorno, con el consiguiente ahorro en grados de libertad. Así, no se considera un vaciado en el suelo, que se modela como un medio continuo.

La sección B.2 presenta la ecuación integral de contorno para el suelo, donde las

fuerzas y las tensiones que aparecen en la interfase pilote-suelo son consideradas como líneas de carga y fuerzas internas que aparecen en el interior del dominio. A continuación, la sección B.3 expone la formulación de elementos finitos utilizada para modelar los pilotes, con lo que ya es posible realizar el acoplamiento entre los elementos finitos y los elementos de contorno, tal y como se hace en la sección B.4. Posteriormente, la agrupación de pilotes por medio de encepados rígidos es presentada la sección B.5, y a partir de ahí, la sección B.6 aborda el modo en que se introducen en el modelo estructuras cimentadas sobre los grupos de pilotes formulados en los apartados anteriores. La exposición del modelo numérico de elementos de contorno y elementos finitos termina en la sección B.7, donde se aborda el proceso de ensamblaje del sistema de ecuaciones final. Algunos aspectos numéricos sobre la evaluación de las integrales relacionadas con las líneas de carga son explicados en la sección B.8. Parte del material presentado en este capítulo ha sido previamente publicado en algunos trabajos realizados por el autor y por sus directores de tesis [138, 139].

B.2. Ecuaciones de elementos de contorno para el suelo

Cada uno de los estratos del suelo es modelado a través del método de los elementos de contorno como una región lineal, homogénea, isótropa, viscoelástica y no acotada, con un módulo de elasticidad transversal complejo μ del tipo $\mu = Re[\mu](1+2\mathrm{i}\beta)$, donde β es el coeficiente de amortiguamiento. La ecuación integral en el contorno para un estado elastodinámico definido en un dominio Ω_m con un contorno Γ^m puede ser escrito de forma general y condensada como

$$\mathbf{c}^\iota \mathbf{u}^\iota + \int_{\Gamma^m} \mathbf{p}^* \mathbf{u}\, d\Gamma = \int_{\Gamma^m} \mathbf{u}^* \mathbf{p}\, d\Gamma + \int_{\Omega_m} \mathbf{u}^* \mathbf{X}\, d\Omega \tag{B.1}$$

donde $\mathbf{c}^\iota$ es el tensor del término libre en el punto de colocación $\mathbf{x}^\iota$, $\mathbf{X}$ son las fuerzas de volumen en el dominio Ω_m, $\mathbf{u}$ y $\mathbf{p}$ son los vectores de desplazamientos y tensiones, y $\mathbf{u}^*$ y $\mathbf{p}^*$ son los tensores de la solución fundamental elastodinámica, que representan la respuesta de una región no acotada a una carga harmónica unitaria concentrada en un punto $\mathbf{x}^\iota$ y con una variación temporal del tipo $e^{\mathrm{i}\omega t}$.

En gran número de aplicaciones, se considera que la fuerzas de volumen $\mathbf{X}$ son nulas. De aquí en adelante, por contra, se considerará que la interacción pilote-suelo se produce, desde el punto de vista de la ecuación integral, a través de fuerzas internas puntuales situadas en la punta de los pilotes y de líneas de carga repartidas a lo largo del eje de los pilotes. Se considera, por tanto, que la continuidad del suelo no se ve alterada por la presencia de los pilotes. Las líneas de carga dentro del suelo, las tensiones a lo largo de la interfase pilote-suelo, actuando sobre el

pilote y en el interior del suelo ($\mathbf{q}^{p_j} = -\mathbf{q}^{s_j}$), y las fuerzas internas puntuales F_{p_j} en la punta de los pilotes, están representadas en la fig. B.1, donde se muestra un esquema del modelo.

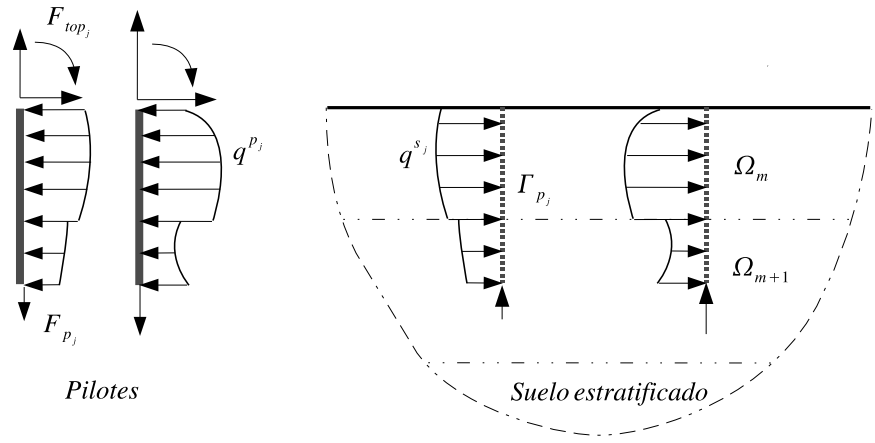

Figura B.1: *Representación de las líneas de carga*

De acuerdo a las hipótesis enumeradas anteriormente, la ec. (B.1) puede ser escrita como

$$\mathbf{c}^{\iota}\mathbf{u}^{\iota} + \int_{\Gamma^m} \mathbf{p}^*\mathbf{u}\, d\Gamma = \int_{\Gamma^m} \mathbf{u}^*\mathbf{p}\, d\Gamma + \sum_{j=1}^{n_{ll}^m} \left[\int_{\Gamma_{p_j}^m} \mathbf{u}^*\mathbf{q}^{s_j}\, d\Gamma_{p_j} - \delta_j \boldsymbol{\Upsilon}_k^j F_{p_j} \right] \tag{B.2}$$

donde $\Gamma_{p_j}^m$ es la interfase pilote-suelo a lo largo de la línea de carga j en el interior del dominio Ω_m; n_{ll}^m es el número total de líneas de carga en el dominio Ω_m; δ_j toma valor unitario si la línea de carga j contiene a la punta de un pilote flotante, o toma el valor cero en caso contrario; y $\boldsymbol{\Upsilon}_k^j$ es un vector de tres componentes que representa la contribución de la fuerza axial F_{p_j} en la punta de la línea de carga j-ésima.

Los contornos Γ^m son discretizados por medio de elementos cuadráticos triangulares o cuadriláteros con seis o nueve nodos, respectivamente. Cuando los contorno han sido discretizados, la ec. (B.2) puede ser escrita para cada región Ω_m, en todos los nodos sobre Γ^m con el fin de obtener una ecuación matricial del tipo

$$\mathbf{H}^{ss}\mathbf{u}^s - \mathbf{G}^{ss}\mathbf{p}^s - \sum_{j=1}^{n_{ll}^m} \mathbf{G}^{sp_j}\mathbf{q}^{s_j} + \sum_{j=1}^{n_{ll}^m} \delta_j \boldsymbol{\Upsilon}^{sj} F_{p_j} = 0 \tag{B.3}$$

donde $\mathbf{u}^s$ y $\mathbf{p}^s$ son los vectores de desplazamientos y tensiones nodales de los elementos de contorno; $\mathbf{H}^{ss}$ y $\mathbf{G}^{ss}$ son las matrices de coeficientes obtenidas de la

integración numérica sobre los elementos de contorno del producto de la solución fundamental por las funciones de forma correspondientes; y $\mathbf{G}^{sp_j}$ es la matriz de coeficientes obtenida de la integración numérica sobre la línea de carga j del producto de la solución fundamental por las funciones de interpolación (B.13), cuando la carga unitaria está aplicada sobre Γ^m.

Por otro lado, la ec. (B.2) será también aplicada sobre los puntos internos que pertenecen a la línea de carga $\Gamma^m_{p_i}$, lo que lleva a la siguiente expresión:

$$\mathbf{c}\,\mathbf{u}^{p_i} + \mathbf{H}^{p_i s}\mathbf{u}^s - \mathbf{G}^{p_i s}\mathbf{p}^s - \sum_{j=1}^{n^m_{ll}} \mathbf{G}^{p_i p_j}\mathbf{q}^{s_j} + \sum_{j=1}^{n^m_{ll}} \delta_j \boldsymbol{\Upsilon}^{p_i j} F_{p_j} = 0 \tag{B.4}$$

donde $\mathbf{H}^{p_i s}$ y $\mathbf{G}^{p_i s}$ son matrices de coeficientes obtenidas a través de la integración numérica sobre los elementos de contorno del producto de la solución fundamental por las funciones de forma correspondientes; y $\mathbf{G}^{p_i p_j}$ es la matriz de coeficientes obtenida a través de la integración numérica sobre la línea de carga j del producto de la solución fundamental por las funciones de interpolación (B.13), cuando la carga unitaria está aplicada sobre la línea de carga $\Gamma^m_{p_i}$. Aquí, $\mathbf{u}^{p_i}$ es el vector de desplazamientos nodales de la línea de carga i, el cual es multiplicado por el vector $\mathbf{c}$, que toma el valor $1/2$ en posiciones correspondientes a nodos del pilote localizados sobre un contorno suave (como en el caso de las cabezas de los pilotes) o toma un valor unitario en los puntos internos. Hay que tener en cuenta que la posición del nodo que define la cabeza del pilote puede coincidir con la posición de algún nodo de la superficie. En este caso existirán dos nodos con idénticas coordenadas espaciales. Entonces, dos de las ecuaciones del sistema, la escrita para el nodo de la superficie y la escrita para el nodo de la línea de carga, serán equivalentes, pero el término libre ocupará diferentes posiciones en la matriz de coeficientes, lo que evitará que se tenga un sistema de ecuaciones singular.

Por otro lado, dado que para pilotes flotantes se considera la existencia de una fuerza axial actuando en la punta, es necesario escribir una ecuación extra. Para ello, la carga puntual debe ser aplicada en la dirección x_3 en algún punto no nodal. Dado su cercanía a la punta del pilote, el punto más idóneo es el de coordenada elemental adimensional $\xi = -1/2$ del elemento inferior (véase la sección B.3.2). De este modo, la ecuación extra es

$$\begin{aligned} &\frac{1}{8}\left(3u_3^{b_k} + 6u_3^{b_l} - u_3^{b_m}\right) + \int_{\Gamma^m} \hat{\mathbf{p}}^*\mathbf{u}\,d\Gamma = \\ &\qquad = \int_{\Gamma^m} \hat{\mathbf{u}}^*\mathbf{p}\,d\Gamma + \sum_{j=1}^{n^m_{ll}} \left[\int_{\Gamma^m_{pj}} \hat{\mathbf{u}}^*\mathbf{q}^{s_j}\,d\Gamma_{p_j} - \delta_j \left(\Upsilon^j_b\right)_3 F_{p_j}\right] \end{aligned} \tag{B.5}$$

donde $u_3^{b_k}$,$u_3^{b_l}$ y $u_3^{b_m}$ son los desplazamientos verticales de los nodos k,l y m del elemento inferior, $\hat{\mathbf{p}}^* = \{p^*_{31}, p^*_{32}, p^*_{33}\}$ y $\hat{\mathbf{u}}^* = \{u^*_{31}, u^*_{32}, u^*_{33}\}$. De forma matricial,

la ec. (B.5) puede ser escrita como

$$\mathbf{D}^T \mathbf{u}_b^{p_i} + \mathbf{H}_e^{p_i s}\mathbf{u}^s - \mathbf{G}_e^{p_i s}\mathbf{p}^s - \sum_{j=1}^{n_{ll}^m} \mathbf{G}_e^{p_i p_j}\mathbf{q}^{s_j} + \sum_{j=1}^{n_{ll}^m} \delta_j \Upsilon_{b_3}^{p_i j} F_{p_j} = 0 \qquad \text{(B.6)}$$

donde $\mathbf{u}_b^{p_i}$ es el vector de desplazamientos nodales en los nodos del elemento inferior de la línea de carga i (que corresponde al extremo inferior de un pilote flotante) donde la carga unitaria está aplicada; $\mathbf{H}_e^{p_i s}$ y $\mathbf{G}_e^{p_i s}$ son vectores obtenidos por integración numérica sobre Γ^m del producto de la solución fundamental elastodinámica por las funciones de forma de los elementos de contorno; y $\mathbf{G}_e^{p_i p_j}$ es el vector obtenido de la integración sobre $\Gamma_{p_j}^m$ del producto de la solución fundamental elastodinámica por las funciones de forma definidas en (B.13), cuando la carga unitaria está aplicada en el punto extra de la línea de carga i. Finalmente, $\mathbf{D}^T = 1/8\{0, 0, 3, 0, 0, 6, 0, 0, -1\}$.

Acerca del paso de un pilote a través de una interfase entre regiones adyacentes

El caso de un pilote que atraviesa una interfase entre regiones adyacentes, tal y como se muestra en la fig. B.2, merece cierta atención. En esta situación, representada en la fig. B.1, la distribución de tensiones q^s a lo largo de la interfase pilote-suelo no es continua entre capas, por lo que diferentes líneas de carga son consideradas en las regiones superior e inferior. Este hecho produce un tipo de problema de esquina que puede ser resuelto aplicando una estrategia de colocación no nodal. Para nodos situados sobre la interfase, la ec. (B.4) se aplica sobre un punto interno del elemento k correspondiente, de tal modo que la ecuación integral queda

$$\mathbf{\Phi}\mathbf{u}_k^{p_i} + \mathbf{H}^{p_i s}\mathbf{u}^s - \mathbf{G}^{p_i s}\mathbf{p}^s - \sum_{j=1}^{n_{ll}^m} \mathbf{G}^{p_i p_j}\mathbf{q}^{s_j} + \sum_{j=1}^{n_{ll}^m} \delta_j \mathbf{\Upsilon}^{p_i j} F_{p_j} = 0 \qquad \text{(B.7)}$$

donde $\mathbf{u}_k^{p_i}$ es el vector de desplazamientos nodales del elemento Γ_k y $\mathbf{\Phi}$ es la matriz de funciones de forma particularizada para el punto de colocación.

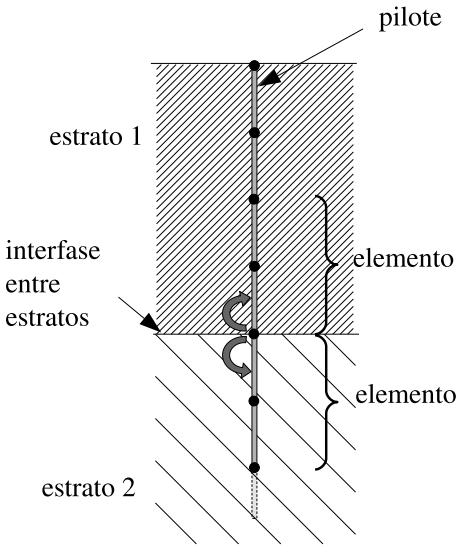

Figura B.2: *Pilote atravesando una interfase entre regiones adyacentes*

B.3. Ecuaciones de elementos finitos para la cimentación pilotada

B.3.1. Ecuación de movimiento

El comportamiento de un pilote sometido a cargas dinámicas puede ser descrito a través de la siguiente ecuación diferencial

$$\mathbf{M}\,\ddot{\mathbf{u}}(t) + \mathbf{C}\,\dot{\mathbf{u}}(t) + \mathbf{K}\,\mathbf{u}(t) = \mathbf{f}(t) \tag{B.8}$$

donde $\mathbf{M}$, $\mathbf{C}$ y $\mathbf{K}$ son las matrices de masa, amortiguamiento y rigidez del pilote, $\mathbf{u}(t)$ es el vector de desplazamientos nodales y $\mathbf{f}(t)$ es el vector de fuerzas nodales sobre el pilote.

Consideremos ahora que el pilote está sujeto a cargas armónicas, en cuyo caso los vectores de desplazamientos y fuerzas nodales pueden ser expresados como

$$\mathbf{u}(t) = \mathbf{u}^p\, e^{\mathrm{i}\omega t} \quad \text{y} \quad \mathbf{f}(t) = \mathbf{F}\, e^{\mathrm{i}\omega t} \tag{B.9}$$

donde $\mathbf{u}^p$ es el vector que contiene las amplitudes de las traslaciones y rotaciones nodales, $\mathbf{F}$ es el vector que contiene las amplitudes de las fuerzas y momentos nodales, ω es la frecuencia angular de la excitación, e $\mathrm{i} = \sqrt{-1}$. De este modo, y considerando un pilote con amortiguamiento interno nulo, la ec. (B.8) puede expresarse ahora como

$$(\mathbf{K} - \omega^2\mathbf{M})\,\mathbf{u}^p = \mathbf{F} \tag{B.10}$$

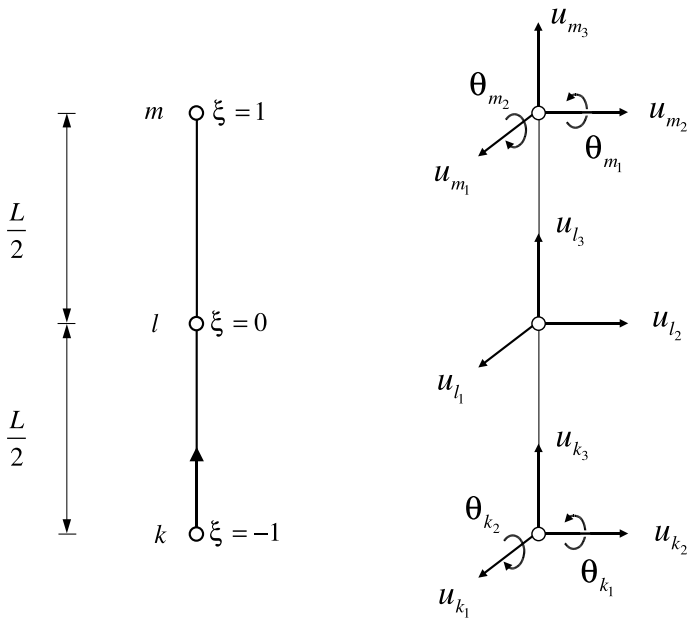

Figura B.3: *Definición del elementos finito*

B.3.2. Definición del elemento viga

Los pilotes son modelados, haciendo uso del método de los elementos finitos, como elementos verticales de acuerdo a la teoría de vigas de Euler-Bernoulli, y son discretizados utilizando elementos de tres nodos (como se muestra en la fig. B.3) que han sido definidos de manera que sea posible aproximar la deformada del pilote con un número bajo de elementos. Se definen 13 grados de libertad sobre dicho elemento: un desplazamiento vertical y dos desplazamientos horizontales en cada nodo, y además, dos rotaciones θ en cada uno de los nodos extremos, uno alrededor del eje x_1 y otro alrededor del eje x_2.

Los desplazamientos laterales u_1 y u_2 a lo largo del elemento son aproximados a través de un conjunto de funciones de forma de cuarto grado, mientras que los desplazamientos verticales u_3 son aproximados por funciones de segundo grado. De este modo

$$u_i = \varphi_1 u_{k_i} + \varphi_2 \theta_{k_i} + \varphi_3 u_{l_i} + \varphi_4 u_{m_i} + \varphi_5 \theta_{m_i} \quad ; \quad i = 1, 2 \tag{B.11a}$$

$$u_3 = \phi_1 u_{k_3} + \phi_2 u_{l_3} + \phi_3 u_{m_3} \tag{B.11b}$$

donde

$$\begin{aligned}
\varphi_1 &= \xi(-\frac{3}{4} + \xi + \frac{1}{4}\xi^2 - \frac{1}{2}\xi^3) \\
\varphi_2 &= \frac{1}{4}\xi(-1 + \xi + \xi^2 - \xi^3) \\
\varphi_3 &= 1 - 2\xi^2 + \xi^4 \\
\varphi_4 &= \xi(\frac{3}{4} + \xi - \frac{1}{4}\xi^2 - \frac{1}{2}\xi^3) \\
\varphi_5 &= \frac{1}{4}\xi(-1 - \xi + \xi^2 + \xi^3)
\end{aligned} \tag{B.12}$$

y

$$\begin{aligned}
\phi_1 &= \frac{1}{2}\xi(\xi - 1) \\
\phi_2 &= 1 - \xi^2 \\
\phi_3 &= \frac{1}{2}\xi(\xi + 1)
\end{aligned} \tag{B.13}$$

siendo ξ la coordenada adimensional elemental que varía desde $\xi = -1$ hasta $\xi = +1$.

Las submatrices de rigidez que definen el comportamiento lateral y axial del elemento (indicadas por los superíndices l y a respectivamente), pueden ser obtenidas haciendo uso de las funciones de forma arriba indicadas y del principio de los desplazamientos virtuales como

$$k_{ij}^l = \int_L \varphi_i'' EI \varphi_j'' \, dx_3 \quad ; \quad i,j = 1,...,5 \tag{B.14}$$

y

$$k_{ij}^a = \int_L \phi_i' EA \phi_j' \, dx_3 \quad ; \quad i,j = 1,2,3 \tag{B.15}$$

donde las primas indican derivada respecto de la coordenada x_3. De este modo, las submatrices de rigidez son

$$\mathbf{K}^l = \frac{EI}{5L}\begin{bmatrix} \frac{316}{L^2} & \frac{94}{L} & \frac{-512}{L^2} & \frac{196}{L^2} & \frac{-34}{L} \\ \frac{94}{L} & 36 & \frac{-128}{L} & \frac{34}{L} & -6 \\ \frac{512}{L^2} & \frac{-128}{L} & \frac{1024}{L^2} & \frac{-512}{L^2} & \frac{128}{L} \\ \frac{196}{L^2} & \frac{34}{L} & \frac{-512}{L^2} & \frac{316}{L^2} & \frac{-94}{L} \\ \frac{-34}{L} & -6 & \frac{-128}{L} & \frac{-94}{L} & 36 \end{bmatrix} \quad , \quad \mathbf{K}^a = \frac{EA}{3L}\begin{bmatrix} 7 & -8 & 1 \\ -8 & 16 & -8 \\ 1 & -8 & 7 \end{bmatrix} \tag{B.16}$$

donde E es el módulo de Young del pilote, A e I son el área y el momento de inercia de la sección del pilote, y L es la longitud del elemento, y donde se ha considerado que los momentos de inercial respecto a ambos ejes principales de inercia son iguales.

De manera similar, los coeficientes de influencia que constituyen la matriz de masa de un elemento, y que representan las fuerzas de inercia que se oponen a la aceleración experimentada por un cierto grado de libertad, pueden ser evaluadas de manera similar como

$$m_{ij}^{l} = \int_{L} \varphi_i \bar{m} \varphi_j \, dx_3 \quad ; \quad m_{ij}^{a} = \int_{L} \phi_i \bar{m} \phi_j \, dx_3 \tag{B.17}$$

De este modo, y considerando un viga con una masa $\bar{m}$ uniformemente distribuida, las matrices de masa consistente que rigen los comportamientos lateral y axial son, respectivamente

$$\mathbf{M}^{l} = L\,\bar{m} \begin{bmatrix} \frac{13}{63} & \frac{L}{63} & \frac{4}{63} & \frac{-23}{630} & \frac{L}{180} \\ \frac{L}{63} & \frac{L^2}{630} & \frac{2L}{315} & \frac{-L}{180} & \frac{L^2}{1260} \\ \frac{4}{63} & \frac{2L}{315} & \frac{128}{315} & \frac{4}{63} & \frac{-2L}{315} \\ \frac{-23}{630} & \frac{-L}{180} & \frac{4}{63} & \frac{13}{63} & \frac{-L}{63} \\ \frac{L}{180} & \frac{L^2}{1260} & \frac{-2L}{315} & \frac{-L}{63} & \frac{L^2}{630} \end{bmatrix} \quad ; \quad \mathbf{M}^{a} = \frac{L\,\bar{m}}{15} \begin{bmatrix} 2 & 1 & \frac{-1}{2} \\ 1 & 8 & 1 \\ \frac{-1}{2} & 1 & 2 \end{bmatrix} \tag{B.18}$$

B.3.3. Fuerzas sobre el pilote

Dentro de las fuerzas externas actuando sobre el pilote, se considera la existencia de fuerzas y momentos puntuales en la cabeza del pilote, fuerzas distribuídas a lo largo del fuste debidas a la interacción pilote-suelo, y una fuerza axial sobre la punta del pilote. De este modo, el vector de fuerzas nodales $\mathbf{F}$ puede ser descompuesto como

$$\mathbf{F} = \mathbf{F}^{ext} + \mathbf{F}^{eq} = \mathbf{F}_{top} + \mathbf{F}_{p} + \mathbf{F}^{eq} \tag{B.19}$$

donde $\mathbf{F}^{ext}$ incluye las fuerzas en la cabeza $\mathbf{F}_{top}$ y la fuerza axial en la punta del pilote $\mathbf{F}_p$; y $\mathbf{F}^{eq}$ es el vector de fuerzas nodales equivalente debido a la interacción pilote-suelo, que puede ser calculado como $\mathbf{F}^{eq} = \mathbf{Q} \cdot \mathbf{q}^{p}$, donde $\mathbf{Q}$ es la matriz que transforma las tensiones en fuerzas nodales equivalentes.

Las fuerzas externas que se definen sobre un elementos genérico están esquematizadas en la fig. B.4. Las tensiones $\mathbf{q}^p$ a lo largo de la interfase pilote-suelo son aproximadas como

$$q_i = \phi_1 q_{k_i} + \phi_2 q_{l_i} + \phi_3 q_{m_i} \quad ; \quad i = 1, 2, 3 \tag{B.20}$$

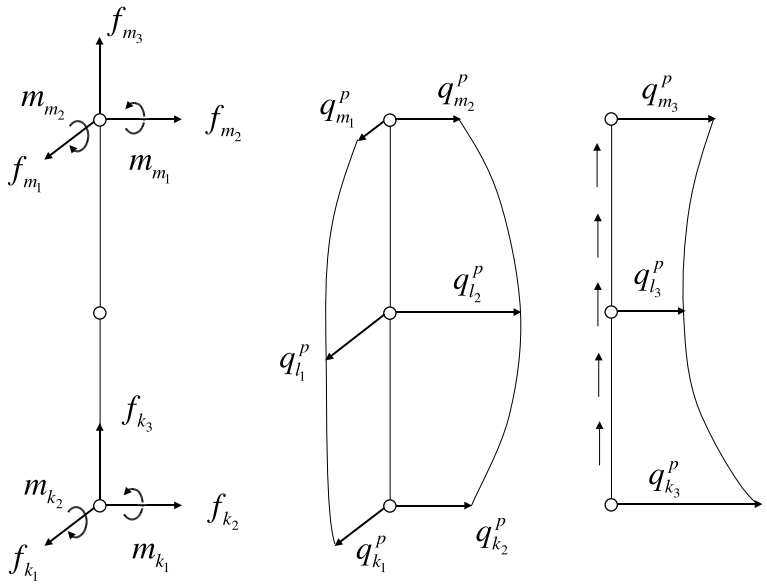

Figura B.4: *Fuerzas puntuales externas (izquierda) y tensiones a lo largo de la interfase pilote-suelo, definidas sobre un elemento genérico*

utilizando el conjunto de funciones de forma definidos por la ec. (B.13). La distribución de tensiones a lo largo de la interfase pilote-suelo es continua entre elementos, excepto para un pilote que atraviesa una interfase entre estratos, caso en el que q_i serán diferentes por encima y por debajo del punto de interés.

De nuevo, los coeficientes de la matriz $\mathbf{Q}$ para la computación de las fuerzas laterales pueden ser obtenidos utilizando el principio de los desplazamiento virtuales

$$q^l_{ij} = \int_L \varphi_i \phi_j \, dx \quad ; \quad i = 1, ..., 5 \; ; \; j = 1, 2, 3 \tag{B.21}$$

mientras que los coeficientes de la matriz correspondiente a las fuerzas axiales se obtienen haciendo

$$q^a_{ij} = \int_L \phi_i \phi_j \, dx \quad ; \quad i, j = 1, 2, 3 \tag{B.22}$$

lo cual arroja las siguientes matrices:

$$\mathbf{Q}^l = \begin{bmatrix} \frac{23L}{140} & \frac{11L}{105} & \frac{-L}{28} \\ \frac{L^2}{84} & \frac{L^2}{105} & \frac{-L^2}{210} \\ \frac{4L}{105} & \frac{16L}{35} & \frac{4L}{105} \\ \frac{-L}{28} & \frac{11L}{105} & \frac{23L}{140} \\ \frac{L^2}{210} & \frac{-L^2}{105} & \frac{-L^2}{84} \end{bmatrix} \quad , \quad \mathbf{Q}^a = \frac{L}{30} \begin{bmatrix} 4 & 2 & -1 \\ 2 & 16 & 2 \\ -1 & 2 & 4 \end{bmatrix} \tag{B.23}$$

B.3.4. Sistema de ecuaciones para el pilote simple

Una vez que todas las matrices elementales han sido obtenidas para el pilote completo, es posible escribir, para cada pilote, la siguiente expresión

$$\bar{\mathbf{K}}\,\mathbf{u}^p = \mathbf{F}^{ext} + \mathbf{Q}\,\mathbf{q}^p \tag{B.24}$$

donde $\bar{\mathbf{K}} = \mathbf{K} - \omega^2\mathbf{M}$. Dado que cada pilote es discretizado utilizando tantos elementos como sea necesario para poder seguir de forma precisa su deformada, las matrices $\bar{\mathbf{K}}$ y $\mathbf{Q}$ deben ser entendidas como matrices globales, obtenidas a partir de las matrices elementales siguiendo los procedimientos usuales del método de los elementos finitos

Nótese que, dado que se asume que la continuidad del suelo no se ve alterada por la presencia de los pilotes, el valor de la masa distribuida asignado a cada pilote debe ser modificado según la expresión $\bar{m} = A(\rho_p - \rho_s)$, con el objetivo de no sobrestimar la masa total del sistema, siendo ρ_p y ρ_s las densidades del pilote y del suelo. Consideraciones de similar naturaleza fueron adoptadas en [28,51,53].

B.4. Acoplamiento BEM-FEM

El siguiente paso es la construcción de un sistema de ecuaciones global a partir de las expresiones deducidas en las secciones anteriores. El acoplamiento será realizado a través de las tensiones $\mathbf{q}^{sj} = -\mathbf{q}^{p_j}$ a lo largo de la interfase pilote-suelo y de los desplazamientos $\mathbf{u}^{p_j}$ a lo largo del pilote j.

La ec. (B.24), escrita para el pilote j, puede ser expresada ahora como

$$\bar{\mathbf{K}}^{p_j}\,\mathbf{u}^{p_j} - \mathbf{F}_{p_j} + \mathbf{Q}\,\mathbf{q}^{sj} = \mathbf{F}^j_{top} \tag{B.25}$$

Imponiendo condiciones de compatibilidad y equilibrio soldados a lo largo de las interfases pilote-suelo, y tomando como criterio de signos que las tensiones $\mathbf{q}^s$ son positivas, las ecuaciones (B.3), (B.4), (B.6) y (B.25) puede ser reordenadas en

un único sistema de ecuaciones que representará al sistema suelo estratificado – cimentación pilotada. Para un semiespacio uniforme, el sistema acoplado será de la forma

$$\begin{bmatrix} \mathbf{H}^{ss} & -\mathbf{G}^{sp} & \boldsymbol{\Upsilon}^{s} & \emptyset \\ \mathbf{H}^{ps} & -\mathbf{G}^{pp} & \boldsymbol{\Upsilon}^{p} & \mathbf{C}' \\ \mathbf{H}_e^{ps} & -\mathbf{G}_e^{pp} & \boldsymbol{\Upsilon}_{b_3}^{p} & \mathbf{D}' \\ \emptyset & \mathbf{Q} & -\mathbf{I}' & \bar{\mathbf{K}} \end{bmatrix} \begin{bmatrix} \mathbf{u}^{s} \\ \mathbf{q}^{s} \\ \mathbf{F}_{p} \\ \mathbf{u}^{p} \end{bmatrix} = \mathcal{B} \tag{B.26}$$

donde $\mathbf{H}^{ss}$ es la matriz de dimensiones $3N \times 3N$ obtenida mediante la integración, sobre los elementos de contorno, del producto de la solución fundamental armónica en tensiones por las funciones de forma correspondientes, cuando la carga es aplicada sobre los contornos; N es el número de nodos en el contorno; $\mathbf{D}'$ es una matriz constituida por los distintos vectores $\mathbf{D}$; $\mathbf{C}'$ es una matriz que contiene los términos libres correspondientes a la colocación sobre los nodos del pilote; e $\mathbf{I}'$ es una matriz llena de elementos nulos excepto en los términos correspondientes a las incógnitas F_{p_j}, donde se coloca un término de valor unidad. El resto de las submatrices son

$$\mathbf{G}^{pp} = \begin{bmatrix} \mathbf{G}^{p_1p_1} & \mathbf{G}^{p_1p_2} & \cdots & \mathbf{G}^{p_1p_n} \\ \mathbf{G}^{p_2p_1} & \mathbf{G}^{p_2p_2} & \cdots & \mathbf{G}^{p_2p_n} \\ \vdots & \vdots & \ddots & \vdots \\ \mathbf{G}^{p_np_1} & \mathbf{G}^{p_np_2} & \cdots & \mathbf{G}^{p_np_n} \end{bmatrix}$$

$$\mathbf{G}_e^{pp} = \begin{bmatrix} \mathbf{G}_e^{p_1p_1} & \mathbf{G}_e^{p_1p_2} & \cdots & \mathbf{G}_e^{p_1p_n} \\ \mathbf{G}_e^{p_2p_1} & \mathbf{G}_e^{p_2p_2} & \cdots & \mathbf{G}_e^{p_2p_n} \\ \vdots & \vdots & \ddots & \vdots \\ \mathbf{G}_e^{p_np_1} & \mathbf{G}_e^{p_np_2} & \cdots & \mathbf{G}_e^{p_np_n} \end{bmatrix}$$

$$\boldsymbol{\Upsilon}^{p} = \begin{bmatrix} \boldsymbol{\Upsilon}^{p_1 1} & \boldsymbol{\Upsilon}^{p_1 2} & \cdots & \boldsymbol{\Upsilon}^{p_1 n} \\ \boldsymbol{\Upsilon}^{p_2 1} & \boldsymbol{\Upsilon}^{p_2 2} & \cdots & \boldsymbol{\Upsilon}^{p_2 n} \\ \vdots & \vdots & \ddots & \vdots \\ \boldsymbol{\Upsilon}^{p_n 1} & \boldsymbol{\Upsilon}^{p_n 2} & \cdots & \boldsymbol{\Upsilon}^{p_n n} \end{bmatrix}$$

$$\boldsymbol{\Upsilon}^{p}_{b_3} = \begin{bmatrix} \Upsilon^{p_1 1}_{b_3} & \Upsilon^{p_1 2}_{b_3} & \cdots & \Upsilon^{p_1 n}_{b_3} \\ \Upsilon^{p_2 1}_{b_3} & \Upsilon^{p_2 2}_{b_3} & \cdots & \Upsilon^{p_2 n}_{b_3} \\ \vdots & \vdots & \ddots & \vdots \\ \Upsilon^{p_n 1}_{b_3} & \Upsilon^{p_n 2}_{b_3} & \cdots & \Upsilon^{p_n n}_{b_3} \end{bmatrix}$$

$$\mathbf{G}^{sp} = \begin{bmatrix} \mathbf{G}^{sp_1} & \mathbf{G}^{sp_2} & \cdots & \mathbf{G}^{sp_n} \end{bmatrix}$$

$$\boldsymbol{\Upsilon}^{s} = \begin{bmatrix} \boldsymbol{\Upsilon}^{s1} & \boldsymbol{\Upsilon}^{s2} & \cdots & \boldsymbol{\Upsilon}^{sn} \end{bmatrix}$$

$$\mathbf{H}^{ps} = \begin{bmatrix} \mathbf{H}^{p_1 s} & \mathbf{H}^{p_2 s} & \cdots & \mathbf{H}^{p_n s} \end{bmatrix}^T$$

$$\mathbf{H}^{ps}_{e} = \begin{bmatrix} \mathbf{H}^{p_1 s}_{e} & \mathbf{H}^{p_2 s}_{e} & \cdots & \mathbf{H}^{p_n s}_{e} \end{bmatrix}^T$$

$$\mathbf{Q} = \begin{bmatrix} \mathbf{Q}^{p_1} & \emptyset & \cdots & \emptyset \\ \emptyset & \mathbf{Q}^{p_2} & \cdots & \emptyset \\ \vdots & \vdots & \ddots & \vdots \\ \emptyset & \emptyset & \cdots & \mathbf{Q}^{p_n} \end{bmatrix}$$

$$\bar{\mathbf{K}} = \begin{bmatrix} \bar{\mathbf{K}}^{p_1} & \emptyset & \cdots & \emptyset \\ \emptyset & \bar{\mathbf{K}}^{p_2} & \cdots & \emptyset \\ \vdots & \vdots & \ddots & \vdots \\ \emptyset & \emptyset & \cdots & \bar{\mathbf{K}}^{p_n} \end{bmatrix}$$

$\mathcal{B}$ es el vector del lado derecho, obtenido de aplicar las condiciones de contorno, mientras que el vector de incógnitas es

$$\mathbf{x} = \{\mathbf{u}^s, \mathbf{q}^{s_1}, \mathbf{q}^{s_2}, \ldots, \mathbf{q}^{s_n}, F_{p_1}, F_{p_2}, \ldots, F_{p_n}, \mathbf{u}^{p_1}, \mathbf{u}^{p_2}, \ldots, \mathbf{u}^{p_n}\}^T \tag{B.27}$$

En el caso de dominios estratificados, la estructura del sistema de ecuaciones es la misma, aunque deben imponerse también condiciones de equilibrio y compatibilidad soldados sobre todas las interfases del problema.

B.5. Formulación del encepado rígido

Diferentes pilotes pueden trabajar juntos en un grupo si sus cabezas son vinculadas a través de un encepado. En este trabajo en concreto, se considerará que los pilotes están fijamente conectados a un encepado rígido. Las restricciones cinemáticas entre los distintos pilotes, junto a las ecuaciones de equilibrio del conjunto, son presentadas en las siguientes secciones.

B.5.1. Restricciones cinemáticas

La vinculación de los desplazamientos de las cabezas de los pilotes de un grupo es ejecutada definiendo las ecuaciones de movimiento de sólido rígido y, posteriormente, condensando los grados de libertad deseados. Con el objetivo de simplificar la implementación, los grados de libertad definidos sobre las cabezas de algunos pilotes serán los utilizados como referencia para condensar el resto de grados de libertad. Sólo existen cinco grados de libertad en la cabeza de un pilote, mientras que se necesitan seis grados de libertad (tres desplazamientos y tres rotaciones) para representar el comportamiento del encepado rígido, por lo que se utilizarán dos pilotes. Éstos serán denominados como *pilote de referencia* y *pilote periférico*, siendo este último necesario tan solo para la definición de la rotación del encepado alrededor de un eje vertical.

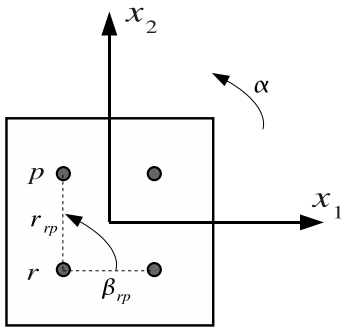

Figura B.5: *Pilote de referencia (r) y pilote periférico (p)*

Sean β_{rp} y r_{rp} el ángulo y la distancia existentes entre las cabezas de los pilotes de referencia y periférico (véase la fig. B.5). Bajo la hipótesis de pequeñas deformaciones, pueden escribirse las siguientes relaciones

$$u_{p_1} = u_{r_1} - r_{rp}\alpha \sin(\beta_{rp}) \tag{B.28a}$$

$$u_{p_2} = u_{r_2} + r_{rp}\alpha \cos(\beta_{rp}) \tag{B.28b}$$

donde los subíndices 1 y 2 indican desplazamientos a lo largo de los ejes x_1 y x_2, respectivamente. De este modo, el ángulo α de rotación del encepado puede ser definido entre ambos pilotes como

$$si \begin{cases} 45^o \leq \beta_{rp} \leq 135^o \\ 225^o \leq \beta_{rp} \leq 315^o \end{cases} \quad \text{entonces} \quad \alpha = \frac{u_{r_1} - u_{p_1}}{r_{rp}\ \sin(\beta_{rp})} \quad \text{(caso a)}$$

$$si \begin{cases} 315^o \leq \beta_{rp} \leq 45^o \\ 135^o \leq \beta_{rp} \leq 225^o \end{cases} \quad \text{entonces} \quad \alpha = \frac{u_{p_2} - u_{r_2}}{r_{rp}\ \cos(\beta_{rp})} \quad \text{(caso b)} \tag{B.29}$$

de tal modo que en el caso a, el grado de libertad auxiliar del pilote periférico es u_{p_1}, mientras que en el caso b, el grado de libertad utilizado es u_{p_2}. Ahora, teniendo en cuenta el conjunto de grados de libertad elegidos para representar el comportamiento del encepado rígido, el acoplamiento entre los pilotes de referencia y periférico puede expresarse, para los casos a y b respectivamente, a través de las siguientes matrices:

$$\begin{bmatrix} u_{p_2} \\ u_{p_3} \\ \theta_{p_1} \\ \theta_{p_2} \end{bmatrix} = \begin{bmatrix} \tan(\beta_{rp})^{-1} & 1 & 0 & 0 & 0 & -\tan(\beta_{rp})^{-1} \\ 0 & 0 & 1 & -d_{rp_1} & -d_{rp_2} & 0 \\ 0 & 0 & 0 & 1 & 0 & 0 \\ 0 & 0 & 0 & 0 & 1 & 0 \end{bmatrix} \begin{bmatrix} u_{r_1} \\ u_{r_2} \\ u_{r_3} \\ \theta_{r_1} \\ \theta_{r_2} \\ u_{p_1} \end{bmatrix} \tag{B.30}$$

y

$$\begin{bmatrix} u_{p_1} \\ u_{p_3} \\ \theta_{p_1} \\ \theta_{p_2} \end{bmatrix} = \begin{bmatrix} 1 & \tan(\beta_{rp}) & 0 & 0 & 0 & -\tan(\beta_{rp}) \\ 0 & 0 & 1 & -d_{rp_1} & -d_{rp_2} & 0 \\ 0 & 0 & 0 & 1 & 0 & 0 \\ 0 & 0 & 0 & 0 & 1 & 0 \end{bmatrix} \begin{bmatrix} u_{r_1} \\ u_{r_2} \\ u_{r_3} \\ \theta_{r_1} \\ \theta_{r_2} \\ u_{p_2} \end{bmatrix} \tag{B.31}$$

donde $d_{rp_i} = x_{p_i} - x_{r_i}$, siendo $\mathbf{x}$ el vector de posición del punto de interés. Sean ahora β_{rj} y r_{rj} el ángulo y la distancia existentes entre la cabeza del pilote de referencia y la de cualquier otro pilote j. Las matrices de acoplamiento, para los casos a y b, son, respectivamente:

$$\begin{bmatrix} u_{j_1} \\ u_{j_2} \\ u_{j_3} \\ \theta_{j_1} \\ \theta_{j_2} \end{bmatrix} = \begin{bmatrix} 1-\frac{r_{rj}}{r_{rp}}\frac{\sin(\beta_{rj})}{\sin(\beta_{rp})} & 0 & 0 & 0 & 0 & \frac{r_{rj}}{r_{rp}}\frac{\sin(\beta_{rj})}{\sin(\beta_{rp})} \\ \frac{r_{rj}}{r_{rp}}\frac{\cos(\beta_{rj})}{\sin(\beta_{rp})} & 1 & 0 & 0 & 0 & -\frac{r_{rj}}{r_{rp}}\frac{\cos(\beta_{rj})}{\sin(\beta_{rp})} \\ 0 & 0 & 1 & -d_{rj_1} & -d_{rj_2} & 0 \\ 0 & 0 & 0 & 1 & 0 & 0 \\ 0 & 0 & 0 & 0 & 1 & 0 \end{bmatrix} \begin{bmatrix} u_{r_1} \\ u_{r_2} \\ u_{r_3} \\ \theta_{r_1} \\ \theta_{r_2} \\ u_{p_1} \end{bmatrix} \tag{B.32}$$

y

$$\begin{bmatrix} u_{j_1} \\ u_{j_2} \\ u_{j_3} \\ \theta_{j_1} \\ \theta_{j_2} \end{bmatrix} = \begin{bmatrix} 1 & \frac{r_{rj}}{r_{rp}}\frac{\sin(\beta_{rj})}{\cos(\beta_{rp})} & 0 & 0 & 0 & -\frac{r_{rj}}{r_{rp}}\frac{\sin(\beta_{rj})}{\cos(\beta_{rp})} \\ 0 & 1-\frac{r_{rj}}{r_{rp}}\frac{\cos(\beta_{rj})}{\cos(\beta_{rp})} & 0 & 0 & 0 & \frac{r_{rj}}{r_{rp}}\frac{\cos(\beta_{rj})}{\cos(\beta_{rp})} \\ 0 & 0 & 1 & -d_{rj_1} & -d_{rj_2} & 0 \\ 0 & 0 & 0 & 1 & 0 & 0 \\ 0 & 0 & 0 & 0 & 1 & 0 \end{bmatrix} \begin{bmatrix} u_{r_1} \\ u_{r_2} \\ u_{r_3} \\ \theta_{r_1} \\ \theta_{r_2} \\ u_{p_2} \end{bmatrix} \tag{B.33}$$

donde $d_{rj_i} = x_{j_i} - x_{r_i}$. Tal y como ya se ha dicho, estas matrices son utilizadas para condensar los grados de libertad definidos en las cabezas de los pilotes de un grupo en sólo seis grados de libertad de referencia.

B.5.2. Ecuaciones de equilibrio

Condiciones de equilibrio dinámico han de ser impuestas sobre el encepado entre las fuerzas externas, las fuerzas de inercia y las reacciones en la cabeza de los pilotes. Sean F_i^e las fuerzas externas aplicadas sobre el centro de gravedad del encepado $\mathbf{x}_{cg}^c$ en dirección i, y M_1^e, M_2^e y M_3^e los momentos externos aplicados alrededor de los ejes x_2, x_1 y x_3, respectivamente. Las propiedades inerciales del encepado son su masa m^c, y sus momentos de inercia I_1, I_2 e I_3 definidos alrededor de los ejes x_2, x_1 y x_3, respectivamente. Finalmente, la reacciones en la cabeza del pilote j-ésimo son las fuerzas F_{j_i} y los momentos M_{j_1} y M_{j_2} definidos alrededor de los ejes x_2 y x_1, respectivamente. Con esta nomenclatura, las ecuaciones de

equilibrio dinámico del encepado c pueden escribirse como

$$F_i^e + \sum_{j=1}^{n_p^c} F_{j_i} = -\omega^2 m^c u_{cg_i} \qquad \text{i} = 1,2,3$$

$$M_i^e + \sum_{j=1}^{n_p^c} \left(M_{j_i} - (x_{j_i} - x_{cg_i}) F_{j_3} + (x_{j_3} - x_{cg_3}) F_{j_i} \right) = -\omega^2 I_i \theta_i \qquad \text{i} = 1,2$$

$$M_3^e + \sum_{j=1}^{n_p^c} \left((x_{j_1} - x_{cg_1}) F_{j_2} - (x_{j_2} - x_{cg_2}) F_{j_1} \right) = -\omega^2 I_3 \alpha \qquad \text{(B.34)}$$

donde n_p^c es el número de pilotes agrupados bajo el encepado c.

B.6. Modelo para las estructuras pilotadas

B.6.1. Introducción

En esta sección se describe la formulación que ha sido adoptada para el análisis dinámico de estructuras pilotadas compuestas por uno a más pilares verticales extensibles y uno o más forjados horizontales infinitamente rígidos, tal y como se muestra en la fig. B.6. Los pilotes son modelados como vigas de Euler-Bernoulli sin masa, con deformación axial y lateral, y con amortiguamiento de tipo viscoelástico, introducido a través de un módulo de rigidez complejo del tipo $k = Re[k](1 + 2\text{i}\zeta)$. La rigidez torsional de los pilares es despreciada. Se considera que los ejes principales de inercia de los forjados rígidos son paralelos a los ejes de coordenadas, aunque la posición de sus centros de gravedad en el plano horizontal puede variar entre distintas plantas.

Con el objetivo de escribir las ecuaciones de movimiento directamente en función de los desplazamientos y rotaciones de los forjados (parámetros de mayor interés en este trabajo), todos los grados de libertad correspondientes a los extremos de los pilares son condensados al centro de gravedad del forjado o del encepado situado a su mismo nivel. Dado que las matrices elementales de rigidez de los pilares serán expresadas inicialmente respecto a los extremos de los pilares, es necesario escribir primero las relaciones cinemáticas existentes entre tales extremos y los centros de gravedad de los forjados o los encepados. Posteriormente, una matriz de rigidez elemental para la entreplanta es definida entre dos niveles consecutivos.

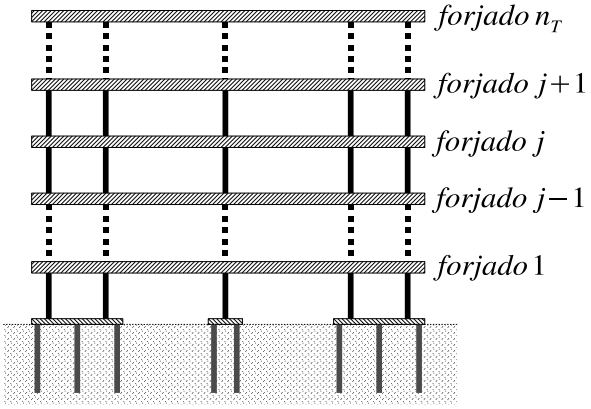

Figura B.6: *Esquema bidimensional del modelo de estructuras pilotadas*

B.6.2. Relaciones cinemáticas

Sea $\mathbf{X}^j = \left\{u_{cg_1{}^j}, u_{cg_2{}^j}, u_{cg_3{}^j}, \alpha_{cg^j}, \Theta_{cg_1{}^j}, \Theta_{cg_2{}^j}\right\}^T$ el vector que define los desplazamientos y rotaciones en el centro de gravedad del forjado o encepado j, donde α_{cg^j}, $\Theta_{cg_1{}^j}$ y $\Theta_{cg_2{}^j}$ son las rotaciones en sentido antihorario alrededor de los ejes x_3, x_2 y x_1, respectivamente. Sea $\mathbf{Y}_i^j = \{u_{i_1}, u_{i_2}, u_{i_3}, \theta_{i_1}, \theta_{i_2}\}_j^T$ el vector que define los desplazamientos y las rotaciones en un extremo del pilar i vinculado al forjado o encepado j. La compatibilidad entre $\mathbf{X}^j$ y $\mathbf{Y}_i^j$ puede ser expresada, de forma matricial, como

$$\begin{bmatrix} u_{i_1} \\ u_{i_2} \\ u_{i_3} \\ \theta_{i_1} \\ \theta_{i_2} \end{bmatrix}_j = \begin{bmatrix} 1 & 0 & 0 & (x_{cg_2^j} - x_{i_2}) & 0 & 0 \\ 0 & 1 & 0 & (x_{i_1} - x_{cg_1^j}) & 0 & 0 \\ 0 & 0 & 1 & 0 & (x_{i_1} - x_{cg_1^j}) & (x_{i_2} - x_{cg_2^j}) \\ 0 & 0 & 0 & 0 & 1 & 0 \\ 0 & 0 & 0 & 0 & 0 & 1 \end{bmatrix} \begin{bmatrix} u_{cg_1^j} \\ u_{cg_2^j} \\ u_{cg_3^j} \\ \alpha_{cg^j} \\ \Theta_{cg_1^j} \\ \Theta_{cg_2^j} \end{bmatrix} \quad \text{(B.35)}$$

Acerca del acoplamiento entre pilares y encepado

Sin embargo, tal y como se vio en la sección B.5, los grados de libertad correspondientes al centro de gravedad del encepado no están presentes de modo explícito en el sistema de ecuaciones final. En cambio, éstos están definidos en función de los correspondientes a dos de los pilotes del grupo. Por esta razón, las columnas de la matriz de rigidez elemental de la entreplanta, correspondientes a la vinculación de los pilares con el encepado, deberán ser escritas en función de dichos grados de libertad auxiliares.

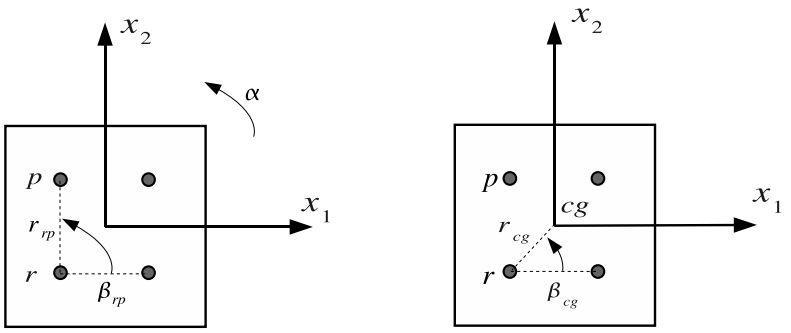

Figura B.7: *Grados de libertad para el acoplamiento entre pilares y encepado*

Para ello, sean β_{rp} y r_{rp} el ángulo y la distancia entre las cabezas de los pilotes de referencia y periférico, y β_{cg} y r_{cg} el ángulo y la distancia entre el pilote de referencia y el centro de gravedad del encepado (véase fig. B.7). En concordancia con el conjunto de seis grados de libertad elegido para definir los desplazamientos y rotaciones del encepado, se definen las matrices de acoplamiento entre la cabeza del pilote de referencia y el centro de gravedad del encepado, que para los casos a y b (véase la sección B.5), son respectivamente:

$$\begin{bmatrix} u_{cg_1} \\ u_{cg_2} \\ u_{cg_3} \\ \alpha_{cg} \\ \Theta_{cg_1} \\ \Theta_{cg_2} \end{bmatrix} = \begin{bmatrix} 1-\frac{r_{cg}}{r_{rp}}\frac{\sin\beta_{cg}}{\sin\beta_{rp}} & 0 & 0 & 0 & 0 & \frac{r_{cg}}{r_{rp}}\frac{\sin\beta_{cg}}{\sin\beta_{rp}} \\ \frac{r_{cg}}{r_{rp}}\frac{\cos\beta_{cg}}{\sin\beta_{rp}} & 1 & 0 & 0 & 0 & -\frac{r_{cg}}{r_{rp}}\frac{\cos\beta_{cg}}{\sin\beta_{rp}} \\ 0 & 0 & 1 & -d_{rp_1} & -d_{rp_2} & 0 \\ \frac{1}{r_{rp}\sin\beta_{rp}} & 0 & 0 & 0 & 0 & -\frac{1}{r_{rp}\sin\beta_{rp}} \\ 0 & 0 & 0 & -1 & 0 & 0 \\ 0 & 0 & 0 & 0 & -1 & 0 \end{bmatrix} \begin{bmatrix} u_{r_1} \\ u_{r_2} \\ u_{r_3} \\ \theta_{r_1} \\ \theta_{r_2} \\ u_{p_1} \end{bmatrix} \tag{B.36}$$

y

$$\begin{bmatrix} u_{cg_1} \\ u_{cg_2} \\ u_{cg_3} \\ \alpha_{cg} \\ \Theta_{cg_1} \\ \Theta_{cg_2} \end{bmatrix} = \begin{bmatrix} 1 & \frac{r_{cg}}{r_{rp}}\frac{\sin\beta_{cg}}{\cos\beta_{rp}} & 0 & 0 & 0 & -\frac{r_{cg}}{r_{rp}}\frac{\sin\beta_{cg}}{\cos\beta_{rp}} \\ 0 & 1-\frac{r_{cg}}{r_{rp}}\frac{\cos\beta_{cg}}{\cos\beta_{rp}} & 0 & 0 & 0 & \frac{r_{cg}}{r_{rp}}\frac{\cos\beta_{cg}}{\cos\beta_{rp}} \\ 0 & 0 & 1 & -d_{rp_1} & -d_{rp_2} & 0 \\ 0 & -\frac{1}{r_{rp}\cos\beta_{rp}} & 0 & 0 & 0 & \frac{1}{r_{rp}\cos\beta_{rp}} \\ 0 & 0 & 0 & -1 & 0 & 0 \\ 0 & 0 & 0 & 0 & -1 & 0 \end{bmatrix} \begin{bmatrix} u_{r_1} \\ u_{r_2} \\ u_{r_3} \\ \theta_{r_1} \\ \theta_{r_2} \\ u_{p_2} \end{bmatrix} \tag{B.37}$$

donde $d_{rp_i} = x_{p_i} - x_{r_i}$.

B.6.3. Matriz de rigidez de entreplanta

La submatriz elemental de rigidez de un pilar i, modelado como una viga de Euler-Bernoulli, de dimensión 10×10, puede ser definida como

$$\begin{bmatrix} \mathbf{f}_i^{j-1} \\ \mathbf{f}_i^{j} \end{bmatrix} = \begin{bmatrix} a_{x_1} & 0 & 0 & -b_{x_1} & 0 & -a_{x_1} & 0 & 0 & -b_{x_1} & 0 \\ & a_{x_2} & 0 & 0 & -b_{x_2} & 0 & -a_{x_2} & 0 & 0 & -b_{x_2} \\ & & c & 0 & 0 & 0 & 0 & -c & 0 & 0 \\ & & & d_{x_1} & 0 & b_{x_1} & 0 & 0 & \frac{d_{x_1}}{2} & 0 \\ & & & & d_{x_2} & 0 & b_{x_2} & 0 & 0 & \frac{d_{x_1}}{2} \\ & & & & & a_{x_1} & 0 & 0 & b_{x_1} & 0 \\ & & & & & & a_{x_2} & 0 & 0 & b_{x_2} \\ & & sim & & & & & c & 0 & 0 \\ & & & & & & & & d_{x_1} & 0 \\ & & & & & & & & & d_{x_2} \end{bmatrix} \begin{bmatrix} \mathbf{Y}_i^{j-1} \\ \mathbf{Y}_i^{j} \end{bmatrix} \tag{B.38}$$

donde

$$a_{x_i} = 12\frac{E\,I_{x_i}}{L^3} \quad ; \quad b_{x_i} = 6\frac{E\,I_{x_i}}{L^2} \quad ; \quad c = \frac{E\,A}{L} \quad ; \quad d_{x_i} = 4\frac{E\,I}{L}$$

y donde $\mathbf{f}_i{}^j = \{f_{x_1{}^i}, f_{x_2{}^i}, f_{x_3{}^i}, m_{x_1{}^i}, m_{x_2{}^i}\}^{jT}$ son las reacciones en la conexión entre el pilar y el forjado.

Con el objetivo de construir una matriz elemental equivalente $\mathcal{K}^i$ para la entreplanta, que relacione directamente los grados de libertad de los forjados superior e inferior, la submatriz de rigidez correspondiente a cada extremo del pilote i es post-multiplicada por la ec. (B.35), obteniéndose las submatrices de rigidez expresadas en términos de los grados de libertad asociados a los centros de gravedad de forjados y encepados. Del mismo modo, se opera también con las filas para definir las fuerzas resultantes respecto a los centros de gravedad de los forjados. Este proceso lleva a la obtención de la siguiente matriz de rigidez elemental del pilar i para la entreplanta situada entre los niveles $j-1$ y j:

$$\begin{bmatrix} \mathcal{F}_{j-1}^i \\ \mathcal{F}_j^i \end{bmatrix} = \begin{bmatrix} \mathcal{K}^i_{11_{(6x6)}} & \mathcal{K}^i_{12_{(6x6)}} \\ \mathcal{K}^i_{21_{(6x6)}} & \mathcal{K}^i_{22_{(6x6)}} \end{bmatrix} \begin{bmatrix} \mathbf{X}^{j-1} \\ \mathbf{X}^{j} \end{bmatrix} \tag{B.39}$$

donde

$$\mathcal{K}_{11} = \begin{bmatrix} 12\frac{EI_{x_1}}{L^3} & 0 & 0 & -12\frac{EI_{x_1}}{L^3}x_2^b & -6\frac{EI_{x_1}}{L^2} & 0 \\ 0 & 12\frac{EI_{x_2}}{L^3} & 0 & 12\frac{EI_{x_2}}{L^3}x_1^b & 0 & -6\frac{EI_{x_2}}{L^2} \\ 0 & 0 & \frac{EA}{L} & 0 & \frac{EA}{L}x_1^b & \frac{EA}{L}x_2^b \\ -12\frac{EI_{x_1}}{L^3}x_2^b & 12\frac{EI_{x_2}}{L^3}x_1^b & 0 & 12\frac{E}{L^3}IX^b & 6\frac{EI_{x_1}}{L^2}x_2^b & -6\frac{EI_{x_2}}{L^2}x_1^b \\ -6\frac{EI_{x_1}}{L^2} & 0 & \frac{EA}{L}x_1^b & 6\frac{EI_{x_1}}{L^2}x_2^b & 4\frac{EI_{x_1}}{L}+\frac{EA}{L}{x_1^b}^2 & \frac{EA}{L}x_2^bx_1^b \\ 0 & -6\frac{EI_{x_2}}{L^2} & \frac{EA}{L}x_2^b & -6\frac{EI_{x_2}}{L^2}x_1^b & \frac{EA}{L}x_2^bx_1^b & 4\frac{EI_{x_2}}{L}+\frac{EA}{L}{x_2^b}^2 \end{bmatrix}$$

$$\mathcal{K}_{12} = \begin{bmatrix} -12\frac{EI_{x_1}}{L^3} & 0 & 0 & 12\frac{EI_{x_1}}{L^3}x_2^a & -6\frac{EI_{x_1}}{L^2} & 0 \\ 0 & -12\frac{EI_{x_2}}{L^3} & 0 & -12\frac{EI_{x_2}}{L^3}x_1^a & 0 & -6\frac{EI_{x_2}}{L^2} \\ 0 & 0 & -\frac{EA}{L} & 0 & -\frac{EA}{L}x_1^a & -\frac{EA}{L}x_2^a \\ 12\frac{EI_{x_1}}{L^3}x_2^b & -12\frac{EI_{x_2}}{L^3}x_1^b & 0 & -12\frac{E}{L^3}IX^{ab} & 6\frac{EI_{x_1}}{L^2}x_2^b & -6\frac{EI_{x_2}}{L^2}x_1^b \\ 6\frac{EI_{x_1}}{L^2} & 0 & -\frac{EA}{L}x_1^b & -6\frac{EI_{x_1}}{L^2}x_2^a & 2\frac{EI_{x_1}}{L}+\frac{EA}{L}x_1^ax_1^b & -\frac{EA}{L}x_2^ax_1^b \\ 0 & 6\frac{EI_{x_2}}{L^2} & -\frac{EA}{L}x_2^b & 6\frac{EI_{x_2}}{L^2}x_1^a & -\frac{EA}{L}x_1^ax_2^b & 2\frac{EI_{x_2}}{L}-\frac{EA}{L}x_2^ax_2^b \end{bmatrix}$$

$$\mathcal{K}_{21} = \begin{bmatrix} -12\frac{EI_{x_1}}{L^3} & 0 & 0 & 12\frac{EI_{x_1}}{L^3}x_2^b & 6\frac{EI_{x_1}}{L^2} & 0 \\ 0 & -12\frac{EI_{x_2}}{L^3} & 0 & -12\frac{EI_{x_2}}{L^3}x_1^b & 0 & 6\frac{EI_{x_2}}{L^2} \\ 0 & 0 & -\frac{EA}{L} & 0 & -\frac{EA}{L}x_1^b & -\frac{EA}{L}x_2^b \\ 12\frac{EI_{x_1}}{L^3}x_2^a & -12\frac{EI_{x_2}}{L^3}x_1^a & 0 & -12\frac{E}{L^3}IX^{ab} & -6\frac{EI_{x_1}}{L^2}x_2^a & 6\frac{EI_{x_2}}{L^2}x_1^a \\ -6\frac{EI_{x_1}}{L^2} & 0 & -\frac{EA}{L}x_1^a & 6\frac{EI_{x_1}}{L^2}x_2^b & 2\frac{EI_{x_1}}{L}-\frac{EA}{L}x_1^ax_1^b & -\frac{EA}{L}x_2^bx_1^a \\ 0 & -6\frac{EI_{x_2}}{L^2} & -\frac{EA}{L}x_2^a & -6\frac{EI_{x_2}}{L^2}x_1^b & -\frac{EA}{L}x_1^bx_2^a & 2\frac{EI_{x_2}}{L}-\frac{EA}{L}x_2^bx_2^a \end{bmatrix}$$

$$\mathcal{K}_{22} = \begin{bmatrix} 12\frac{EI_{x_1}}{L^3} & 0 & 0 & -12\frac{EI_{x_1}}{L^3}x_2^a & 6\frac{EI_{x_1}}{L^2} & 0 \\ 0 & 12\frac{EI_{x_2}}{L^3} & 0 & 12\frac{EI_{x_2}}{L^3}x_1^a & 0 & 6\frac{EI_{x_2}}{L^2} \\ 0 & 0 & \frac{EA}{L} & 0 & \frac{EA}{L}x_1^a & \frac{EA}{L}x_2^a \\ -12\frac{EI_{x_1}}{L^3}x_2^a & 12\frac{EI_{x_2}}{L^3}x_1^a & 0 & 12\frac{E}{L^3}IX^a & -6\frac{EI_{x_1}}{L^2}x_2^a & 6\frac{EI_{x_2}}{L^2}x_1^a \\ 6\frac{EI_{x_1}}{L^2} & 0 & \frac{EA}{L}x_1^a & -6\frac{EI_{x_1}}{L^2}x_2^a & 4\frac{EI_{x_1}}{L}+\frac{EA}{L}x_1^{a\,2} & \frac{EA}{L}x_2^a x_1^a \\ 0 & 6\frac{EI_{x_2}}{L^2} & \frac{EA}{L}x_2^b & 6\frac{EI_{x_2}}{L^2}x_1^a & \frac{EA}{L}x_2^a x_1^a & 4\frac{EI_{x_2}}{L}+\frac{EA}{L}x_2^{a\,2} \end{bmatrix}$$

siendo

$$IX^a = I_{x_1}x_2^{a2} + I_{x_2}x_1^{a2}$$
$$IX^{ab} = I_{x_1}x_2^a x_2^b + I_{x_2}x_1^a x_1^b$$
$$IX^b = I_{x_1}x_2^{b\,2} + I_{x_2}x_1^{b\,2}$$

En estas expresiones, $x_k^a = x_{i_k} - x_{cg_k^a}$ y $x_k^b = x_{i_k} - x_{cg_k^b}$ son las coordenadas horizontales relativas del eje del pilar respecto al centro de gravedad del forjado superior o inferior, respectivamente, y $\mathcal{F}_j^T = \{F_{x_1}, F_{x_2}, F_{x_3}, M_\alpha, M_{x_1}, M_{x_2}\}^j$ corresponde a las reacciones que aparecen en la conexión entre el pilar y el forjado, expresadas también respecto al centro de gravedad correspondiente.

Habiendo definido una matriz de rigidez de la entreplanta con carácter genérico, puede seguirse el procedimiento de ensamblaje usual del método de los elementos finitos para obtener la ecuación de movimiento de la estructura una vez discretizada, quedando de la forma

$$\left(\mathcal{K} - \omega^2\mathcal{M}\right)\mathcal{X} = \mathcal{F} \tag{B.40}$$

donde $\mathcal{K}$ es la matriz de rigidez global de la estructura, $\mathcal{X}$ es el vector de desplazamientos y rotaciones en los forjados, $\mathcal{F}$ es el vector de fuerzas externas sobre la estructura y $\mathcal{M}$ es la matriz de propiedades inerciales de la estructura, definida para cada forjado.

B.7. Ensamblaje de la matriz global del sistema

La manera en que las ecuaciones (B.24), (B.3), (B.4), (B.6) y (B.40) son reorganizadas en un único sistema de ecuaciones depende de la configuración de

estructuras, cimentaciones y suelos, y de las condiciones de contorno. Sin embargo, siempre deben aplicarse las condiciones de equilibrio y de compatibilidad, considerando contacto soldado entre las diferentes interfases del sistema. En la situación más general, existen múltiples estructuras cimentadas sobre diferentes grupos de pilotes que están embebidos en suelos estratificados, y el sistema está siendo sometido a fuerzas externas o a ondas sísmica. En tal caso, el sistema de ecuaciones es

$$\mathcal{A}\left\{\mathbf{u}^s, \mathbf{p}^s, \mathbf{q}^s, \mathbf{F}_p, \mathbf{u}^p, \mathbf{X}^j, \mathbf{F}_{top}, \mathbf{f}_o\right\}^T = \mathcal{B} \tag{B.41}$$

donde $\mathcal{A}$, cuya estructura está esquematizada en la fig. B.8, es la matriz de coeficientes, y $\mathcal{B}$ es el vector del lado derecho, ambos obtenidos después de aplicar las condiciones de contorno y de reordenar las ecuaciones. El vector de incógnitas incluye los desplazamientos $\mathbf{u}^s$ y/o las tensiones $\mathbf{p}^s$ en los nodos correspondientes a los elementos de contorno, las tensiones en la interfase pilote-suelo $\mathbf{q}^s$, las fuerzas en la punta de los pilotes $\mathbf{F}_p$, las traslaciones y rotaciones nodales a lo largo del pilote $\mathbf{u}^p$, los grados de libertad definidos en las superestructuras $\mathbf{X}^j$, las reacciones en las uniones pilote-encepado $\mathbf{F}_{top}$, y las fuerzas en la base de la estructura $\mathbf{f}_o$.

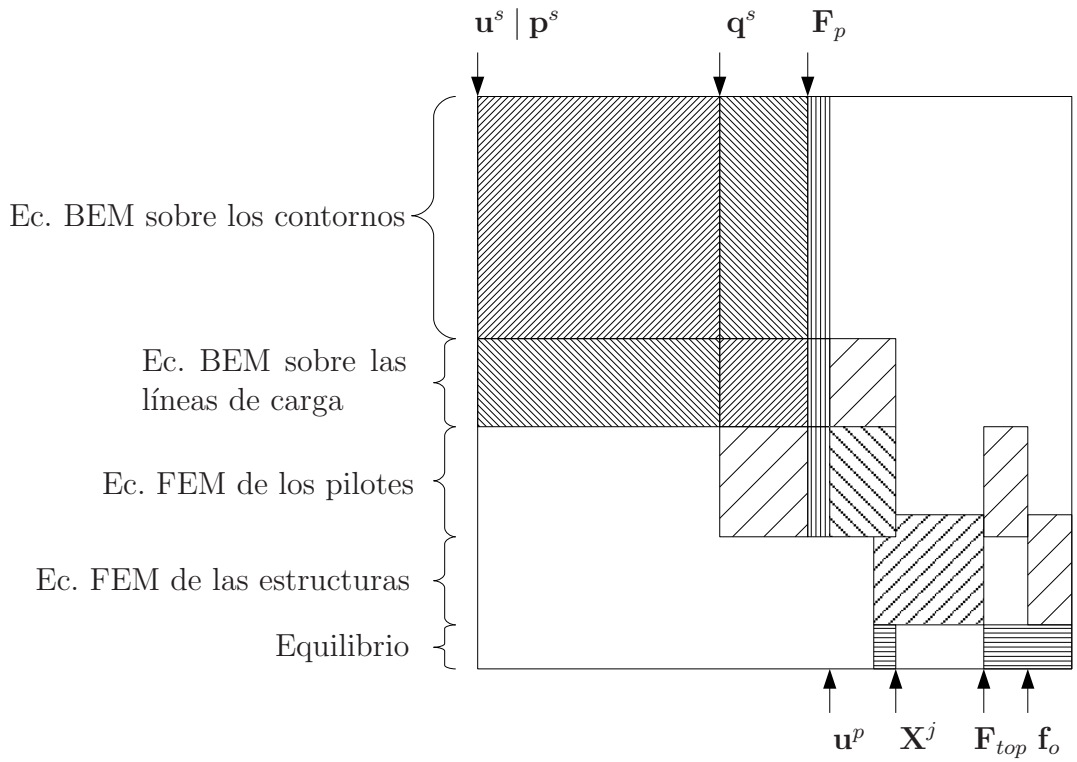

Figura B.8: *Estructura de la matriz de coeficientes $\mathcal{A}$ del sistema*

B.8. Evaluación numérica de las integrales definidas sobre las líneas de carga

Siempre que la fuente esté situada fuera de la línea de carga j, las integrales de $\mathbf{u}^*\mathbf{q}^{s_j}$ y $\hat{\mathbf{u}}^*\mathbf{q}^{s_j}$, definidas sobre la línea de carga Γ_{p_j}, y que aparecen en las ecs. (B.2) y (B.5) respectivamente, son calculadas como integrales monodimensionales extendidas sobre una línea definida por el eje del pilote correspondiente. Por contra, estas mismas integrales poseen una singularidad cuando la fuente está situada sobre la línea que está siendo integrada. En este caso, y para evitar esta singularidad, las integrales se evalúan sobre un cilindro cuyo radio R_p tiene valor $\sqrt{A/\pi}$. Consideremos entonces que la interfase Γ_p entre el pilote (cualquiera que sea su sección) y el suelo es un cilindro de radio R_p, sobre el que existen unas tensiones σ_{ps}. En este caso, el último sumando de la ec. (B.1) incluye integrales del tipo

$$\int_{\Gamma_p} \mathbf{u}^* \boldsymbol{\sigma}_{ps}\, d\Gamma_p = \int_{\Gamma_p} \mathbf{u}^* \frac{\mathbf{q}^s}{2\pi R_p}\, d\Gamma_p = \frac{1}{2\pi R_p} \sum_{e=1}^{N_e} \sum_{i=k,l,m} \left[\int_{\Gamma_{pe}} \mathbf{u}^* \phi_i\, d\Gamma_p \right] \mathbf{q}_i^s \tag{B.42}$$

donde N_e es el número de elementos en que se ha discretizado la línea de carga, y donde la ec. (B.20) ha sido utilizada para expresar $\mathbf{q}^s$ a lo largo del elemento. Tal y como se vio en el capítulo 2, la solución fundamental elastodinámica utilizada en este trabajo, que da el desplazamiento en el punto $\mathbf{x}$ y en la dirección k cuando la fuente es aplicada en el punto $\mathbf{x}^\iota$ y en la dirección l, tiene la siguiente expresión:

$$\begin{aligned} u_{lk}^* &= \frac{1}{4\pi\mu} \left[\psi \delta_{lk} - \chi r_{,k} r_{,l} \right] \\ \psi &= -\left(\frac{c_s}{c_p}\right)^2 \left(\frac{1}{z_p^2 r^2} - \frac{1}{z_p r} \right) \frac{e^{z_p r}}{r} + \left(\frac{1}{z_s^2 r^2} - \frac{1}{z_s r} + 1 \right) \frac{e^{z_s r}}{r} \\ \chi &= -\left(\frac{c_s}{c_p}\right)^2 \left(\frac{3}{z_p^2 r^2} - \frac{3}{z_p r} + 1 \right) \frac{e^{z_p r}}{r} + \left(\frac{3}{z_s^2 r^2} - \frac{3}{z_s r} + 1 \right) \frac{e^{z_s r}}{r} \end{aligned} \tag{B.43}$$

donde μ es el módulo de elasticidad transversal, δ_{lk} es la función delta de Kronecker, y $r = |\mathbf{x} - \mathbf{x}^\iota|$. Para este caso específico (véase la fig. B.9), las derivadas del vector posición $\mathbf{r} = \mathbf{x} - \mathbf{x}^\iota$ son

$$r_{,1} = \frac{x_1^r}{r} = \frac{R_p \cos(\gamma)}{r} \tag{B.44a}$$

$$r_{,2} = \frac{x_2^r}{r} = \frac{R_p \sin(\gamma)}{r} \tag{B.44b}$$

$$r_{,3} = \frac{x_3^r}{r} \tag{B.44c}$$

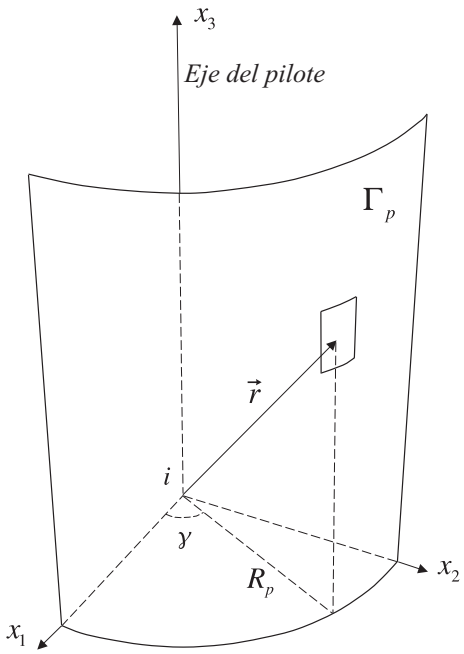

Figura B.9: *Superficie cilíndrica de integración sobre la interfase pilote-suelo cuando el punto de colocación pertenece al pilote*

Entonces, las integrales del último término de la ec. (B.42) pueden ser evaluadas, en coordenadas cilíndricas (véase fig. B.9), como

$$\begin{aligned}\int_{\Gamma_{pe}} \mathbf{u}^* \phi_i \, d\Gamma_p &= \int_{x_3^r} \int_\theta \frac{1}{4\pi\mu} \left[\psi \delta_{lk} - \chi r_{,k} r_{,l}\right] \phi_i R_p \, d\theta \, dx_3 \\ &= \frac{R_p}{4\pi\mu} \int_{x_3^r} \left[2\pi\psi\delta_{lk} - \chi \int_0^{2\pi} r_{,k} r_{,l} \, d\theta\right] \phi_i \, dx_3 \\ &= \frac{R_p}{4\mu} \int_{x_3^r} \left[2\psi\delta_{lk} - \frac{1}{r^2}\chi \mathbf{R}_{lk}\right] \phi_i \, dx_3\end{aligned} \tag{B.45}$$

donde $x_3^r = x_3 - x_3^k$ y

$$\mathbf{R}_{lk} = \begin{pmatrix} R_p^2 & 0 & 0 \\ 0 & R_p^2 & 0 \\ 0 & 0 & 2(x_3^r)^2 \end{pmatrix} \tag{B.46}$$

Ahora, la integral de la ec. (B.42) puede ser expresada de la siguiente forma:

$$\int_{\Gamma_p} \mathbf{u}^* \boldsymbol{\sigma}_{ps}\, d\Gamma_p = \sum_{e=1}^{N_e} \frac{L_e}{16\pi\mu} \sum_{i=k,l,m} \left[\int_{-1}^{1} \left(2\psi\delta_{lk} - \frac{\chi}{r^2}\mathbf{R}_{lk} \right) \phi_i \, d\xi \right] \mathbf{q}_i^s \tag{B.47}$$

En cambio, para computar las integrales sobre Γ_{p_j} desde el mismo pilote, también podría adoptarse una estrategia de colocación no nodal. Esto llevará a un procedimiento que permite la reinterpretación de la ecuación anterior. En tal caso, deben elegirse al menos cuatro puntos no nodales, colocados simétricamente alrededor del pilote (tal y como se muestra en la fig. B.10), para evitar romper la simetría del problema. Se obtiene así, por superposición de las cuatro ecuaciones procedentes de esta estrategia de colocación no nodal, una sola ecuación, que es dividida entre cuatro para mantener el orden de los coeficientes resultantes. En tal caso, e integrando sobre la línea de carga, el último término de la ec. (B.1) se convierte en

$$\begin{aligned} \int_{\Gamma_p} \mathbf{u}^* \mathbf{q}^s \, d\Gamma_p =& \frac{1}{4} \sum_{\substack{n=1 \\ c.p.}}^{4} \sum_{e=1}^{N_e} \sum_{i=k,l,m} \frac{1}{4\pi\mu} \left[\int_{x_3^r} \left(\psi\delta_{lk} - \chi r_{,k} r_{,l} \right) \phi_i \, dx_3 \right] \mathbf{q}_i^s \\ =& \frac{1}{4} \sum_{\substack{n=1 \\ c.p.}}^{4} \sum_{e=1}^{N_e} \sum_{i=k,l,m} \frac{1}{4\pi\mu} \left[\int_{x_3^r} \phi_i \left(\psi\delta_{lk} - \frac{\chi}{r^2}\mathbf{R}_{lk}^n \right) \, dx_3 \right] \mathbf{q}_i^s \end{aligned} \tag{B.48}$$

donde

$$\begin{aligned} \underset{n=1,2}{\mathbf{R}_{lk}^n} &= \begin{pmatrix} 0 & 0 & 0 \\ 0 & R_p^2 & (-1)^n R_p x_3^r \\ 0 & (-1)^n R_p x_3^r & (x_3^r)^2 \end{pmatrix} \\ \underset{n=3,4}{\mathbf{R}_{lk}^n} &= \begin{pmatrix} R_p^2 & 0 & (-1)^n R_p x_3^r \\ 0 & 0 & 0 \\ (-1)^n R_p x_3^r & 0 & (x_3^r)^2 \end{pmatrix} \end{aligned} \tag{B.49}$$

Tal y como puede apreciarse, este procedimiento lleva a una ecuación completamente equivalente a la ec. (B.47), con lo que se demuestra que ambas aproximaciones son análogas.

Por otro lado, cuando el punto de colocación 'k' está situado fuera de la línea de carga j, puede afirmarse que

$$\boldsymbol{\Upsilon}_k^j = \{ u_{13}^* \; u_{23}^* \; u_{33}^* \}_k \tag{B.50}$$

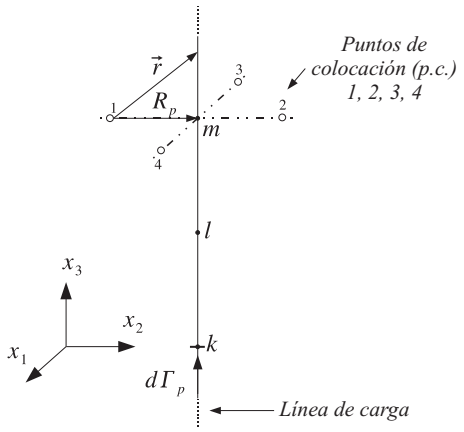

Figura B.10: *Estrategia de colocación no nodal*

Sin embargo, cuando el punto de colocación está situado en el nodo inferior de la línea de carga j, y éste coincide con el extremo inferior del pilote, $\boldsymbol{\Upsilon}^j_k F_{p_j}$ pasa a contener una singularidad. En tal caso, y para evitar tal singularidad, la fuerza axial en la punta del pilote puede modelarse como una presión uniforme σ_b aplicada sobre una superficie circular con radio $R_p = \sqrt{A/\pi}$. En este trabajo, esta estrategia ha sido utilizada siempre que el punto de colocación está situado a lo largo de la línea de carga j. De este modo, puede escribirse

$$\boldsymbol{\Upsilon}^j_k F_{p_j} = \int_{\Gamma_b} u^*_{i3}\, \sigma_b \, d\Gamma_b \tag{B.51}$$

donde Γ_b es la superficie de la punta del pilote y $\sigma_b = F_p/A$. Así, y utilizando coordenadas polares (véase la fig. B.11), la ec. (B.51) pasa a ser expresada como

$$\boldsymbol{\Upsilon}^j_k = \frac{1}{4\pi\mu A} \int_0^{2\pi} \int_0^{R_p} \left[\psi \delta_{i3} - \chi r_{,i} r_{,3}\right] a \, da \, d\theta = \\ = \frac{1}{2\mu A} \int_0^{R_p} \delta_{i3} \left[\psi - (x^r_3)^2 \, \frac{\chi}{r^2}\right] a \, da \tag{B.52}$$

donde la integral es regular y puede ser evaluada numéricamente.

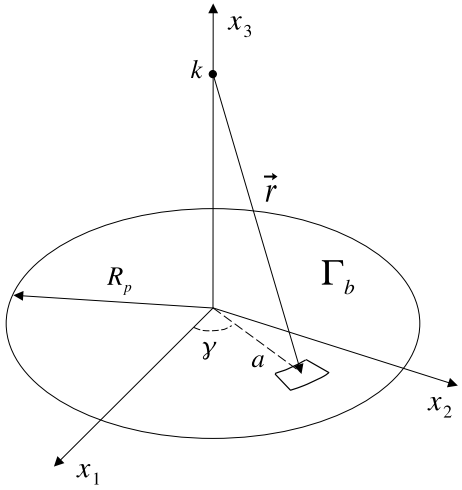

Figura B.11: *Integración sobre la superficie de la punta del pilote*

Apéndice C

Análisis dinámico de cimentaciones pilotadas

C.1. Introducción

El modelo acoplado de elementos finitos y elementos de contorno presentado en el capítulo B será utilizado aquí para obtener las funciones de impedancia y la respuesta sísmica de cimentaciones pilotadas embebidas es suelos viscoelásticos formados por estratos homogéneos horizontales.

En primer lugar, se presentan, en la sección C.2, impedancias harmónicas verticales, horizontales y de cabeceo de pilotes simples y de grupos de 2×2 pilotes embebidos en un estrato sobre una base rígida. Se estudian diferentes profundidades del estrato y tres configuraciones distintas de la cimentación, y se discuten, en cada caso, los efectos asociados a estos parámetros. En segundo lugar, en la sección C.3 se analiza la influencia de la estratigrafía en la respuesta sísmica de un grupo de 3×3 pilotes. Para ello, se obtienen las funciones de transferencia del sistema, cuando es sometido a ondas de corte de incidencia vertical, para varias estratigrafías diferentes. A partir de ahí, se calculan espectros de respuesta máxima correspondientes a dos señales sísmicas distintas.

C.2. Impedancias de cimentaciones pilotadas en estratos homogéneos

Cuando es necesario evitar suelos superficiales de baja capacidad portante para transferir carga a suelos o rocas de mayor carga portante que están situados a cierta profundidad, se opta, generalmente, por cimentaciones pilotadas. Por esta razón, un caso de especial interés a la hora de estudiar el comportamiento dinámico de pilotes es el correspondiente a pilotes embebidos en un estrato sobre una base

rígida, tanto para pilotes flotantes como para pilotes hincados en la roca. Por todo ello, el objetivo de esta sección es investigar la influencia de la presencia de una base rocosa en las funciones de impedancia de cimentaciones pilotadas. La fig. C.1 ilustra el problema planteado, donde L y d son la longitud y diámetro de los pilotes, s se refiere a la distancia entre pilotes adyacentes, y H representa la profundidad del estrato.

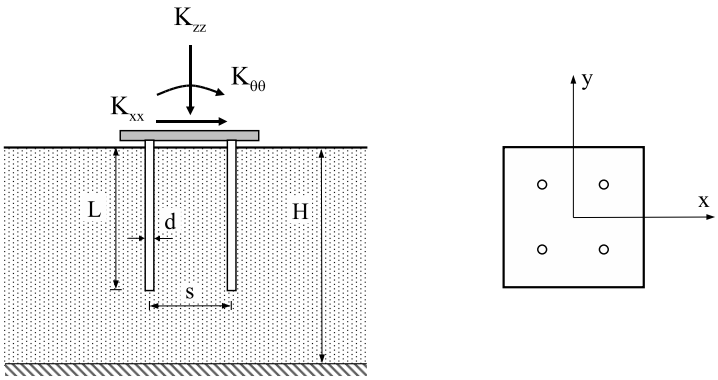

Figura C.1: *Grupo de* 2×2 *pilotes embebidos en un estrato sobre base rocosa. Definición de los parámetros geométricos del problema.*

A continuación se presentan impedancias verticales, horizontales y de cabeceo de distintas cimentaciones pilotadas. En el caso de pilotes simples, las funciones de rigidez y de amortiguamiento están normalizadas por la rigidez estática correspondiente. En cuanto a los grupos de pilotes, las impedancias vertical y horizontal se normalizan por el producto de la rigidez estática correspondiente a un pilote simple (k_{zz_o} y k_{xx_o}) multiplicado por el número (N) de pilotes en el grupo. Por su parte, las impedancias de cabeceo son normalizadas con respecto a la suma de los productos de la rigidez estática vertical del pilote simple correspondiente (k_{zz_o}) multiplicado por el cuadrado de la distancia al eje de rotación (x_i). Todos los resultados son representados frente a la frecuencia adimensional $a_o = \omega\, d/c_s$. Se consideran diferentes relaciones H/L y dos valores para el cociente E_p/E_s entre módulos de Young de pilote y suelo.

Las impedancias verticales de un pilote simple embebido en un estrato homogéneo de profundidad H, que descansa sobre una base rocosa, son presentadas en la fig. C.2. Se muestran resultados correspondientes a dos relaciones distintas entre las rigideces de suelo y pilotes: $E_p/E_s = 10^3$ (suelo blando) y $E_p/E_s = 10^2$ (suelo duro). Las propiedades del estrato son: coeficiente de amortiguamiento interno $\beta = 0.05$ y coeficiente de Poisson $\nu_s = 0.4$. La relación de densidades es $\rho_s/\rho_p = 0.7$ y la esbeltez de los pilotes es $L/d = 15$. Se presentan resultados

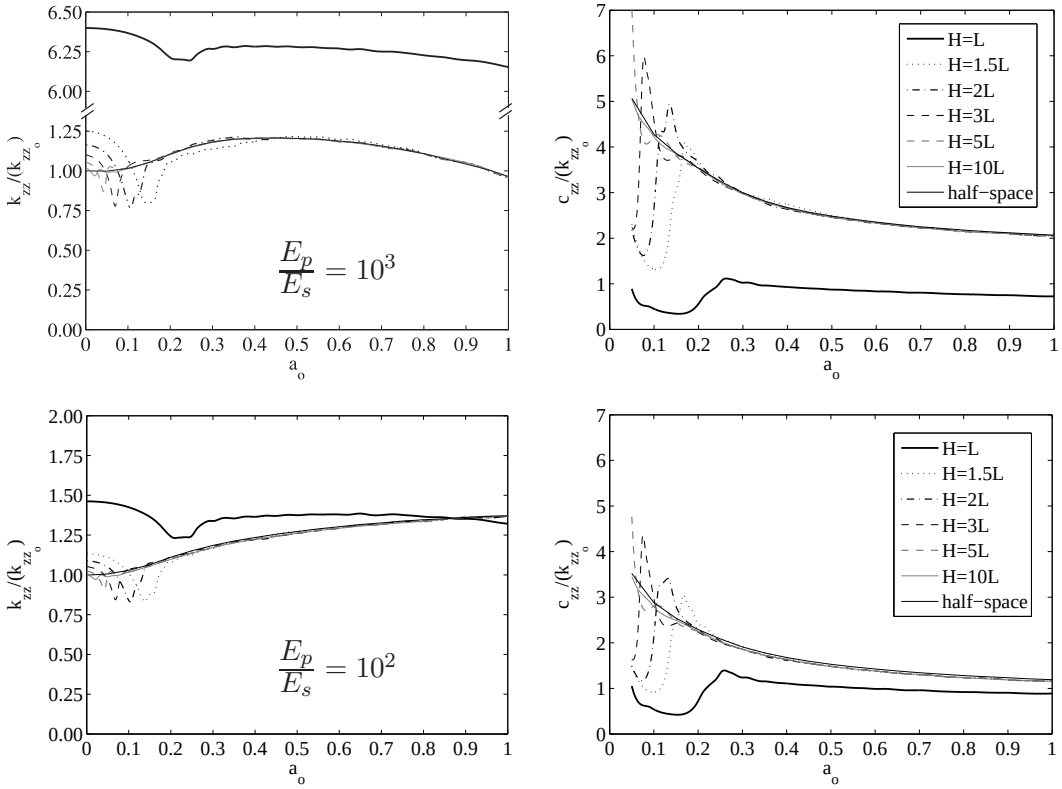

Figura C.2: *Impedancias verticales de un pilote simple en suelo blando ($E_p/E_s = 10^3$) y suelo duro ($E_p/E_s = 10^2$).*

correspondientes a cocientes entre profundidad del estrato y longitud del pilote $H/L = 1$ (pilote hincado), 1.5, 2, 3, 5 y 10, así como la respuesta del pilote en un semiespacio homogéneo.

Tal y como puede verse en las figuras, la presencia de una base rígida bajo un pilote flotante tiene una fuerte influencia en las funciones de impedancias en un rango de frecuencias que va desde el valor estático hasta aproximadamente 1.5 veces la frecuencia fundamental del estrato en el modo de compresión-extensión. Por encima de esta frecuencia, los coeficientes de rigidez y de amortiguamiento son coincidentes con los obtenidos para un pilote en el semiespacio, lo que revela que el principal mecanismo de amortiguamiento a frecuencias medias y altas está relacionado con la disipación de energía a través de ondas de tipo superficial, tanto en el caso de un semiespacio como en el caso de un estrato. Por debajo de la primera frecuencia natural, los coeficientes de amortiguamiento son significativamente más pequeños que los correspondientes a un pilote simple en el semiespacio. Esto es debido a que no pueden existir ondas superficiales a bajas frecuencias en el estrato y, por esa razón, gran parte de la energía permanece confinada en él. Por

otro lado, y como era de esperar, el valor estático de la rigidez vertical de un pilote hincado es, en el caso de un suelo blando, mucho mayor que el correspondiente al pilote flotante. Para ser más precisos, es 5.1 veces mayor que el correspondiente a un pilote flotante embebido en un estrato de profundidad $H = 1.5L$, siendo esta relación aproximadamente constante para todas las frecuencias. Por el contrario, en el caso de un suelo duro, es solamente 1.3 veces mayor, y la diferencia disminuye con la frecuencia. Por otro lado, la frecuencia fundamental del sistema, asociada al modo de compresión-extensión, se aprecia claramente en cada caso. Nótese que la presencia de una base rocosa tiene aún influencia sobre la respuesta de un pilote en un estrato con profundidad $H = 5L$, mientras que la influencia es ya imperceptible para $H = 10L$.

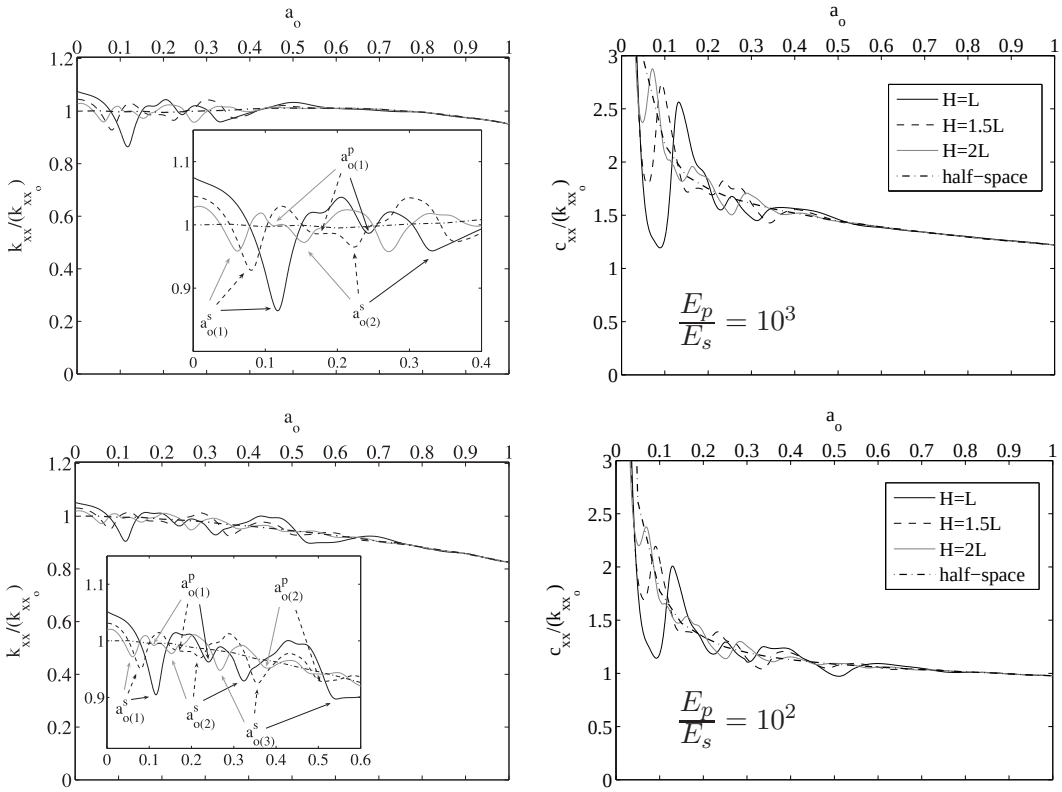

Figura C.3: *Impedancias horizontales de un pilote simple en suelo blando ($E_p/E_s = 10^3$) y suelo duro ($E_p/E_s = 10^2$).*

Las funciones de impedancia horizontal y de cabeceo de un pilote simple embebido en un estrato homogéneo de profundidad H, que descansa sobre una base rocosa, se muestran en las figs. C.3 y C.4 respectivamente. Las propiedades de pilotes y suelo para este y posteriores casos son los que fueron definidos anteriormente. Para mayor claridad, se presentan únicamente resultados para $H/L =$

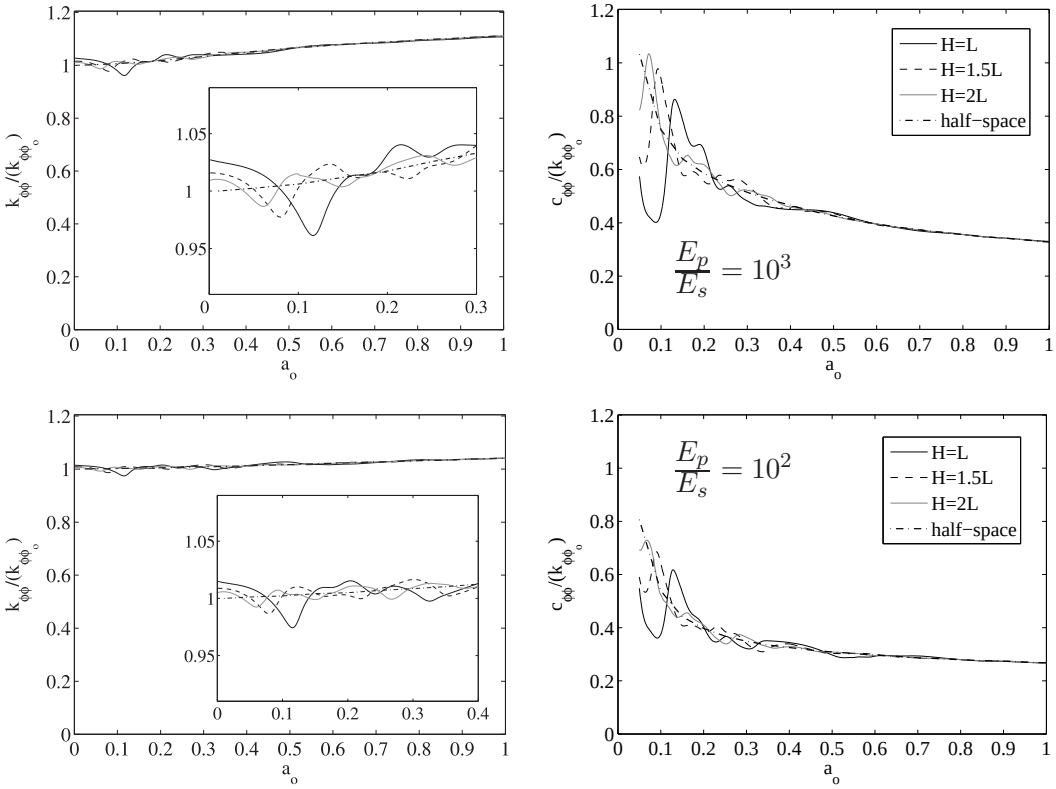

Figura C.4: *Impedancias de cabeceo de un pilote simple en suelo blando ($E_p/E_s = 10^3$) y suelo duro ($E_p/E_s = 10^2$).*

1, 1.5 y 2, junto con la respuesta para el semiespacio. En este caso, los efectos de resonancia están asociados tanto al modo de corte como al modo de compresión-extensión. La influencia de la base rocosa es significativa aproximadamente hasta la segunda frecuencia natural relacionada con el modo de corte, para suelos blandos, y hasta la tercera, para suelos duros. En este rango, tanto los coeficientes de rigidez como los de amortiguamiento fluctúan alrededor de la solución para el semiespacio. Para frecuencias altas, el comportamiento es similar al de un pilote embebido en un semiespacio.

Las funciones de impedancia vertical y horizontal de un grupo de 2×2 pilotes, embebido en un estrato homogéneo de profundidad H sobre un suelo rocoso, se muestran en las figs. C.5 y C.6, y figs. C.7 y C.8, respectivamente. Se presentan resultados correspondientes a relaciones de separación entre pilotes adyacentes $s/d = 2$, 5 y 10, y a relaciones entre la profundidad del estrato y la longitud del pilote $H/L = 1$, 1.5 y 2, así como a la respuesta para el semiespacio.

Por razones de escala, los picos asociados a las frecuencias naturales del estrato no aparecen claramente en las figuras, pero su magnitud es proporcional a los

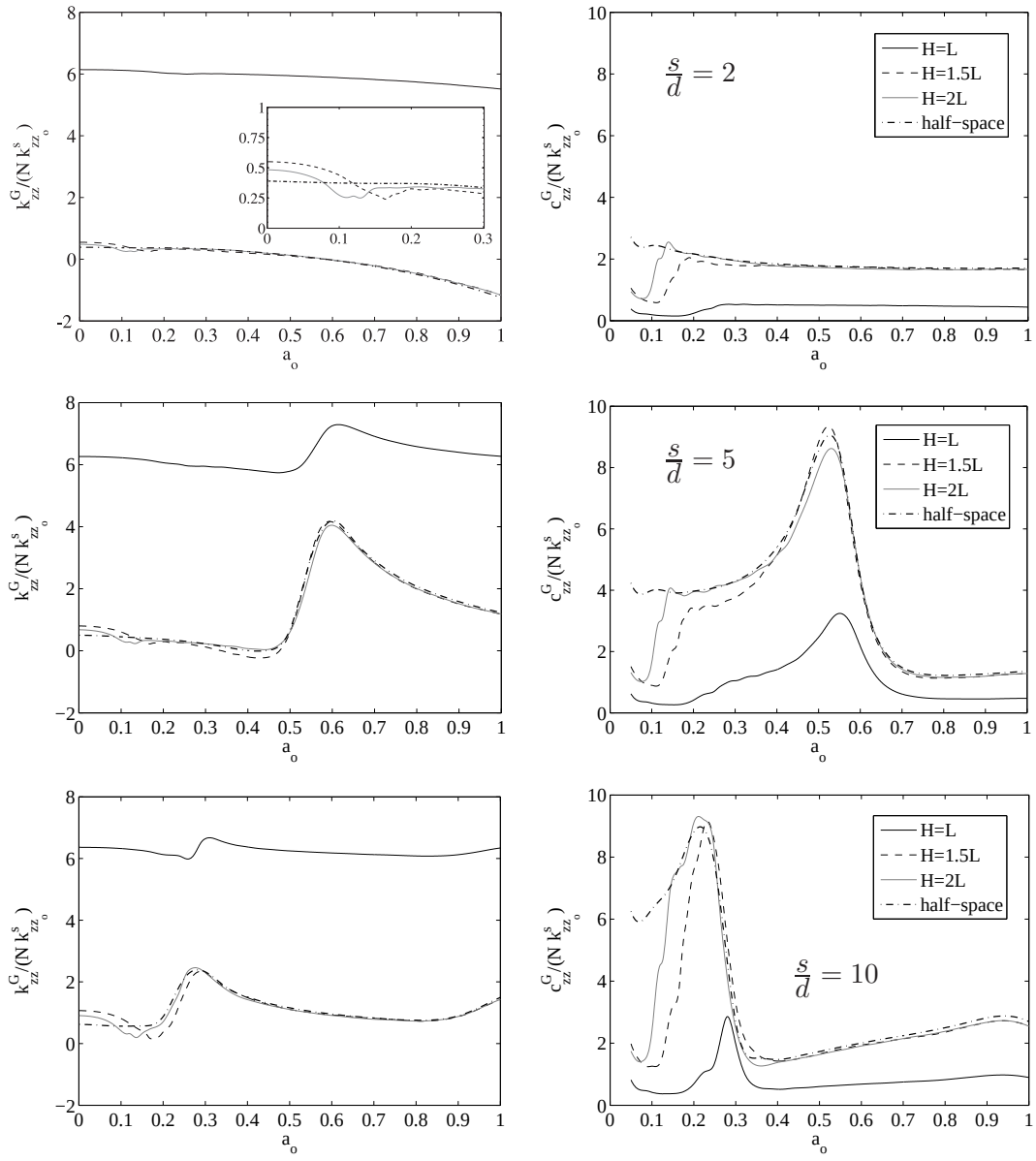

Figura C.5: *Impedancias verticales de un grupo de* 2×2 *pilotes en suelo blando* $(E_p/E_s = 10^3)$*.* $s/d = 2, 5$ *y* 10*.*

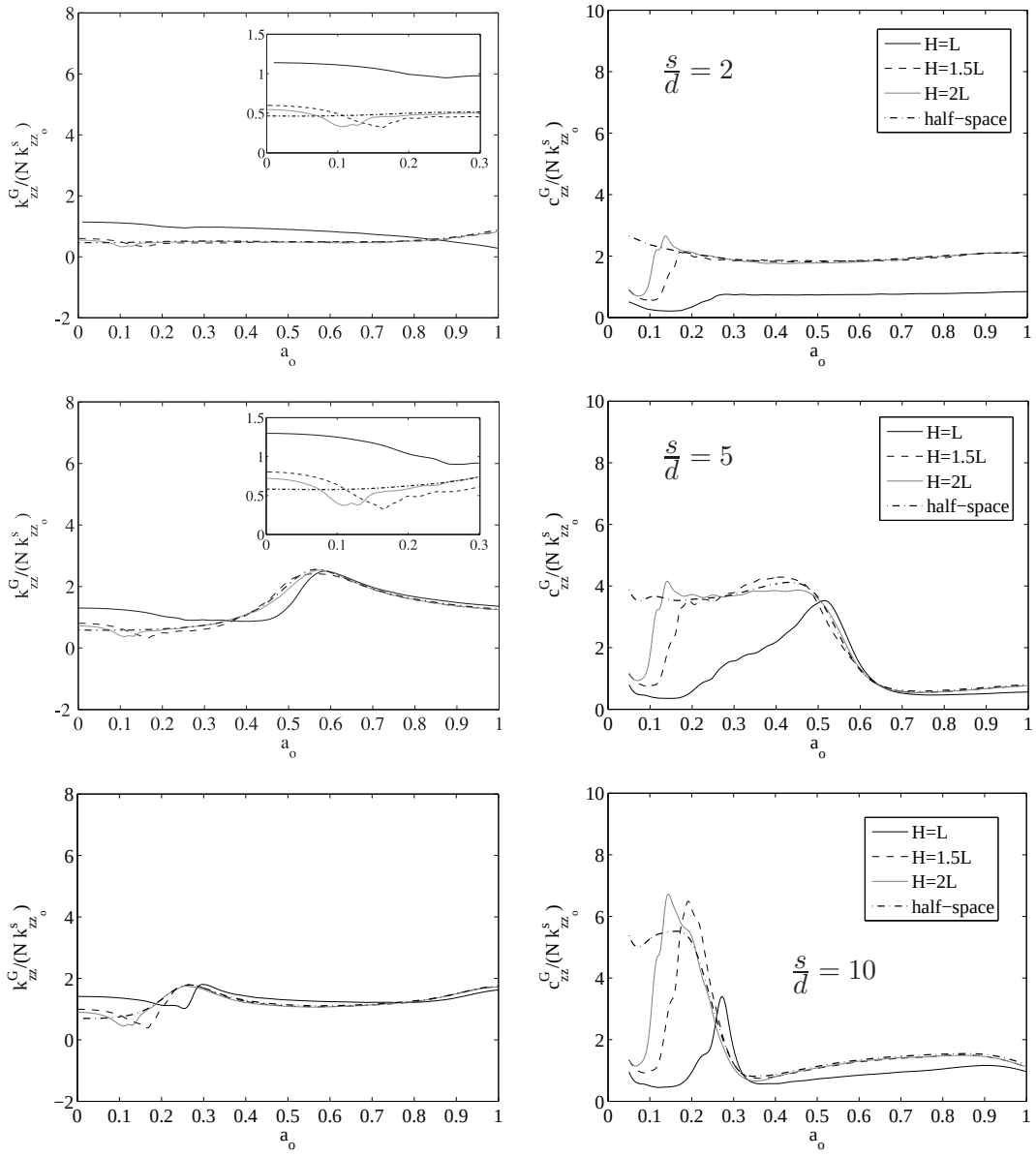

Figura C.6: *Impedancias verticales de un grupo de* 2×2 *pilotes en suelo duro* $(E_p/E_s = 10^2)$*.* $s/d = 2, 5$ *y* 10*.*

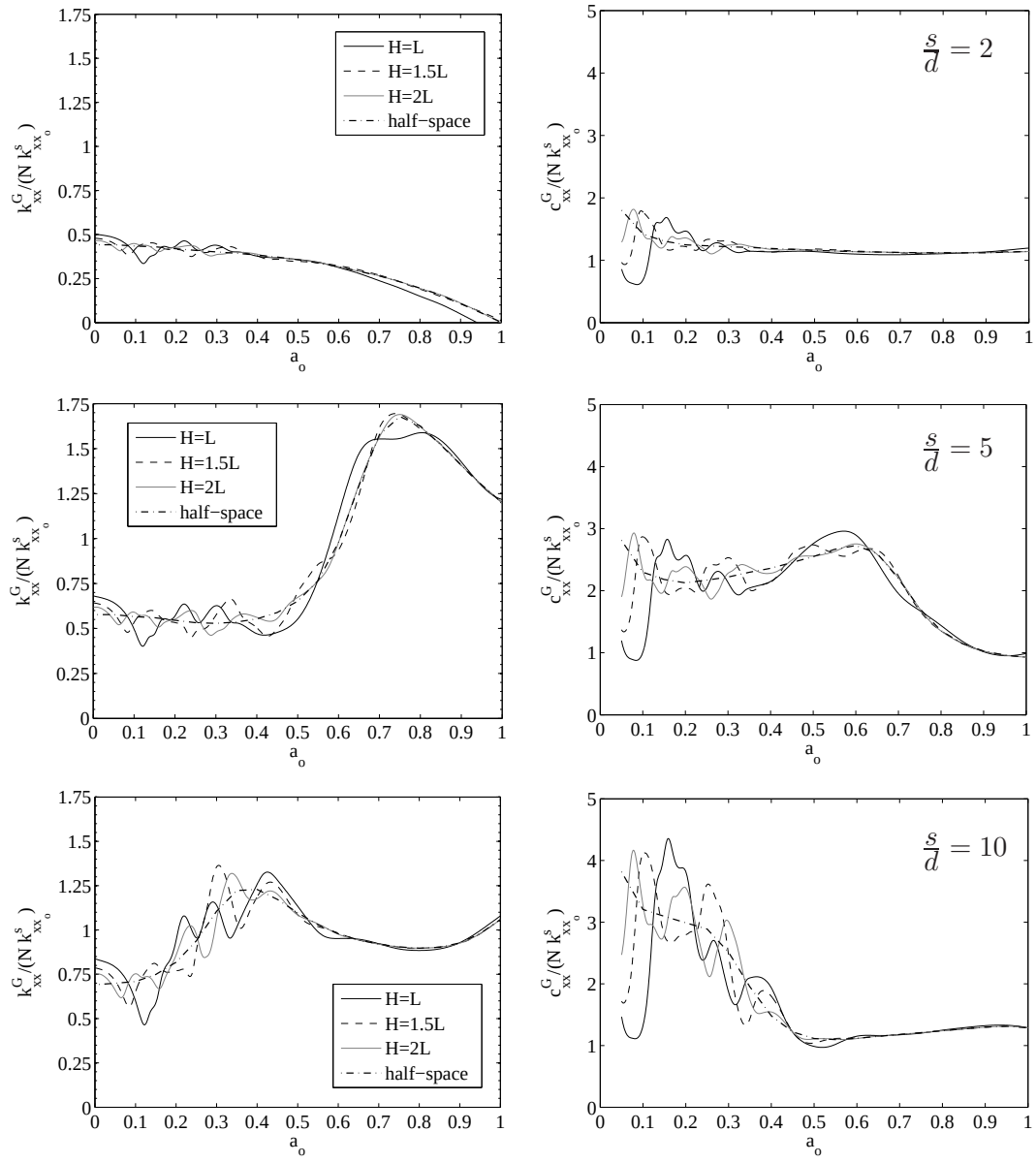

Figura C.7: *Impedancias horizontales de un grupo de* 2×2 *pilotes en suelo blando* $(E_p/E_s = 10^3)$*.* $s/d = 2, 5$ *y* 10*.*

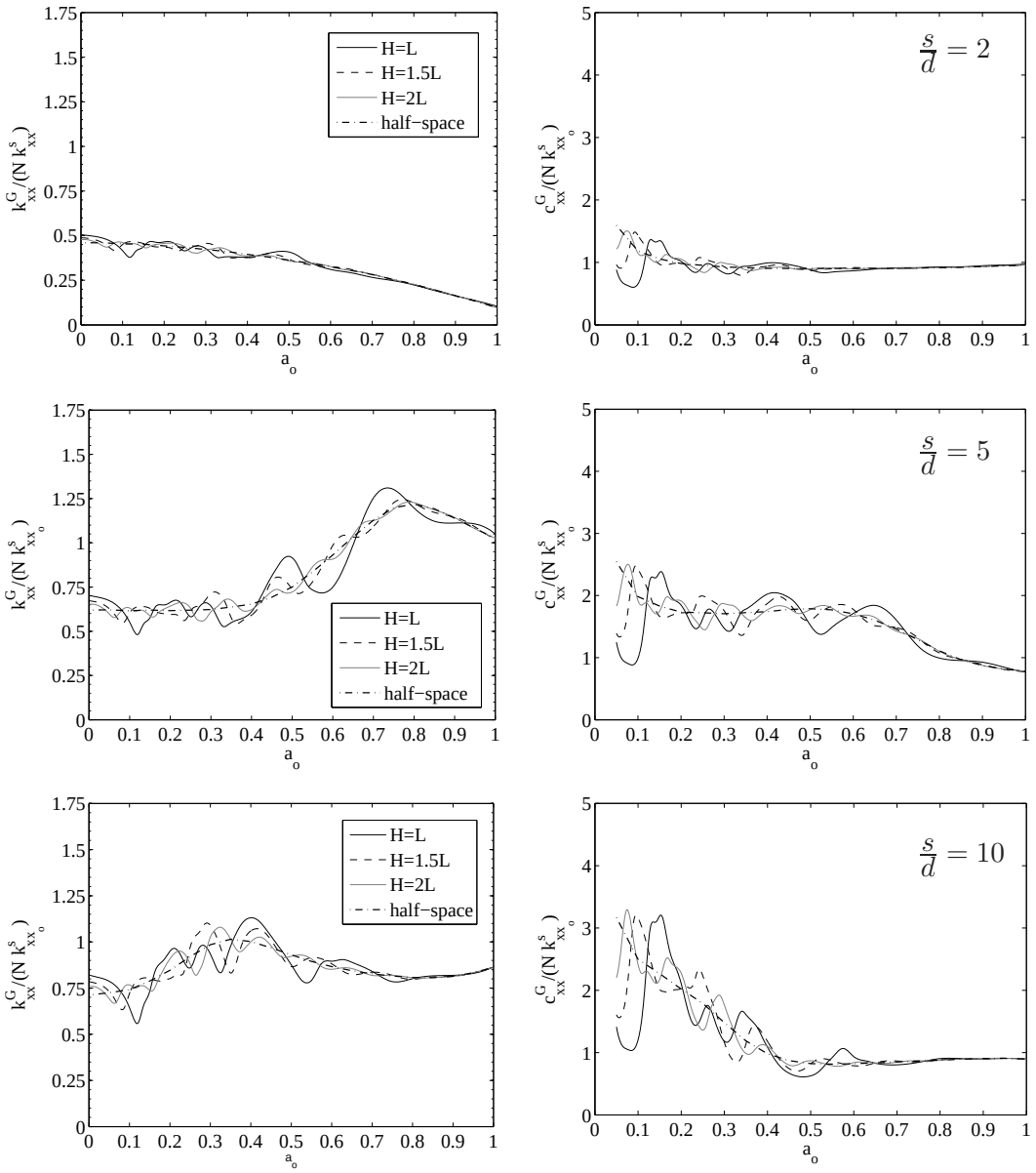

Figura C.8: *Impedancias horizontales de un grupo de* 2×2 *pilotes en suelo duro* $(E_p/E_s = 10^2)$*.* $s/d = 2, 5$ *y* 10*.*

valores presentados para el caso del pilote simple, e incluso crecen con la relación s/d. Además, las funciones de impedancia vertical, a frecuencias medias y altas, son equivalentes a las de un grupo de pilotes flotantes en un semiespacio. Sin embargo, el efecto grupo ejerce mayor influencia que la presencia de la base rocosa.

Por otro lado, en el caso horizontal, la base rígida es relativamente mucho más importante, incluso a pesar de que el efecto grupo sigue siendo predominante. Las funciones de impedancia fluctúan alrededor de la solución para el semiespacio, y la amplitud de esta fluctuación aumenta con la relación s/d.

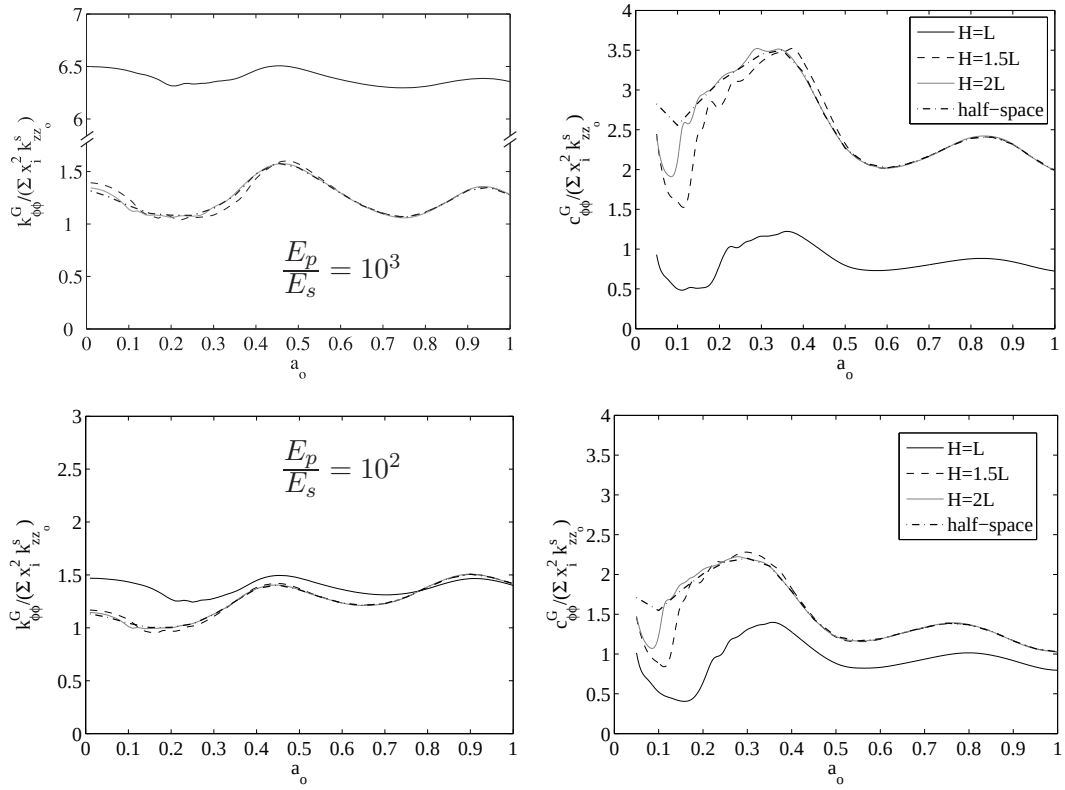

Figura C.9: *Impedancias de cabeceo de un grupo de* 2×2 *pilotes en suelo blando* ($E_p/E_s = 10^3$) *y suelo duro* ($E_p/E_s = 10^2$). *s/d=10.*

Finalmente, las impedancias de cabeceo de un grupo de 2×2 pilotes, embebidos en un estrato homogéneo sobre una base rocosa, se muestran en la fig. C.9. Sólo se muestran resultados correspondientes a la relación de separación s/d =10, para la que la influencia de la base rígida es mayor. De este modo se ilustra el hecho de que las funciones de impedancia de cabeceo de un grupo de pilotes se ven poco influenciadas por la presencia de la base rocosa.

C.3. Respuesta sísmica de un grupo de pilotes ante ondas S de incidencia vertical

En esta sección se pretende estudiar la influencia del modelado de la estratigrafía sobre el comportamiento sísmico estimado para una cimentación pilotada. Para ello se analiza la respuesta sísmica de un grupo de pilotes hincados sometidos a ondas tipo S de incidencia vertical. Los casos incluidos en el experimento están esquematizados en la fig. C.10. Se consideran tres suelos estratificados diferentes, formados por hasta cuatro estratos, de modo que la velocidad de la onda de corte aumenta con la profundidad. Además, se incluyen, a modo de comparación, dos casos límite, correspondientes a suelos homogéneos con las propiedades de las capas más blanda o más rígida, y el caso del semiespacio. Las propiedades del estrato más rígido son tomadas como propiedades de referencia. Por otro lado, y dado que es bien conocido que el número de pilotes no es un parámetro significativo en la respuesta sísmica horizontal de una cimentación pilotada (véase por ejemplo [69]), sólo se presentarán resultados correspondientes a una cimentación cuadrada de 3×3 pilotes hincados.

Las propiedades adimensionales del suelo de referencia (con velocidad de la onda de corte c_s) y de los pilotes son: coeficiente de amortiguamiento interno del suelo $\beta = 0.05$, coeficiente de Poisson para el suelo $\nu_s = 0.4$, relación entre densidades $\rho_s/\rho_p = 0.7$, cociente entre los módulos de Young del pilote y del suelo $E_p/E_s = 10^2$, relación de aspecto de los pilotes $L/d = 15$, y relación de separación entre pilotes adyacentes $s/d = 10$. El coeficiente de Poisson, el coeficiente de amortiguamiento y la densidad son considerados constantes para todos los estratos.

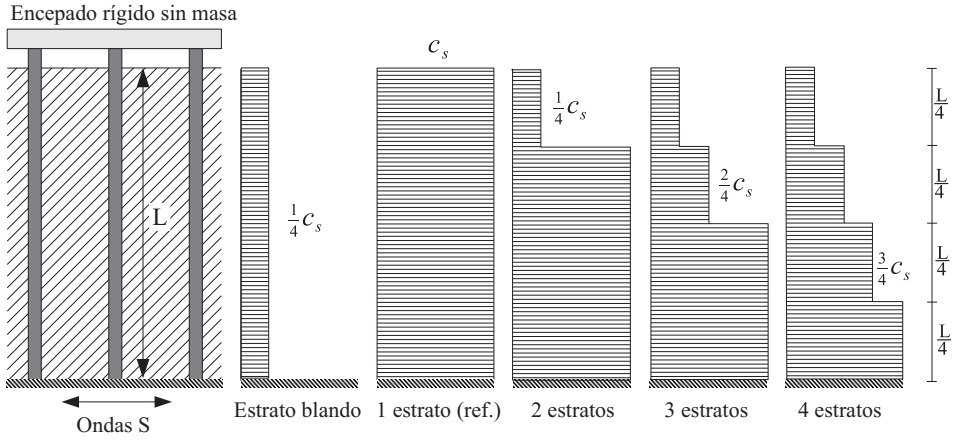

Figura C.10: *Esquema de los casos considerados.*

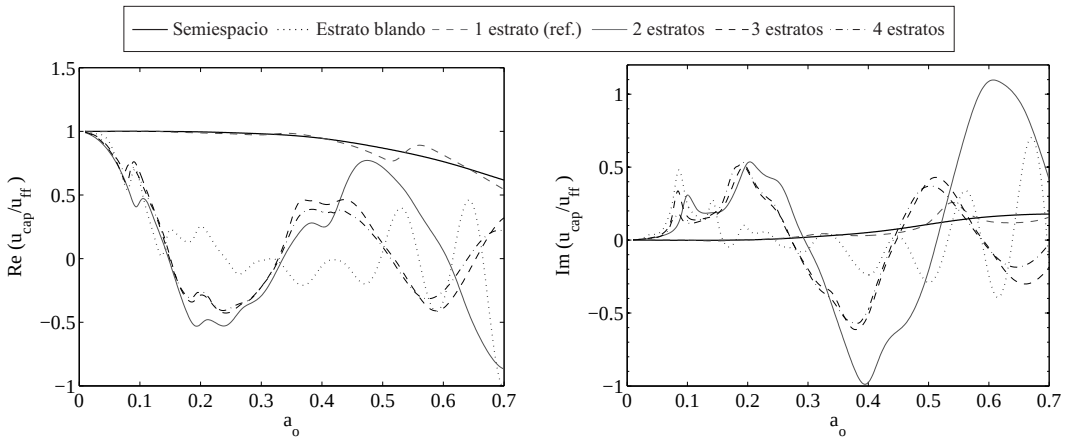

Figura C.11: *Función de transferencia en desplazamientos en el encepado.*

El primer paso es la obtención de las funciones de transferencia que relacionan los desplazamientos horizontales en el encepado (u_{cap}) con los desplazamientos de campo libre (u_{ff}), cuando el sistema es sometido a ondas planas tipo S de incidencia vertical. En la fig. C.11 se presentan las partes real e imaginaria de estas funciones de transferencia para los seis casos definidos anteriormente, donde a_o está referido siempre al suelo más duro. Comparando el caso del estrato compuesto por el suelo de referencia, con el caso de dos estratos, puede verse que el hecho de tener en cuenta una capa blanda superficial lleva a funciones de transferencia que decrecen mucho más rápidamente (véase por ejemplo [69, 71]), mientras que la adición de más capas intermedias no altera significativamente la respuesta para frecuencias por debajo de $a_o = 0.4$. Además, las diferencias entre las funciones de transferencia del semiespacio y de un único estrato son muy pequeñas, excepto a frecuencias coincidentes con las frecuencias naturales del estrato.

A partir de aquí, pueden obtenerse respuestas en el dominio del tiempo y espectros de respuesta máxima para casos específicos. El ejemplo que va a ser estudiado aquí, cuyos parámetros se resumen en la tabla C.1, corresponde a un grupo de pilotes de hormigón de diámetro $d = 1.0$ m., sometido a las siguientes dos señales sísmicas, especificadas en la superficie libre:

- La componente N-S, registrada en subestación 'Imperial Valley Irrigation District' en 'El Centro', California, durante el terremoto que tuvo lugar en 'Imperial Valley' el 18 de Mayo de 1940.
- La componente S50W, registrada en la subestación 'Bonds Corner' en 'El Centro', California, durante el terremoto que tuvo lugar en 'Imperial Valley' el 15 de Octubre de 1979.

Suelo	Pilotes	Grupo de pilotes
$c_s = 239\ m/s$	$E_p = 2.76 \cdot 10^{10}\ N/m^2$	$s/d = 10$
$\rho_s = 1750\ kg/m^3$	$\rho_p = 2500\ kg/m^3$	$L/d = 15$
$\nu_s = 0.4$	$d = 1\ m$	$H/L = 1$

Tabla C.1: *Propiedades del suelo de referencia, de los pilotes y de la cimentación.*

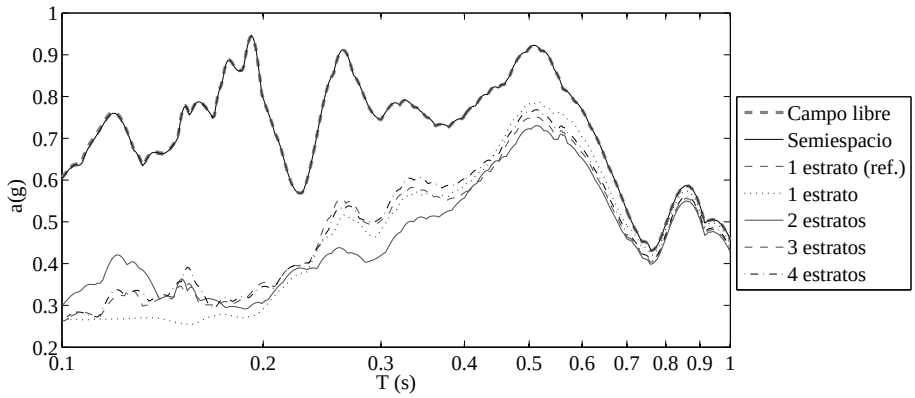

Figura C.12: *Espectro de respuesta máxima obtenido para el terremoto de El Centro (1940), especificado en la superficie libre, con un 5 % de amortiguamiento.*

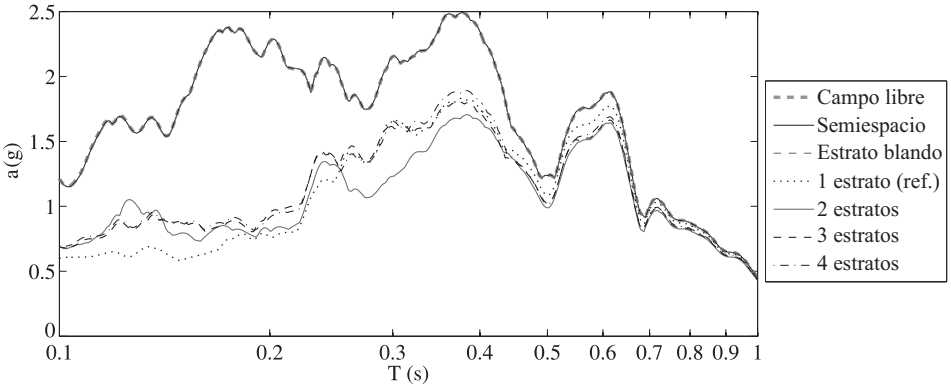

Figura C.13: *Espectro de respuesta máxima obtenido para el terremoto de El Centro (1979), especificado en la superficie libre, con un 5 % de amortiguamiento.*

Las figs. C.12 y C.13 muestran, para ambos terremotos, los espectros de re-

spuesta máxima en aceleraciones ($\xi = 5\,\%$) medidos en el encepado. Como era de esperar a la vista de las funciones de transferencia presentadas anteriormente, las respuestas de la cimentación pilotada en un semiespacio, y en un estrato, ambos con las propiedades del suelo de referencia, son prácticamente coincidentes con la señal de excitación. En cuanto al resto de casos, los valores de la aceleración espectral son significativamente menores en el rango de períodos mostrado. Sin embargo, no es posible relacionar la bondad de la solución con el número de capas incluidas en el modelo.

Para poder generalizar las conclusiones de este estudio, deberían llevarse a cabo análisis paramétricos que incluyan una amplia variedad de perfiles del terreno, y que tengan en cuenta la variabilidad de parametros tales como densidad, coeficientes de amortiguamiento y coeficientes de Poisson. Por otro lado, nótese que sólo se ha estudiado la respuesta horizontal de la cimentación, pero que, en función del problema, el cabeceo podría ser un factor importante.

Apéndice D

Interacción dinámica estructura-suelo-estructura entre edificios pilotados cercanos bajo excitación sísmica

D.1. Introducción

El método de la subestructuración constituye una herramienta precisa, simple y eficiente para el análisis de algunos problemas de interacción suelo-estructura, tales como los correspondientes a un edificio aislado cimentado sobre una única cimentación. Sin embargo, esta metodología no es tan conveniente para muchos otros problema de interacción suelo estructura, como puedan ser, por ejemplo, los referidos a estructuras largas con múltiples soportes (puentes), grandes estructuras muy masivas (presas) o grupos de estructuras o elementos que puedan interactuar entre sí.

Por esta razón, el modelo acoplado de elementos de contorno y elementos finitos, para el análisis dinámico de estructuras pilotadas, que fue presentado en el capítulo B, es usado aquí para estudiar los efectos de la interacción, a través del suelo, que tiene lugar entre estructuras pilotadas cercanas distribuídas de forma tridimensional, tal y como se muestra en la fig. D.1. En esta primera aproximación, el problema ha sido deliberadamente simplificado para: en primer lugar, poder concentrar la atención en los fenómenos relacionados con la interacción estructura-suelo-estructura; y en segundo lugar, establecer un vínculo con trabajos previos en este campo. De este modo, cada edificio han sido modelado como una estructura a cortante de una sola altura, cimentada sobre un grupo de 3×3 pilotes sobre un semiespacio viscoelástico, y se ha realizado el estudio sobre un con-

junto definido de configuraciones. Por lo tanto, los resultados presentados aquí no aspiran a constituir un análisis exhaustivo del problema, sino una ilustración de los fenómenos que pueden tener lugar.

Figura D.1: *Grupo de estructuras pilotadas cercanas*

El problema es planteado en la sección D.2, tras lo cual, en la sección D.3, se definen los parámetros y las propiedades seleccionados para el estudio. Entonces, en la sección D.4.1 se presenta un conjunto de resultados numéricos en el dominio de la frecuencia con los que se busca evaluar los efectos de la interacción estructura-suelo-estructura en la respuesta sísmica de edificios. Estos resultados son presentados en términos de la deflexión espectral de las estructuras, la frecuencia fundamental del sistema, las respuestas verticales y rotacionales, y los esfuerzos cortantes que aparecen en la cabeza de los pilotes. También se presentan, en la sección D.4.2, varios espectros de respuesta máxima obtenidos para una señal sísmica sintetizada de forma artificial.

D.2. Definición del problema

El sistema a estudiar está compuesto por varias estructuras a cortante de una sola altura, situadas relativamente cerca las unas de las otras, y cimentadas cada una de ellas sobre un grupo de 3×3 pilotes embebidos en un semiespacio de naturaleza viscoelástica. Un esquema del problema puede verse en la fig. D.2, donde se muestran los parámetros geométricos utilizados en la definición de los edificios. Por su parte, los grupos de pilotes están definidos por la longitud L y el diámetro d de los pilotes, la distancia entre centros de pilotes adyacentes s, y

el semiancho de la cimentación b, cumpliéndose en este caso que $b = s$. El resto de los parámetros son: distancia entre los centros de cimentaciones adyacentes D, período fundamental T y coeficiente de amortiguamiento estructural ζ para la estructura sobre base rígida, masa m_o y momento de inercia I_o del encepado rígido, y por último, la altura h y la masa m efectivas adoptadas para caracterizar el comportamiento dinámico de la estructura.

En este trabajo, a modo de primera aproximación, y con el objetivo de centrarse en los fenómenos de interacción estructura-suelo-estructura, las superestructuras son modeladas como estructuras a cortante que se comportarían como sistemas de un grado de libertad sobre base rígida. Sin embargo, este modelo puede ser entendido también como una aproximación al primer modo de una estructura multi-modal. De este modo, h, m y ζ deben ser entendidos como la altura, la masa y el coeficiente de amortiguamiento equivalentes para el primer modo. Por otro lado, nótese que la fig. D.2 es una representación bidimensional del modelo tridimensional utilizado. Se consideran, pues, ocho grados de libertad para definir el comportamiento de cada subsistema cimentación-superestructura: dos deformaciones laterales u de la estructura, dos desplazamientos horizontales u^c de la cimentación, un desplazamiento vertical u_z, dos giros φ alrededor de los ejes horizontales, y un giro ϕ alrededor del eje vertical. Nótese también que, debido a que se ha modelado el edificio como una estructura a cortante, los desplazamientos verticales del encepado y del forjado son considerados idénticos.

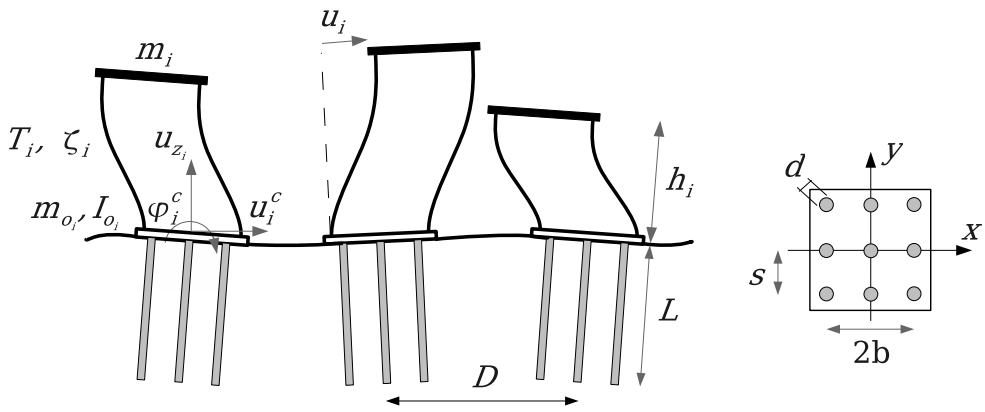

Figura D.2: *Definición geométrica del problema*

A lo largo de este capítulo se analizará el comportamiento dinámico de distintos grupos de edificios, sometidos a ondas S de incidencia vertical (produciendo desplazamientos a lo largo del eje y), o a ondas de Rayleigh (propagándose a lo largo del eje y desde $y < 0$ hacia $y > 0$). Para ello, la respuesta de cada una de las estructuras de un grupo es comparada con la de una sola estructura sin más

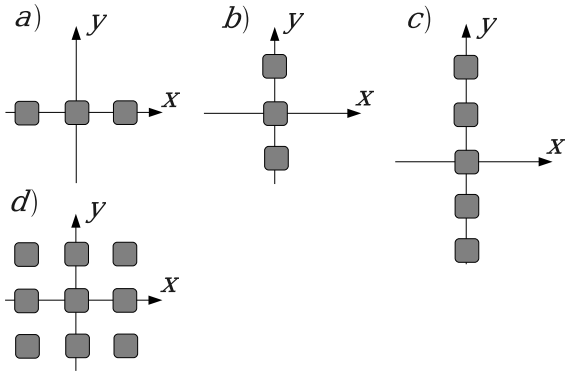

Figura D.3: *Las diferentes configuraciones consideradas en el trabajo*

construcciones alrededor. De este modo, se investigará la importancia de los efectos de interacción estructura-suelo-estructura sobre las cuatro configuraciones que se muestran en la fig. D.3. Nótese que, en todas las configuraciones, la distancia D entre estructuras adyacentes es medida paralelamente a los ejes x e y, y es la misma para todas las estructuras de una misma configuración.

D.3. Parámetros del problema

Las propiedades mecánicas y geométricas de la cimentación pilotada y del suelo están definidas por los siguientes parámetros: relación de separación entre pilotes $s/d = 5$, ratios entre los módulos de Young del pilote y el suelo $E_p/E_s = 100$ y 1000, ratio entre las densidades del suelo y del pilote $\rho_s/\rho_p = 0.7$, relación de esbeltez de los pilotes $L/d = 15$, coeficiente de amortiguamiento del suelo $\beta = 0.05$, y coeficiente de Poisson $\nu_s = 0.4$.

Por otro lado, los parámetros más importantes a la hora de definir el comportamiento dinámico de las superestructuras son: relación de esbeltez de la estructura $h/b = 2$, 3 y 4; ratio entre las rigideces de la estructura y del suelo $h/(T\,c_s) = 0.3$, donde c_s es la velocidad de la onda de corte en el suelo; y coeficiente de amortiguamiento de la estructura $\zeta = 0.05$. La elección del valor para el ratio entre las rigideces de la estructura y del suelo se justifica más adelante. Otros parámetros son: momento de inercia de la cimentación $I_o = 5\,\%$, $2.2\,\%$ y $1.25\,\%$ de mh^2 para $h/b = 2$, 3 y 4, respectivamente; ratio entre las masas de la estructura y del suelo $m/4\rho_s b^2 h = 0.20$; y ratio entre las masas del encepado y de la estructura $m_o/m = 0.25$. Los valores seleccionados para estos tres últimos parametros son considerados representativos para las construcciones usuales, y valores similares han sido utilizados con anterioridad por otros autores [82, 83, 86]. En cualquier

caso, los resultados relacionados con los efectos de interacción suelo-estructura y estructura-suelo-estructura no son sensibles a la variación de tales parámetros.

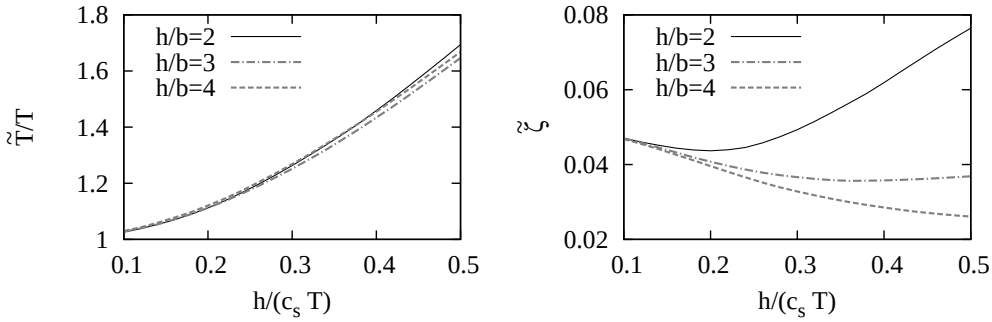

Figura D.4: *Evaluación de los efectos de interacción suelo-estructura en estructuras a cortante cimentadas sobre grupos de* 3×3 *pilotes.* $s/d = 5$*,* $L/d = 15$*,* $E_p/E_s = 1000$*.*

Los efectos de interacción suelo-estructura para un solo edificio pueden ser medidos por los parámetros $\tilde{T}/T$ y $\tilde{\zeta}$, donde $\tilde{T}$ es el período fundamental del sistema, y $\tilde{\zeta}$ es su amortiguamiento estructural equivalente. El primero de los parámetros mide la variación de la frecuencia fundamental del sistema, mientras que el amortiguamiento efectivo está relacionado con el máximo valor absoluto de la pseudo-aceleración que experimenta la estructura. Es decir, si $\tilde{\zeta} > \zeta$, la respuesta máxima del sistema suelo-estructura es menor que la correspondiente a la estructura sobre base rígida, y viceversa. Para relacionar los efectos de la interacción estructura-suelo-estructura que van a ser estudiados aquí, con la magnitud de los efectos de interacción suelo-estructura de un solo edificio, la fig. D.4 muestra la evolución de $\tilde{T}/T$ y $\tilde{\zeta}$ con $h/(T\,c_s)$, para $E_p/E_s = 1000$. Dado que éste es el caso de una sola estructura cimentada sobre un único grupo de pilotes con un encepado rígido, el estudio puede ser realizado a través del método de subestructuración, que requiere menor esfuerzo computacional en comparación con el método directo. Tal y como se dijo anteriormente, este estudio ha sido realizado para $h/(T\,c_s) = 0.3$, que está dentro del rango de los valores correspondiente a estructuras reales, pero que implica que los fenómenos de interacción suelo-estructura son visibles. Obviamente, para $h/(T\,c_s) \to 0$ (suelo relativamente duro o estructura muy blanda o alta), el comportamiento de la estructura es similar al que experimentaría sobre una base rígida y, como consecuencia de ello, los efectos de interacción estructura-suelo-estructura serían inapreciables.

D.4. Resultados numéricos

D.4.1. Respuesta estacionaria

En esta sección se presentan resultados con el objetivo de investigar la influencia de los efectos de interacción estructura-suelo-estructura en la respuesta dinámica de estructuras pilotadas. Para ello, se analiza la respuesta sísmica horizontal de los edificios en términos de su espectro de deformación lateral, definida como $Q = \mathrm{Abs}[\Omega^2 u/\omega^2 u_{ff}]$, donde Ω es la frecuencia fundamental de la estructura sobre base rígida, ω es la frecuencia de excitación y u_{ff} es el desplazamiento horizontal de campo libre en la superficie. El producto de esta variable Q por la masa de la estructura y por la aceleración de campo libre da como resultado la amplitud de los esfuerzos cortantes que aparecen en la base de la estructura. Por otro lado, la respuesta vertical de las estructuras será estudiada a través de las funciones de transferencia $\mathrm{Abs}[u_z/u_{ff}]$ o $\mathrm{Abs}[u_z/u_{z_{ff}}]$, cuando el sistema es sometido a ondas tipo S o a ondas de Rayleigh, respectivamente, siendo u_z la amplitud del desplazamiento vertical harmónico de las estructuras, y $u_{z_{ff}}$ el desplazamiento vertical de campo libre en la superficie para una onda de Rayleigh. La respuesta rotacional de las estructuras ,ϕ, alrededor de un eje vertical, será también estudiada a través de la función de transferencia $\mathrm{Abs}[\phi{\cdot}b/u_{ff}]$. Todas las gráficas mostradas en esta sección están presentadas frente a la frecuencia adimensional $a_o = \omega d/c_s$.

La distancia D entre los centros de encepados adyacentes será expresada, bien de forma proporcional al semiancho b de la cimentación, o bien como una fracción de la longitud de onda de corte a la frecuencia fundamental del sistema $\lambda = c_s\tilde{T}$. El objetivo que se persigue al establecer esta relación entre D y λ es vincular la separación entre estructuras de características dinámicas similares con las propiedades dinámicas del sistema.

La fig. D.5 muestra la respuesta dinámica de un sistema suelo-estructura con un único edificio (línea continua) junto a la respuesta de grupos de tres edificios con idénticas propiedades dinámicas (líneas discontinuas) bajo ondas incidentes tipo S, en términos de su deformación lateral espectral, para $E_p/E_s = 1000$. Se incluyen en el estudio tres relaciones de aspecto distintas para las estructuras ($h/b = 2$, 3 y 4) y tres distancias entre edificios adyacentes ($D = \lambda/2$, $3\lambda/4$ y $\lambda/4$). La dirección del movimiento producido por la onda incidente es siempre paralela o perpendicular a la dirección de alineación de las estructuras (tal y como se muestra en las figs. D.3*a* y *b*, respectivamente). Puede verse que la respuesta lateral de una estructura puede verse influenciada de forma significativa por la presencia de edificios cercanos. Se produce un ligero desplazamiento en el período fundamental del sistema, mientras que el valor pico de las fuerzas de corte en la base puede verse considerablemente amplificado. Por ejemplo, cuando $D = \lambda/2$, la respuesta lateral del edificio central del caso de tres estructuras alineadas a lo largo de la dirección de la excitación se

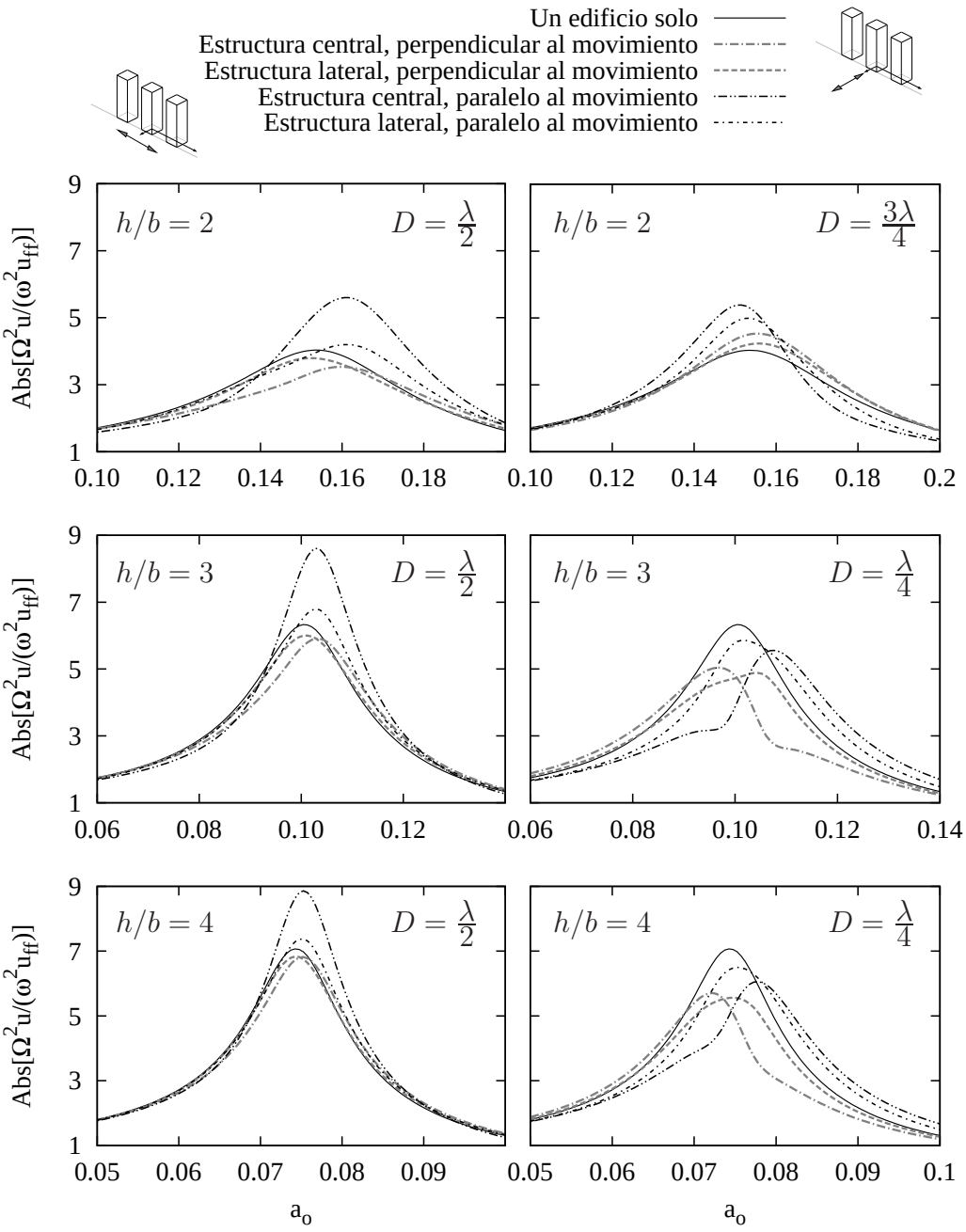

Figura D.5: *Interacción entre tres estructuras con idéntica frecuencia fundamental en términos de sus espectros de repuesta. Ondas S de incidencia vertical.* $E_p/E_s = 1000$

ve incrementada en un 40, 35 y 25 por ciento para $h/b = 2$, 3 y 4, respectivamente. La magnitud de la influencia de la interacción estructura-suelo-estructura varía entre una posición y otra, y también lo hace para distintas distancias entre edificios adyacentes o para distintas relaciones de aspecto. Incluso, hay casos en los que la magnitud de la respuesta crece respecto al caso de un solo edificio, y hay casos en los que dicha magnitud decrece, en función de la configuración. Sin embargo, la construcción que ocupa la posición central es generalmente la que experimenta mayores desplazamientos. Nótese también que aunque problemas con distintos h/b e igual D no son dimensionalmente equivalentes, pueden observarse tendencias similares para problemas con idéntica D, si ésta está expresada en términos de λ.

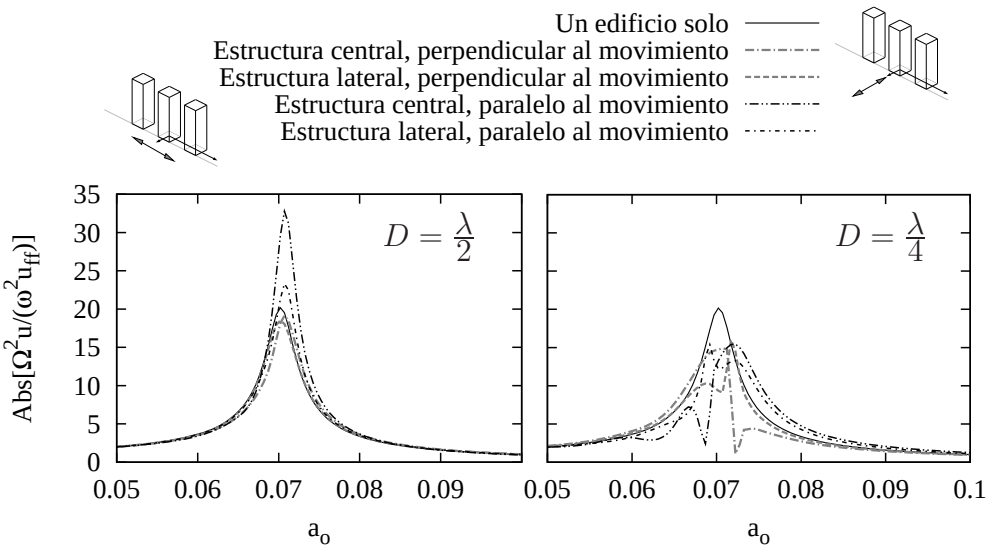

Figura D.6: *Interacción entre tres estructuras con frecuencias fundamentales similares en términos de sus espectros de respuesta. Ondas S de incidencia vertical.* $E_p/E_s = 100$. $h/b = 4$. *Compárese con las gráficas inferiores de la fig. D.5.*

La relación que existe entre la respuesta sísmica de las diferentes estructuras de un mismo grupo, y la del sistema de una sola superestructura, permanece también aproximadamente constante para diferentes ratios E_p/E_s. Para ilustrar esta afirmación, se muestran en la fig. D.6 la respuesta dinámica de un sistema suelo-estructura con un único edificio (línea continua) junto a la respuesta de grupos de tres edificios con idénticas propiedades dinámicas (líneas discontinuas) bajo ondas incidentes tipo S, en esta ocasión para $E_p/E_s = 100$. Sólo se muestran resultados para $h/b = 4$ y para $D = \lambda/2$ y $\lambda/4$. Comparando estas gráficas con las

mostradas en la fig. D.5 para las mismas relaciones de esbeltez, puede observarse que el comportamiento del sistema es cualitativamente equivalente para ambos valores de E_p/E_s.

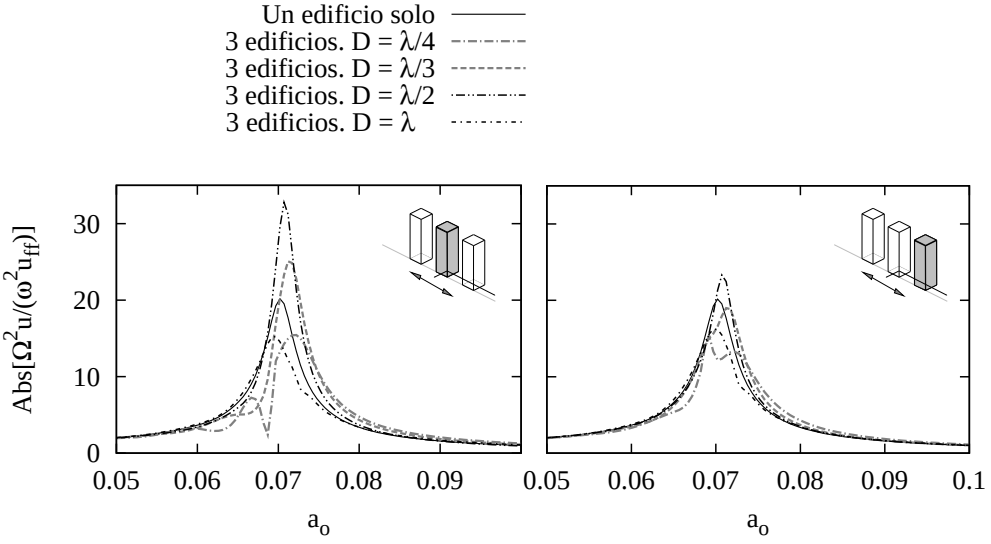

Figura D.7: *Influencia de la distancia en la interacción entre tres estructuras con idéntica frecuencia fundamental. Ondas S de incidencia vertical.* $h/b = 4$, $E_p/E_s = 100$

La interacción entre estructuras de idénticas características dinámicas, en relación con la distancia entre edificios adyacentes, es estudiada a continuación con la ayuda de la fig. D.7, para $h/b = 4$ y $E_p/E_s = 100$. En este caso, las estructuras están alineadas a lo largo de la dirección del movimiento producido por ondas tipo S de incidencia vertical. Se presentan resultados para los edificios central y lateral, y para varias distancias diferentes: $D = \lambda/4$, $\lambda/3$, $\lambda/2$ y λ. Una vez más se puede observar que la estructura central es la más influenciada por la presencia de construcciones cercanas, y que, para el conjunto de propiedades utilizado en estos experimentos, la distancia $D = \lambda/2$ arroja las mayores deformaciones laterales, que llegan a ser hasta un 65 por ciento más grandes que las correspondientes a un sistema con un solo edificio. Por contra, a distancias $D = \lambda/4$ y λ se producen atenuaciones en la respuesta de hasta un 25 por ciento.

Las figuras D.8 y D.9 muestran la respuesta dinámica de un sistema suelo-estructura con un único edificio (línea continua) junto a la respuesta de grupos de tres edificios con propiedades dinámicas diferentes (líneas discontinuas) bajo ondas incidentes tipo S que producen desplazamientos paralelos o perpendiculares a la

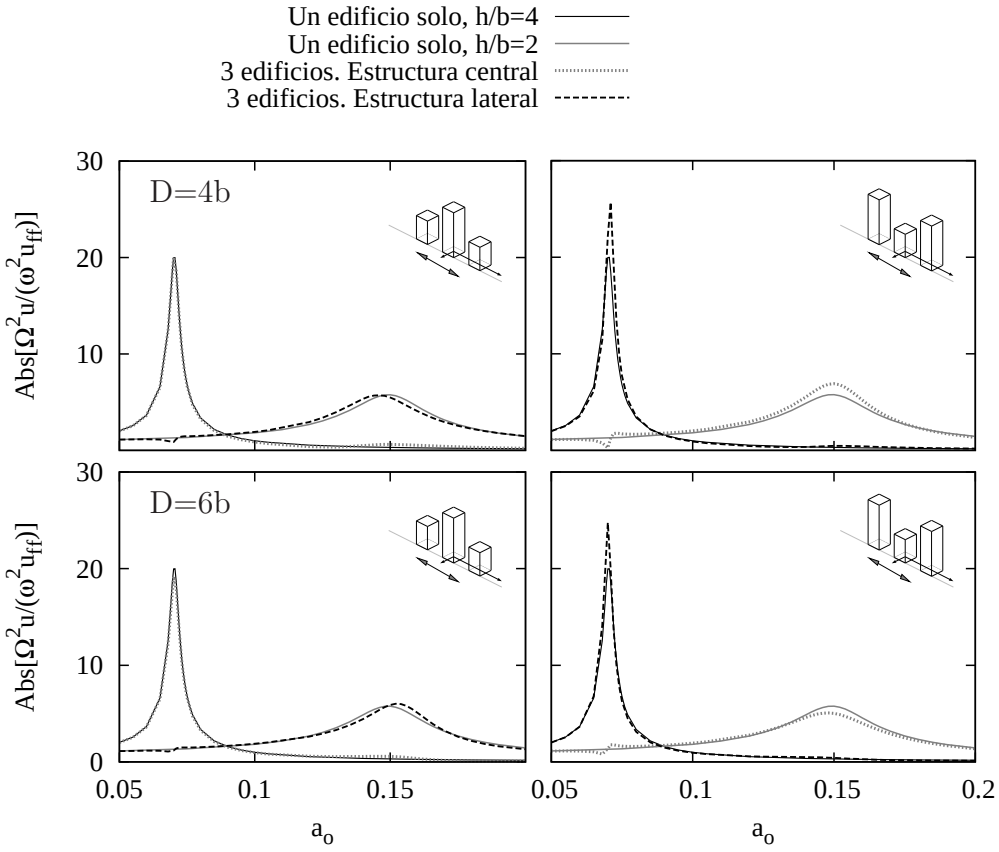

Figura D.8: *Interacción entre tres estructuras de frecuencias fundamentales distintas en términos de sus espectros de respuesta. Ondas S de incidencia vertical. Estructuras alineadas a lo largo de la dirección de excitación.* $h/b = 2$ *y* 4. $E_p/E_s = 100$.

dirección de alineación de las estructuras. En este caso, los edificios adyacentes tienen diferentes relaciones de aspecto ($h/b = 2$ y 4) y, en cuanto al resto de propiedades, sus períodos fundamentales sobre base rígida difieren por un factor de 2. Se han utilizado dos distancias entre edificios adyacentes ($D = 4b$ y $6b$), y la relación entre los módulos de elasticidad de pilotes y suelo es $E_p/E_s = 100$. Se observa que, para estas configuraciones, los efectos de interacción estructura-suelo-estructura parecen ser despreciables en la mayoría de los casos, aunque para estructuras de bajo período natural situada entre dos edificios idénticos de mayor período natural, la respuesta de ambos tipos de edificios se ve incrementada un 20 y un 30 por ciento, respectivamente.

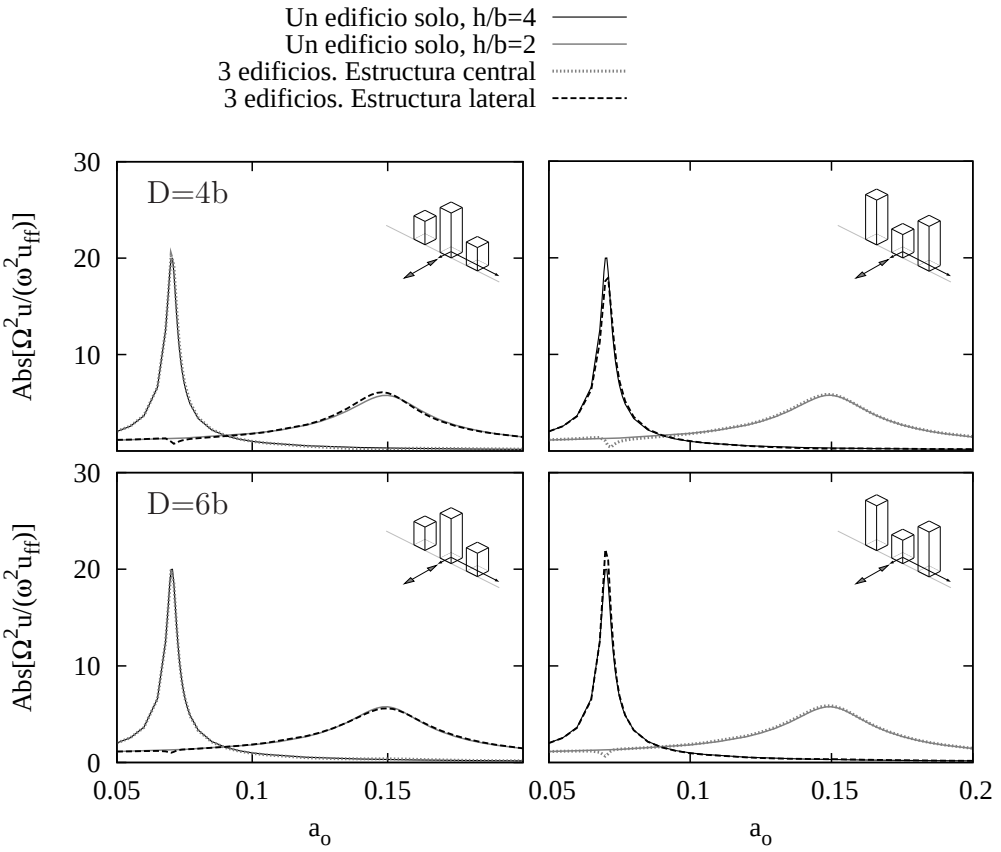

Figura D.9: *Interacción entre tres estructuras de frecuencias fundamentales distintas en términos de sus espectros de respuesta. Ondas S de incidencia vertical. Estructuras alineadas perpendicularmente a la dirección de excitación.* $h/b = 2$ *y* 4. $E_p/E_s = 100$.

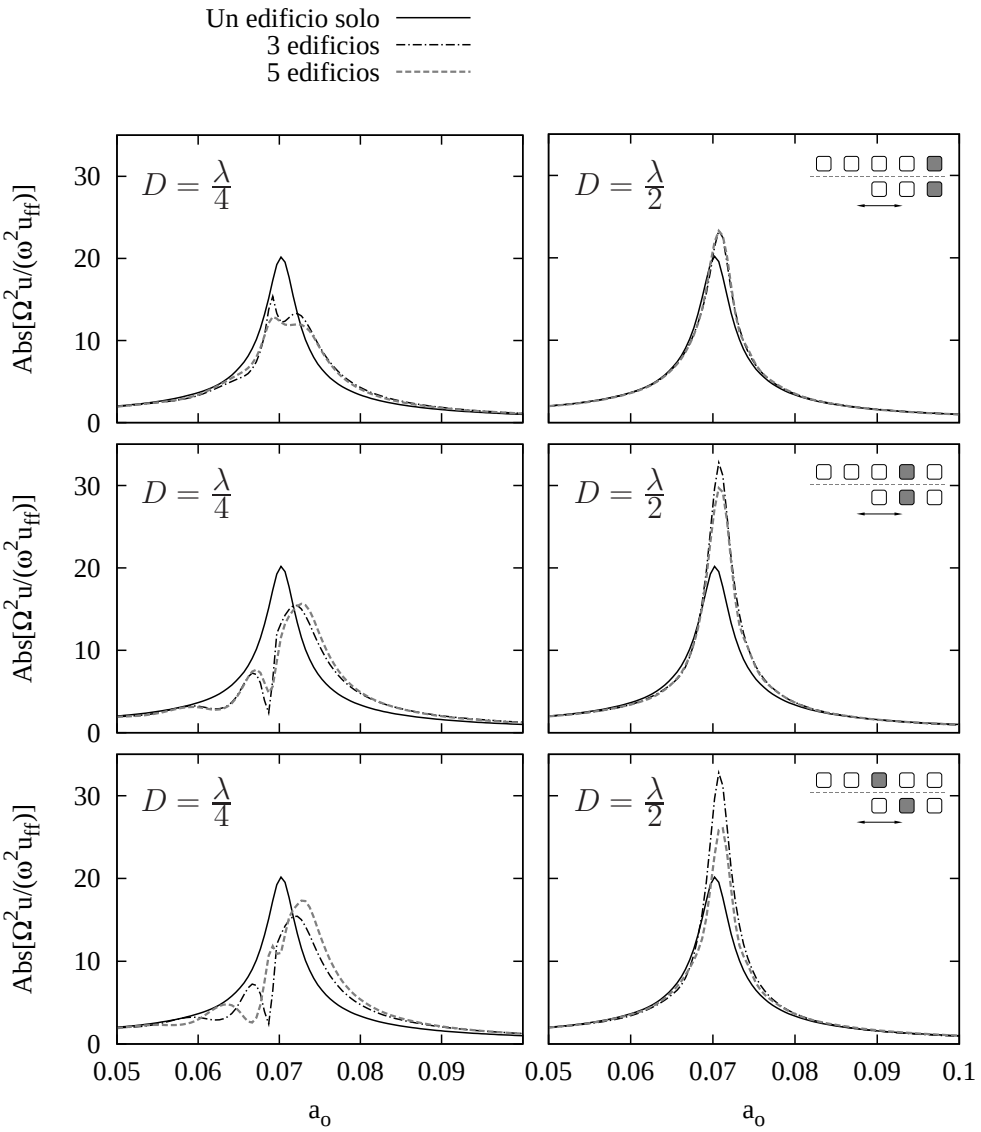

Figura D.10: *Interacción entre tres o cinco estructuras con idéntica frecuencia fundamental. Ondas S de incidencia vertical. Estructuras alineadas a lo largo de la dirección de excitación. Comparación entre las dos configuraciones en relación con la posición de la estructura.* $h/b = 4$. $E_p/E_s = 100$.

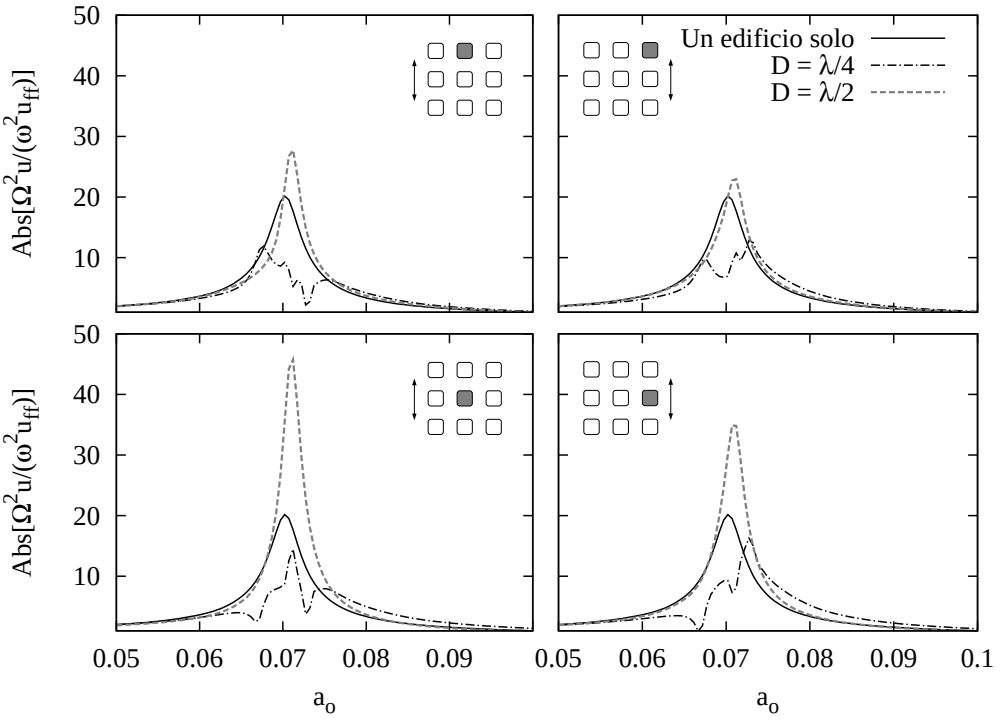

Figura D.11: *Interacción entre nueve estructuras con idéntica frecuencia fundamental en términos de sus espectros de repuesta. Ondas S de incidencia vertical.* $h/b = 4$. $E_p/E_s = 100$.

A continuación, la respuesta dinámica de un grupo de cinco estructuras ante ondas tipo S de incidencia vertical es comparada con la correspondiente a un grupo de tres en la fig. D.10, para $E_p/E_s = 100$ y para dos valores de la distancia D: $\lambda/4$ y $\lambda/2$. Los edificios están alineados a lo largo de la dirección de excitación (tal y como se muestra en las figs. D.3*b* y *c*), y ambos casos son comparados entre sí en función de la posición que ocupa la estructura en la fila. El comportamiento dinámico de las estructuras es significantemente similar cuando se comparan edificios por parejas empezando desde los extremos de la configuración. Sin embargo, las respuestas de los edificios centrales son considerablemente distintas. Por otro lado, la configuración de cinco estructuras es ligeramente menos desfavorable que la de tres.

Se estudia ahora el caso de nueve estructuras similares, con relaciones de aspecto $h/b = 4$, y situadas siguiendo la configuración mostrada en la fig. D.3d. La fig. D.11 muestra la respuesta dinámica de un sistema suelo-estructura con un único edificio (línea continua) junto a la respuesta de los elementos que con-

forman el grupo de nueve edificios con idénticas propiedades dinámicas (líneas discontinuas) bajo ondas incidentes tipo S, en términos de su deformación lateral espectral, para $E_p/E_s = 100$. Se consideran dos distancias distintas entre edificios adyacentes ($D = \lambda/2$ y $\lambda/4$). Estos resultados pueden ser comparados como los mostrados en la fig. D.6, donde se estudia el mismo problema para un grupo de sólo tres estructuras. Puede verse, de nuevo, que la tendencia general se conserva, es decir, que distancias $D = \lambda/2$ son mucho más desfavorables que, por ejemplo, distancias de $D = \lambda/4$, y que las estructuras que ocupan las posiciones centrales experimentan desplazamientos considerablemente mayores. En este caso concreto, la respuesta del edificio central se ve incrementada un 130 por ciento debido a la presencia de los edificios vecinos.

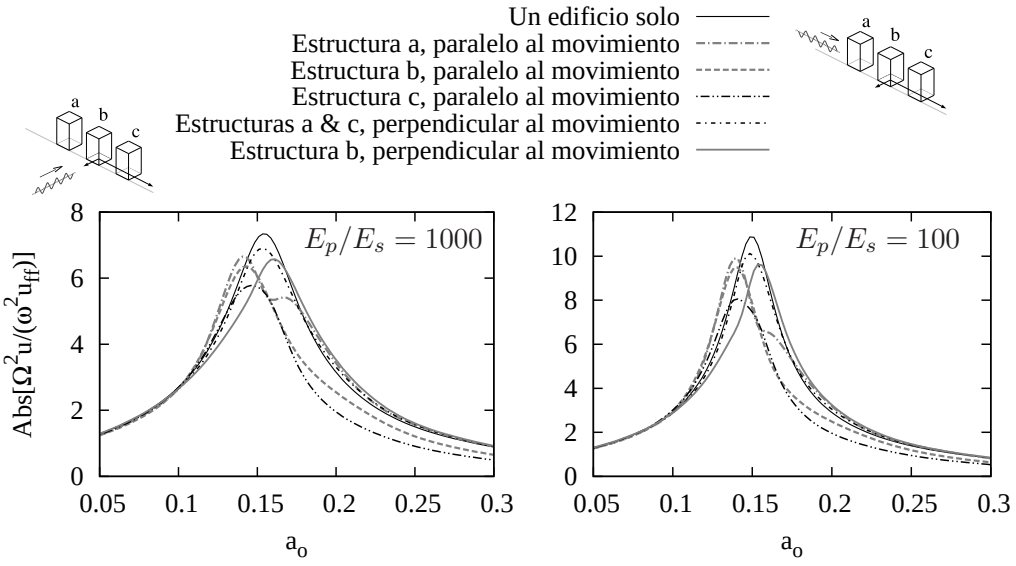

Figura D.12: *Interacción entre tres estructuras con idéntica frecuencia fundamental en términos de sus espectros de repuesta. Ondas de Rayleigh.* $h/b = 2$. $D = \lambda/2$.

Las tres figuras siguientes muestran la respuesta de varios grupos de estructuras sometidas a ondas de Rayleigh. En la fig. D.12 se presenta la respuesta dinámica de un sistema suelo-estructura con un único edificio junto a la respuesta de los edificio de un grupo de tres construcciones con idénticas propiedades dinámicas en términos de su deformación lateral espectral, siendo $h/b = 2$ y $D = \lambda/2$. En la fig. D.13 se presenta la misma información pero para el caso de una relación de aspecto $h/b = 4$ y dos distancias ($D = \lambda/2$ y $\lambda/4$). Estas gráficas incluyen

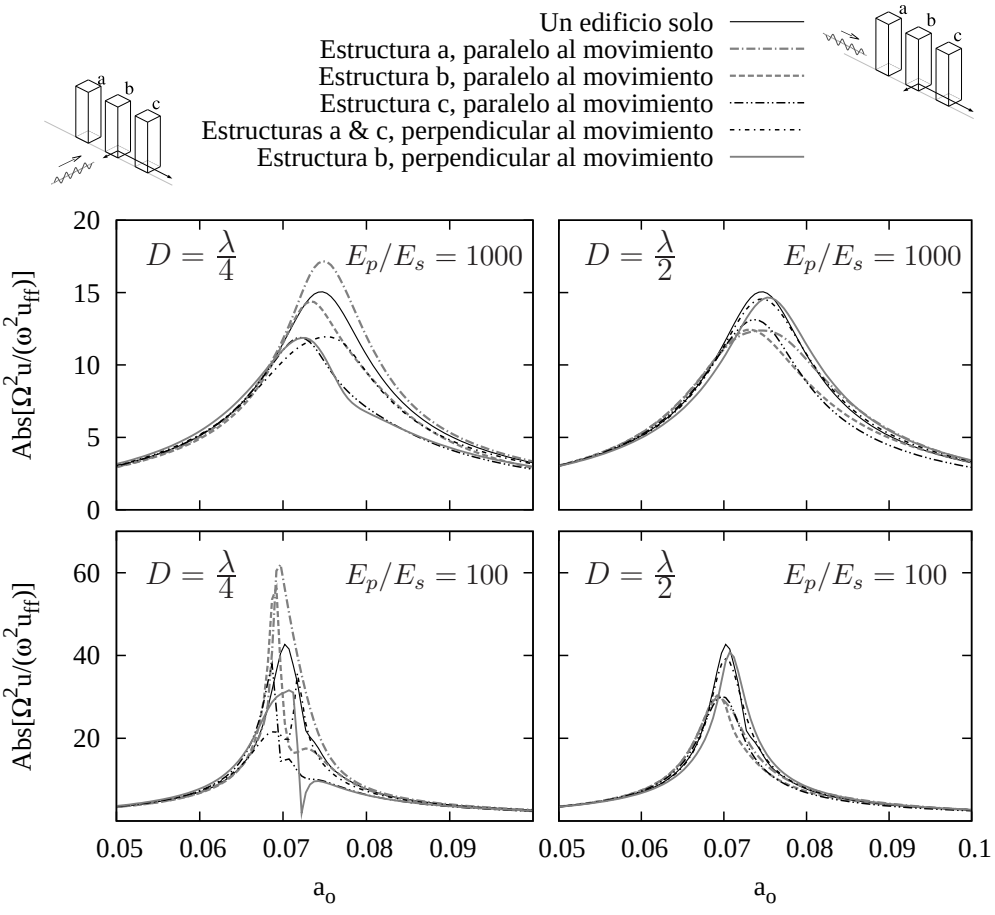

Figura D.13: *Interacción entre tres estructuras con idéntica frecuencia fundamental en términos de sus espectros de repuesta. Ondas de Rayleigh.* $h/b = 4$.

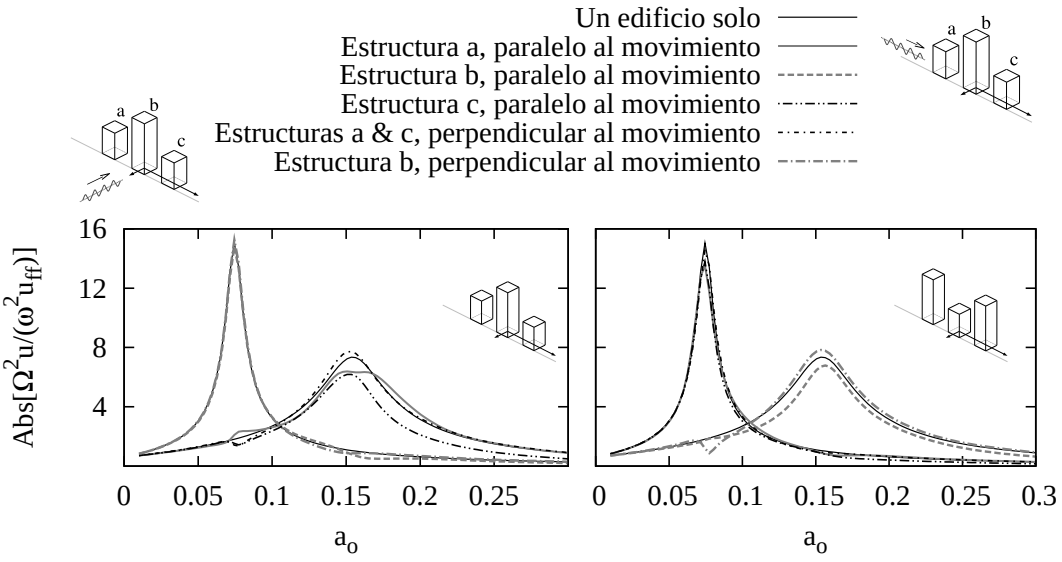

Figura D.14: *Interacción entre tres estructuras con frecuencias fundamentales distintas en términos de sus espectros de repuesta. Ondas de Rayleigh.* $h/b = 2$ *y* 4. $E_p/E_s = 1000$. $D = 4b$.

resultados para $E_p/E_s = 100$ y 1000, y para ondas de Rayleigh incidiendo paralelamente o perpendicularmente a la dirección de alineación de las estructuras. En primer lugar, nótese que, para las propiedades utilizadas en este estudio, y entre las distancias consideradas, la situación más desfavorable corresponde a $D = \lambda/4$, contrariamente a lo que ocurría con las ondas sísmicas tipo S de incidencia vertical. De hecho, en este caso, el agrupamiento de las estructuras a una distancia $D = \lambda/2$ reduce la respuesta sísmica del sistema. En segundo lugar, cuando las ondas sísmicas atacan en la dirección de alineación de las estructuras, tiene lugar un pequeño desplazamiento del período fundamental del sistema: hasta un 8 por ciento menor que el correspondiente a un sistema suelo-estructura con un único edificio. También se observan fenómenos de apantallamiento, de modo que, alrededor de la frecuencia fundamental, la respuesta sísmica de la primera estructura que es alcanzada por las ondas sísmicas (denominada "*a*" en las figuras) es significativamente superior a la respuesta de las otras dos. La última estructura (denominada estructura "*c*") es normalmente la que está más débilmente excitada por las ondas incidentes, siendo su repuesta hasta un 50 por ciento menor. Finalmente, ambas figuras muestran que el comportamiento general del sistema es independiente del parámetro E_p/E_s (aunque, obviamente, la magnitud de la respuesta cambia de

uno al otro). La última de las figuras que componen este conjunto de resultados es la fig. D.14, donde se muestra la respuesta de tres estructuras diferentes con relaciones de aspecto $h/b = 2$ y 4 para $E_p/E_s = 1000$ y $D = 4b$. En este caso, tal y como ocurría con las ondas tipo S, los efectos de interacción son despreciables, exceptuado los que están relacionados con los fenómenos de apantallamiento.

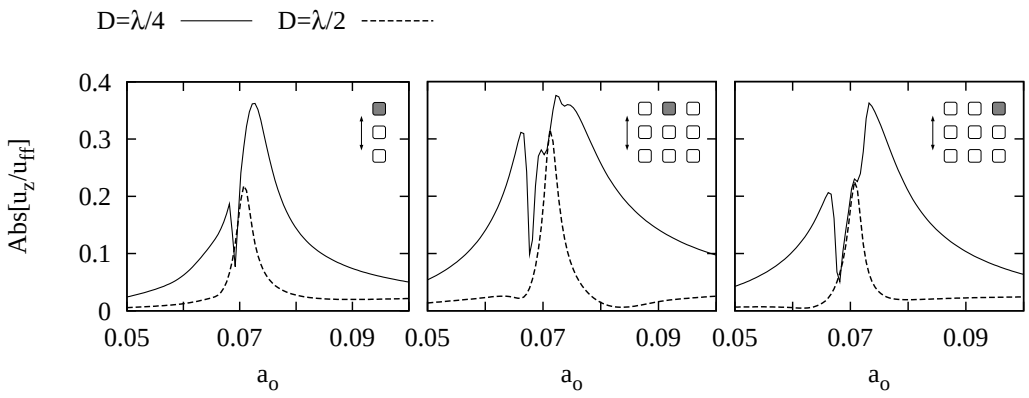

Figura D.15: *Funciones de transferencia del desplazamiento vertical de estructuras pilotas debido a la interacción estructura-suelo-estructura. Ondas S de incidencia vertical.* $h/b = 4$. $E_p/E_s = 100$.

El comportamiento vertical y rotacional de estructuras pilotadas adyacentes es presentado, en términos se sus respectivas funciones de transferencia, en las figs. D.15 y D.16, para ondas S de incidencia vertical, y en la fig. D.17 para ondas de Rayleigh. Todos los resultados corresponden a valores del ratio entre módulos de elasticidad de pilotes y suelo de $E_p/E_s = 100$ y a relaciones de aspecto $h/b = 4$. En estas figuras se muestran resultados correspondientes a grupos de tres y nueve edificios sometidos a ondas de corte, y a grupos de tres edificios sometidos a ondas de Rayleigh. En todos los casos, se muestran solamente las posiciones y configuraciones cuyas funciones de transferencia son distintas de cero. Los desplazamientos verticales, que están medidos en el centro de gravedad del encepado, están normalizados por los desplazamientos horizontales de campo libre de la ondas S, y por los verticales para la onda de Rayleigh, mientras que los giros son multiplicados por el semiancho de la cimentación y normalizados por el desplazamiento horizontal de campo libre, de tal modo que el valor resultante es indicativo de los desplazamiento horizontales en las cabezas de los pilotes horizontales debidos a la rotación. En la fig. D.15 se muestra cómo los desplazamientos verticales producidos por las ondas de cortes son mayores para la menor de las distancias consideradas. Para $D = \lambda/4$, los desplazamientos verticales producidos por los efectos de interac-

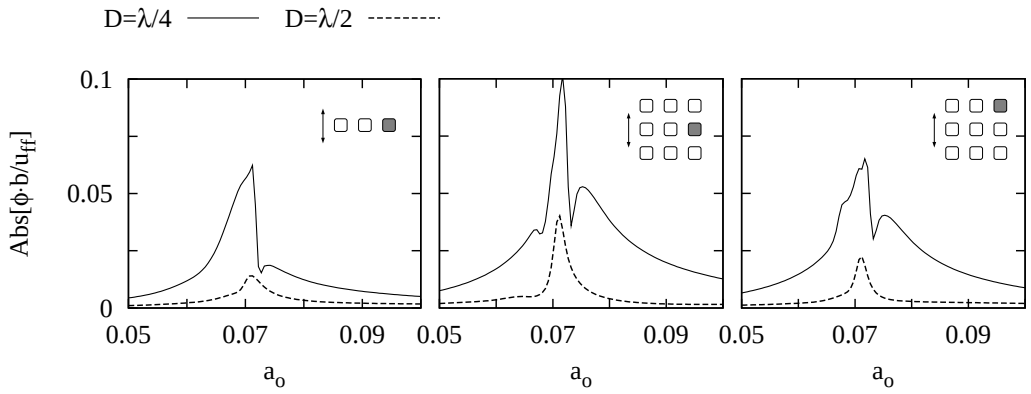

Figura D.16: *Funciones de transferencia del giro de estructuras pilotas debido a la interacción estructura-suelo-estructura. Ondas S de incidencia vertical.* $h/b = 4$. $E_p/E_s = 100$.

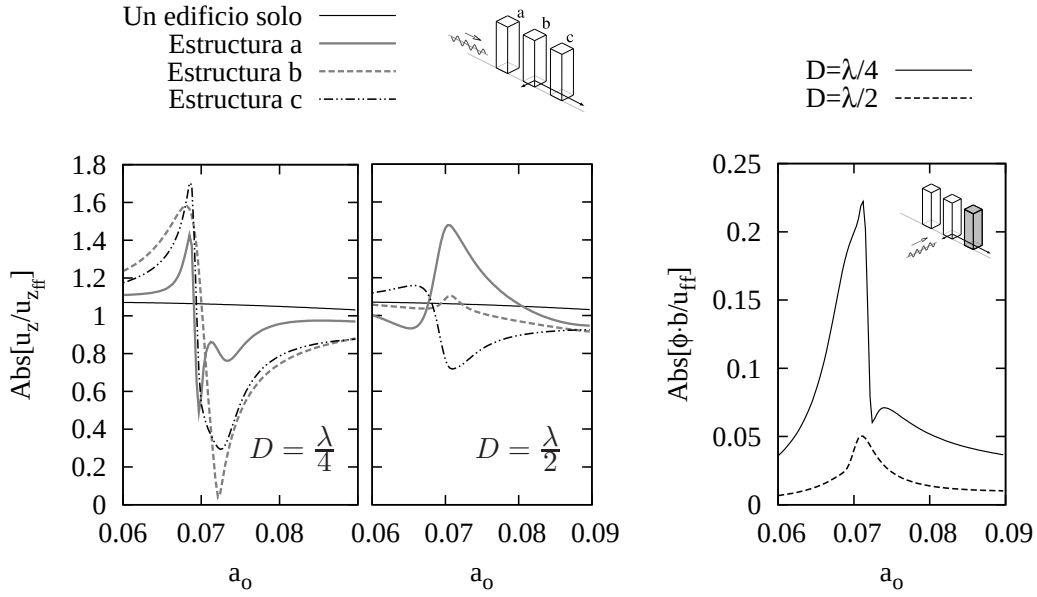

Figura D.17: *Funciones de transferencia del desplazamiento vertical y del giro de estructuras pilotas debido a la interacción estructura-suelo-estructura. Ondas de Rayleigh.* $h/b = 4$. $E_p/E_s = 100$.

ción estructura-suelo-estructura alcanzan magnitudes superiores al 35 por ciento de los desplazamientos horizontales de campo libre en la superficie debidos a las ondas de corte incidentes, mientras que para $D = \lambda/2$, alcanzan valores de entre el 20 y el 30 por ciento. La respuesta rotacional, mostrada en la fig. D.16, tiene también importancia, dado que produce desplazamientos horizontales en los pilotes del orden del 5 al 10 por ciento de los desplazamientos de campo libre. El sistema manifiesta tendencias similares cuando se encuentra bajo la acción de ondas de Rayleigh. En tal caso, mostrado en la fig. D.17, los efectos de interacción estructura-suelo-estructura pueden producir desplazamientos verticales hasta un 70 por ciento superiores que los correspondientes a una sola estructura. Al mismo tiempo, los desplazamientos horizontales en los pilotes debidos a la respuesta rotacional de los edificios son un 20 por ciento superiores a los desplazamientos horizontales de campo libre.

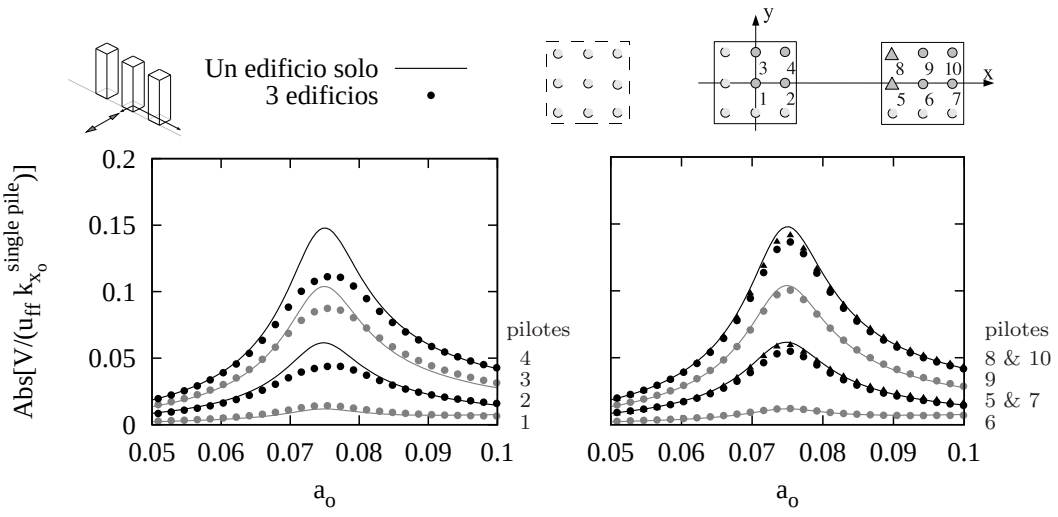

Figura D.18: *Esfuerzos cortantes en la cabeza de los pilotes producidos por la ondas de corte incidentes. Tres edificios alineados perpendicularmente a la dirección de la excitación.* $h/b = 4$. $E_p/E_s = 1000$. $D = \lambda/3$.

Finalmente, en las figs. D.18 y D.19, se comparan los esfuerzos cortantes que aparecen en las cabezas de los pilotes del encepado de una estructura alejada de otras construcciones, con los que aparecen cuando hay tres edificios distanciados $D = \lambda/3$ que están alineados perpendicularmente o paralelamente a la dirección de excitación. En estos casos, correspondientes a la respuesta ante ondas de corte incidentes verticalmente, todos los edificios tienen una relación de aspecto $h/b = 4$. Los esfuerzos cortantes están normalizados por la rigidez estática horizontal de un pilote simple y por el desplazamiento horizontal de campo libre producido por

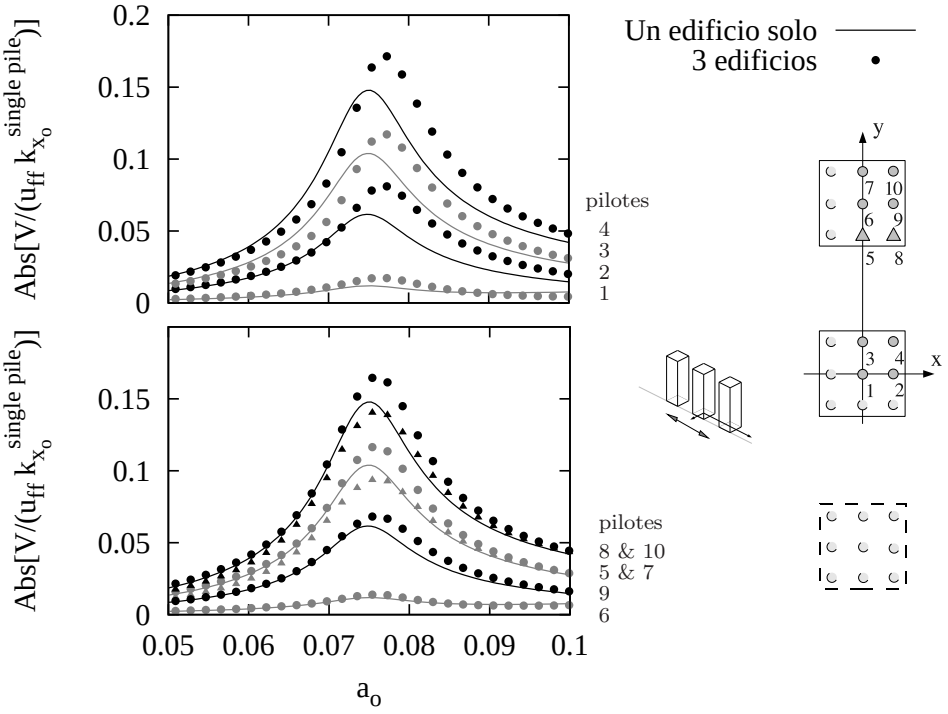

Figura D.19: *Esfuerzos cortantes en la cabeza de los pilotes producidos por la ondas de corte incidentes. Tres edificios alineados a lo largo de la dirección de la excitación.* $h/b = 4$. $E_p/E_s = 1000$. $D = \lambda/3$.

las ondas incidentes. Cuando las estructuras está alineadas perpendicularmente a la dirección de excitación, los esfuerzos cortantes que aparecen en las cabezas de los edificios laterales son prácticamente idénticos a los que aparecen en el caso de un edificio solo. Por el contrario, cuando la excitación produce movimientos en la dirección de alineación de las estructuras, los esfuerzos cortantes se ven incrementados tanto en el edificio central como en los laterales. Más concretamente, los pilotes situados en las esquinas del encepado pueden estar sujetos a fuerzas hasta un 16 por ciento superiores.

D.4.2. Respuesta ante una señal sísmica

En esta sección se presentan algunos espectros de respuesta en aceleraciones con el objetivo de evaluar la influencia de la interacción estructura-suelo-estructura en la respuesta sísmica de las estructuras. Haciendo uso de la transformada rápida

de Fourier (FFT), se obtuvieron resultados en el dominio del tiempo. Se generó, haciendo uso del programa SIMQKE, un acelerograma compatible con el espectro de respuesta normalizado que aparece en el capítulo 5.7 de la AFPS-90 (mostrado en la fig. D.20). La duración total de la señal sintética es de 18 s, y su aceleración pico toma un valor de 0.17 g. Midiendo sobre el espectro de respuesta máxima obtenido con un 5 % de amortiguamiento, la aceleración pico del espectro objetivo normalizado es 0.425 g, mientras que la correspondiente a la señal sintética es de 0.463 g (véase de nuevo la fig. D.20). Por otro lado, la razón por la que se ha utilizado un acelerograma sintético en lugar del registro de un terremoto real es por la mayor suavidad del espectro de respuesta máxima del primero, lo que permite analizar los efectos de los fenómenos de interacción con mayor claridad. Para este ejemplo se han seleccionado una propiedades concretas para el suelo y los pilotes, las cuales han sido resumidas en tabla D.1. Nótese que la frecuencia fundamental del sistema suelo-estructura es $\tilde{T} \simeq 0.40\ s$, y que la relación de aspecto es $h/b = 4$.

Suelo	**Pilotes**	**Estructuras**
$c_s = 239\ m/s$	$E_p = 2.76 \cdot 10^{10}\ N/m^2$	$T = 0.28\ s$
$\rho_s = 1750\ kg/m^3$	$\rho_p = 2500\ kg/m^3$	$m = 7 \cdot 10^5\ kg$
$\nu_s = 0.4$	$d = 1\ m$	$h = 20\ m$
$\beta_s = 0.05$	$L = 15\ m$	$\zeta = 0.05$

Tabla D.1: *Propiedades correspondientes al suelo, los pilotes y las estructuras.*

Se mostrarán a continuación los espectros de respuesta máxima, para un amortiguamiento del 5 por ciento, obtenidos para una única estructura, y para el edificio central de un grupo de tres construcciones con separaciones $D = \lambda/4$ o $D = \lambda/2$, considerando que las estructuras están alineadas en la dirección de excitación, la cual está producida exclusivamente por ondas de corte de incidencia vertical. Dicha excitación está definida por el acelerograma descrito arriba, que es prescrito en la superficie libre. De este modo, las funciones de transferencia de este problema está incluídas entre los resultados mostrados en la fig.D.7.

La fig. D.20 muestra la respuesta del sistema, medida en el encepado, junto a los espectros objetivo y de campo libre, mientras que en la fig. D.21 se presenta la respuesta medida en el forjado a altura h. Obviamente, el valor de la respuesta pico en el encepado se ve fuertemente influenciada por la presencia de la superestructura a frecuencias cercanas al período fundamental del sistema. Por el contrario, se ve poco influenciada por la presencia de otras construcciones vecinas, siendo la variación no superior al 5.6 por ciento. Sin embargo, para períodos cercanos a 0.32

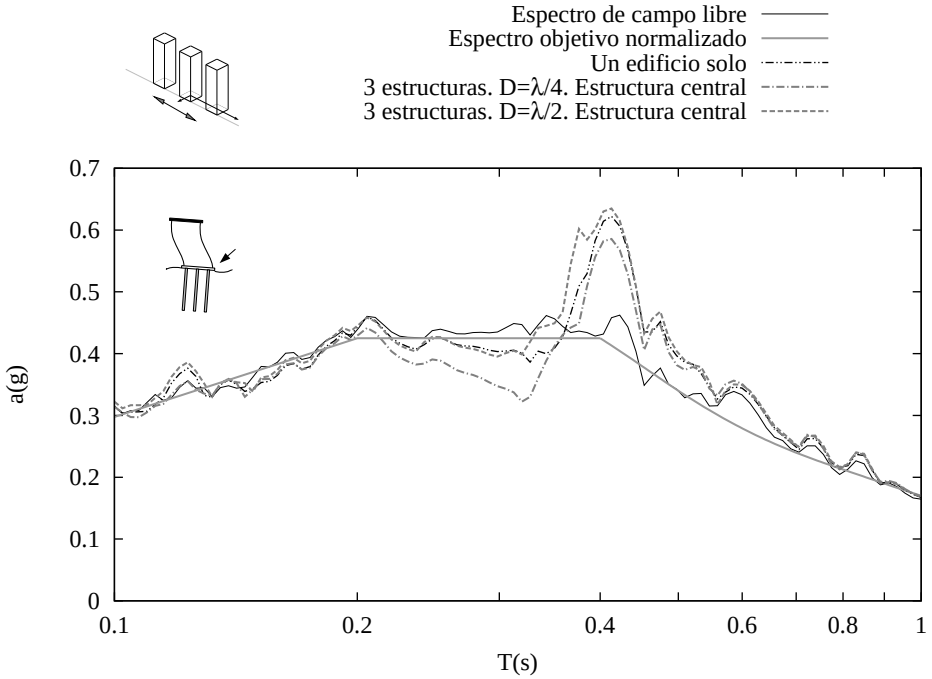

Figura D.20: *Espectros de respuesta máxima (5 % de amortiguamiento). Grupo de tres estructuras ($h/b = 4$) sometido a ondas S de incidencia vertical. Respuesta en el encepado.*

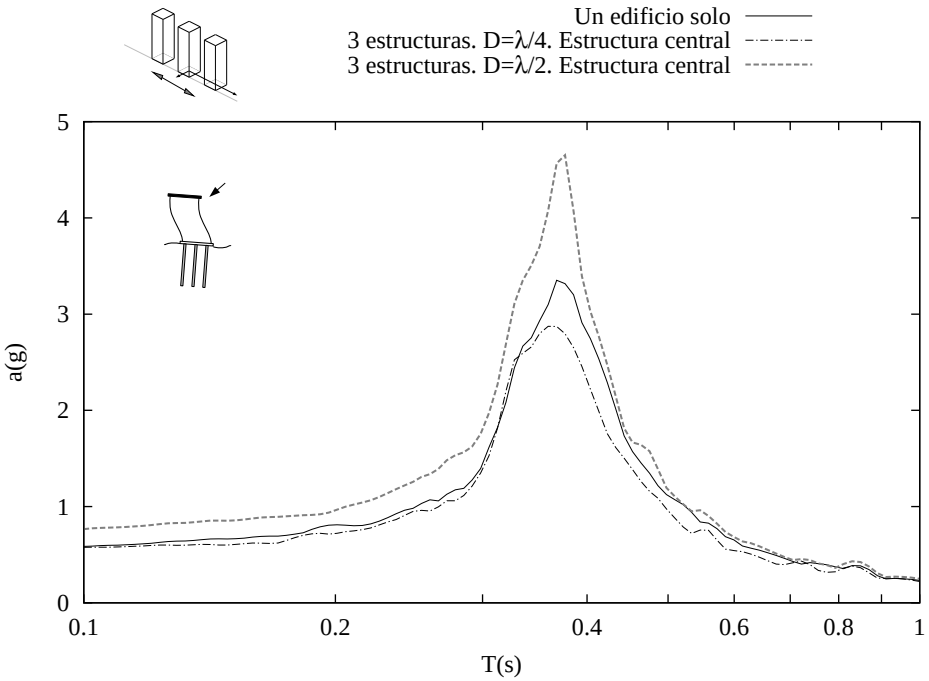

Figura D.21: *Espectros de respuesta máxima (5 % de amortiguamiento). Grupo de tres estructuras ($h/b = 4$) sometido a ondas S de incidencia vertical. Respuesta en el forjado a altura h.*

segundos, las diferencias debidas a la interacción suelo-estructura alcanzan el 20 por ciento. Por otro lado, la respuesta pico del espectro de aceleraciones medida en el forjado a altura h se ve considerablemente influenciada por la presencia de estructuras cercanas. En comparación con la respuesta pico de una única estructura, la estructura central experimenta aceleraciones espectrales un 15 % menores para $D = \lambda/4$ y un 38 % mayores para $D = \lambda/2$, con lo que se muestra que la presencia de estructuras cercanas de características dinámicas similares puede influir significativamente en la respuesta dinámica de una estructura.

Apéndice E

Resumen, conclusiones y desarrollos futuros

E.1. Resumen y conclusiones

Este trabajo propone un nuevo modelo acoplado elementos finitos – elementos de contorno, para el análisis dinámico tridimensional de cimentaciones y estructuras pilotadas. En esta formulación, cada región del suelo es modelada con elementos de contorno como un dominio lineal, homogéneo, isótropo y viscoelástico, mientras que cada pilote es modelado con elementos finitos como una viga vertical de Euler-Bernoulli. Este enfoque considera las tensiones en la interfase pilote-suelo como fuerzas de volumen actuando en el interior del dominio, mientras que la rigidez de los pilotes es introducida a través de elementos finitos longitudinales, sin necesidad de discretizar la interfase pilote-suelo con elementos de contorno. De este modo, la presencia de los pilotes no implica la existencia de un hueco en el dominio que representa el suelo. Por contra, la región suelo es continua en la posición de los pilotes. A primera vista, este hecho podría dar la impresión de que el modelo no es capaz de representar correctamente los efectos de los fenómenos de interacción múltiple que tienen lugar en el sistema pilote-suelo, incluyendo la refracción y reflexión de ondas. Sin embargo, se ha mostrado que la formulación es capaz de ofrecer resultados precisos en problemas con múltiples pilotes sometidos a ondas sísmicas.

Las fuerzas de volumen son consideradas nulas en gran parte de las aplicaciones del método de los elementos de contorno a problemas elastodinámicos. De este modo, la integral de dominio que aparece en la ecuación integral es idénticamente nula. Aquí, por el contrario, las fuerzas de volumen son distintas de cero en la interfase pilote-suelo, por lo que la integral extendida al dominio debe ser evaluada en esa región. Esto no implica, por tanto, que deba discretizarse el dominio, dado la nueva integral es calculada solamente sobre el lugar geométrico de los pilotes.

De hecho, las integrales se evalúan, por lo general, a lo largo de una línea definida por el eje del pilote, sin que ello implique una pérdida de precisión. La excepción aparece cuando el punto de colocación pertenece al elemento que está siendo integrado, en cuyo caso existe una singularidad. Esta situación es resuelta integrando dicho elemento sobre la interfase pilote-suelo, aunque se mostró también que este procedimiento es totalmente equivalente a una estrategia de colocación no nodal.

El modelo de acoplamiento ha sido satisfactoriamente formulado e implementado en un código 3D de elementos de contorno previamente existente, y que pertenece al grupo de investigación de Mecánica de los Medios continuos y Estructuras de la Universidad de Las Palmas de Gran Canaria. De hecho, esta tesis no es más que otro paso en la línea de investigación sobre problemas de interacción suelo-estructura que está siendo llevada a cabo en colaboración con la Universidad de Sevilla, bajo la supervisión de los profesores José Domínguez y Orlando Maeso. El trabajo del grupo de Las Palmas de Gran Canaria se ha centrado principalmente, aunque no en exclusiva, en el desarrollo de una herramienta numérica para el análisis de la respuesta sísmica de presas [111–113, 116]. Este trabajo culminó en la tesis doctoral del profesor Juan José Aznárez [114] quien amplió las posibilidades del código al incluir, entre otras cosas, la posibilidad de modelar regiones de naturaleza poroelástica de acuerdo a la teoría de Biot. Haciendo uso de este código multidominio para problemas tridimensionales, se han realizado diversos estudios sobre el comportamiento dinámico de presas bóveda en presencia de sedimentos porosos [115, 117, 118]. Dicho programa fue también utilizado para obtener impedancias de pilotes y grupos de pilotes en suelos viscoelásticos y poroelásticos [63,64], y fue posteriormente la base del código desarrollado durante la realización de esta tesis doctoral.

Obviamente, el hecho de que no haya necesidad de discretizar las interfases pilote-suelo, provoca una reducción drástica en el número de grados de libertad necesarios. Este era uno de los objetivos del trabajo. Otros objetivos planteados al inicio fueron también alcanzados. En concreto, el código permite un modelado general y relativamente simple de múltiples cimentaciones compuestas por pilotes verticales y encepados rígidos. La discretización del suelo, capaz de modelar la topografía y la estratigrafía del terreno, es completamente independiente de la discretización de las cimentaciones, de modo que distintos análisis que impliquen distintas configuraciones de las cimentaciones, pueden ser realizadas con un pequeño esfuerzo extra a la hora de generar los nuevos ficheros de datos. También se ha formulado e implementado la presencia de múltiples estructuras pilotadas, y hay un amplio conjunto de condiciones de contorno disponibles para el usuario. Finalmente, la formulación completa es relativamente sencilla de implementar en códigos BEM previamente existentes, lo cual puede incrementar su interés y su utilidad para la comunidad científica.

Este esquema acoplado de elementos de contorno y elementos finitos ha sido

utilizado para estudiar diversos problemas relacionados con la respuesta sísmica de cimentaciones y estructuras pilotadas. De estos estudios pueden obtenerse las conclusiones que se exponen a continuación.

Análisis de la distribución de esfuerzos cortantes a lo largo de los pilotes de un grupo

Se ha realizado un análisis de la distribución de esfuerzos cortantes a lo largo de algunos de los pilotes de un grupo de 5×5 sometido a un desplazamiento horizontal impuesto en la cabeza de los pilotes, de donde pueden extraerse las siguientes conclusiones:

- En el estado cuasi-estático,
  - la distribución de los esfuerzos cortantes disminuye de manera aproximadamente exponencial con la profundidad, siendo la parte superior de los pilotes la que soporta la mayor parte de la carga.
  - la *longitud activa* de los pilotes es menor para $E_p/E_s = 10^2$ (suelo duro)
  - el pilote central a, y el que ocupa la esquina d, son los que soportan, respectivamente, las menores y las mayores fracciones de carga.
- Para frecuencias intermedias y altas,
  - la distribución de esfuerzos cortantes en un instante determinado, fluctúa alrededor de cero con la profundidad, con una 'longitud de onda' más corta a mayores frecuencias.
  - la magnitud de los esfuerzos cortantes es máxima en la cabeza de los pilotes, pero puede alcanzar también valores relativamente altos en la mitad inferior del pilote.
  - esfuerzos cortantes significativos pueden aparecer a lo largo de toda la longitud del pilote, y no solamente a lo largo de su *longitud activa*.
  - la fracción de carga soportada por cada pilote del grupo, así como la posición del pilote sometido a mayor carga, dependen de la frecuencia de la excitación.

Rigideces dinámicas de cimentaciones pilotadas en estratos homogéneos

El modelo acoplado de elementos de contorno y elementos finitos, presentado en este trabajo, ha sido utilizado para obtener funciones de impedancia de cimentaciones pilotadas en estratos homogéneos de naturaleza viscoelástica, que descansan

sobre un lecho rocoso. Se han presentado diversos resultados de impedancias verticales, horizontales y de cabeceo para pilotes simples y para tres configuraciones diferentes de grupos de 2×2 pilotes. Se han estudiado distintos valores de la profundidad del estrato, y dos ratios distintos entre los módulos de Young del pilote y el suelo, analizándose los efectos asociados a la variación de estos parámetros. Del análisis de estos resultados pueden extraerse las siguientes conclusiones:

- El sistema pilote-suelo presenta pequeños picos asociados a las frecuencias naturales del estrato, que son estimadas adecuadamente por el modelo numérico.

- Las funciones de impedancia vertical de una cimentación pilotada, embebida en un estrato de las profundidas analizadas, son equivalentes a las de la misma cimentación en un semi-espacio, para frecuencias superiores en más de 1.5 veces a la frecuencia fundamental del estrato en el modo de compresión-extensión. Además, el comportamiento vertical de la cimentación sólo se ve influenciado por esta primera frecuencia.

- La influencia de la profundidad del estrato sobre las funciones de impedancia horizontal de la cimentación es apreciable sobre una banda más ancha de frecuencias. De este modo, aparecen en la curva de respuesta dinámica de la cimentación, diversos picos asociados tanto a modos de corte como a modos de compresión-extensión.

- Esta influencia es incluso más evidente en las funciones de amortiguamiento, que a bajas frecuencias exhiben un valor muy pequeño en comparación con el correspondiente al semiespacio. Por el contrario, sus valores son similares a frecuencias mayores, lo que revela que el principal mecanismo de disipación de energía a frecuencias intermedias y altas está asociado a las ondas superficiales, tanto para el semiespacio como para el estrato.

- La influencia de la presencia de una base rígida es aún apreciable para profundidades del estrato 5 veces superior a la longitud del pilote.

- El efecto grupo es predominante sobre la presencia de la base rígida, especialmente en las impedancias vertical y de cabeceo, casos en los que los picos asociados a las frecuencias naturales del estrato son de pequeña magnitud. Sin embargo, en el caso horizontal, la presencia del lecho rocoso ejerce una influencia mayor y en un rango de frecuencia más amplio. En todos los casos, su influencia aumenta con el ratio s/d.

- El rango de frecuencias en el cual la respuesta de la cimentación se ve influenciada por la presencia de la base rígida, se ve también aumentado con

el incremento de la rigidez del suelo y, al mismo tiempo, un conjunto más amplio de frecuencias naturales del estrato aparecen en las respuestas horizontal y de cabeceo.

- El efecto grupo gana importancia a medida que crece el ratio E_p/E_s.
- El comportamiento a cabeceo es el que se ve menos influenciado por la presencia del lecho rocoso.
- La diferencia entre la respuesta vertical de cimentaciones flotantes y de cimentaciones con pilotes hincados se incrementa con el ratio E_p/E_s, y es siempre apreciable.
- El efecto grupo gana importancia en el caso de pilotes hincados. De hecho, para grupos de pilotes hincados en un estrato duro, las funciones de impedancia vertical tienden a ser equivalentes a las de grupos de pilotes flotantes por encima de una cierta frecuencia que decrece cuando el ratio s/d crece. Así, en estos casos, la longitud activa del pilote es mucho más corta que la profundidad del estrato.

Como puede verse, el efecto de la presencia de un lecho rocoso es de vital importancia para el comportamiento horizontal de pilotes simples y grupos de pilotes, y también para el comportamiento a cabeceo de pilotes simples, mientras que es casi inapreciable para el comportamiento a cabeceo de grupos de pilotes. Respecto al comportamiento vertical de cimentaciones de pilotes flotantes, el efecto de la base rígida no es tan importante, excepto para frecuencias por debajo de 1.5 veces la frecuencia fundamental del estrato. Al mismo tiempo, la influencia del suelo circundante es de gran importancia incluso para pilotes hincados, dado que la influencia de las condiciones de contorno en la punta del pilote tienen menos influencia a medida que el ratio E_p/E_s decrece.

Respuesta sísmica de grupos de pilotes sometidos a ondas de corte de incidencia vertical

Se ha estudiado la respuesta sísmica de un grupo de 3×3 pilotes hincados, embebidos en suelos con diferentes estratigrafías, sometidos a ondas planas armónicas de incidencia vertical, y a dos terremotos diferentes. No pueden extraerse conclusiones generales sin realizar análisis más amplios sobre este tema, pero para este caso concreto, se ha mostrado que:

- la presencia de una capa blanda en la superficie del suelo produce funciones de transferencia en desplazamientos que decrecen mucho más rápidamente

que las correspondientes a cimentaciones en el suelo homogéneo de referencia. De hecho, pueden identificarse claramente dos tendencias distintas, dependiendo de si dicha capa blanda en la superficie es considerada o no.

- la incorporación al modelo de más capas, a distintas profundidades, de materiales con velocidades de corte intermedias, es de menor importancia.

- el campo incidente en la superficie libre es perturbado por la presencia de la cimentación pilotada, siendo la magnitud de dicha perturbación mayor cuando existe una capa superior de material blando. El valor máximo de la perturbación es de orden similar en ambas direcciones: la dirección de los movimientos producidos por la onda S, y su perpendicular.

- la interacción pilote-pilote bajo excitación sísmica es casi inexistente.

- las cimentaciones pilotadas embebidas en suelos no homogéneos, filtran gran parte de los componentes armónicos de la señal sísmica, de tal modo que los espectros de respuesta en aceleraciones resultantes tienen valores significativamente menores que los correspondientes al campo libre.

- la simplificación del perfil del suelo a sólo un estrato o un semiespacio, llevaría a sobrestimar o subestimar, dependiendo de las propiedades del sistema, la excitación en la base de una estructura, en un análisis por subestructuración.

- estas conclusiones son válidas para movimientos sísmicos especificados tanto en la superficie libre como en la base rocosa.

Análisis dinámico de zapatas pilotadas

El comportamiento dinámico, en régimen armónico, de zapatas pilotadas, fue investigado con el ánimo de: en primer lugar, saber si su respuesta sísmica puede ser estimada a partir de la correspondiente a sus componentes analizados por separado; y en segundo lugar, estudiar la influencia, sobre las funciones dinámicas de impedancia, de la pérdida de contacto entre el suelo y la cara inferior de la zapata, lo cual sucede debido a la consolidación del suelo. Con estos objetivos se llevaron a cabo diversos estudios paramétricos.

Se vio que los valores de impedancia obtenidas por superposición de las correspondientes al grupo de pilotes y a la zapata, por separado, son generalmente mayores que los que ofrecidos por el análisis del sistema conjunto. Las diferencias pueden ser atribuídas a los fenómenos de interacción que tienen lugar entre el grupo de pilotes y la zapata embebida, y que son despreciados en la superposición. Más concretamente, los términos de impedancia vertical, horizontal, de cabeceo

y cruzado, pueden ser hasta un 100 %, 50 %, 20 % y 20 % superiores, respectivamente, aunque las diferencias decrecen rápidamente con la frecuencia. Por otro lado, las diferencias en fase están normalmente por debajo de los 20^o, y en el sentido de indicar que el amortiguamiento del sistema actuando conjuntamente, es mayor que el estimado mediante superposición. Este efecto es particularmente significativo en los modos vertical y horizontal, y a bajas frecuencias. Además, se investigó también la dependencia de la respuesta respecto a parámetros tales como la separación entre pilotes adyacentes, o el ratio entre las rigideces de pilote y suelo. El embebimiento de la zapata se reveló como un parámetro de gran importancia, observándose que a mayores embebimientos, menor es la diferencia entre la respuesta del sistema conjunto y la obtenida por superposición. Esta tendencia puede entenderse gracias a la omisión de los efectos de embebimiento en la evaluación de las impedancias de la cimentación pilotada. En conjunto, la aproximación por superposición demostró ser una herramienta ingenieril con posibilidades de uso, con discrepancias medias no superiores al 20 %.

Respecto a los efectos de interacción cinemática, se encontró que las zapatas pilotadas tienden a ser más resistentes al movimiento del suelo que sus partes analizadas por separado. Los factores de interacción cinemática correspondientes al desplazamiento lateral decrecen con la frecuencia a mayor velocidad que los correspondientes al grupo de pilotes o a la zapata por separado, mientras que los factores de interacción cinemática de cabeceo crecen más rápidamente. En general, la respuesta cinemática de las zapatas embebidas constituye una estimación razonable de la respuesta de las zapatas pilotadas.

Respecto a la influencia de la separación zapata-suelo sobre las rigideces dinámicas de las zapatas pilotadas, se ha mostrado que:

- la influencia de la separación es despreciable para frecuencias inferiores a aquellas para las que el efecto grupo comienza a ser importante.

- el efecto de la separación tiene más influencia en la respuesta vertical, y podría disminuir la rigidez del sistema en un 50 % más allá de $a_o = 0.5$. Por otro lado, el cambio en la rigidez es minimizado en el modo de vibración lateral, para el que las diferencias no superan el 20 %.

- La rigidez conjunta de la cimentación no tiene necesariamente que disminuir con la aparición de una separación debida a la consolidación del terreno. En cuanto a las rigideces dinámicas, la relación existente entre las correpondientes a los casos en que existe o no separación, depende del resultado de las interferencias constructivas y destructivas entre las distintas ondas generadas en las interfases pilote-suelo y zapata-suelo, por lo que es una relación dependiente de la frecuencia.

- la pérdida de rigidez de la zapata, debido a la separación por consolidación del terreno, es contrarrestada por el aumento en la rigidez del grupo de pilotes.
- la contribución del grupo de pilotes a la rigidez del sistema es independiente del embebimiento, aunque sí depende de la condición de contacto suelo-encepado. Esta propiedad puede utilizarse para simplificar los modelos cuando se estiman las funciones de impedancia de las zapatas pilotadas por procedimientos de superposición.

Análisis de los efectos de interacción suelo-estructura sobre la respuesta de estructuras pilotadas utilizando el método de la subestructuración

La influencia de los efectos de interacción suelo-estructura en la respuesta dinámica de estructuras pilotadas ha sido estudiada por medio de varios análisis paramétricos en los que se tomaron en cuenta la configuración de la cimentación, la esbeltez de las estructuras, y la rigidez relativa entre estructura y suelo, entre otros parámetros. Se ha visto que los efectos de interacción suelo-estructura pueden ser de importancia para el caso de estructuras pilotadas sobre suelos relativamente blandos, o para estructuras relativamente rígidas, y que esta influencia puede ser tanto beneficiosa como perjudicial, dependiendo principalmente de la esbeltez de la estructura. Posteriormente, se evaluó la sensibilidad de estos resultados a la variación de algunos otros, generalmente considerados de menor importancia, encontrándose que, efectivamente, ejercen una influencia mínima sobre la respuesta del sistema. La influencia de los efectos de interacción cinemática sobre la respuesta dinámica de las estructuras fue también estudiada, viéndose que afecta solamente al factor de amortiguamiento equivalente del sistema.

Interacción estructura-suelo-estructura entre edificios pilotados cercanos bajo excitación sísmica

El modelo numérico propuesto en este trabajo para el análisis dinámico de estructuras pilotadas lineales ha sido utilizado para abordar el problema de la interacción, a través del suelo, entre edificios cercanos. El estudio ha sido realizado sobre un conjunto determinado de parámetros y configuraciones, y no constituye en análisis paramétrico exhaustivo del problema. Se han considerado estructuras a cortante de una sola altura, cimentados sobre un grupo de 3×3 pilotes en un suelo viscoelástico, con diferentes relaciones de aspecto y separaciones entre edificios adyacentes. Se han presentado diversos resultados en forma de espectros de deformación lateral, funciones de transferencia del desplazamiento vertical y del giro, funciones de transferencia de los esfuerzos cortantes en cabeza de pilotes, y espectros de respuesta máxima. Todo ello, con el objetivo de evaluar la influencia

de los fenómenos de interacción estructura-suelo-estructura en la respuesta sísmica de edificios cercanos sujetos a ondas de corte o a ondas de Rayleigh incidentes.

Se ha encontrado que los efectos de interacción estructura-suelo-estructura tienen importancia en el caso de grupos de estructuras con características dinámicas similares, principalmente en cuanto a la respuesta estructural en el entorno de la frecuencia fundamental del sistema. Dependiendo de la distancia entre edificios adyacentes, la cual es expresada en función de la longitud de onda en el suelo $\lambda = c_s\tilde{T}$ a la frecuencia fundamental $\tilde{T}$ del sistema suelo-estructura, la respuesta estructural de cada miembro del grupo puede verse tanto reducida como incrementada. Para ondas de corte de incidencia vertical, y para el conjunto de propiedades y configuraciones utilizado en este estudio, la distancia más desfavorable parece ser $D = \lambda/2$. Para este valor de la separación entre edificios adyacentes, se han observado grandes amplificaciones en la respuesta de los miembros de grupos de tres o cinco estructuras alineadas, e incluso mayores movimientos para el caso de un grupo cuadrado de nueve edificios. Las mayores amplificaciones ocurren en los elementos centrales cuando la onda incidente produce movimientos en la dirección de alineación de las estructuras. Por otro lado, en el caso de grupos de estructuras de características dinámicas muy diferentes, los efectos de interacción estructura-suelo-estructura no son tan importantes, siendo la situación más desfavorable la correspondiente a estructuras rígidas situadas entre estructuras relativamente menos rígidas.

Otro caso estudiado es el de la incidencia de ondas de Rayleigh. Cuando la dirección de propagación de éstas coincide con la dirección de alineación de las estructuras, el primero de los edificios en ser alcanzado es el que sufre los mayores desplazamientos, y los efectos de apantallamiento son claramente observables. En este caso, al contrario de lo que ocurría para las ondas tipo S, la más desfavorable de las distancias ensayadas es $D = \lambda/4$. Por otro lado, cuando las ondas inciden perpendicularmente a la dirección de alineación de las estructuras, las respuestas estructurales se ven, generalmente, atenuadas.

Se ha podido constatar también que los movimientos verticales y rotacionales inducidos por los efectos de interacción estructura-suelo-estructura son significativos. Por ejemplo, la amplitud de los desplazamientos verticales en los edificios laterales de grupos sujetos a ondas S, puede alcanzar valores del orden del 35 por ciento de los desplazamientos horizontales de campo libre. Además, los esfuerzos cortantes en la cabeza de los pilotes también pueden verse considerablemente amplificados.

A la vista de estos resultados, y dado que se ha visto que la respuesta sísmica de una estructura puede verse significativamente amplificada por la presencia de estructuras cercanas, queda claro que es necesario estudiar los efectos de la interacción estructura-suelo-estructura y su influencia en el riesgo sísmico de las estructuras. Debería abordarse la influencia, sobre la respuesta del sistema, de las car-

acterísticas de la cimentación, la configuración y el diseño estructurales, las relaciones entre las propiedades dinámicas de las estructuras vecinas, las propiedades y estratigrafía del subsuelo, y las características de la excitación sísmica.

E.2. Desarrollos futuros

La formulación BEM-FEM presentada en este trabajo ha sido utilizada para realizar varios estudios acerca de la respuesta dinámica y sísmica de cimentaciones pilotadas y de estructuras pilotadas. Utilizando el código en su forma actual, otros estudios interesantes que podrían llevarse a cabo son:

- Un estudio paramétrico sobre la respuesta sísmica de grupos de pilotes sometidos a ondas P y S de incidencia vertical, y a ondas de Rayleigh. De este modo, el estudio presentado en el capítulo C sería ampliado para incluir un conjunto más amplio de configuraciones de la cimentación, de configuraciones del subsuelo, y de características del emplazamiento, considerando distintos tipos de ondas incidentes y ángulos de incidencia. Los resultados deberían presentarse, además de en el dominio de la frecuencia, en el dominio del tiempo para distintos acelerogramas (registrados o sintetizados) con características coherentes con el emplazamiento. De este modo, la influencia de cada parámetro podría ser evaluada, no sólo a través de sus funciones de transferencia, sino también en términos de sus respuestas temporales.

- Un análisis exhaustivo de la influencia de construcciones cercanas sobre la respuesta sísmica de estructuras pilotadas. Este estudio constituiría una extensión del trabajo presentado en el capítulo D, y debería incluir la influencia de parámetros tales como las características de la cimentación, la configuración y el diseño estructurales, las relaciones entre las propiedades dinámicas de las estructuras vecinas, las propiedades y estratigrafía del subsuelo, y las características de la excitación sísmica.

- Un análisis de los esfuerzos cortantes y los momentos flectores inducidos en los pilotes de una estructura pilotada sometida a excitación sísmica. En los modelos lineales de interacción suelo-estructura, estos esfuerzos son considerados como el resultado de dos fenómenos diferentes: (i) los movimientos de la superestructura, y (ii) los movimientos del suelo debidos a las ondas incidentes. El primero produce las denominadas *fuerzas de interacción inercial*, mientras que el segundo da lugar a *fuerzas de interacción cinemática*. En la práctica común, se considera que las fuerzas de interacción inercial, que pueden ser estimadas con relativa facilidad, constituyen la componente de

mayor importancia, mientras se presta, por lo general, menos atención a las fuerzas de interacción cinemática. Sin embargo, algunos trabajos recientes (véase por ejemplo [75–77]) han puesto de manifiesto la importancia de este último componente en el funcionamiento de los pilotes. Por esta razón, es de interés analizar los esfuerzos de origen sísmico en función de parámetros tales como: relación de aspecto de la superestructura, ratio entre las rigideces de suelo y estructura, ratio entre las masas de suelo y estructura, número y posición de las cimentaciones, configuración de las cimentaciones, ratio entre las rigideces de los pilotes y el suelo, estratigrafía del suelo, presencia de estructuras cercanas, y tipo y ángulo de incidencia de la ondas sísmicas.

Por otro lado, el código podría ser mejorado, desde el punto de vista de su implementación, de diferentes maneras, algunas de las cuales son:

- Mediante la implementación de un formato de almacenamiento para matrices escasas, lo que haría posible el almacenamiento y la utilización sólo de los términos de la matriz que sean distintos de cero, con el consiguiente ahorro en espacio de memoria. Es necesario recordar aquí que los bloques de ceros existentes en la matriz de coeficientes son generados, no sólo por el acoplamiento BEM-FEM, sino también por el acoplamiento entre las diferentes regiones BEM.

- Mediante la implementación de nuevos algoritmos iterativos de resolución de los sistemas de ecuaciones y precondicionadores.

- Mediante la paralelización del código, incluso en su forma actual, lo que implicaría una reducción importante en los tiempos de computación.

- Con el objetivo de simplificar el trabajo de mallado y, al mismo tiempo, aumentar la precisión de la solución, podrían implementarse técnicas de refinamiento y suavizado de mallas (ver, por ejemplo, [164, 165]).

- Mediante la reformulación del modelo y su implementación en un código del "fast multipole boundary element method", lo cual permitiría la solución de problemas muy grandes con tiempos de computación muy cortos y con escasos requerimientos de memoria.

Finalmente, tanto la formulación como el código, pueden ser ampliados de diferentes maneras, algunas de las cuales son:

- La formulación de pilotes inclinados, tema que está recibiendo una atención creciente. Incluso, puede generalizarse el problema mediante la consideración de elementos curvilíneos genéricos, con la posibilidad de modelar diferentes

elementos estructurales con múltiples puntos comunes. De este modo, el código puede ser aplicado al análisis de pilotes inclinados, de cimentaciones pilotadas con configuraciones en forma de árbol, y de otras estructuras enterradas, como por ejemplo túneles.

- La implementación de ondas incidentes tipo S y P, con cualquier dirección de incidencia, de modo que sea posible evaluar los efectos de este parámetro sobre la respuesta sísmica de las cimentaciones y las estructuras pilotadas. Esto también permitiría la evaluación del terremoto más desfavorable en relación a algún parámetro, como por ejemplo, la magnitud de los desplazamientos en la superficie del terreno.

- La formulación de un nuevo modelo, basado en la misma aproximación utilizada aquí, para el análisis dinámico de muros embebidos. Dichos muros podrían ser discretizados con elementos finitos tipo placa.

- La formulación de un esquema BEM-FEM capaz de modelar la interacción entre el pilote y el agua circundante, es decir, entre el pilote y una región potencial. Esto conduciría a una formulación más general capaz de modelar el comportamiento dinámico del pilote embebido en un suelo poroelástico.

- La formulación de encepados flexibles a través de elementos finitos tipo placa. Esto permitiría el análisis de grupos de pilotes muy grandes, en los que la consideración de rigidez del encepado es, en general, inaceptable, e implicaría el establecimiento de condiciones de equilibrio y compatibilidad entre el encepado (modelado con elementos finitos) y la superficie del suelo (modelado con elementos de contorno).

- La formulación de una solución fundamental para el semiespacio, con lo que se evitaría la necesidad de discretizar tanto la superficie libre como, en el caso de suelos con estratos horizontales, las interfases horizontales.

Bibliografía

[1] Hall, W. S. and Oliveto, G. (eds.) (2003) *Boundary element methods for soil-structure interaction*. Kluwer Academic Publishers, The Netherlands.

[2] Beskos, D. E. (1987) Boundary element methods in dynamic analysis. *Appl Mech Rev*, **40**, 1–23.

[3] Beskos, D. E. (1997) Boundary element methods in dynamic analysis: Part II (1986-1996). *Appl Mech Rev*, **50**, 149–197.

[4] Domínguez, J. (1978) Dynamic stiffness of rectangular foundations. Report R78-20, Massachusetts Institute of Technology, Cambridge, MA.

[5] Alarcón, E. and Domínguez, J. (1980) Impedance of foundations using the boundary integral equation method. *In Proc. of 2nd Int Symposium on innovative numerical analysis in applied Engineering Sciences*, Montreal.

[6] Alarcón, E., Del Caño, F., and Domínguez, J. (1981) Dynamic stiffness matrices for layered viscoelastic halfspaces and rectangular embedded foundations. *In Proc. of the Annual Meeting of the Seismological Society of America.*, Bechtel Engineering Center. University of California, USA.

[7] Abascal, R. and Domínguez, J. (1986) Vibrations of footings on zoned viscoelastic soils. *J Eng Mech ASCE*, **112**, 433–447.

[8] Apsel, R. J. and Luco, J. E. (1987) Impedance functions for foundations embedded in a layered medium: an integral equation approach. *Earthquake Eng Struct Dyn*, **12**, 213–231.

[9] Luco, J. E. and Wong, H. L. (1987) Seismic response of foundations embedded in a layered half-space. *Earthquake Eng Struct Dyn*, **15**, 233–247.

[10] Gazetas, G. and Tassoulas, J. L. (1987) Horizontal stiffness of arbitrarily shaped embedded foundations. *J Geotech Eng ASCE*, **113**, 440–457.

[11] Gazetas, G. and Tassoulas, J. L. (1987) Horizontal damping of arbitrarily shaped embedded foundations. *J Geotech Eng ASCE*, **113**, 458–475.

[12] Luco, J. E. and Mita, A. (1987) Response of a circular foundation on a uniform half-space to elastic waves. *Earthquake Eng Struct Dyn*, **15**, 105–118.

[13] Rajapakse, R. K. N. D. and Shah, A. H. (1988) Impedances of embedded rigid strip foundations. *Earthquake Eng Struct Dyn*, **16**, 255–273.

[14] Emperador, J. M. (1988) *El Método de los elementos de contorno en problemas elastodinámicos con simetría de revolución*. Ph.D. thesis, Universidad de Las Palmas de Gran Canaria, Las Palmas de G.C., Spain.

[15] Emperador, J. M. and Domínguez, J. (1989) Dynamic response of axisymetric embedded foundations. *Earthquake Eng Struct Dyn*, **18**, 1105–1117.

[16] Alarcón, E., Cano, J. J., and Domínguez, J. J. (1989) Boundary element approach to the dynamic stiffness functions of circular foundations. *Int J Num Meth Geomech*, **13**, 645–664.

[17] Domínguez, J. and Abascal, R. (1989) Seismic response of strip footings on zoned viscoelastic soils. *J Eng Mech ASCE*, **115**, 913–934.

[18] Israil, A. S. M. and Ahmad, S. (1989) Dynamic vertical compliance of strip foundations in layered soils. *Earthquake Eng Struct Dyn*, **18**, 933–950.

[19] Gonsalves, I. R., Shippy, D. J., and Rizzo, F. J. (1990) Direct boundary integral equations for elastodynamics in 3-D half-spaces. *Comput Mech*, **6**, 279–292.

[20] Israil, A. S. M. and Banerjee, P. K. (1990) Effects of geometrical and material properties on the vertical vibration of three-dimensional foundations by BEM. *Int J Num Anal Meth Geomech*, **14**, 49–70.

[21] Ahmad, S. and Bharadwaj, A. (1991) Horizontal impedance of embedded strip foundations in layered soil. *J Geotech Eng ASCE*, **117**, 1021–1041.

[22] Ahmad, S. and Gazetas, G. (1992) Torsional stiffness of arbitrarily shaped embedded foundations. *J Geotech Eng ASCE*, **118**, 1168–1185.

[23] Ahmad, S. and Gazetas, G. (1992) Torsional radiation damping of arbitrarily shaped embedded foundations. *J Geotech Eng ASCE*, **118**, 1186–1199.

[24] De Barros, F. C. P. and Luco, J. E. (1995) Dynamic response of a two-dimensional semi-circular foundation embedded in a layered viscoelastic half-space. *Soil Dyn Earthquake Eng*, **14**, 45–57.

[25] Poulos, H. G. and Davis, E. H. (1980) *Pile foundation analysis and design*. John Wiley & Sons, NY.

[26] Novak, M. (1991) Piles under dynamic loads. *Proc. of the 2nd Int Conf Recent Adv Geotech Earthquake Eng Soil Dyn*, St Louis, Missouri, vol. 3, pp. 250–273.

[27] Pender, M. (1993) Aseismic pile foundation design analysis. *Bull New Zealand Nat Soc Earthquake Eng*, **26**, 49–160.

[28] Pak, R. S. Y. and Jennings, P. C. (1987) Elastodynamic response of the pile under transverse excitation. *J Eng Mech, ASCE*, **113**, 1101–1116.

[29] Rajapakse, R. K. N. D. and Shah, A. H. (1987) On the longitudinal harmonic motion of an elastic bar embedded in an elastic half-space. *Int J Solids Struct*, **23**, 267–285.

[30] Rajapakse, R. K. N. D. and Shah, A. H. (1987) On the lateral harmonic motion of an elastic bar embedded in an elastic half-space. *Int J Solids Struct*, **23**, 287–303.

[31] Abedzadeh, F. and Pak, R. Y. S. (2004) Continuum mechanics of lateral soil-pile interaction. *J Eng Mech ASCE*, **130**, 1309–1318.

[32] Matlock, H. and Reese, L. C. (1960) Generalized solutions for laterally loaded piles. *J Soil Mech Found Div*, **85**, 63–91.

[33] Penzien, J., Scheffley, C. F., and Parmelee, R. A. (1964) Seismic analysis of bridges on long piles. *J Eng Mech Div ASCE*, **90**, 223–254.

[34] Dobry, R., O'Rourke, M. J., Roesset, J. M., and Vicente, E. (1982) Horizontal stiffness and damping of single piles. *J Geotech Eng Div, ASCE*, **108**, 439–459.

[35] Nogami, T. (1985) Flexural responses of grouped piles under dynamic loading. *Earthquake Eng Struct Dyn*, **13**, 321–336.

[36] Dobry, R. and Gazetas, G. (1988) Simple method for dynamic stiffness and damping of floating pile groups. *Géotechnique*, **38**, 557–574.

[37] Gazetas, G. and Makris, N. (1991) Dynamic pile-soil-pile interaction. Part I: Analysis of axial vibration. *Earthquake Eng Struc Dyn*, **20**, 115–132.

[38] Gazetas, G., Fan, K., Kaynia, A. M., and Kausel, E. (1991) Dynamic interaction factors for floating pile groups. *J Geotech Eng Div, ASCE*, **117**, 1531–1548.

[39] Makris, N. and Gazetas, G. (1992) Dynamic pile-soil-pile interaction. Part II: Lateral and seismic response. *Earthquake Eng Struc Dyn*, **21**, 145–162.

[40] Guo, W. and Randolph, M. F. (1997) Vertically loaded piles in nonhomogeneous media. *Int J Numer Analyt Meth Geomech*, **21**, 507,532.

[41] Mylonakis, G. and Gazetas, G. (1999) Lateral vibration and internal forces of grouped piles in layered soil. *J Geotech Geoenviron Eng ASCE*, **125**, 16–25.

[42] Cairo, R., Conte, E., and Dente, G. (2005) Interaction factors for the analysis of pile groups in layered soils. *J Geotech Geoenviron Eng ASCE*, **131**, 525–528.

[43] Cairo, R., Conte, E., and Dente, G. (2005) Analysis of pile groups under vertical harmonic vibration. *Comput Geotech*, **32**, 545–554.

[44] Kausel, E. and Roesset, J. M. (1974) Soil-structure interaction for nuclear containment. *Power Div. ASCE Specialty Conf*, Boulder, Colorado, pp. 469–498.

[45] Blaney, G. W., Kausel, E., and Roesset, J. M. (1976) Dynamic stiffness of piles. *Proc. of 2nd Int Conf Num Meth Geomech*, Virginia Polytech Inst and State Un Blacksburg, VA, pp. 1010–1012.

[46] Kuhlemeyer, R. L. (1979) Static and dynamic laterally loaded floating piles. *J Geotech Eng, ASCE*, **105**, 289–304.

[47] Wolf, J. P. and von Arx, G. A. (1978) Impedance functions of a group of vertical piles. *Proc of ASCE Specialty Conf Earthquake Eng Soil Dyn*, Pasadena, CA.

[48] Velez, A., Gazetas, G., and Krishnan, R. (1983) Lateral dynamic response of constrained-head piles. *J Geotech Eng, ASCE*, **109**, 1063–1081.

[49] Blaney, G. W. and ElÑaggar, M. H. (2000) Numerical analysis of kinematic response of single piles. *Can Geotech J*, **37**, 1368–1382.

[50] Tuladhar, R., Maki, T., and Mutsuyoshi, H. (2007) Cyclic behavior of laterally loaded concrete piles embedded into cohesive soil. *Earthquake Eng Struct Dyn*, **37**, 43–59.

[51] Kaynia, A. M. (1982) Dynamic stiffness and seismic response of pile groups. Report R83-03, Massachusetts Institute of Technology, Cambridge, MA.

[52] Kaynia, A. M. and Kausel, E. (1982) Dynamic behavior of pile groups. *2nd Int Conf on Numerical Methods for offshore piling*, Austin, Texas.

[53] Sen, R., Davies, T. G., and Banerjee, P. K. (1985) Dynamic analysis of piles and pile groups embedded in homogeneous soils. *Earthquake Eng Estruc Dyn*, **13**, 53–65.

[54] Sen, R., Kausel, E., and Banerjee, P. K. (1985) Dynamic analysis of piles and pile groups embedded in non-homogeneous soils. *Int J Numer Anal Geomech*, **9**, 507–524.

[55] Davies, T. G., Sen, R., and Banerjee, P. K. (1985) Dynamic behavior of pile groups in inhomogeneous soil. *J Geotech Eng*, **111**, 1365–1379.

[56] Mamoon, S. M., Kaynia, A. M., and Banerjee, P. K. (1990) Frequency domain dynamic analysis of piles and pile groups. *J Eng Mech, ASCE*, **116**, 2237–2257.

[57] Kaynia, A. M. and Kausel, E. (1991) Dynamics of piles and pile groups in layered soil media. *Soil Dyn Earthquake Eng*, **10**, 386–401.

[58] Miura, K., Kaynia, A. M., Masuda, K., Kitamura, E., and Seto, Y. (1994) Dynamic behaviour of pile foundations in homogeneous and non-homogeneous media. *Earthquake Eng Estruc Dyn*, **23**, 183–192.

[59] Guin, J. and Banerjee, P. K. (1998) Coupled soil-pile-structure interaction analysis under seismic excitation. *J Struct Eng*, **124**, 434–444.

[60] Millán, M. A. and Domínguez, J. (2008) Simplified BEM/FEM model for dynamic analysis of structures on piles and pile groups in viscoelastic and poroelastic soils. *Eng Anal Bound Elem*, p. doi:10.1016/j.enganabound.2008.04.003.

[61] Kattis, S. E., Polyzos, D., and Beskos, D. E. (1999) Vibration isolation by a row of piles using a 3-D frequency domain BEM. *Int J Numer Meth Eng*, **46**, 713–728.

[62] Kattis, S. E., Polyzos, D., and Beskos, D. E. (1999) Modelling of pile wave barriers by effective trenches and their screening effectiveness. *Soil Dyn Earthquake Eng*, **18**, 1–10.

[63] Vinciprova, F., Aznárez, J. J., Maeso, O., and Oliveto, G. (2003) *Problems in structural identification and diagnostic: General aspects and applications*, chap. Interaction of BEM analysis and experimental testing on pile-soil systems, pp. 195–227. Springer-Verlag.

[64] Maeso, O., Aznárez, J. J., and García, F. (2005) Dynamic impedances of piles and groups of piles in saturated soils. *Comput Struct*, **83**, 769–782.

[65] Wolf, J. P., von Arx, G. A., de Barros, F. C. P., and Kakubo, M. (1981) Seismic analysis of the pile foundation of the reactor building of the NPP Angra 2. *Nuclear Eng Design*, **65**, 329–341.

[66] Flores-Berrones, R. and Whitman, R. V. (1982) Seismic response of end-bearing piles. *J Geotech Eng Div ASCE*, **108**, 554–569.

[67] Mamoon, S. M. and Banerjee, P. K. (1990) Response of piles and pile groups to travelling SH-waves. *Earthquake Eng Estruc Dyn*, **19**, 597–610.

[68] Mamoon, S. M. and Ahmad, S. (1990) Seismic response of piles to obliquely incident SH, SV and P waves. *J Geotech Eng, ASCE*, **116**, 186–204.

[69] Fan, K., Gazetas, G., Kaynia, A. M., Kausel, E., and Ahmad, S. (1991) Kinematic seismic response of single piles and pile groups. *J Geotech Eng, ASCE*, **117**, 1860–1879.

[70] Kaynia, A. M. and Novak, M. (1992) Response of pile foundations to Rayleigh waves and obliquely incident body waves. *Earthquake Eng Estruc Dyn*, **21**, 303–318.

[71] Gazetas, G., Fan, K., Tazoh, T., Shimizu, K., Kavvadas, M., and Makris, N. (1992) Seismic pile-group-structure interaction. *Geotech Spec Publ, ASCE*, **34**, 56–93.

[72] Kavvadas, M. and Gazetas, G. (1993) Kinematic seismic response and bending of free-head piles in layered soil. *Géotechnique*, **43**, 207–222.

[73] Ji, F. and Pak, R. Y. S. (1996) Scattering of vertically-incident P-waves by an embedded pile. *Soil Dyn Earthquake Eng*, **15**, 211–222.

[74] Masayuki, H. and Shoichi, N. (1991) A study on pile forces of a pile group in layered soil under seismic loadings. *Proc. of the II Int Conf on Recent Advances in Geotech Earthquake Eng and Soil Dyn*, St Louis, Missouri.

[75] Kaynia, A. M. and Mahzooni, S. (1996) Forces in pile foundations under seismic loading. *J Eng Mech, ASCE*, **122**, 46–53.

[76] Nikolaou, S., Mylonakis, G., Gazetas, G., and Tazoh, T. (2001) Kinematic pile bending during earthquakes: analysis and field measurements. *Géotechnique*, **51**, 425–440.

[77] Mylonakis, G. (2001) Simplified model for seismic pile bending at soil layer interfaces. *Soils Found, Jap Geotech Soc*, **41**, 47–58.

[78] Parmelee, R. A. (1967) Building-foundation interaction effects. *J Eng Mech Div, ASCE*, **93**, 131–152.

[79] Perelman, D. S., Parmelee, R. A., and Lee, S. L. (1968) Seismic response of single-storey interaction systems. *J Struct Div, ASCE*, **94**, 2597–2608.

[80] Parmelee, R. A., Perelman, D. S., and Lee, S. L. (1969) Seismic response of multiple-storey structures on flexible foundation. *Bull Seism Soc Ame*, **59**, 1061–1070.

[81] Sarrazin, M. A., Roesset, J. M., and Whitman, R. V. (1972) Dynamic soil-structure interaction. *J Struct Div, ASCE*, **98**, 1525–1544.

[82] Veletsos, A. S. and Meek, J. W. (1974) Dynamic behaviour of building-foundation systems. *Earthquake Eng Struct Dyn*, **3**, 121–138.

[83] Bielak, J. (1975) Dynamic behavior of structures with embedded foundations. *Earthquake Eng Struct Dyn*, **3**, 259–274.

[84] Wolf, J. P. (1985) *Dynamic soil-structure interaction*. Prentice-Hall, Englewood Cliffs, NJ.

[85] Todorovska, M. I. (1992) Effects of the depth of the embedment on the system response during building-soil interaction. *Soil Dyn Earthquake Eng*, **11**, 111–123.

[86] Avilés, J. and Pérez-Rocha, L. E. (1996) Evaluation of interaction effects on the system period and the system damping due to foundation embedment and layer depth. *Soil Dyn Earthquake Eng*, **15**, 11–27.

[87] Avilés, J. and Pérez-Rocha, L. E. (1998) Effects of foundation embedment during building-soil interaction. *Earthquake Eng Struct Dyn*, **27**, 1523–1540.

[88] Avilés, J. and Suárez, M. (2002) Effective periods and dampings of building-foundation systems including seismic wave effects. *Eng Struct*, **24**, 553–562.

[89] Takemiya, H. and Yamada, Y. (1981) Layered soil-pile-structure dynamic interaction. *Earthquake Eng Struct Dyn*, **9**, 437–457.

[90] Mylonakis, G. (1995) *Contributions to static and seismic analysis of piles and pile-supported bridge piers*. Ph.D. thesis, State University of New York at Buffalo.

[91] Mylonakis, G. and Nikolaou, A. (1997) Soil-pile-bridge seismic interaction: kinematic and inertial effects. Part I. *Earthquake Eng Struct Dyn*, **26**, 337–359.

[92] Kumar, S. and Prakash, S. (1997) Effect of type of foundation on period and base shear response of structures. *Geotech Spec Publ, ASCE*, **70**, 52–68.

[93] Han, Y. and Cathro, D. (1997) Seismic behavior of tall buildings supported on pile foundations. *Geotech Spec Publ, ASCE*, **70**, 36–51.

[94] Koo, K. K., Chau, K. T., Yang, X., Lam, S. S., and Wong, Y. L. (2003) Soil-pile-structure interaction under SH wave excitation. *Earthquake Eng Struct Dyn*, **32**, 395–415.

[95] Stewart, J. P., Fenves, G. L., and Seed, R. B. (1999) Seismic soil-structure interaction in buildings. I: Analytical Methods. *J Geotech Geoenviron Eng ASCE*, **125**, 26–37.

[96] Stewart, J. P., Fenves, G. L., and Seed, R. B. (1999) Seismic soil-structure interaction in buildings. II: Empirical Findings. *J Geotech Geoenviron Eng ASCE*, **125**, 38–48.

[97] Lee, T. H. and Wesley, D. A. (1973) Soil-structure interaction of nuclear reactor structures considering through-soil coupling between adjacent structures. *Nuclear Eng Design*, **24**, 374–387.

[98] Luco, J. E. and Contesse, L. (1973) Dynamic structure-soil-structure interaction. *Bull Seism Soc Ame*, **63**, 1289–1303.

[99] Wong, H. L. and Trifunac, M. D. (1975) Two-dimensional, antiplane, building-soil-building interaction for two or more buildings and for incident plane SH waves. *Bull Seism Soc Ame*, **65**, 1863–1885.

[100] Wang, S. and Schmid, G. (1992) Dynamic structure-soil-structure interaction by FEM and BEM. *Comput Mech*, **9**, 347–357.

[101] Lehmann, L. and Antes, H. (2001) Dynamic structure-soil-structure interaction applying the Symmetric Galerkin Boundary Element Method (SGBEM). *Mech Research Comm*, **3**, 297–304.

[102] Clouteau, D. and Aubry, D. (2001) Modifications of the ground motion in dense urban areas. *J Comput Acoustics*, **9**, 1659–1675.

[103] Tsogka, C. and Wirgin, A. (2003) Simulation of seismic response in an idealized city. *Soil Dyn Earthquake Eng*, **23**, 391–402.

[104] Kham, M., Semblat, J. F., Bard, P. Y., and Dangla, P. (2006) Seismic site-city interaction: main governing phenomena through simplified numerical models. *Bull Seism Soc Ame*, **96**, 1934–1951.

[105] Bard, P. Y., Guéguen, P., Chazelas, J. L., Kham, M., and Semblat, J. F. (2007) Seismic hazard in urban environments: Can man modify the hazard? Martínez-Guevara, J.-B. (ed.), *Proc. of 3ed Congreso Nacional de Ingeniería sísmica*, CIMNE.

[106] Boulanger, R. W., Curras, C. J., Kutter, B. L., Wilson, D. W., and Abghari, A. (1999) Seismic soil-pile-structure interaction experiments and analyses. *J Geotech Geoenviron Eng ASCE*, **125**, 750–759.

[107] Rollins, K. M., Olsen, R. J., Egbert, J. J., Olsen, K. G., Jensen, D. H., and Garrett, B. H. (2003) Response, analysis and design of pile groups subjected to static and dynamic lateral loads. Report UT-03.03, Utah Deparment of Transportation Research and Development Division.

[108] Finn, W. D. L. (2005) A study of piles during earthquakes: issues of design and analysis. *Bull Earthquake Eng*, **3**, 141:234.

[109] Domínguez, J. and Alarcón, E. (1981) *Elastodynamics*. Progress in Boundary Element Methods, Pentech Press Ltd., London, UK.

[110] Medina, F. and Domínguez, J. (1989) Boundary elements for the analysis of the seismic response of dams including dam-water-foundation interaction effects. *Eng Anal Bound Elem*, **6**, 152–157.

[111] Maeso, O. (1992) *Modelo para el análisis sísmico de presas bóveda incluyendo los efectos de interacción suelo-agua-estructura*. Ph.D. thesis, University of Las Palmas de Gran Canaria, Las Palmas de G.C., Spain.

[112] Maeso, O. and Domínguez, J. (1993) Earthquake analysis of arch dams. I: dam-foundation interaction. *J Eng Mech ASCE*, **119**, 496–512.

[113] Domínguez, J. and Maeso, O. (1993) Earthquake analysis of arch dams. II: dam-water-foundation interaction. *J Eng Mech ASCE*, **119**, 513–530.

[114] Aznárez, J. J. (2002) *Efectos de los fenómenos de interacción incluyendo los factores espaciales y sedimentos de fondo en la respuesta sísmica de presas bóveda*. Ph.D. thesis, University of Las Palmas de Gran Canaria, Las Palmas de G.C., Spain.

[115] Aznárez, J. J., Maeso, O., and Domínguez, J. (2001) A 3-D boundary element model for the dynamic analysis of arch dams with porous sediments. *Advan Earthquake Eng*, **9**, 713–722.

[116] Maeso, O., Aznárez, J. J., and Domínguez, J. (2002) Effects of space distribution of excitation on seismic response of arch dams. *J Eng Mech*, **128**, 759–768.

[117] Maeso, O., Aznárez, J. J., and Domínguez, J. (2004) Three-dimensional models of reservoir sediment and effects on the seismic response of arch dams. *Earthquake Eng Struct Dyn*, **33**, 1103–1123.

[118] Aznárez, J. J., Maeso, O., and Domínguez, J. (2006) BE analysis of bottom sediments in dynamic fluid-structure interaction problems. *Eng Anal Bound Elem*, **30**, 124–136.

[119] Matos Filho, R., Mendonça, A. V., and Paiva, J. B. (2005) Static boundary element analysis of piles submitted to horizontal and vertical loads. *Eng Anal Boundary Elem*, **29**, 195–203.

[120] Padrón, L. A., Aznárez, J. J., and Maeso, O. (2006) A BEM-FEM model for studying dynamic impedances of piles in elastic soils. Topping, B. H. V., Montero, G., and Montenegro, R. (eds.), *Proc. of the Fifth Int Conf on Eng Comput Technology*, Stirlingshire, UK, no. 163, Civil-Comp Press.

[121] Padrón, L. A., Aznárez, J. J., and Maeso, O. (2007) BEM-FEM coupling model for the dynamic analysis of piles and pile groups. *Eng Anal Bound Elem*, **31**, 473–484.

[122] Escobar, J. M., Rodríguez, E., Montenegro, R., Montero, G., and González-Yuste, J. M. (2003) Simultaneous untangling and smoothing of tetrahedral meshes. *Comput Meth Appl Mech Eng*, **192**, 2775–2787.

[123] González-Yuste, J. M., Montenegro, R., Escobar, J. M., Montero, G., and Rodríguez, E. (2004) Local refinement of 3-D triangulations using object-oriented methods. *Adv Eng Software*, **35**, 693–702.